

Detector R&D and Sensitivity Study with the First Data
for the Sterile Neutrino Search using J-PARC MLF
Decay at Rest Neutrino

(J-PARC MLFからの静止崩壊ニュートリノを用いた
ステライルニュートリノ探索のための
最初のデータを使用した
探索感度の研究と検出器の開発)

Ph. D. Thesis

Yota Hino

Department of Physics, Tohoku University

December 2020

Abstract

Recently, a variety of neutrino experiments have performed measurement of neutrino oscillation parameters precisely and constructed strict evidences to the fact that neutrinos have non-zero mass. Difference between each neutrino Δm^2 is a unique observable related to the information of neutrino mass in neutrino oscillation experiment, and the largest Δm^2 reported ever is at most $\sim 10^{-3} \text{ eV}^2$. On the other hand, there exists the experimental results: LSND experiment, as a representative, reported muon anti-neutrino to electron anti-neutrino ($\bar{\nu}_\mu \rightarrow \bar{\nu}_e$) oscillation at short baseline equivalent to $\Delta m^2 > 0.2 \text{ eV}^2$ which conflicts the facts reported ever, and it has been left as an anomaly of neutrino oscillation (LSND anomaly).

JSNS² is a neutrino oscillation experiment to search for $\bar{\nu}_\mu \rightarrow \bar{\nu}_e$ oscillation caused by sterile neutrino reported in LSND experiment, which is held in the Material and Life Science Experimental Facility (MLF) of Japan Proton Accelerator Research Complex (J-PARC). The mercury target of MLF produces plenty of $\bar{\nu}_\mu$ from μ^+ decay-at-rest (DAR) which well reflects timing structure of low duty factor proton beam so that not only cosmic-ray induced background but also neutrino background from other mother particles, e.g., pion and kaon, using timing information. The inverse beta decay (IBD) reaction $\bar{\nu}_e + p \rightarrow e^+ + n$ is used to detect $\bar{\nu}_e$ using Gadolinium loaded liquid scintillator (Gd-LS): the positron energy proportional to the original neutrino energy, and gamma rays ($\sim 8 \text{ MeV}$ in total) from thermal neutron capture on Gd can also contribute to accidental background reduction in term of energy and shorter timing difference from the positron timing. These features enable us to perform a direct test to the result of LSND experiment.

The JSNS² detector has been constructed recently, and JSNS² experiment just launched the first data taking on Jun 2020. The data taking period is amount to 10 days equivalent to 1.0 % of the proposed experimental duration, and the data enable us to understand detector response and evaluate the event rate of backgrounds. As a result of the background measurement, we found that cosmic fast neutron gives one of the severe background rate. In order to recover the situation, we investigated hardware upgrades. Based on the behavior of floor gamma ray, it was found that changing the pattern of the lead brick shield efficiently reduces its event rate to 1/6. DIN mixture to the Gd-LS shows good pulse shape discrimination (PSD) capability to reject fast neutron so that the rejection power to neutron can be enhanced from 100, the current design, to 200.

In this thesis, studies and works for detector construction are reported. In addition, the background estimation and expected sensitivity of JSNS² experiment based on the real data are shown.

Contents

1	Introduction	1
1.1	Neutrino Oscillation	1
1.1.1	Sterile Neutrino in $3 + 1$ model	2
1.2	Situation for Sterile Neutrino Search	3
1.3	Motivation of This Thesis	5
2	The JSNS² experiment	7
2.1	Experimental Setup	7
2.1.1	$\bar{\nu}_e$ detection technique	7
2.1.2	Detector design	12
2.1.3	Shield	12
2.1.4	Annual Operation for Experiment	13
2.2	Decay at Rest Neutrino Beam	14
2.3	Signal selection criteria	21
2.4	Detector Simulation	23
2.4.1	Detector geometry	24
2.4.2	Generators for MC simulation	24
3	Detector	33
3.1	The stainless steel tank and the anti-oil-leak tanks	33
3.2	The acrylic vessel	35
3.2.1	Optical quality test	35
3.2.2	Thickness survey	37
3.2.3	Leakage survey	37
3.2.4	Installation	38
3.3	Liquid Level Stabilization System	38
3.4	Internal structures of the detector	39
3.4.1	Veto layer	41
3.5	Photomultiplier tubes	42
3.5.1	Pre-calibration	43
3.5.2	Assembling and Installation	43
3.5.3	Cable feed through	45
3.5.4	High voltage supply and Signal-HV Splitter	47
3.6	Liquid Scintillators	47
3.6.1	Gd-loaded liquid scintillator	47
3.6.2	Gd-LS storage	47
3.6.3	Unloaded Liquid Scintillator	49
3.6.4	Gd-LS/LS Filling and Extraction	51

3.7	Nano-pulsar optical calibration system	51
3.8	Monitoring system	55
3.8.1	Camera system for oil leak alert [41]	57
4	Background Measurement	59
4.1	Triggers and DAQ for the first run	59
4.2	Waveform Analysis	63
4.2.1	Event extraction from wide range waveform	63
4.2.2	Trigger efficiency of the self trigger	67
4.2.3	Variable definition	67
4.2.4	Beam information identification	69
4.3	Calibration	71
4.3.1	PMT Gain	72
4.3.2	Relative FEE Gain	74
4.3.3	Relative Timing Offset	75
4.3.4	Monte Carlo simulation tuning	76
4.4	Event Vertex and Energy Reconstruction	77
4.5	Measurement of Background Rate of each component	82
4.5.1	Cosmic muon tagging (offline muon veto)	83
4.5.2	^{252}Cf data for validation	84
4.5.3	Michel electron	94
4.5.4	Cosmic-ray induced fast neutron	98
4.5.5	Cosmic ray induced gamma ray	103
4.5.6	Gamma ray from the surface of the hatch	104
4.6	Event rate in the signal window	109
4.6.1	Estimation of Event rate in the signal window	109
4.7	Summary of Background Measurement	113
5	Sensitivity Study for Sterile Neutrino Search	115
5.1	Fit Method	115
5.1.1	Systematic Uncertainty	116
5.2	Optimization of Signal Efficiency	116
5.2.1	Summary of Signal Efficiency	127
5.3	Possible Hardware Upgrade	130
5.3.1	Shield Upgrade	130
5.3.2	Reinforcing PSD Capability	130
5.4	Sensitivity for Sterile Neutrino Search	134
5.4.1	Expected Number of Event Estimation	134
5.4.2	Sensitivity	137
6	Future extension	145
6.1	Pion production measurement	145
6.1.1	NA61/SHINE	145
6.2	JSNS ² - II	146
6.2.1	Background estimation	146
6.2.2	Sensitivity	147
7	Conclusion	155

CONTENTS

iii

acknowledgement

160

List of Figures

1.1	Left: a schematic view of the experimental setup of LSND experiment. Right: L/E distribution of the observed $\bar{\nu}_e$ event in LSND experiment, where L is the baseline, and E is the neutrino energy. The blue area corresponds to the expectation of $\bar{\nu}_e$ event on the oscillation assumption. It describes the data (black point) [3] well.	4
1.2	Left: Constraints on short-baseline $\nu_\mu \rightarrow \nu_e/\bar{\nu}_\mu \rightarrow \bar{\nu}_e$ appearance oscillations in 3 active + 1 sterile scenario at 99 % C.L.. Right: Comparison between 99.73 % exclusion limit from disappearance data and the combined allowed region from the appearance data. Their horizontal axis shows the effective mixing angle $\sin^2 2\theta_{\mu e} = 4 U_{e4} ^2 U_{\mu 4} ^2$, and the vertical axis corresponds to Δm^2 [4].	5
1.3	The result of Neutrino-4 experiment [8]. Left: Comparison of the allowed regions of LSND (1, 2), MiniBooNE (3 - 5) and Neutrino-4 (red contour). 6 and 7 shows KARMEN and OPERA [60] 90 % exclusion line, respectively. The parameter $\sin^2 2\theta_{\mu e} \sim \frac{1}{4} \sin^2 2\theta_{14} \sin^2 2\theta_{24}$ is determined by the production of $\sin^2 2\theta_{14}$ from Neutrino-4 and $\sin^2 2\theta_{24}$ from IceCube experiment. Right: Constraints on the parameter space $(\Delta m^2, \sin^2 2\theta_{14})$ among various short baseline reactor neutrino experiments.	6
2.1	The overview of J-PARC facilities.	8
2.2	The MLF building and the location of the JSNS ² experimental setup.	8
2.3	A drawing of the MLF third floor in the bird-eye's view. The detector position is pointed as the red box.	9
2.4	A cross section of the MLF building in the orthogonal plain to the beam direction [11]. The red shaded area corresponds to the hot cell where the mercury target is placed. The detector position is pointed as the green box.	9
2.5	A cross section of the MLF building in the parallel plain to the beam direction [12].	10
2.6	A schematic diagram of delayed coincidence IBD detection used JSNS ² experiment.	11
2.7	A schematic view of the JSNS ² detector.	12
2.8	A photo of the shield below the JSNS ² detector.	13
2.9	The detector and LS operation during the experiment throughout a year [9].	14
2.10	A cut model of an ISO tank with the dimensions labeled [14].	14
2.11	A schematic drawing of the J-PARC spallation neutron source [10].	15

2.12	A schematic drawing of the mercury target in the J-PARC MLF [10].	16
2.13	Time distribution of neutrinos from pion, muon and kaon decays. The origin of the horizontal axis corresponds to beam collision time. Only neutrinos from μ DAR survive after 1 μ s from the proton beam collision timing [10].	17
2.14	Estimated neutrino flux for all components (left) and components after 1 μ s from proton beam timing (right). As a result of timing selection, the μ^+ DAR components are selected and main background component is from μ^- decays [10].	18
2.15	Feynman diagram of μ^+ decay (left) and μ^- decay (right).	20
2.16	Energy (normalized flux) spectrum of μ^+ decay (left) and μ^- decay (right).	20
2.17	$Q_{\text{tail}}/Q_{\text{total}}$ distributions of the IBD events (red) and the cosmic fast neutron events (blue).	23
2.18	The implemented geometry in the JSNS ² RAT simulation. (a) size view, (b) top view, and (c) top view of the shield consist of lead bricks and iron plates	24
2.19	Kinetic energy of positron (red) and neutrino (blue) in IBD interaction. Left: the signal $\bar{\nu}_\mu \rightarrow \bar{\nu}_e$. Right: the background $\bar{\nu}_e$ from μ^-	26
2.20	Kinetic energy of generated electron (left) and positron (right) as final state particles in $^{12}\text{C}(\nu_e, e^-)^{12}\text{N}_{g.s.}$ reaction.	26
2.21	Cross section of $^{12}\text{C}(\nu_e, e^-)^{12}\text{N}_{g.s.}$ reaction. Left: dependence on ν_e energy. Right: angle between the ν_e and the projectile electron [26].	26
2.22	Reproducibility of the ^{252}Cf generator in the Double Chooz far detector [27]. Left: energy distribution for the prompt signal by fission. Right: neutron multiplicity by fission.	27
2.23	Left: kinetic energy distribution of generated electron/positron. Right: 2D histogram for generated vertices in the inner detector in zr^2 plain.	28
2.24	Generator information of cosmic fast neutron. Top left: kinetic energy distribution. Top center: $\cos\theta$ distribution for zenith angle θ . Top right: multiplicity. Bottom left: particle generation point in XY plain. Bottom center: particle generation point in XZ plain. The origin of XYZ coordinate is set to the detector center.	29
2.25	A model of concrete walls in the MLF third floor shows spatial relations to the detector in the XZ plane (left) and the YZ plane (right), respectively. We assumes that cosmic ray induced fast neutron/gamma ray generated in the concrete volume as a result of an interaction between cosmic muon and matter in the concrete. . . .	30
2.26	Neutron generated position distribution in XY plane (left) and in XZ plane (right). The origin of XYZ coordinate is set to the detector center.	30
2.27	Generator information of cosmic fast neutron. Top left: kinetic energy distribution. Top right: $\cos\theta$ distribution for zenith angle θ . Bottom left: particle generation point in XY plain. Bottom right: particle generation point in XZ plain. The origin of XYZ coordinate is set to the detector center.	31
2.28	Kinetic energy distribution of floor gamma.	32

3.1	A side view of the tank and the anti oil-leak tank. The red circles correspond to the LS buffer space, which forms a large ring shape, to prevent a change of liquid level due to thermal expansion of LS. There are eight anti-sloshing blades in the buffer space to disturb the surface of LS from sloshing during crane work for detector installation to MLF, which is drawn as the trapezoid shapes in the red circles.	34
3.2	An entire viewing photo of the detector at HENDEL building. The red-painted square shape wall is anti-oil-leak wall welded on the edge of the tank base. The outer cylindrical structure with JSNS ² logo on the surface is the 1-st anti-oil-leak wall. The most inner and highest structure is the s.s.tank of the detector. There are ladders and decks on the 1st anti-oil-leak tank for accessing to the detector.	34
3.3	A drawing of entire vessel structure.	35
3.4	Drawings and 3D models of leg structure of the vessel. The leg structure above optical separator is glued on the bottom plate of the vessel, and has 6 beams with flat plate (left). I-shaped beam structures is placed below optical separator and fixed on the bottom of the s.s.tank with bolts.	36
3.5	Measured 5 cm transmittance spectrum of the quarried acrylic sample. Note that the transmittance includes an effect of reflection at the boundary.	36
3.6	(a): Detailed thickness survey on the side wall. (b): A histogram of thickness difference from the mean value. The number of measured points is around 100 along the circumference at the center of the side wall. The measured data shows periodical fluctuation as a function of azimuth angle because of manufacturing process; however, the thickness fluctuation is within 1 mm displayed as light blue region.	37
3.7	Left: Environmental conditions as a function of time. The left vertical axis is for the inner gas and atmospheric temperature data, and the right one is for the atmospheric pressure. Right: time evolution of the inner gas pressure with respect to atmospheric pressure. The black markers with error bar corresponds to the data points, and the blue line shows the prediction from no leak assumption. The horizontal axes show time. 30000 is the start time of the measurement.	38
3.8	(a): The installed acrylic vessel. (b): A photo of work for fixing the vessel to the detector from the vessel lid.	39
3.9	Top left: a conceptual diagram of the liquid level stabilization system. Bottom left: a photo of entire view of the system. Right: a photo of pipe lines for making inverse siphon.	40
3.10	A design of support skeleton units for barrel part. Left shows the position of the base L-angles for fixing the skeleton structures. Right exhibits a box unit support structure and an image of installed status. Each unit contains 5 PMTs with 5 rectangle black boards.	40
3.11	(a) A 3D model of the PMTs on the top lid and their support structures. (b) Drawings of the optical separators for the bottom part. The white lines shows the drawings of supplemental optical separator for filling gaps among the boards.	41

3.12	(a) A photo of the reflection sheet attached to the black board. (b) A photo of the top lid veto layer after installation. One can find that most of the surfaces, such as the PMTs, the s.s.tank, and the optical separator, is covered with reflections sheet.	42
3.13	(a) A side view drawing of PMT R7081 [34]. (b) A drawing of the dark box used for the pre-calibration.	42
3.14	(a) An example of the result of gain curve measurement. The black dots shows the measured gain at each high voltage value, and the red line is a fitting result with the function defined in equation (3.1) [36]. (b) A distribution of high voltage values at a gain of 10^7 [36]. The dashed line shows a distribution of the newly purchased PMTs. The solid line is that of the donated PMTs.	43
3.15	(a) A drawing of the PMT support ring. (b) A photo of fused deposition modeling 3D Printer for JSNS ² . The maximum printable size is 30 cm × 30 cm × 30 cm. It takes roughly 8 hours for printing out one ring.	44
3.16	(a): The covers and support ring to be assembled to one PMT. (b) to (e) shows the order of assembling covers, ring and angle jigs. . .	44
3.17	(a): A photo of an installed PMT before being covered with a black board. PMTs are eventually fixed at the angle jig and the black board via the PMT ring. (b) A photo of PMT installation work to the top lid. (c) A part view of complete installation of PMTs and optical separators.	45
3.18	A drawing of cable feed through flange.	46
3.19	A series of photos of the sealing process. Left: preparation before filling epoxy. Center: after filling. Right: after being closed and fixed to the flange port on the s.s. tank.	46
3.20	Left: A photo of sealing test setup. Center: A schematic view of the test setup. Right: Measured inner gas pressure with respect to the atmospheric pressure as a function of time (black marker). The blue line is the fit result with an exponential function.	47
3.21	A series of photos exhibiting the procedure of the titration.	48
3.22	Left: Measured 10 cm transmittance spectra of the sampled Gd-LS in the entire range. Right; The spectra zoomed in the region surrounded by the dashed box in the left plot. The blue line indicates spectrum of the sample in the first survey with the expected uncertainty displayed as gray shaded region. The black line is that of the sample obtained in the second survey. Both spectra are identical within the uncertainty in the range of 350 to 600 nm.	49
3.23	(a) A photo of LS production facility in RENO site. (b) A schematic diagram of the LS mass production system modified from the one that was used for the RENO experiment. The LAB goes through a micro-filter of 0.5 μm pore size. The black, blue and gray line correspond to the route of LAB (or LS) flow, ultra-pure water (not used), and nitrogen gas flow, respectively.	50

3.24	Left: a schematic of the setup for light yield measurement. Right: distributions of charge corresponding to scintillation light yield at ~ 0.48 MeV electron recoil. The red marker shows the measurement result of the LS, and the green one corresponds to that of the Gd-LS.	50
3.25	A schematic diagram of the LS filling and extraction. The light blue lines indicate pipe lines for the Gd-LS, and the light green one is for the LS. Sequences of filling and extraction operation is categorized into four stages corresponding to boundaries of the optical separator and the vessel for safe operation.	51
3.26	(a) A photo of the entire view of the setup for filling and extraction. The stacked ISO tanks contain the LS, and the other next to the detector is for the Gd-LS. (b) photos of the veto layer (left) and the inner detector region (right) during the filling. The red arrows point the liquid level at that time.	52
3.27	A history of liquid level height during the filling, data-taking, and extraction. The black and red line corresponds to the level of the Gd-LS and the LS, respectively.	52
3.28	A schematic view of the pulserhead positions and cable routing to the controller box. The blue and violet markers correspond to the visible and UV LEDs, respectively.	53
3.29	The emission spectrum of the UV LEDs (left) and the visible LEDs (right).	54
3.30	The timing structure of emitted light pulse of the UV LEDs (left) and the visible LEDs (right).	54
3.31	(a): A drawing of covers for the pulser head made using 3D printer. In order to avoid cable connector interference the cover separately consists of front and back part. (b): A photo of the LED module installed in the detector. The module and cover are tightly fixed with a bolt and a nut on to the black board, and finally surrounded by reflector sheet.	54
3.32	A schematic view of the positions of devices for monitoring. The red arrows indicates the range of each level sensor or the direction which the web camera looks towards.	55
3.33	A block diagram of data acquisition system for sensors and HV [38].	56
3.34	A screenshot of the grafana page for sensor log.	56
3.35	A screenshot of the grafana page for HV log.	57
3.36	A photo of the oil test paper before (left) and after oil exposure (right).	57
4.1	(a) History of beam power at MLF in the data taking period. Averaged beam power over a hour is plotted as a function of time in date. Sudden decreases in power were caused by short time beam stop for some reason in the facility side. Note that there was facility maintenance beam off period for 24 hours on June 10. (b) The integrated POT recorded in data.	60
4.2	A schematic diagram of DAQ and data flow for the first run.	61
4.3	A schematic diagram of timing structure of the kicker trigger. The red pulse illustrates activity in the detector caused by beam spill to the target, which can be a signal of IBD interaction and so on.	61

4.4	(a) A block diagram of trigger logic for the self trigger. (b) A block diagram of logic for the online muon veto.	62
4.5	A schematic diagram of timing structure of the trigger pulse (top one) and the associated veto logic pulses illustrated in inverse of the trigger pulse.	63
4.6	A history of DAQ efficiency in the first run. The total efficiency was 94.5%. The efficiency loss is caused by setup change and HV crate exchange.	64
4.7	An example of waveform with low frequency noise observed during the dry-run commissioning. The vertical axis indicates pulse height in a unit of FADC count. The sharp peak around 700 ns corresponds to a pulse from the LED illumination.	65
4.8	An example of hit discrimination using differential waveform. the top panel shows a raw waveform recorded at the FADC. Its differential waveform is displayed in the bottom panel. The red line in the bottom panel exhibits threshold level to discriminate single p.e. hit.	65
4.9	Left: a correlation between pulse height of differential waveform (horizontal axis) and that of raw waveform (vertical axis). The red dashed line corresponds to the threshold level for the single p.e. hit discrimination. Right: pulse height distributions of all events (black markers) and events with hit (red markers). The blue line shows a fit result with an exponential and gaussian function as a model for single p.e..	66
4.10	Left: single p.e. detection efficiency of the hit discrimination condition for each ID PMT. Right: the distribution of the single p.e. detection efficiency. It indicates that the condition can ensure at least 60 % efficiency for single p.e. detection over the PMTs.	66
4.11	Top: the total number of p.e. distributions of all generate events (red) and the events with more than 20 hit. Note that they are obtained from the MC simulation of neutron capture events. The peaks at ~ 250 and ~ 900 p.e. correspond to nH and nGd peak, respectively. Bottom: the efficiency of the event definition condition (the number of hit > 20) as a function of the total number of p.e.. The efficiency reaches to 99 % at 100 p.e. equivalent to 1 MeV.	68
4.12	An example of number of hit waveform. The dashed rectangles colored green, blue and orange indicate the defined event windows. The red solid box shows beam on-bunch timing region.	69
4.13	Top: the total number of p.e. distributions of all events (red) and the events with more than 80 mV A.S.PH (blue). Bottom: the trigger efficiencies of all events (black line), events in the top half volume (red) and events in the bottom half volume (blue) as a function of the total number of p.e.. The efficiencies are consistent with 100 % above 450 p.e. equivalent to 4 MeV.	70
4.14	(a) The definition of variables computed from a waveform. (b) an example of CFD waveform. The red point indicates zero crossing point used as timing.	71

4.15	An example waveform of kicker (blue) and CT (red) pulses. The vertical axis corresponds to pulse height in a unit of FADC count, and the horizontal axis shows time in a unit of nano second. The CT pulse has 2 bunch structure reflecting the proton beam spill.	71
4.16	Left: Charge distribution of PMT No.4 in the inner detector as a result of gain calibration run using LED 12. Right: Charge distributions PMT No.103 in the veto layer. The blue marker shows data, and green line represents fitting result with single gaussian.	73
4.17	Gain distribution for all PMTs. The blue shaded one shows gain distribution of the inner PMTs, and the green one is for veto PMTs.	74
4.18	Correlation between NPE ratio of LG to HG and NPE in high gain channel assuming that the typical gain of FEE is 0.7 and 16 for low gain and high gain, respectively. The dashed green line exhibits the selection region for correction factor computation.	75
4.19	A schematic diagram of timing calibration using the nano-pulsar LED system.	75
4.20	(a) A histogram of timing difference between signal on PMT 7 and external trigger pulse from LED 4. (b) Relative timing difference for all PMTs. Trigger timing difference unique to each LED are corrected using timing of the overlapped PMTs. The origin in the vertical axis is arbitrary; however, the relative values among PMTs are calibrated. The colors of marker classify cable length of PMT.	77
4.21	Event selection criterion displayed by blue dashed box for the data (a) and the MC (b), respectively.	77
4.22	A map of the PMT groups.	78
4.23	The observed NPE response of each PMT group when the ^{252}Cf source deployed at the center ($z = 0$ cm). Both response of the data (black dots) and the MC (red dashed line) are overlaid to compare them.	78
4.24	The observed NPE response of each PMT group when the ^{252}Cf source deployed at $z = 50$ cm (left) and -50 cm (right). Both response of the data (black dots) and the MC (red dashed line) are overlaid to compare them.	79
4.25	The observed NPE response of each PMT group when the ^{252}Cf source deployed at $z = +75$ cm (left) and -75 cm (right). Both response of the data (black dots) and the MC (red dashed line) are overlaid to compare them.	79
4.26	The observed NPE response of each PMT group when the ^{252}Cf source deployed at $z = +100$ cm (left) and -100 cm (right). Both response of the data (black dots) and the MC (red dashed line) are overlaid to compare them.	80
4.27	An example of the response map of the group top 0. The vertical and horizontal axes correspond to a distance between a vertex and PMT r and $\cos\theta$ of a zenith angle to the vertex θ . The z axis exhibited as color graduation represents expected number of p.e. per MeV at each vertex.	81
4.28	A schematics of the coordinate in the response map.	81

4.29	The measured PMT response representing a saturation effect in 10 inch PMT R7081 at the gain of the inner PMT [46]. The red points are the measured data, the black line indicates the fitting result based on the model function given by Eq. (4.12), respectively. The uncertainty of the fitting is displayed as the green area.	82
4.30	Left: selection criteria for cosmic muon tagging. Events in the outside of the red dashed box are defined as activities caused by cosmic muon. Right: Energy distribution in common logarithm scale before (black) and after muon veto (red) in the horizontal axis.	83
4.31	Correlation between pulse height of the veto top analog sum signal (vertical) and total charge in the veto layer $Q_{\text{total}}^{\text{Veto}}$ (horizontal). The former is used for online muon veto by applying 75 mV threshold equivalent to 200 p.e..	84
4.32	Delayed coincidence for the data with the ^{252}Cf source positioned at $z = 0$ cm along the z axis. Top left: prompt visible energy. Top right: delayed visible energy. Middle left: $\Delta t_{\text{p-d}}$. Middle right: $\Delta VTX_{\text{p-d}}$. Bottom left: multiplicity of delayed signal. Bottom right: total charge in the veto layer. Each distribution of variable is applied all selections except for the selection to itself. The red boxes show the selection criterion to each variable. The green marker corresponds to correlated event candidates, and the blue one shows the estimated accidental coincidence events. The accidental subtracted distribution is displayed as the black marker in the plots.	86
4.33	A schematic of delayed coincidence for correlated events. Accidental coincidence is estimated using off timing window.	87
4.34	Time constant τ as a result of the fitting to the $\Delta t_{\text{p-d}}$ distribution with an exponential function at each source position. They are in agreement within 2 % each other.	87
4.35	Left: the delayed energy spectrum with the nGd and nH peak fittings in case the source is at $Z = 0$ cm. Right: the energy resolution at each position as a function of the visible energy.	88
4.36	Delayed visible energy (left) and Δt distribution (right) at $z = 0$ cm. The black marker shows the data points after accidental subtraction. The blue shaded histogram is the MC simulation output.	89
4.37	Delayed visible energy (left) and Δt distribution (right) at $z = +50, +75, +100$ cm from the top. The black marker shows the data, and the blue shaded area corresponds to the MC simulation output, respectively.	90
4.38	Delayed visible energy (left) and Δt distribution (right) at $z = -50, -75, -100$ cm from the top. The black marker shows the data, and the blue shaded area corresponds to the MC simulation output, respectively.	91
4.39	The selection efficiency of delayed visible energy (left) and that of Δt selection (right) at each source position. The efficiencies estimated based on the data (black) and the MC simulation (blue) are displayed simultaneously.	92

4.40 Comparisons of the reconstructed vertex between data and MC at $z = 0$ cm. Top: x , middle: y , bottom: z of the reconstructed vertex, respectively. 92

4.41 Difference of reconstructed vertex between data and MC about z at various source positions. They agreed with each other within \pm cm difference over the range. 93

4.42 Delayed coincidence for Michel electron selection. Top left: prompt visible energy. Top right: delayed visible energy. Middle left: Δt_{p-d} . Middle right: ΔVTX_{p-d} . Bottom left: multiplicity of delayed signal. Bottom right: total charge in the veto layer. Each distribution of variable is applied all selections except for the selection to itself. The red boxes show the selection criterion to each variable. The green marker corresponds to correlated event candidates, and the blue one shows the estimated accidental coincidence events. The accidental subtracted distribution is displayed as the black marker in the plots. 95

4.43 Fitting result to Δt_{p-d} distribution with an exponential function exhibited as the blue line. The black marker shows the accidental-subtracted histogram identical with the middle left plot in Fig. 4.42. 96

4.44 Left: the fitting result (blue line) to the Michel electron spectrum obtained from the data (black markers). Right: $\Delta\chi^2$ curve of the fitting. The estimated constant term is $4.61^{+0.20}_{-0.18}$ %, which can be interpreted as an averaged value over the target volume. 97

4.45 Comparative plots of Michel electron events between data and MC simulation. Top left: the visible energy spectrum. Top right: Z distribution. Bottom left: $\rho = \sqrt{x^2 + y^2}$ distribution. Bottom right: $R = \sqrt{x^2 + y^2 + z^2}$ distribution. The black marker shows spectrum of the accidental-subtracted data, and the blue shaded area is that of the MC simulation. 97

4.46 Delayed coincidence for cosmic fast neutron selection to the data obtained using the self trigger without the online veto. Top left: prompt visible energy. Top right: delayed visible energy. Middle left: Δt_{p-d} . Middle right: ΔVTX_{p-d} . Bottom left: multiplicity of delayed signal. Bottom right: total charge in the veto layer. Each distribution of variable is applied all selections except for the selection to itself. The red boxes show the selection criterion to each variable. The green marker corresponds to correlated event candidates, and the blue one shows the estimated accidental coincidence events. The accidental subtracted distribution is displayed as the black marker in the plots. 99

- 4.47 Delayed coincidence for cosmic fast neutron selection to the data obtained using the self trigger with the online veto. Top left: prompt visible energy. Top right: delayed visible energy. Middle left: Δt_{p-d} . Middle right: ΔVTX_{p-d} . Bottom left: multiplicity of delayed signal. Bottom right: total charge in the veto layer. Each distribution of variable is applied all selections except for the selection to itself. The red boxes show the selection criterion to each variable. The green marker corresponds to correlated event candidates, and the blue one shows the estimated accidental coincidence events. The accidental subtracted distribution is displayed as the black marker in the plots. 100
- 4.48 Distributions of prompt visible energy (top left), delayed visible energy (top right), Δt (bottom left), and ΔVTX (bottom right). The blue shaded area shows MC output of each variable overlaid with the data (black marker) in order to compare them. 101
- 4.49 The event vertex distribution in the detector. The histograms of z , $\rho = \sqrt{x^2 + y^2}$ and $R = \sqrt{x^2 + y^2 + z^2}$ are placed in the order of the top to the bottom. The plots in the left hand size corresponds to the histogram of the prompt signal, and the plots in the right hand side shows that of the delayed signals, respectively. The blue shaded area shows MC output of each variable overlaid with the data (black marker) in order to compare them. 102
- 4.50 Left: the single rate energy spectrum in the beam off period (black marker) with its components classified by color. Right: the residual energy spectrum after subtraction (green marker) corresponding to the green shaded area in the left plot. The overlaid spectrum (blue shaded area) shows the MC simulation of cosmic gamma, and consistently agree with the residual spectrum from the data above 5 MeV. 104
- 4.51 Left: Correlation between visible energy and event timing of the prompt signal. Right: Correlation between visible energy and event timing of the delayed signal. The origin of the horizontal axes in each plot are set to the beam timing. The red dashed boxes show the selection criteria to the prompt and the delayed signal, respectively. 105
- 4.52 Delayed coincidence for nGd events correlated to on-bunch neutron in run 1416. Top left: prompt visible energy. Top right: delayed visible energy. Middle left: Δt_{p-d} . Middle right: ΔVTX_{p-d} . Bottom left: multiplicity of delayed signal. Bottom right: total charge in the veto layer. Each distribution of variable is applied all selections except for the selection to itself. The red boxes show the selection criterion to each variable. The green marker corresponds to correlated event candidates, and the blue one shows the estimated accidental coincidence events. The accidental subtracted distribution is displayed as the black marker in the plots. 106
- 4.53 The prompt vertex (left) and the delayed vertex distribution (right) in the XY plane. The biased vertex distributions in $y > 0$ cm region reflects the incoming direction of beam on-bunch fast neutron. The mercury target exists in the +y direction in the detector coordinate. 107

4.54	The nGd event subtraction from single rate spectrum in run 1416 for example. Left: all range. Right: zoomed into the red arrow region in the left plot.	107
4.55	The nGd event subtracted spectrum (black marker) for all runs listed in table 4.6. The spectrum shape is described by floor gamma (blue shaded area), cosmic gamma (red shaded area) and Michel electron (green shaded area) in the range of 4 to 100 MeV.	108
4.56	ΔVTX_{OB-d} distribution in the condition $7 < E_{vis}^{ID} < 12$ MeV when on-bunch event exists. The beam unrelated events, e.g., IBD and cosmic fast neutron, belongs to the accidental distribution (blue markers). The black marker distribution shows nGd events correlated with beam on-bunch neutron.	111
4.57	A schematic of algorithm for accidental coincidence estimation.	111
4.58	Delayed coincidence for the IBD event selection. Top left: prompt visible energy. Top right: delayed visible energy. Middle left: Δt_{p-d} . Middle right: ΔVTX_{p-d} . Bottom left: ΔVTX_{OB-d} . Each distribution of variable is applied all selections except for the selection to itself. The red boxes show the selection criterion to each variable. The green marker corresponds to correlated event candidates, and the blue one shows the estimated accidental coincidence events. The accidental subtracted distribution is displayed as the black marker in the plots.	112
4.59	Correlation between Δt_{beam-p} (vertical axis) and Δt_{p-d} (horizontal axis). The FADC window size ($25 \mu s$) naturally limits timing information used in the selection.	113
5.1	The measured timing profile of the proton beam to the mercury target [55].	118
5.2	Left: The timing profile of signal as a function of signal timing with respect to beam timing. Right: The estimated signal efficiency as a function of end point of the selection criterion. The red line indicates the efficiency value in case of $1.5 < \Delta t_{beam-p} < 10 \mu s$	118
5.3	Correlations between Δt_{beam-p} (vertical axis) and Δt_{p-d} (horizontal axis) of the signal (top), the accidental backgrounds (middle), and cosmic fast neutron events (bottom).	120
5.4	Top: distributions of log-likelihood value, middle: selection efficiency as a function of selection value of log-likelihood for the signal (red), the accidental events (green) and cosmic fast neutron (blue). Bottom: the enhance curves of signal to accidental (green) and signal to fast neutron (blue).	121
5.5	Top: The delayed energy distribution of the IBD simulation (black) and the accidental events during beam operation (green). Middle: selection efficiency as a function of the endpoint of the delayed energy selection of signal (black) and background (green). Bottom: The enhance curve of signal to accidental background efficiency.	123
5.6	Δt_{p-d} distribution of the data with ^{252}Cf at the $Z = 0$ cm (black marker) and the signal MC output.	124

- 5.7 Prompt visible energy spectra of the signal (blue shaded area) and the background IBD events (orange line). The red dashed box corresponds to the selection criterion. The selection efficiencies are 95.5 % for the signal and 93.4 % for the background IBD, respectively. Note that the signal spectrum shows the 100 % oscillation case. 125
- 5.8 Top: Distributions of ΔVTX_{OB-d} for the correlated delayed event with on-bunch activity (black) and the events accidentally coincided with on-bunch activity (blue). Note that the signal IBD will be accidental in this case. Middle: efficiency curves as a function of cut line of the selection to the signal (blue) and the on-bunch correlated event (black). Bottom: enhance curve of signal to on-bunch correlated delayed event. 126
- 5.9 Top: ΔVTX_{p-d} distribution of the fast neutron sample (red marker) and the accidental sample (green) in the data, respectively. The blue dashed line shows that of the IBD from the signal MC simulation. Middle: efficiency curves as a function of cut line of the selection in the same color classification. Bottom: enhance curves: signal to fast neutron (red), signal to accidental (blue) and fast neutron to accidental (green). Spike on the curves is due to poor statistics below 80 cm. 128
- 5.10 MC simulation result in the current JSNS² shield configuration. Left: True deposited energy in the detector. Right: Event vertex distribution in the detector. The horizontal axis shows r^2 of the vertex, and the vertical axis corresponds to z of the vertex. The gray rectangles illustrate the lead shield coverage. 131
- 5.11 MC simulation result in the upgraded shield configuration. Left: True deposited energy in the detector. Right: Event vertex distribution in the detector. The horizontal axis shows r^2 of the vertex, and the vertical axis corresponds to z of the vertex. The gray rectangles illustrate the lead shield coverage. 131
- 5.12 (a) A photo of the setup for PSD capability measurement. 100 mL of each DIN mixed Gd-LS sample contained in the 2 inch vial was exposed to ²⁵²Cf source, and 10 inch PMT (R7081) observed scintillation light from the sample. (b) Definition of variables especially Q_{tail} . The integration range is from 30 ns to 200 ns after the peak. 132
- 5.13 The results of PSD capability measurement for each sample. Top panel shows a correlation of Q_{tail}/Q_{total} (vertical axis) and Q_{total} (horizontal axis). The bottom panel displays Q_{tail}/Q_{total} distribution in the selection region (600 - 1200 p.e.) shown in the top panel. 133
- 5.14 The estimated PSD capability of the DIN mixed Gd-LS in the JSNS² detector. Left: Q_{tail}/Q_{total} versus Q_{total} in the unit of the number of p.e.. Right: Q_{tail}/Q_{total} distribution in the prompt signal region. The black line shows the criterion at neutron rejection power 200. 133

5.15 The measured transmittance spectrum. The top panel shows raw transmittance spectra of the DIN mixed sample measured in the first day (black) and 23 day later (red). The bottom panel displays the ratio spectrum of the red one to the black one as a function of wavelength. The drop below 410 nm is because of divergence of the ratio. 134

5.16 The delayed coincidence of $\nu_e + {}^{12}\text{C} \rightarrow e^- + {}^{12}\text{N}_{\text{g.s.}}$. Top left: prompt energy spectrum. Top right: delayed energy spectrum. Bottom left: $\Delta VTX_{\text{p-d}}$ distribution. Bottom right: $\Delta VTX_{\text{p-d}}$ distribution. The red dashed boxes on each plot show selection criteria to each variable. 136

5.17 Top: Expected energy spectrum of prompt signal in the current configuration. Bottom: that of the upgraded configuration in the condition of 1 MW \times 3 years \times 1 detector. The oscillated signal in case of $(\Delta m^2, \sin^2 2\theta) = (2.5 \text{ eV}^2, 3.0 \times 10^{-3})$ (brown shaded area), the IBD of $\bar{\nu}_e$ from μ^- (red), $\nu_e + {}^{12}\text{C} \rightarrow e^- + {}^{12}\text{N}_{\text{g.s.}}$ (blue), cosmic fast neutron (green) and total accidental background (orange) are displayed together. The spectrum shown in the black points corresponds to the summation of all spectra. 140

5.18 Top: Expected energy spectrum of prompt signal in the current configuration. Bottom: that of the upgraded configuration in the condition of 1 MW \times 3 years \times 1 detector. The oscillated signal in case of $(\Delta m^2, \sin^2 2\theta) = (1.2 \text{ eV}^2, 3.0 \times 10^{-3})$ (brown shaded area), the IBD of $\bar{\nu}_e$ from μ^- (red), $\nu_e + {}^{12}\text{C} \rightarrow e^- + {}^{12}\text{N}_{\text{g.s.}}$ (blue), cosmic fast neutron (green) and total accidental background (orange) are displayed together. The spectrum shown in the black points corresponds to the summation of all spectra. 141

5.19 Sensitivity of JSNS² experiment based on the real data. 90% C.L. exclusion lines of the expectation in reference [9] (black), the upgraded configuration (red) and the current configuration (green) are displayed. The star points at the parameters of LSND best-fit. The exclusion line of the OPERA experiment is also shown [60]. 142

5.20 90% C.L. exclusion to 3 + 1 sterile oscillation from JSNS² experiment in case of 3 years (blue), 6 years (green) and 8 years experimental duration (red) after the upgrade. It is turned out that 6 years experimental duration improves the sensitivity within 19 % loss with respect to the designed performance on sensitivity in reference [9] (black). 142

5.21 A comparison between the global fit result (red region) and 90% C.L. (orange), 99 % C.L. sensitivities of JSNS² experiment in case of 3 years experimental duration after the upgrade. It is shown that the sensitivity is insufficient to cover the global fit favored region even it can reach to the KARMEN exclusion limit [5]. 143

5.22 A comparison between the global fit result (red region) and 90% C.L. (orange), 99 % C.L. sensitivities of JSNS² experiment in case of 6 years experimental duration after the upgrade. Extending the experimental duration from 3 to 6 years gives a slight improvement. 143

6.1 A schematic view of the detectors in NA61/SHINE experiment [62]. 146

6.2 The planned detector location for the far detector with 48 m baseline. 147

6.3	A schematic design of the far detector. The basic design is identical with the near detector.	148
6.4	A model of concrete walls around the far detector cite shows spatial relations to the far detector in the XZ plane (left) and the YZ plane (right), respectively. We assumes that cosmic ray induced fast neutron/gamma ray generated in the concrete volume as a result of an interaction between cosmic muon and matter in the concrete.	149
6.5	The MC simulation results of the cosmic fast neutron. Prompt energy spectra (top left), delayed energy spectra (top right), Δt distributions (bottom left), ΔVTX distributions (bottom right) of the near detector (black line) and the far detector (blue line), respectively. The red dashed boxes show the selection criteria for each variables.	150
6.6	The MC simulation result of the cosmic gamma ray. The energy spectra in the prompt energy range (left) and in the delayed energy (right) of the near detector (black line) and the far detector (blue line) are shown, respectively. The red dashed boxes show the selection criteria for each variables.	151
6.7	Top: Expected prompt energy spectrum of the near detctor for 8 years. Rihgt: that of the far detector for 5 years. The oscillated signal in case of $(\Delta m^2, \sin^2 2\theta) = (2.5 \text{ eV}^2, 3.0 \times 10^{-3})$ (brown shaded area), the IBD of $\bar{\nu}_e$ from μ^- (red), $\nu_e + {}^{12}\text{C} \rightarrow e^- + {}^{12}\text{N}_{\text{g.s.}}$ (blue), cosmic fast neutron (green) and total accidental background (orange) are displayed together. The spectrum shown in the black points corresponds to the summation of all spectra.	152
6.8	Top: Expected prompt energy spectrum of the near detctor for 8 years. Rihgt: that of the far detector for 5 years. The oscillated signal in case of $(\Delta m^2, \sin^2 2\theta) = (1.2 \text{ eV}^2, 3.0 \times 10^{-3})$ (brown shaded area), the IBD of $\bar{\nu}_e$ from μ^- (red), $\nu_e + {}^{12}\text{C} \rightarrow e^- + {}^{12}\text{N}_{\text{g.s.}}$ (blue), cosmic fast neutron (green) and total accidental background (orange) are displayed together. The spectrum shown in the black points corresponds to the summation of all spectra.	153
6.9	A comparison between the global fit result (red region) and 90% C.L. sensitivities of the JSNS ² -II configuration in case the uncertainty on $\bar{\nu}_e$ from μ^- flux are 50 % (green dashed line), 20 % (light blue dashed line) and 10 % (magenta line) are shown.	154
6.10	A comparison between the global fit result (red region) and 3σ C.L. sensitivities of the JSNS ² -II configuration in case the uncertainty on $\bar{\nu}_e$ from μ^- flux are 50 % (green dashed line), 20 % (light blue dashed line) and 10 % (magenta line) are shown.	154

List of Tables

2.1	Classification of Beam Neutrinos.	18
2.2	An estimate of μ DAR neutrino production by 3 GeV protons using FLUKA hadron simulation package [10].	18
2.3	An estimate of μ DAR neutrino production by 3 GeV protons using QGSP-BERT hadron simulation package [10].	19
2.4	IBD selection conditions and their efficiencies in the JSNS ² experiment [9].	21
2.5	The optical parameters used in the JSNS ² RAT simulator.	24
3.1	The result of the EDTA titration to the Gd-LS.	48
3.2	List of devices for monitoring.	55
4.1	Trigger menu for the first run.	63
4.2	Table of LED intensity for gain calibration.	73
4.3	Table of LED intensity for gain calibration.	74
4.4	Table of LED intensity for relative timing calibration.	76
4.5	The estimated constant term from the ²⁵² Cf data.	88
4.6	Run list for floor gamma estimation.	104
4.7	The results of floor gamma estimation for each run.	109
4.8	Run list for event rate estimation.	109
4.9	A summary of background measurement for each component.	114
5.1	Component classification in lifetime.	119
5.2	Efficiencies of lifetime cut.	119
5.3	Efficiencies of delayed energy selection.	122
5.4	Efficiencies of $\Delta VT X_{\text{OB-d}}$ selection.	125
5.5	Efficiencies of $\Delta VT X_{\text{p-d}}$ cut.	127
5.6	A summary of signal efficiency estimation.	129
5.7	Summary of the expected number of events for 5000 hours \times 3 years.	138
6.1	Summary of the expected number of events for 5000 hours \times 8 years for the near detector and 5 years for the far detector, respectively.	149

Chapter 1

Introduction

1.1 Neutrino Oscillation

While neutrino mass is zero in the standard model of elementary particles. It has been turned out that neutrinos have finite but small mass from observations of neutrino oscillation. The transition among flavor eigenstates occurs if they consist of superposition of mass eigenstates with non-zero mass. This phenomenon in neutrinos is called neutrino oscillation. The mixing of mass eigenstate and three flavor neutrinos in the standard model (ν_e, ν_μ, ν_τ) is described by Pontecorvo-Maki-Nakagawa-Sakata (PMNS) Matrix [1], U , as follows:

$$\begin{pmatrix} |\nu_e\rangle \\ |\nu_\mu\rangle \\ |\nu_\tau\rangle \end{pmatrix} = U^* \begin{pmatrix} |\nu_1\rangle \\ |\nu_2\rangle \\ |\nu_3\rangle \end{pmatrix} = \begin{pmatrix} U_{e1}^* & U_{e2}^* & U_{e3}^* \\ U_{\mu 1}^* & U_{\mu 2}^* & U_{\mu 3}^* \\ U_{\tau 1}^* & U_{\tau 2}^* & U_{\tau 3}^* \end{pmatrix} \begin{pmatrix} |\nu_1\rangle \\ |\nu_2\rangle \\ |\nu_3\rangle \end{pmatrix}, \quad (1.1)$$

where $|\nu_\alpha\rangle$ ($\alpha = e, \mu, \tau$) and $|\nu_i\rangle$ ($i = 1, 2, 3$) are flavor and mass eigenstates, respectively. $U_{\alpha i}^*$ is the complex conjugate of the matrix element. The PMNS matrix is parametrized by

$$\begin{aligned} U &= \begin{pmatrix} 1 & 0 & 0 \\ 0 & c_{23} & s_{23} \\ 0 & -s_{23} & c_{23} \end{pmatrix} \begin{pmatrix} c_{13} & 0 & s_{13}e^{-i\delta} \\ 0 & 1 & 0 \\ -s_{13}e^{i\delta} & 0 & c_{13} \end{pmatrix} \begin{pmatrix} c_{12} & s_{12} & 0 \\ -s_{12} & c_{12} & 0 \\ 0 & 0 & 1 \end{pmatrix} \\ &= \begin{pmatrix} c_{12}c_{13} & s_{12}c_{13} & s_{13}e^{-i\delta} \\ -s_{12}c_{23} - c_{12}s_{23}s_{13}e^{i\delta} & c_{12}c_{23} - s_{12}s_{23}s_{13}e^{i\delta} & s_{23}c_{13} \\ s_{12}s_{23} - c_{12}c_{23}s_{13}e^{i\delta} & -c_{12}s_{23} - s_{12}c_{23}s_{13}e^{i\delta} & c_{23}c_{13} \end{pmatrix}, \end{aligned} \quad (1.2)$$

where $s_{ij} = \sin\theta_{ij}$ and $c_{ij} = \cos\theta_{ij}$. θ_{ij} ($i, j = 1, 2, 3$) stand for mixing angles between ν_i and ν_j . There is a phase factor δ expressing the CP violation in lepton sector. If neutrinos are Majorana particles, two additional phase factors, Majorana phase, appear in the matrix. However, they have no contribution to the oscillation probability described below because it is proportional to $U_{\alpha j}U_{\beta j}^*U_{\alpha k}^*U_{\beta k}$.

Non-zero mixing causes neutrino flavor transition as a function of time. The time evolution of neutrino with definite mass and energy in vacuum is written by Schrödinger equation as

$$i\frac{\partial}{\partial t}|\nu_i(t)\rangle = \mathcal{H}|\nu_i(t)\rangle = E_i|\nu_i(t)\rangle, \quad (1.3)$$

where E_i is the energy of the neutrino ν_i and \mathcal{H} is the Hamiltonian operator in vacuum. Its solution is given by

$$|\nu_i(t)\rangle = |\nu_i(t=0)\rangle e^{-iE_it}. \quad (1.4)$$

Therefore, the propagation of a flavor eigenstate α is expressed using the eigenstate of the other flavor β as

$$\begin{aligned} |\nu_\alpha(t)\rangle &= \sum_{i=1}^3 U_{\alpha i}^* |\nu_i(t=0)\rangle e^{-iE_it} \\ &= \sum_{\beta} \sum_{i=1}^3 U_{\alpha i}^* U_{\beta i} |\nu_\beta(t=0)\rangle e^{-iE_it}. \end{aligned} \quad (1.5)$$

And then, the probability of the flavor transition, ν_α to ν_β , is calculated as

$$\begin{aligned} P(\nu_\alpha \rightarrow \nu_\beta) &= |\langle \nu_\beta | \nu_\alpha(t) \rangle|^2 \\ &= \sum_{i=1}^3 \sum_{j=1}^3 U_{\alpha i} U_{\beta i}^* U_{\alpha j}^* U_{\beta j} e^{-i(E_i - E_j)t}. \end{aligned} \quad (1.6)$$

Because it is possible to assume that the neutrino mass is negligibly small compared to the momentum of neutrino in ordinary experimental conditions, the neutrino energy in the mass eigenstate i can be approximated by

$$E_i = \sqrt{|\mathbf{p}|^2 + m_i^2} \sim |\mathbf{p}| + \frac{m_i^2}{2E_\nu}, \quad (1.7)$$

where E_ν is the neutrino energy. Therefore, Eq. (1.6) can be rewritten using $\Delta m^2/2E_\nu \equiv (m_i^2 - m_j^2)/2E_\nu \sim E_i - E_j$ and flight length of the neutrino $L \sim t$ (in the unit of $c = 1$) as

$$\begin{aligned} P(\nu_\alpha \rightarrow \nu_\beta) &= \sum_{i=1}^3 \sum_{j=1}^3 U_{\alpha i} U_{\beta i}^* U_{\alpha j}^* U_{\beta j} e^{-i \frac{\Delta m_{ij}^2 L}{4E_\nu}} \\ &= \delta_{\alpha\beta} - 4 \sum_{i < j} \text{Re}(U_{\alpha i} U_{\beta i}^* U_{\alpha j}^* U_{\beta j}) \sin^2 \left(\frac{\Delta m_{ij}^2 L}{4E_\nu} \right) \\ &\quad + 2 \sum_{i < j} \text{Im}(U_{\alpha i} U_{\beta i}^* U_{\alpha j}^* U_{\beta j}) \sin \left(\frac{\Delta m_{ij}^2 L}{2E_\nu} \right), \end{aligned} \quad (1.8)$$

where $\delta_{\alpha\beta}$ is the Kronecker delta. The phase of oscillation Φ_{ij} can be expressed in the different unit system for convenience by explicitly considering c and \hbar as

$$\Phi_{ij} = \frac{\Delta m_{ij}^2 c^4 L}{4\hbar c E_\nu} = 1.27 \times \frac{\Delta m_{ij}^2 [\text{eV}^2] \times L [\text{m}]}{E_\nu [\text{MeV}]}. \quad (1.9)$$

1.1.1 Sterile Neutrino in 3 + 1 model

The current knowledge about neutrino mass from the neutrino oscillation observation is listed below [2]:

$$\begin{aligned} \Delta m_{21}^2 &= (7.42_{-0.20}^{+0.21}) \times 10^{-5} \text{ eV}^2, \\ \Delta m_{31}^2 &= (2.517_{-0.028}^{+0.026}) \times 10^{-3} \text{ eV}^2 \text{ (Normal Hierarchy)}, \\ \Delta m_{32}^2 &= (2.498_{-0.028}^{+0.028}) \times 10^{-3} \text{ eV}^2 \text{ (Inverted Hierarchy)}. \end{aligned} \quad (1.10)$$

In contrast, the observations of $\bar{\nu}_\mu \rightarrow \bar{\nu}_e$ oscillation in LSND (Liquid Scintillator Neutrino Detector) experiment [3] suggests an existence of oscillation corresponding to $\Delta m^2 \sim 1 \text{ eV}^2$ which conflicts with the measured Δm^2 of three neutrinos in the standard model. This is called LSND anomaly. According to the measurement of the probability of $e^+ + e^- \rightarrow Z^0 \rightarrow \nu + \bar{\nu}$ reaction, the number of generation of weakly interacting neutrino is limited to 3. Therefore, it is necessary to introduce a non-weakly interacting neutral lepton mixing with the three active neutrinos via neutrino oscillation in order to describe the LSND oscillation. It is called sterile neutrino. Assuming the number of sterile neutrino is 1, i.e., 3 + 1 model, the PMNS matrix can be extended as

$$\begin{pmatrix} \nu_e \\ \nu_\mu \\ \nu_\tau \\ \nu_s \end{pmatrix} = U' \begin{pmatrix} \nu_1 \\ \nu_2 \\ \nu_3 \\ \nu_4 \end{pmatrix} = \begin{pmatrix} U_{e1} & U_{e2} & U_{e3} & U_{e4} \\ U_{\mu 1} & U_{\mu 2} & U_{\mu 3} & U_{\mu 4} \\ U_{\tau 1} & U_{\tau 2} & U_{\tau 3} & U_{\tau 4} \\ U_{s1} & U_{s2} & U_{s3} & U_{s4} \end{pmatrix}, \quad (1.11)$$

where ν_s shows a neutrino in the sterile flavor, and ν_4 is an additional mass eigenstate. The probability of oscillation $\bar{\nu}_\mu \rightarrow \bar{\nu}_e$ reported by LSND experiment is written as

$$\begin{aligned} P(\nu_\mu \rightarrow \nu_e) = & -4 \sum_{j>k} \text{Re}(U_{ej}U_{\mu j}^*U_{ek}^*U_{\mu k}) \sin^2 \Delta_{jk} \\ & -2 \sum_{j>k} \text{Im}(U_{ej}U_{\mu j}^*U_{ek}^*U_{\mu k}) \sin 2\Delta_{jk}, \end{aligned} \quad (1.12)$$

where

$$\Delta_{jk} \equiv \frac{(m_j^2 - m_k^2)L}{4E}. \quad (1.13)$$

Assuming $m_4 \gg m_{1,2,3}$ and $U_{s4} \sim 1 \gg U_{f4}$ ($f = e, \mu, \tau$), Eq. (1.12) can be approximated by

$$\begin{aligned} P(\nu_\mu \rightarrow \nu_e) & \sim 4|U_{e4}|^2|U_{\mu 4}|^2 \sin\left(\frac{\Delta m^2 L}{4E}\right), \\ & = \sin^2 2\theta \sin\left(\frac{1.27\Delta m^2 [\text{eV}^2] \times L [\text{m}]}{E [\text{MeV}]}\right), \end{aligned} \quad (1.14)$$

where $\Delta m^2 \sim m_4$. Note that the production of transition amplitudes are replaced with a mixing parameter as $\sin^2 2\theta$, and the unit of the phase is changed in the same way as Eq. (1.9).

1.2 Situation for Sterile Neutrino Search

As mentioned above, LSND reported the positive result on $\bar{\nu}_\mu \rightarrow \bar{\nu}_e$ appearance oscillation. They utilized $\bar{\nu}_\mu$ beam produced in μ decay at rest: $\pi^- \rightarrow \mu^- + \bar{\nu}_\mu$; $\mu^- \rightarrow e^- + \bar{\nu}_e + \nu_\mu$ using 800 MeV proton beam in LAMPF (Los Alamos Meson Physics Facility). The experimental setup, shown as the left drawing in figure 1.1, consists of a 176 tons liquid scintillator detector placed at 30 m away from the beam target. The right plot in figure 1.1 shows L/E distribution of the observed $\bar{\nu}_e$ events detected via inverse beta decay. They observed $87.9 \pm 22.4(\text{stat.}) \pm 6.0(\text{syst.})$ event excess

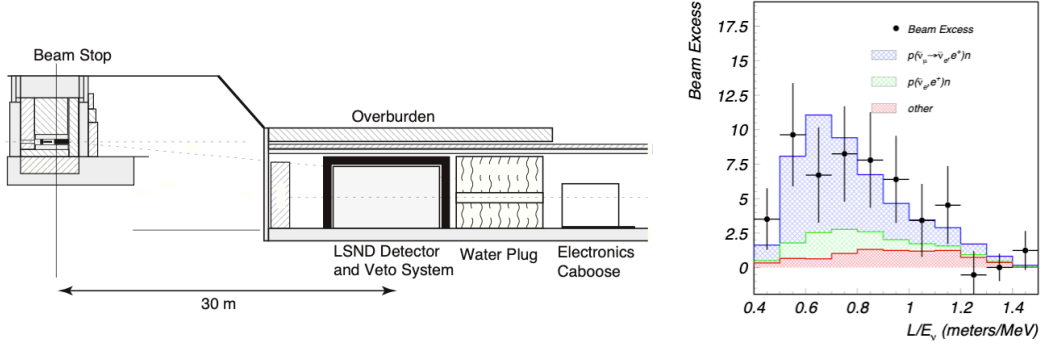


Figure 1.1: Left: a schematic view of the experimental setup of LSND experiment. Right: L/E distribution of the observed $\bar{\nu}_e$ event in LSND experiment, where L is the baseline, and E is the neutrino energy. The blue area corresponds to the expectation of $\bar{\nu}_e$ event on the oscillation assumption. It describes the data (black point) [3] well.

against backgrounds (blue shaded area), which corresponds to the allowed oscillation parameters $\Delta m^2 > 3 \times 10^{-2} \text{ eV}^2$, $\sin^2 2\theta > 10^{-3}$ [3].

There have been experiments searching for $\nu_\mu \rightarrow \nu_e$ ($\bar{\nu}_\mu \rightarrow \bar{\nu}_e$) oscillation reported in LSND. Figure 1.2 (a) shows the oscillation parameter space of $\nu_\mu \rightarrow \nu_e$ and $\bar{\nu}_\mu \rightarrow \bar{\nu}_e$ oscillation from results of various experiments at 99 % confidence level (C.L.) [4]. Even though the negative result from KARMEN [5] (blue dashed line) and OPERA [6] (purple line) gives strong constraints on the positive result from LSND and MiniBooNE [7], the allowed parameter space (red area) survives and indicates an oscillation caused by sterile neutrino.

In addition to the appearance observation, ν_e ($\bar{\nu}_e$) and ν_μ ($\bar{\nu}_\mu$) disappearance data can also give constraints on the survived region from the appearance global fit. Figure 1.2 (b) displays 99.73 % C.L. exclusion line (blue) to the parameter space around the survived region from the appearance data result [4]. Although there is an uncertainty from reactor neutrino flux in $\bar{\nu}_e$ disappearance experiments, it gives strong tension between the appearance and the disappearance channel and excludes the favored oscillation by LSND + MiniBooNE at the 4.7σ level. On the other hand, recently Neutrino-4 experiment, short baseline $\bar{\nu}_e$ disappearance measurement using reactor neutrino, reported a positive result at 1σ level around the LSND+MiniBooNE indicated parameters (figure 1.3) [8], while this also conflicts the constraint from the further disappearance experiments.

To solve this chaotic situation, confirming the experimental facts giving the positive result on sterile neutrino existence, e.g., LSND and MiniBooNE, is a urgent task to give conclusion to it. For the result from LSND experiment, an experiment which can perform a direct test to their $\bar{\nu}_\mu \rightarrow \bar{\nu}_e$ channel covering all the indicated parameter space is highly desired.

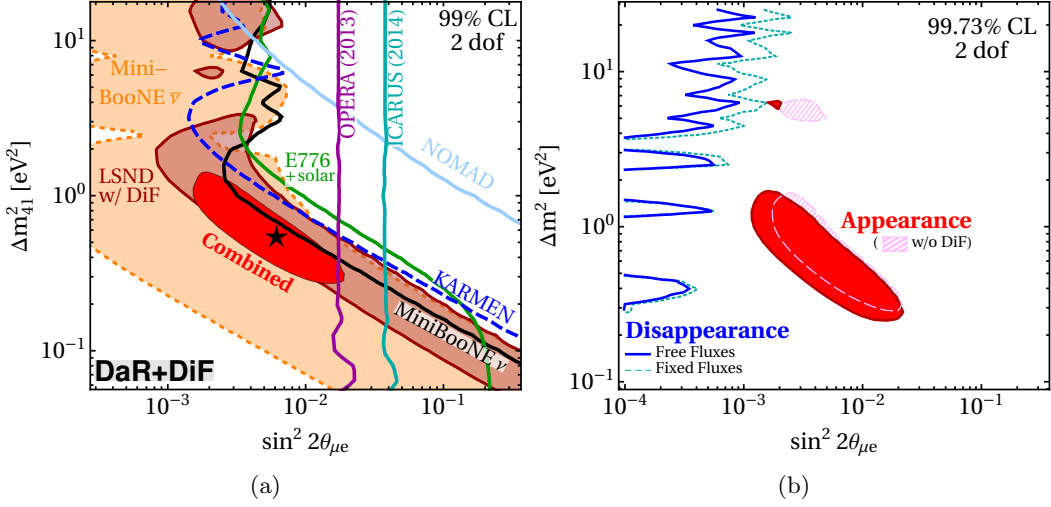


Figure 1.2: Left: Constraints on short-baseline $\nu_\mu \rightarrow \nu_e/\bar{\nu}_\mu \rightarrow \bar{\nu}_e$ appearance oscillations in 3 active + 1 sterile scenario at 99 % C.L.. Right: Comparison between 99.73 % exclusion limit from disappearance data and the combined allowed region from the appearance data. Their horizontal axis shows the effective mixing angle $\sin^2 2\theta_{\mu e} = 4|U_{e4}|^2|U_{\mu 4}|^2$, and the vertical axis corresponds to Δm^2 [4].

1.3 Motivation of This Thesis

The search for sterile neutrinos has been one of the hottest topics in the neutrino physics recently. The JSNS² experiment aims to search for the existence of neutrino oscillations with $\Delta m^2 \sim 1$ eV² at the Materials and Life Science Experimental Facility (MLF) of Japan Proton Accelerator Research Complex (J-PARC) as a direct test to the LSND anomaly. The experiment begin with single detector with 17 tons target mass in 3 years experimental duration as a first phase. The JSNS² detector has been constructed since 2016, and the construction was done on February, 2020. We had an ten days data taking opportunity on June, 2020, and successfully completed it. The obtained data can be used for background estimation and performance check for sterile neutrino search in the first phase. Therefore, studies about the detector development, the background measurement and the performance estimation based on the first run data are described in the following chapters as:

- Chapter 2: JSNS² Experiment
The experimental setup of the JSNS² experiment including neutrino beam at the MLF in J-PARC, concept and design of the detector are described. In addition, Monte Carlo (MC) simulation for the JSNS² experiment and background models used there are described as well.
- Chapter 3: Detector Research and Development
The detailed description about each component of the detector, studies for their development and construction are given.
- Chapter 4: Background Measurement
Background events in the signal selection region based on the data obtained in

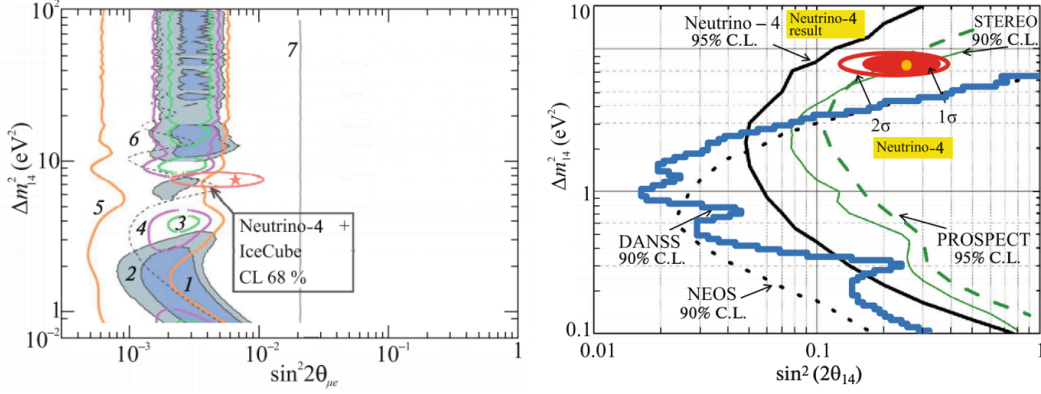


Figure 1.3: The result of Neutrino-4 experiment [8]. Left: Comparison of the allowed regions of LSND (1, 2), MiniBooNE (3 - 5) and Neutrino-4 (red contour). 6 and 7 shows KARMEN and OPERA [60] 90 % exclusion line, respectively. The parameter $\sin^2 2\theta_{\mu e} \sim \frac{1}{4} \sin^2 2\theta_{14} \sin^2 2\theta_{24}$ is determined by the production of $\sin^2 2\theta_{14}$ from Neutrino-4 and $\sin^2 2\theta_{24}$ from IceCube experiment. Right: Constraints on the parameter space ($\Delta m^2, \sin^2 2\theta_{14}$) among various short baseline reactor neutrino experiments.

the first run are estimated and explained here. Understandings of each background component are also demonstrated by comparing them to the simulation result. The estimated background rates are compared to the expectation in reference [9].

- Chapter 5: Sensitivity Study for Sterile Neutrino Search
Sensitivity to sterile neutrino search in the first phase of the JSNS² experiment is estimated based on the first data. It is compared to the LSND anomaly, the allowed oscillation parameter space by the LSND result, and the expected sensitivity in reference [9] for a performance check.
- Chapter 6: Future Extension
The prospective of the JSNS² experiment with future extensions for improvement on sterile neutrino search are described. A combined sensitivity with an additional detector in the farther baseline than the first detector is estimated based on the background model confirmed by the first data. In addition, a possibility for a systematic uncertainty reduction by an external measurement is described.
- Chapter 7: Conclusion
The studies shown in this thesis are summarized.

Chapter 2

The JSNS² experiment

Observing $\bar{\nu}_\mu \rightarrow \bar{\nu}_e$ oscillation at muon decay-at-rest (μ DAR) neutrino beam via inverse beta decay reaction is an identical method with LSND experiment, and following this scheme with improved detection technique ensure a direct test to the result of LSND observation. The JSNS² (J-PARC Sterile Neutrino Search at J-PARC Spallation Neutron Source) experiment, proposed in 2013 [10], is designed to search for the existence of neutrino oscillations indicated by LSND experiment at the Material and Life science experimental Facility (MLF) in J-PARC. The facility provides an intense neutrino beam from μ DAR thanks to the high power and short pulsed proton beam from the Rapid Cycling Synchrotron (RCS) and a spallation neutron target in the MLF. The experiment uses a Gadolinium (Gd) liquid scintillator (Gd-LS) detector placed at 24 m away from the mercury target. Both the beam and the detector contribute to detection improvement on $\bar{\nu}_\mu \rightarrow \bar{\nu}_e$ oscillation. In this chapter, details about the experimental setup and the basic concepts of the JSNS² experiment are described.

2.1 Experimental Setup

The JSNS² experiment is held in J-PARC located in Tokai village, Ibaraki prefecture in east Japan. Figure 2.1 exhibits the bird-eyes view photo of the entire J-PARC facilities. The proton beam is accelerated at the Rapid Cycling Synchrotron (RCS) up to 3 GeV, and sent to a spallation neutron target consisting of mercury in the MLF (the central building in the photo). The JSNS² detector is placed at 24 m away from the mercury target in the MLF as shown in Fig. 2.2. The location is the third floor of the MLF building. Figures 2.3-2.5 show the spatial relation between the detector and the mercury target. The vertical distance from the target to the detector is 13.5 m, and the horizontal one is 20 m. The experimental position is a maintenance area for targets in the MLF. Thus, it is needed to move the detector annually in order to avoid a conflict with the facility works in the summer maintenance period (~ 2 months).

2.1.1 $\bar{\nu}_e$ detection technique

As described above, the JSNS² detector observes oscillated $\bar{\nu}_e$ via inverse beta decay (IBD) interaction on free proton as $\bar{\nu}_e + p \rightarrow e^+ + n$. One of the advantage of $\bar{\nu}_e$ detection via IBD is that the final state particles, positron and neutron, can be detected

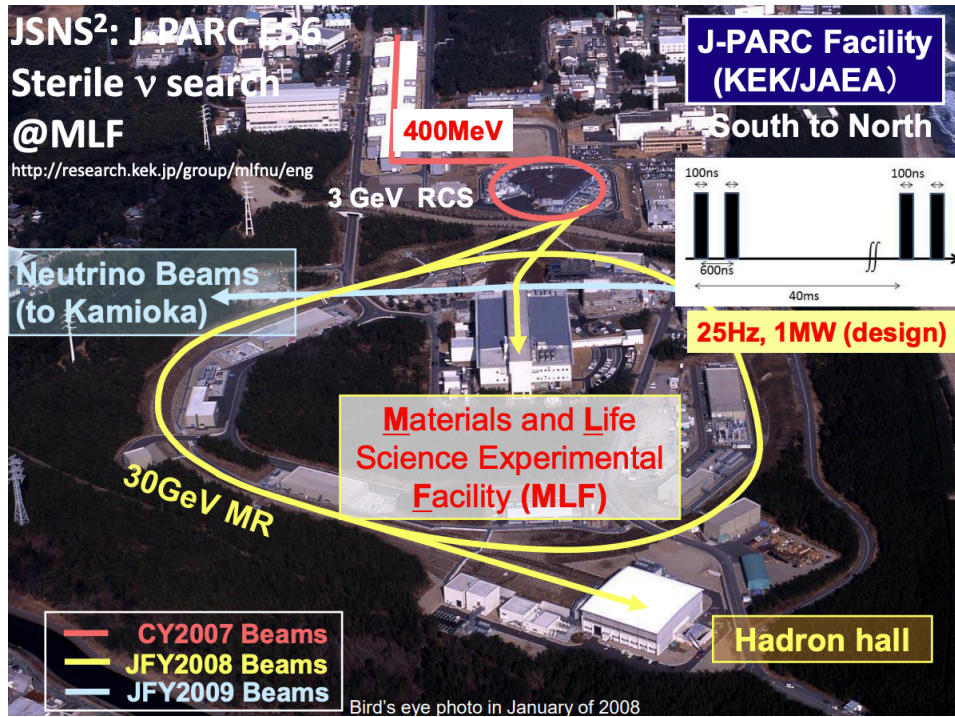
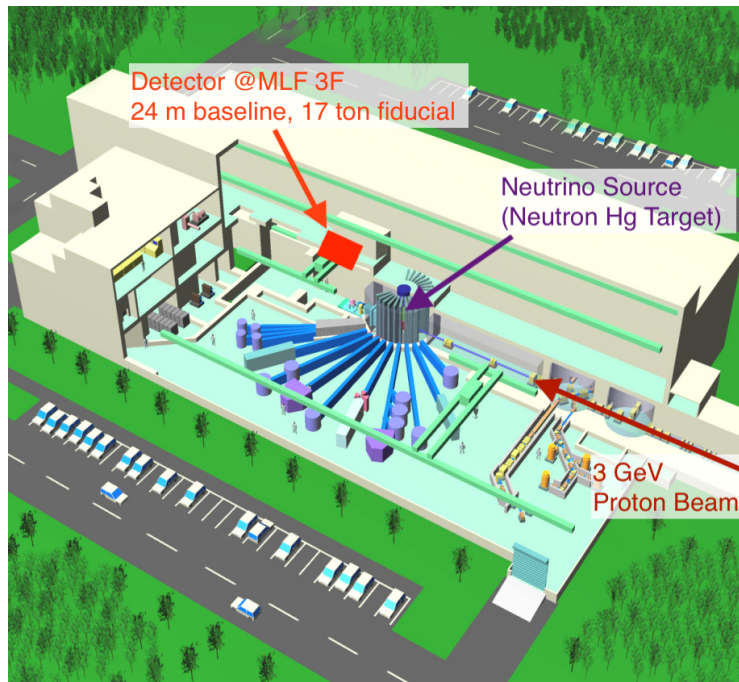


Figure 2.1: The overview of J-PARC facilities.

Figure 2.2: The MLF building and the location of the JSNS² experimental setup.

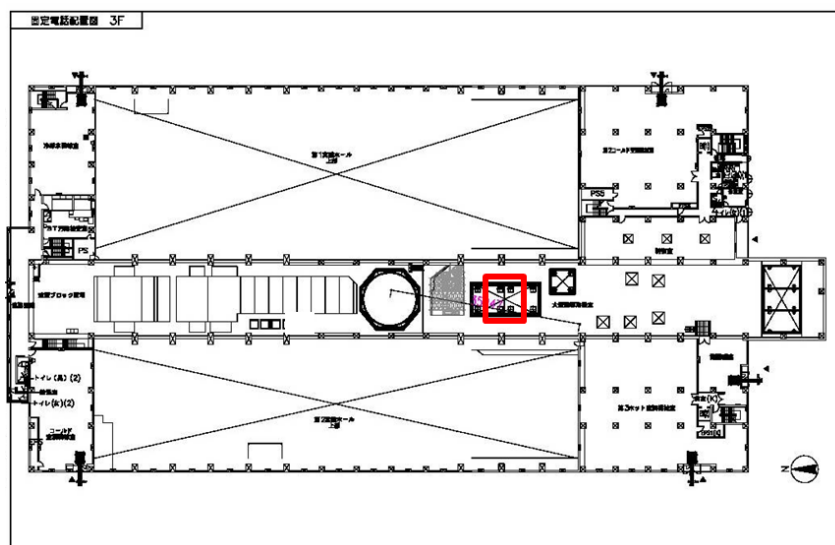


Figure 2.3: A drawing of the MLF third floor in the bird-eye's view. The detector position is pointed as the red box.

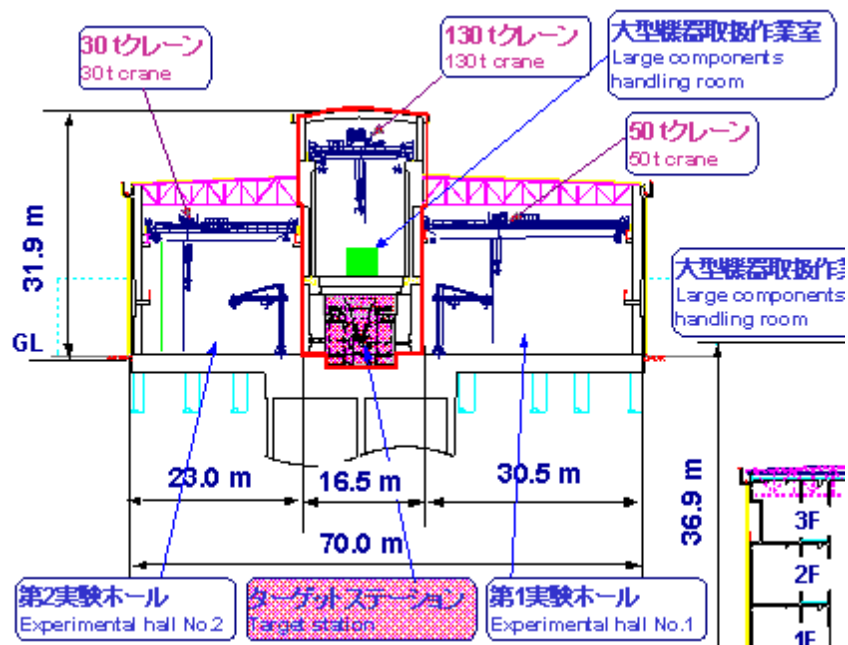


Figure 2.4: A cross section of the MLF building in the orthogonal plain to the beam direction [11]. The red shaded area corresponds to the hot cell where the mercury target is placed. The detector position is pointed as the green box.

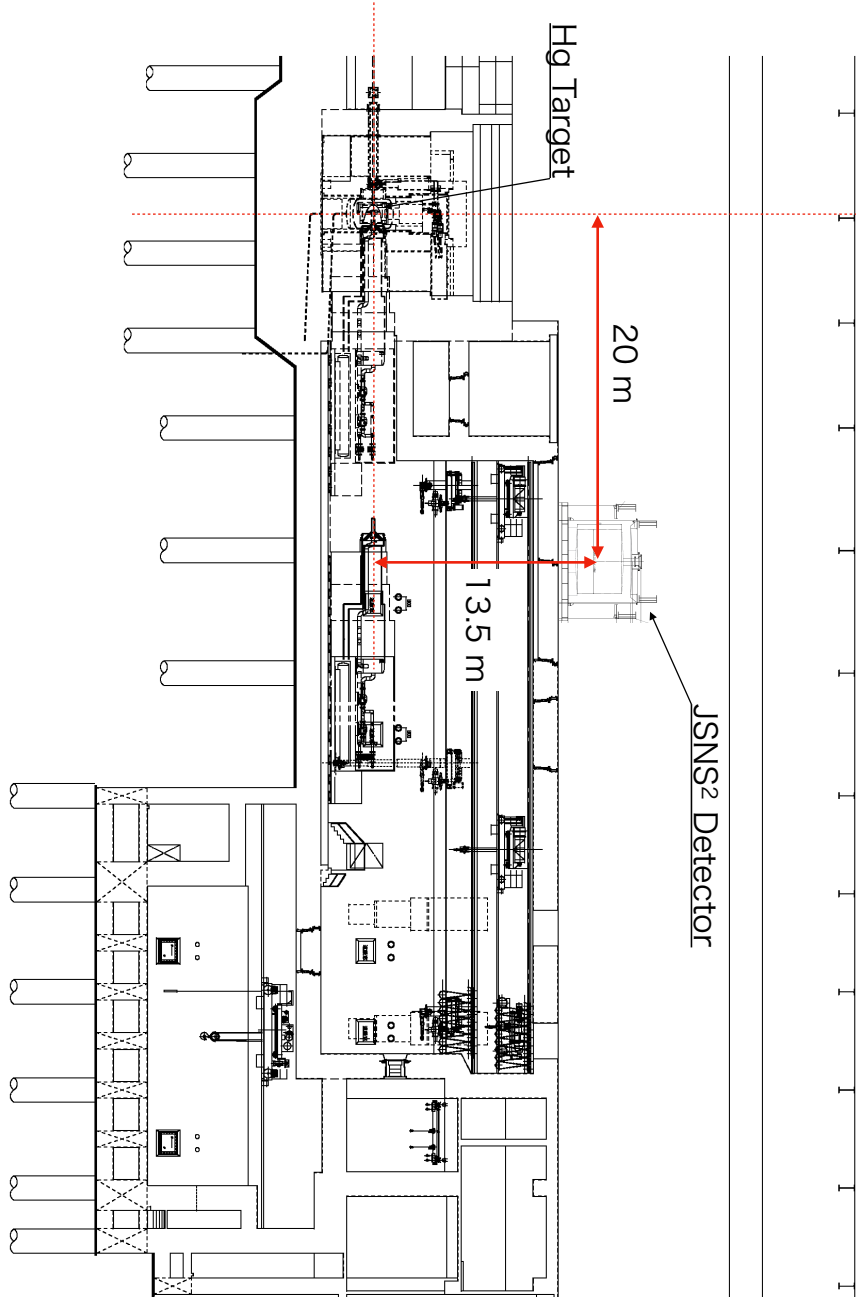


Figure 2.5: A cross section of the MLF building in the parallel plain to the beam direction [12].

in delayed coincidence method, which significantly suppresses background compared to single event detection. The neutron is captured on nucleus after thermalization,

prompt signal

$$E_{prompt} = E - 1.8\text{MeV}(\text{threshold}) + 2m_e(1.0\text{MeV})$$

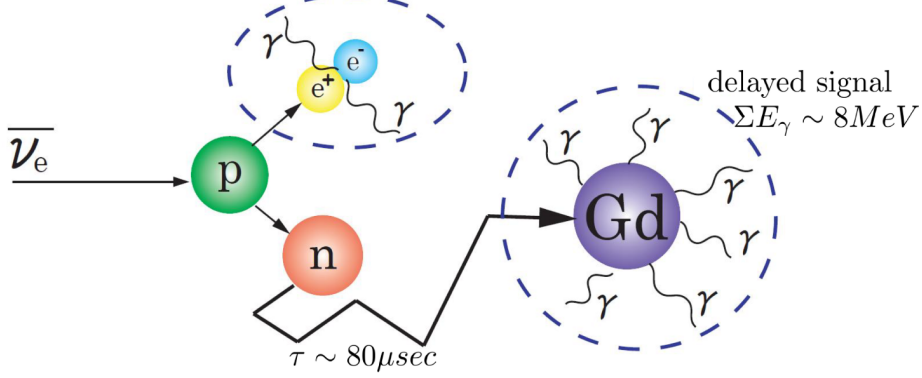


Figure 2.6: A schematic diagram of delayed coincidence IBD detection used JSNS² experiment.

and emits several gamma rays in a certain time interval from the interaction. The positron immediately generates scintillation light whose amount shows the energy of the anti-electron neutrino. In particular, capture on ¹⁵⁵Gd or ¹⁵⁷Gd is used in JSNS² case. The schematic of this process is illustrated in Fig. 2.6. Compared to hydrogen capture used in LSND experiment, Gd capture has the following advantages:

- large capture cross section: 61 kbarn for thermal neutron (0.0253 eV) on ¹⁵⁵Gd, and 254 kbarn on ¹⁵⁷Gd.
- total gamma rays energy from thermal neutron capture is roughly 8 MeV, which exceeds the endpoint energy of environmental gamma ray background; ~ 2.6 MeV from ²⁰⁸Tl (c.f., capture on hydrogen: 2.2 MeV).
- neutron capture time on Gd ~ 30 μs is shorter than hydrogen capture time ~ 200 μs .

Therefore, the Gd-LS is a quite strong tool for eliminating the accidental background by detecting both positron as a prompt signal and gamma rays from neutron capture on Gd as a delayed signal.

The cross section of the IBD interaction is approximately written down based on the approximation in zeroth order of $1/M$ from Vogel et al. [13] as a function of neutrino energy E_ν :

$$\sigma_{\text{IBD}}(E_\nu) = 0.0952 \left(\frac{E_{e^+} p_{e^+}}{1 \text{ MeV}^2} \right) \times 10^{-42} \text{ cm}^2, \quad (2.1)$$

where E_{e^+} and p_{e^+} are the positron energy and the momentum in a unit of MeV, respectively. The positron energy can be approximated by

$$E_{e^+} \sim E_\nu + (M_p - M_n). \quad (2.2)$$

Therefore, it can be said that the positron keeps the energy information of $\bar{\nu}_e$. As neutrino oscillation distorts neutrino energy spectrum depending on Δm^2 , the observed positron energy spectrum also well reflects the oscillation information.

2.1.2 Detector design

Figure 2.7 shows a schematic of the detector design and structure for the JSNS² experiment. The JSNS² detector consists of 17 tons Gd-LS contained in an inner acrylic vessel, and ~ 33 tons Gd unloaded liquid scintillator (LS) in the space between the acrylic vessel and an outer stainless steel tank. The LS layer is separated into two different functional layers by optical separators and forms two independent detector volumes in the one detector. The region inside of the optical separator, called "inner detector", consists of 17 tons Gd-LS and 25 cm thick LS layer surrounding the Gd-LS volume. The outer layer, called "veto layer", has a function to detect cosmic ray induced particles coming into the detector, e.g., cosmic μ . Scintillation light from the inner and veto layers is observed by 10-inch photomultiplier tube (PMT), Hamamatsu R7081: 96 PMTs are mounted in the inner detector and 24 PMTs cover the veto layer. The surfaces in the veto layer carefully covered with reflection material to improve scintillation light collection by the PMTs. The details about R&D for the detector components are described in the later chapter.

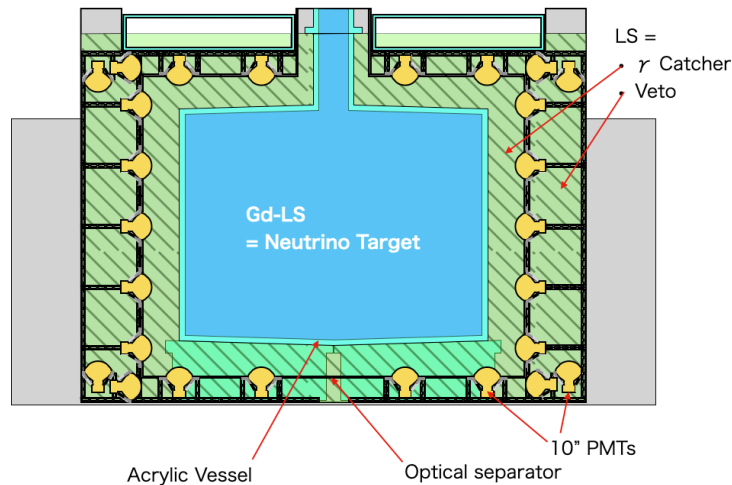


Figure 2.7: A schematic view of the JSNS² detector.

2.1.3 Shield

The shield is laid right below the detector in order to suppress gamma ray background. Figure 2.8 shows a photo of the shield before detector installation. It consists of lead bricks and iron plates. The dimension of iron shield is 6 m width \times 9 m length \times 44 mm thickness. Note that the long side of the iron shield is along the beam direction. On the iron shield, two round-shape lead shield layers are constructed using about 1500 lead bricks which has 10 cm width, 20 cm length and 5 cm thickness. The radius of them is 1.6 m and 2.5 m, respectively, which means that the Gd-LS region is fully covered with most thick part of the shield (10 cm lead + 4.4 cm iron).

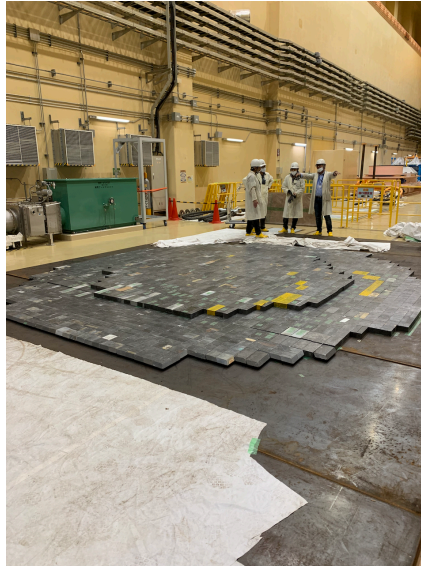


Figure 2.8: A photo of the shield below the JSNS² detector.

2.1.4 Annual Operation for Experiment

As mentioned above, the JSNS² experiment has to be moved from the MLF building during the maintenance period of J-PARC in summer. Besides that, Japanese fire law requires that detector contains no flammable materials (= the Gd-LS and the LS) outside of the MLF. Therefore, the following operations (illustrated in figure 2.9) is needed as well as a slow control and data acquisition monitoring during data taking periods.

1. The empty detector is transported from the storage building (HENDEL) to the MLF, and we fill the detector with Gd-LS/LS at the first floor of the MLF from ISO (International Organization for Standardization) tanks, the external storage container.
2. The filled detector is transferred to the experimental position on the 3rd floor of the MLF using a 130-ton crane. The shields consisting of lead and iron beneath the detector is fully laid before this transportation.
3. Data taking launches and is going on until the end of the MLF beam operation (amount to 5000 hours).
4. After the data taking, the detector is moved back the first floor again. The Gd-LS/LS is extracted to each ISO tank, and the empty detector is transported to the HENDEL building for storage until the next beam time.
5. The ISO tanks containing the Gd-LS/LS are stored and managed by Nichiriku company in Kawasaki city.

The ISO tank for Gd-LS/LS storage (shown in figure 2.10) is a container satisfying the ISO international standard for liquid storage and transportation, whose inner surface in contact with the Gd-LS/LS is made of stainless steel (SUS316L). Impurity removal and passivation of the stainless steel surface was done by acid

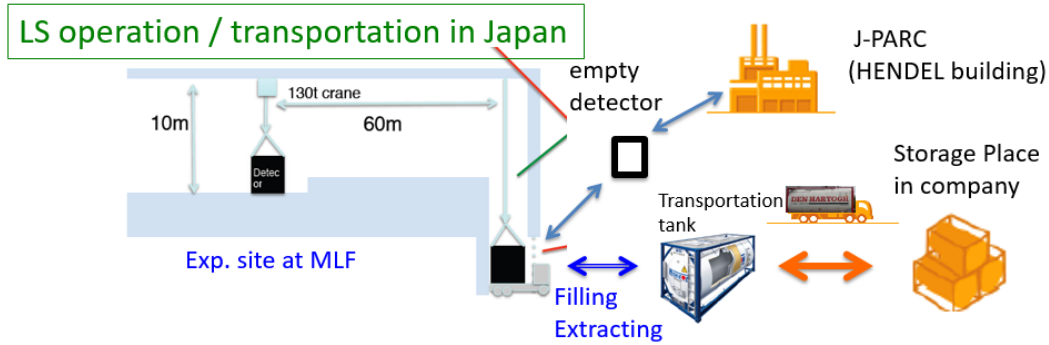


Figure 2.9: The detector and LS operation during the experiment throughout a year [9].

wash. An examination for an effect of metal surface on the Gd-LS is described in the next chapter. The ISO tank has a capacity of 21 kL so that we use two tanks for the LS and one tank for the Gd-LS storage.



Figure 2.10: A cut model of an ISO tank with the dimensions labeled [14].

2.2 Decay at Rest Neutrino Beam

The J-PARC MLF is the best suited facility to search for neutrino oscillations using neutrinos from stopped muon decay in the mass range $\Delta m^2 \sim \text{eV}^2$ for the following reasons:

1. High beam power (1 MW)
2. Suppression of μ^- free decay through absorption by the mercury target
3. A low duty factor, pulsed beam which enables elimination of decay-in-flight components and separation of μDAR from other background sources. The resulting $\nu_e, \bar{\nu}_e$ have well-defined spectra and known cross sections.

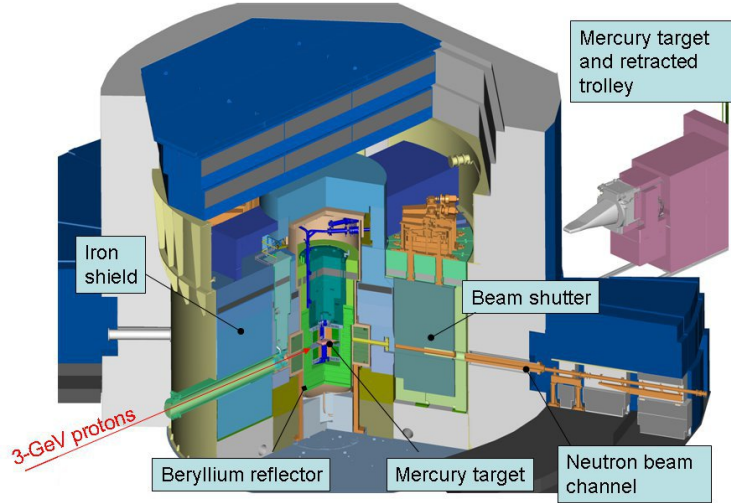


Figure 2.11: A schematic drawing of the J-PARC spallation neutron source [10].

In this section, the details about beam facility and their advantages for the JSNS² experiment mentioned above is explained.

2.2.0.1 The RCS beam and the target

The RCS accelerates protons up to 3 GeV, and periodically sends them to the MLF target in 25 Hz, which corresponds to 40 ms time interval from the previous beam spill. Each spill of beam bunch consists of 100 ns width double pulse with 540 ns interval between them, and the design value of proton intensity is 0.33 mA (1 MW). The 1 MW beam provides 3.8×10^{22} protons-on-target (POT) during 5000 hours / year operation (i.e. 4.5×10^8 spills are provided during one year).

Figure 2.11 shows a schematic drawing of the J-PARC spallation neutron source. As a result of mercury spallation via interaction with 3 GeV protons, plenty of hadrons including pion and kaon as well as neutron are produced. The mesons decay and generates neutrinos. The target are surrounded by cooling pipes, beryllium reflectors and steel shielding. In addition, there are cryogenic liquid hydrogen moderators located at the top and bottom of the target for neutron beamlines.

The proton beam sent from the RCS enters beamline in the MLF, and collides on the mercury target after passing through a carbon target for μ beamlines. The beam loss due to collision with the carbon target is less than 5%. Figure 2.12 show a 3D model of the mercury target, which has dimensions of 54 cm in width by 19 cm in height by 210 cm in length. The target material, mercury, is encapsulated within multiple wall structure made of stainless steel, and constantly circulated at a rate of 154 kg/sec for cooling.

2.2.0.2 Neutrino beam

The neutrino beam generated in the mercury target has unique timing structure because of the short pulsed beam and lifetime of mother particle of each neutrino. The beam neutrinos can be qualitatively categorized as follows:

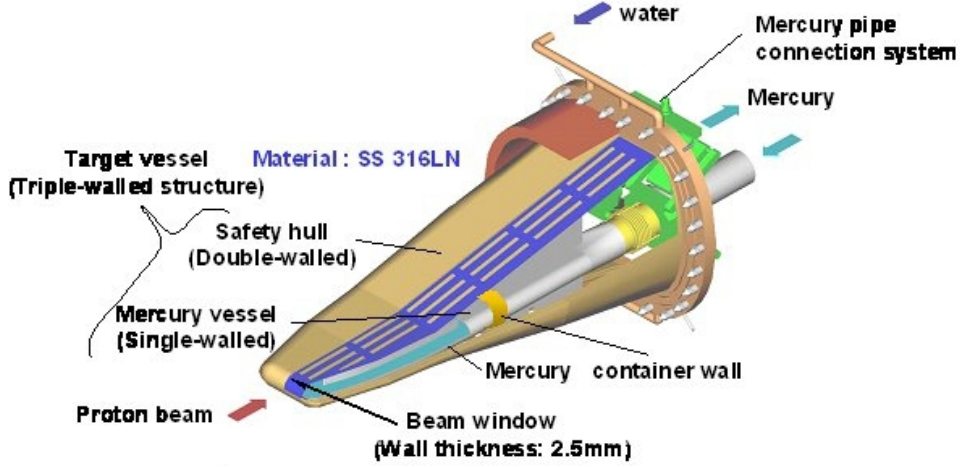


Figure 2.12: A schematic drawing of the mercury target in the J-PARC MLF [10].

- on-bunch: neutrinos produced within $1 \mu\text{s}$ with respect to the beam collision timing (mainly π , K decay),
- off-bunch: neutrinos produced $1 \mu\text{s}$ after the beam collision timing (mainly μDAR).

Quantitatively, MC simulation for beam neutrino flux estimation was performed in the following sequences:

1. Secondary particle production by 3 GeV protons
The interaction of 3 GeV proton beam with the mercury target and beam-line components has been simulated using FLUKA [18] and QGSP-BERT (in Geant4 [19]) hadron interaction simulation packages [10].
2. π^\pm interactions and decay
The charged pion (π^+ and π^-) produced in the target deposits its kinetic energy to materials via ionization. The charge exchange reaction ($\pi^+n \rightarrow \pi^0p$ or $\pi^-p \rightarrow \pi^0n$, then $\pi^0 \rightarrow \gamma\gamma$) decreases the number of the charged pions. The behavior of charged pions differ depending on their sign of charge: π^+ stops and decays with its lifetime in vacuum (26 ns) because it is repulsed by positive charge of nucleus. On the other hand, the survived π^- are absorbed by forming a π -mesic atoms. π decay-in-flight is highly suppressed to $\sim 8 \times 10^{-3}$ of the produced π^\pm .
3. μ^\pm absorption and decay
 μ^+ decays in the reaction $\mu^+ \rightarrow e^+\nu_e\bar{\nu}_\mu$. Because of the muon lifetime and energy loss process, the decay-in-flight is negligible. μ^- is captured by nuclei by forming a mu-mesic atom, and eventually produces ν_μ with an endpoint energy of 105 MeV. The absorption rate depends on the atomic number of nucleus, i.e., the effect becomes larger in heavier nuclei. The total rate of μ^- capture on nucleus have been measured in terms of effective muon lifetime [20].

Figure 2.13 shows the timing profile of neutrinos generated in the mercury target obtained from the MC simulation. The black square pulse corresponds to the proton

beam bunch timing, and the time distribution of neutrinos from pion, muon and kaon decays is shown. One can find that only neutrinos from muon decay at rest survive 1 μs after the beam timing. Thus, neutrinos from decay of short-lived particles as well as beam induced fast neutrons are rejected by simply selecting 1 μs after the start of beam bunch.

The beam existence in the off-bunch timing may cause background depending on its amount. Technically, it is heavily suppressed because of two features of the RCS: the large kicker angle of the extraction and the fast extraction. The first one suppresses an accidental extraction when the kicker magnet is off. In addition, the fast extraction ejects all protons in the RCS ring to the beamline towards the MLF target at once so that no protons remain in the ring after extraction. The quantitative estimation and measurement shows that the beam existence after the beam bunch timing is less than 10^{-18} with respect to the number of proton in the main pulse in the on-bunch timing [?, ?, ?]. Thus, the effect is negligibly small in the JSNS² experiment.

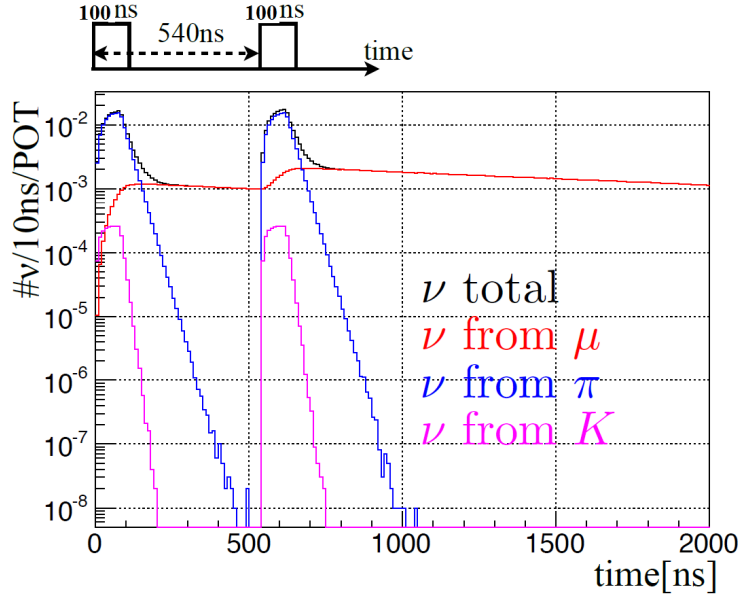


Figure 2.13: Time distribution of neutrinos from pion, muon and kaon decays. The origin of the horizontal axis corresponds to beam collision time. Only neutrinos from μDAR survive after 1 μs from the proton beam collision timing [10].

Figure 2.14 compares the expected neutrino energy spectrum from the mercury target before (left) and after (right) the timing selection ($t > 1 \mu\text{s}$). Note that the resulting $\bar{\nu}_\mu$ and ν_e fluxes have different spectra with endpoint energy of 52.8 MeV. The component from $\mu^- \text{DAR}$ is highly suppressed by π^- and μ^- absorptions on heavy nucleus. A possible survived μ^- decay will be an order of 10^{-3} , and produces ν_μ and $\bar{\nu}_e$ with same spectrum as those of $\bar{\nu}_\mu$ and ν_e from $\mu^+ \text{DAR}$, respectively.

Table 2.1 shows a summary of neutrino beam classification based on beam timing information.

In reality, a timing gate from 1 to 10 μs from the beam timing is applied to prompt signal selection. This timing window reduces cosmic ray induced backgrounds by factor of 9/40000, because of the 40 ms time interval to the next beam spill. Note

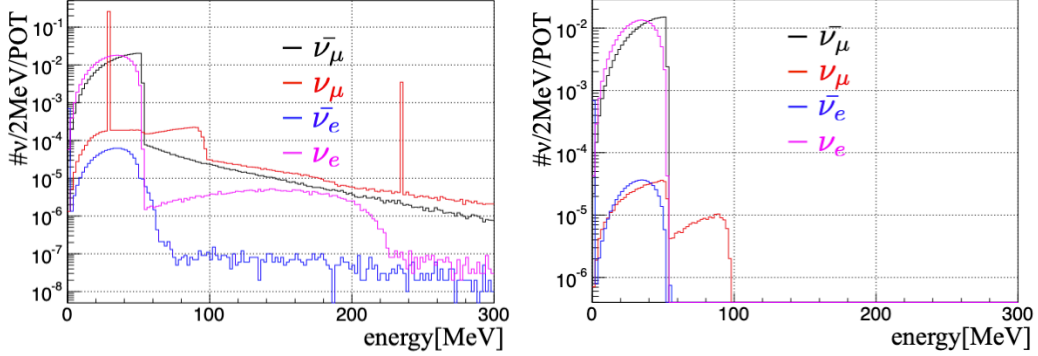


Figure 2.14: Estimated neutrino flux for all components (left) and components after 1 μ s from proton beam timing (right). As a result of timing selection, the μ^+ DAR components are selected and main background component is from μ^- decays [10].

Table 2.1: Classification of Beam Neutrinos.

Mode	Timing Type	Process	Comments on E_ν
$\pi^+ \rightarrow \mu^+ + \nu_\mu$	On-bunch	π DAR	monochromatic 30 MeV
$\mu^- + A \rightarrow \nu_\mu + A$	On-bunch	Absorption	endpoint 105 MeV
$K^+ \rightarrow \mu^+ + \nu_\mu$	On-bunch	K DAR	236 MeV monochromatic
$K^+ \rightarrow \mu^+ + \pi^0 + \nu_\mu$	On-bunch	K DAR	endpoint 215 MeV
$K^+ \rightarrow e^+ + \pi^0 + \nu_e$	On-bunch	K DAR	endpoint 228 MeV
$\mu^+ \rightarrow e^+ + \nu_e + \bar{\nu}_\mu$	Off-bunch	μ^+ DAR	endpoint 52.8 MeV
$\mu^- \rightarrow e^- + \nu_\mu + \bar{\nu}_e$	Off-bunch	μ^- DAR	endpoint 52.8 MeV

that LSND experiment used 600 μ s beam bunches with 120 Hz period from LINAC beam, and therefore the on-bunch neutrinos and neutrons could not be removed by timing information. In addition, the beam duty factor was 600 μ s \times 120 Hz = 7.2%, which is much higher than that of the MLF by factor of \sim 14400.

2.2.0.3 Neutrino Flux Estimation

Tables 2.2 and 2.3 are expected production rates of π^\pm by 3 GeV protons on the mercury target and the resulting μ^+ and μ^- decay neutrinos per proton, based on a pion production model.

Table 2.2: An estimate of μ DAR neutrino production by 3 GeV protons using FLUKA hadron simulation package [10].

	$\pi^+ \rightarrow \mu^+ \rightarrow \bar{\nu}_\mu$	$\pi^- \rightarrow \mu^- \rightarrow \bar{\nu}_e$
π/p	6.49×10^{-1}	4.02×10^{-1}
μ/p	3.44×10^{-1}	3.20×10^{-3}
ν/p	3.44×10^{-1}	7.66×10^{-4}
ν after 1 μ s	2.52×10^{-1}	4.43×10^{-4}

There are many sources of ambiguities in pion production, e.g., the production rates are sensitive to production of secondary particles, target geometry, and uncertainty on pion production process in mercury. We use these calculations as

Table 2.3: An estimate of μ DAR neutrino production by 3 GeV protons using QGSP-BERT hadron simulation package [10].

	$\pi^+ \rightarrow \mu^+ \rightarrow \bar{\nu}_\mu$	$\pi^- \rightarrow \mu^- \rightarrow \bar{\nu}_e$
π/p	5.41×10^{-1}	4.90×10^{-1}
μ/p	2.68×10^{-1}	3.90×10^{-3}
ν/p	2.68×10^{-1}	9.34×10^{-4}
ν after $1\mu s$	1.97×10^{-1}	5.41×10^{-4}

estimates, and the actual μ^- backgrounds should be finally determined from the data based on their known spectrum and known cross section. In this thesis, the numbers from table 2.2 are used to estimate the central values.

For the flux estimation, the proton intensity is assumed to be 0.33 mA, delivering 3.8×10^{22} protons on target (POT) per 5000 hour operation in one year, and the stopping ν/p ratio is estimated from the FLUKA simulations to be 0.344. Then, the $\bar{\nu}_\mu$ flux from $\pi^+ \rightarrow \nu_\mu + \mu^+$; $\mu^+ \rightarrow e^+ + \nu_e + \bar{\nu}_\mu$ chain at 24 m is then equal to 1.8×10^{14} $\nu/\text{year}/\text{cm}^2$.

2.2.0.4 Energy Spectrum of μ DAR Neutrino

Muons decay in the following channel with almost 100% branching ratio;

$$\begin{aligned}\mu^- &\rightarrow e^- + \nu_\mu + \bar{\nu}_e, \\ \mu^+ &\rightarrow e^+ + \bar{\nu}_\mu + \nu_e.\end{aligned}\tag{2.3}$$

The Feynman diagram of each decay mode is shown in Fig. 2.15, and matrix element of μ^- decay can be written in

$$\mathcal{M}_{\mu \rightarrow e \nu \bar{\nu}} = 2\sqrt{2}G_F [\bar{e}_L \gamma_\rho \nu_{eL}] [\bar{\nu}_{\mu L} \gamma^\rho \mu_L],\tag{2.4}$$

where G_F is Fermi constant, and $e_L, \nu_{eL}, \nu_{\mu L}$ and μ_L are spinors for each fermion. Ignoring the small term m_e/m_μ , computation of the matrix element shows the energy spectrum of ν_μ is given by [21]

$$\frac{d\Gamma}{dE_{\nu_\mu}} = \frac{G_F^2 m_\mu^4}{12\pi^3} \left(\frac{E_{\nu_\mu}}{m_\mu}\right)^2 \left(3 - 4\frac{E_{\nu_\mu}}{m_\mu}\right),\tag{2.5}$$

in the muon rest frame. On the other hand, the energy spectra of $\bar{\nu}_e$ and e^- are expressed as follows respectively:

$$\begin{aligned}\frac{d\Gamma}{dE_{\bar{\nu}_e}} &= \frac{G_F^2 m_\mu^4}{2\pi^3} \left(\frac{E_{\bar{\nu}_e}}{m_\mu}\right)^2 \left(1 - 2\frac{E_{\bar{\nu}_e}}{m_\mu}\right), \\ \frac{d\Gamma}{dE_{e^-}} &= \frac{G_F^2 m_\mu^4}{12\pi^3} \left(\frac{E_{e^-}}{m_\mu}\right)^2 \left(3 - 4\frac{E_{e^-}}{m_\mu}\right).\end{aligned}\tag{2.6}$$

The electron from muon decay is called Michel electron. Note that the domain of each energy is $[0, m_\mu/2]$, i.e., the endpoint of the spectra is $m_\mu/2 \sim 52.8$ MeV. In case of μ^+ decay at rest, the $\bar{\nu}_\mu$ and the ν_e has the same energy spectrum as ν_μ and $\bar{\nu}_e$ in μ^- decay case. Figure 2.16 shows an area normalized energy spectrum of $\bar{\nu}_\mu$ from μ^+ DAR and $\bar{\nu}_e$ from μ^- DAR, respectively. These are used for calculation for the number of IBD event and input for MC IBD event generator.

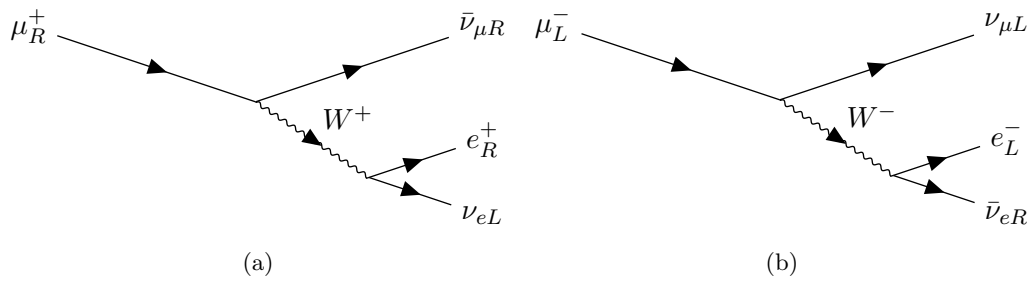


Figure 2.15: Feynman diagram of μ^+ decay (left) and μ^- decay (right).

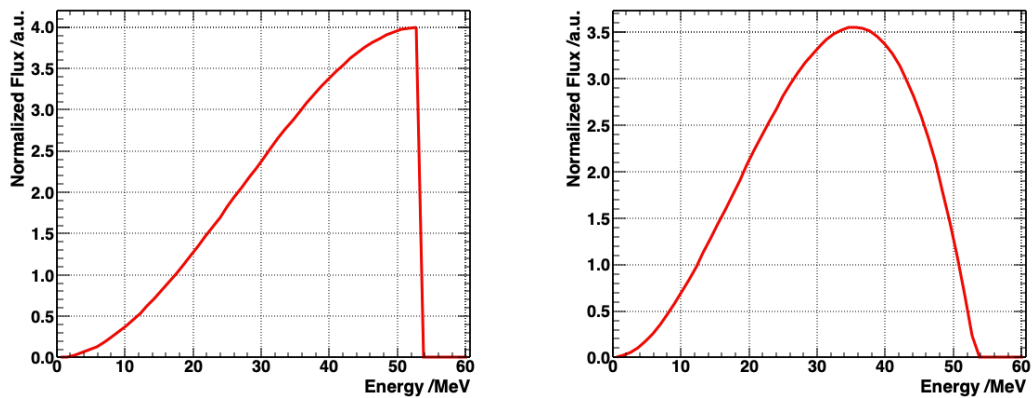


Figure 2.16: Energy (normalized flux) spectrum of μ^+ decay (left) and μ^- decay (right).

2.3 Signal selection criteria

Table 2.4 summarizes the signal selection conditions of the IBD and their selection efficiencies. Because references [9, 30] give descriptions about each criterion in detail, brief discreptions are given in this section. The signal selection efficiencies and background rejection power will be estimated based on the data obtained in the first run in order to compare with the expectation shown here.

Table 2.4: IBD selection conditions and their efficiencies in the JSNS² experiment [9].

Cut condition	Efficiency
$1 \leq \Delta t_{\text{beam-prompt}} \leq 10 \mu\text{s}$	74%
$20 \leq E_{\text{prompt}} \leq 60 \text{ MeV}$	92%
$\Delta t_{\text{delayed}} \leq 100 \mu\text{s}$	93%
$7 \leq E_{\text{delayed}} \leq 12 \text{ MeV}$	71%
$\Delta \text{VTX}_{\text{prompt-delayed}} \leq 60 \text{ cm}$	96%
$\Delta \text{VTX}_{\text{OB-delayed}} \geq 110 \text{ cm}$	98%
Lifetime ≤ 11	91%
PSD cut	$\sim 99\%$
Total	38%

- $\Delta t_{\text{beam-prompt}}$
 - ... a timing window for a prompt signal. It is possible to reject beam induced fast neutron in the on-bunch timing as well as neutrino events from kaon and pion decay by selecting $1 \mu\text{s}$ after beam timing.
- E_{prompt}
 - ... an energy selection condition to a prompt signal of an IBD event. The range is determined based on the energy spectrum of IBD positron (Fig. 2.19) and energy resolution of the JSNS² detector.
- $\Delta t_{\text{prompt-delayed}}$
 - ... a condition of timing difference between the prompt and the delayed signals. Because the neutron capture time in the JSNS² detector is $\sim 30 \mu\text{s}$, this selection can significantly reduce accidental backgrounds compared to no condition case.
- E_{delayed}
 - ... an energy selection condition to a delayed signal of an IBD event. The range covers 8 MeV peak of gamma rays from thermal neutron capture on Gd. Note that the selection efficiency includes an effect of Gd capture fraction with respect to total neutron capture. Therefore, the neutron detection efficiency in reference [9] is computed as 66 %.
- $\Delta \text{VTX}_{\text{prompt-delayed}}$

- ... a condition to spatial correlation between prompt and delayed signals of IBD events. The accidental coincided events have weak correlation between their prompt and delayed signals compared to the correlated events, e.g., IBD and fast neutron. The selection can reduce the accidental events to 2.3 ± 0.1 % [10].

- $\Delta VTX_{OB-delayed}$

- ... a selection condition in order to reject nGd events from neutron intruding into the detector in the beam on-bunch timing. This process has a prompt signal in the on-bunch timing ($0 \leq \Delta t_{beam-prompt} \leq 1 \mu s$) so that the condition to the spatial correlation between on-bunch event and delayed signal can reject the nGd events from on-bunch neutron. The rejection efficiency of this selection criterion is estimated as ~ 97 % as discussed in [30].

Particle identification using pulse shape discrimination

It is necessary to reduce an event rate of cosmic ray induced fast neutron to the same level as the rate in the underground experiments. We achieve the requirement using particle identification with pulse shape discrimination (PSD). Because scintillation light emission timing profile depends on energy loss per distance (dE/dx), the observed waveform on PMTs reflects the difference of the timing profile as a shape of the waveform. Fast neutron makes a prompt signal by a proton recoil so that the waveform from fast neutron event have a different shape from the IBD prompt signal due to the large dE/dx . Figure 2.17 shows the Q_{tail}/Q_{total} distributions of the IBD events (red) and the cosmic fast neutron events (blue) obtained using a Monte-Carlo simulation based on the waveform data measured using 70 MeV neutron beam [9]. Q_{tail}/Q_{total} is a ratio of tail charge to total charge of waveform, which characterizes a shape of waveform. There is a clear separation between prompt signals of IBD and fast neutron, and the estimated rejection efficiency reaches 99 % at ~ 99 % signal efficiency.

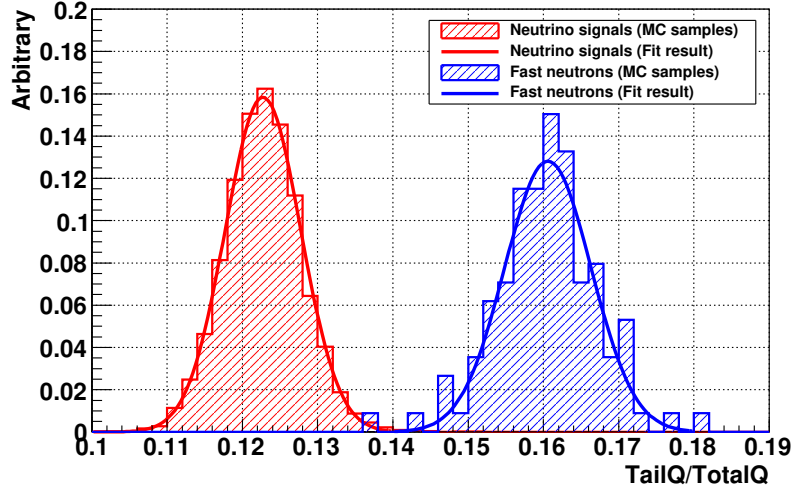


Figure 2.17: $Q_{\text{tail}}/Q_{\text{total}}$ distributions of the IBD events (red) and the cosmic fast neutron events (blue).

2.4 Detector Simulation

The detector Monte-Carlo simulation (MC) tool was developed using Reactor Analysis Tool (RAT) framework [22], which is based on Geant4 [19] and GLG4sim [57] for liquid scintillation detector simulation. Geant4 is a simulation tool kit provided by CERN, and widely used in the field of particle and nuclear physics to simulate particle interaction and behavior in matter. GLG4sim is a self-contained application, a generalized version of the KamLAND MC simulator, intended to simulate liquid scintillator neutrino detector with optical simulation based on Geant4 framework. RAT utilizes the classes defined in GLG4sim to create a MC event producer that integrates with the rest of the RAT framework. The JSNS² RAT uses Shielding physic list for hadronic and electromagnetic process simulation in Geant4.10.2.3. For neutron interaction and transportation in low energy, below 20 MeV, high precision (HP) model including elastic scattering, inelastic scattering, radiative capture, and fission is utilized. Yield of optical photon generated in Cerenkov radiation and/or scintillation processes by energy loss of an incident particle in liquid scintillator is computed with quenching effect described by Birk's law [24],

$$\frac{dL}{dx} = L_0 \frac{\frac{dE}{dx}}{1 + k_B \frac{dE}{dx}}, \quad (2.7)$$

where L_0 is a scintillation light yield constant in case of no quenching, and k_B is an empirical parameter depending on materials, which expresses an effect of quenching to energy loss. The JSNS² RAT uses optical parameters measured in RENO experiment which utilizes the same type liquid scintillator detector as JSNS² [25]. The essential parameters for Gd-LS and LS are listed and summarized in table 2.5 (value at 440 nm for attenuation length and refractive index).

Table 2.5: The optical parameters used in the JSNS² RAT simulator.

Material	Attenuation length /m	Refractive index	Birk's constant /mm/MeV
Gd-LS	13	1.45	0.124
LS	18	1.45	0.117

2.4.1 Detector geometry

The JSNS² RAT contains modeled geometries of the JSNS² detector and the shield. Figure 2.18 shows the graphics of the implemented detector geometry and shields. The shape of 10 inch PMT R7081, the acrylic vessel, the s.s. tank as well as the anti-oil-leak walls are modeled based on the drawings of them. The lead shield is composed of 1500 lead bricks with the dimension of 20 cm width, 10 cm height, and 5 cm thickness. In the veto layer of the MC detector, L-angle support structures are also implemented to simulate detector response to an event in the veto layer, such as cosmic μ from the outside of the detector. The surface of the materials in the veto layer has reflectivity based on the reflection coefficient of the reflection sheet covering the layer surface. The detailed descriptions of the detector components is in the following chapter.

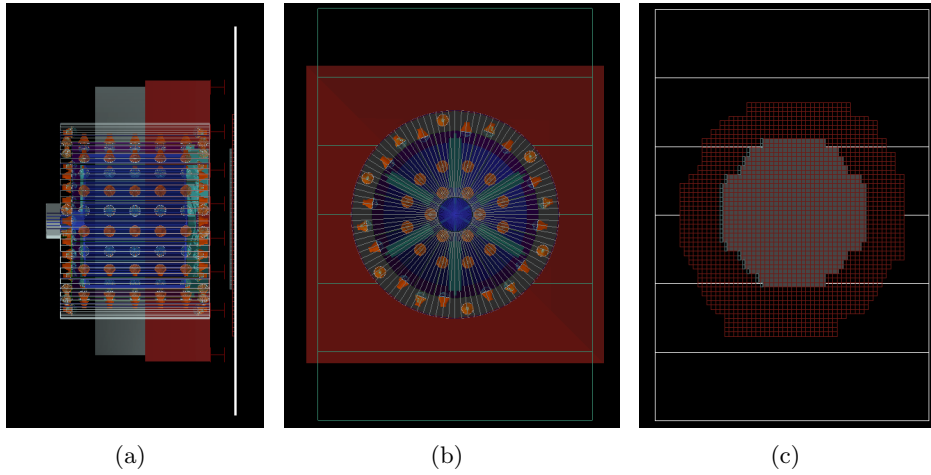


Figure 2.18: The implemented geometry in the JSNS² RAT simulation. (a) size view, (b) top view, and (c) top view of the shield consist of lead bricks and iron plates

2.4.2 Generators for MC simulation

IBD generator

In order to simulate IBD behavior in the detector, the IBD generator is developed taking the approximated angular distribution from Vogel et al. [13]. The differential cross section of IBD at zeroth order of inverse average nucleon mass $1/M$, limit of infinite nucleon mass, is expressed as

$$\left(\frac{d\sigma}{d\cos\theta} \right)^{(0)} = \frac{\sigma_0}{2} \left[(f^2 + 3g^2) + (f^2 - g^2)v_e^{(0)} \cos\theta \right] E_e^{(0)} p_e^{(0)}, \quad (2.8)$$

where the positron energy at this order is defined as $E_e^{(0)} = E_\nu - \Delta$, the mass difference $\Delta = M_n - Mp$, and the definition of the positron momentum and the velocity at each order is $p_e = \sqrt{E_e^2 - m_e^2}$ and $v_e = p_e/E_e$, respectively. The constant $f = 1$ and $g = 1.26$ corresponds to the vector and axial-vector coupling constant. The normalization factor σ_0 including the energy independent inner radiative correction is expressed as

$$\sigma_0 = \frac{G_F^2 \cos^2 \theta_C}{\pi} (a + \Delta_{\text{inner}}^R), \quad (2.9)$$

where $\Delta_{\text{inner}}^R \sim 0.024$. At the first order in $1/M$, the positron energy depends on the scattering angle, i.e.,

$$E_e^{(1)} = E_e^{(0)} \left[1 - \frac{E_\nu}{M} (1 - v_e^{(0)} \cos \theta) \right] - \frac{y^2}{M}, \quad (2.10)$$

where $y^2 = (\Delta^2 - m_e^2)/2$. Then, the differential cross section at this order is

$$\left(\frac{d\sigma}{d \cos \theta} \right)^{(1)} = \frac{\sigma_0}{2} \left[(f^2 + 3g^2) + (f^2 - g^2) v_e^{(1)} \cos \theta \right] E_e^{(1)} p_e^{(1)} - \frac{\sigma_0 \Gamma}{2M} E_e^{(0)} p_e^{(0)}, \quad (2.11)$$

where

$$\begin{aligned} \Gamma = & 2(f + f_2)g \left[(2e_e^{(0)} + \delta)(1 - v_e^{(0)} \cos \theta) - \frac{m_e^2}{E_e^{(0)}} \right] \\ & + (f^2 + g^2) \left[\Delta(1 + v_e^{(0)} \cos \theta) + \frac{m_e^2}{E_e^{(0)}} \right] \\ & + (f^2 + 3g^2) \left[(E_e^{(0)} + \Delta) \left(1 - \frac{1}{v_e^{(0)}} \cos \theta \right) - \Delta \right] \\ & + (f^2 - g^2) \left[(E_e^{(0)} + \Delta) \left(1 - \frac{1}{v_e^{(0)}} \cos \theta \right) - \Delta \right] v_e^{(0)} \cos \theta, \end{aligned} \quad (2.12)$$

and the anomalous nucleon isovector magnetic moment $f_2 = \mu_p - \mu_n = 3.706$. Therefore, the positron momentum at given neutrino energy and a direction is computed based on Eqs. (2.10) and (2.11). The neutron momentum is led to from 4-momentum conservation in the proton rest. Figure 2.19 shows energy spectrum of positron (red) and neutrino (blue) from the IBD generator for the signal $\bar{\nu}_\mu \rightarrow \bar{\nu}_e$ (left) and the background $\bar{\nu}_e$ from μ^- (right). The event vertices of the IBD are generated uniformly in the detector.

$^{12}\text{C}(\nu_e, e^-)^{12}\text{N}_{g.s.}$ generator

ν_e interacts with ^{12}C in the detector, and generates electron and ^{12}N . The electron immediately causes scintillation, and is detected as a prompt signal. The nitrogen will be produced in the ground state in $\sim 95\%$ of the cases, and decays via β^+ decay, whose positron makes a delayed signal. The lifetime of the β^+ decay is 15.9 ms, and the endpoint of the positron kinetic energy is ~ 16 MeV. Figure 2.20 shows the kinetic energy spectrum of the electron (left) as the prompt signal and the positron (right) as the delayed signal.

The kinetic energy and momentum direction are determined from cross section and angular dependence of $^{12}\text{C}(\nu_e, e^-)^{12}\text{N}_{g.s.}$ reaction shown in Fig. 2.21 as well as ν_e spectrum (same shape as the right plot of Fig. 2.16).

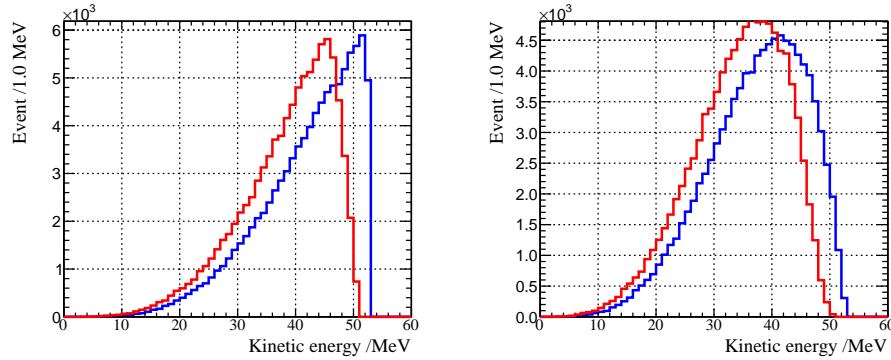


Figure 2.19: Kinetic energy of positron (red) and neutrino (blue) in IBD interaction. Left: the signal $\bar{\nu}_\mu \rightarrow \bar{\nu}_e$. Right: the background $\bar{\nu}_e$ from μ^- .

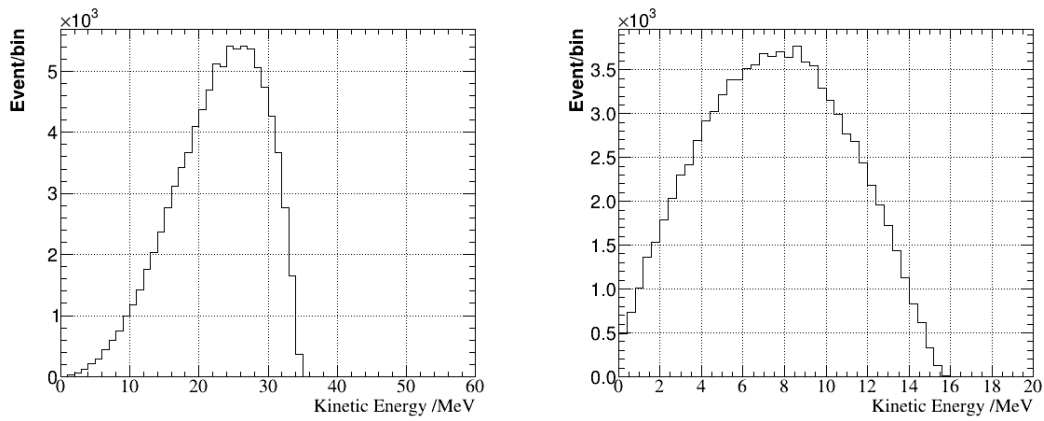


Figure 2.20: Kinetic energy of generated electron (left) and positron (right) as final state particles in $^{12}\text{C}(\nu_e, e^-)^{12}\text{N}_{g.s.}$ reaction.

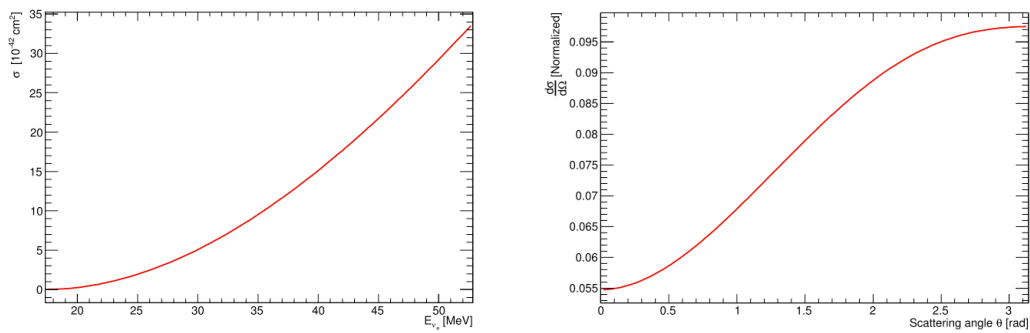


Figure 2.21: Cross section of $^{12}\text{C}(\nu_e, e^-)^{12}\text{N}_{g.s.}$ reaction. Left: dependence on ν_e energy. Right: angle between the ν_e and the projectile electron [26].

^{252}Cf generator

^{252}Cf is an unstable isotope which emits multiple neutrons by fission with an average number of 3.7 neutrons/decay, accompanied with emission of gamma rays of energy up to 30 MeV. The model of ^{252}Cf developed in the Double Chooz experiment is used as a generator for MC simulation in this thesis. Figure 2.22 shows data and MC comparison in the Double Chooz experiment [27]. The left plot is the prompt signal energy spectrum, and the distribution of the number of the delayed signals is shown in the right plot. They indicate that the model well describes neutron multiplicity from ^{252}Cf in spite of energy distribution disagreement due to uncertainties on fission process. Because we calibrate only nGd signal by ^{252}Cf source, the discrepancy on the prompt energy spectrum is no problem for our purpose.

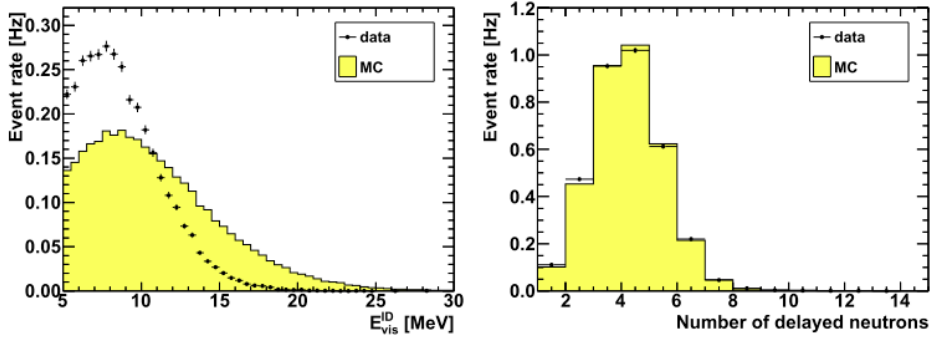


Figure 2.22: Reproducibility of the ^{252}Cf generator in the Double Chooz far detector [27]. Left: energy distribution for the prompt signal by fission. Right: neutron multiplicity by fission.

Michel electron generator

Michel electron (positron) comes from cosmic muon decay, which stops in the detector. It has the same energy spectrum as $\bar{\nu}_\mu$ from $\mu^+\text{DAR}$; therefore, it is useful to calibrate energy scale of the signal region of JSNS² experiment. Because cosmic muon gives large energy deposit to the detector, its simulation with the optical process consumes large amount of time and CPU power. In order to avoid the difficulty, we generate electron (or positron) with the Michel energy spectrum. The ratio of positron to electron follows the charge ratio of cosmic muon in reference [52]. We assume that the vertices of Michel electron (positron) distribute uniformly in the detector. Figure 2.23 shows energy distribution of generated electron/positron (left) and vertex distribution (right).

Cosmic-ray induced fast neutron generator

Cosmic-ray induced fast neutron generator is developed for MC simulation based on parametrization in reference [28], except for kinetic energy distribution. Fast neutrons are produced as a result of interactions between cosmic muon and materials, such as nuclei in concrete. In the reference, the distribution of neutron multiplicity

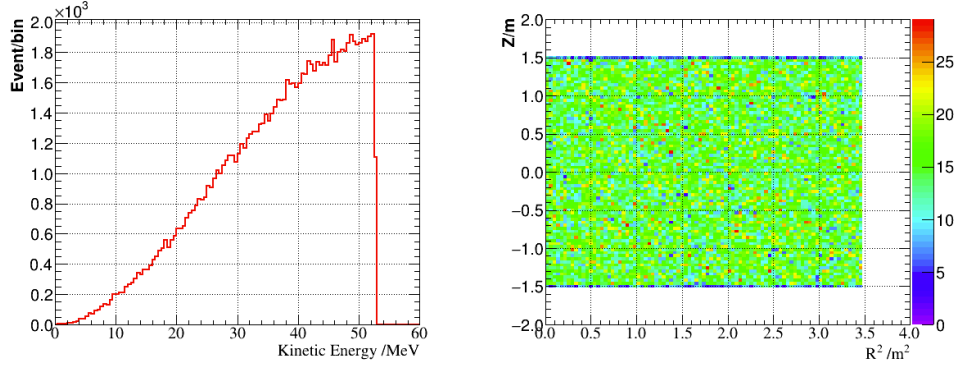


Figure 2.23: Left: kinetic energy distribution of generated electron/positron. Right: 2D histogram for generated vertices in the inner detector in zr^2 plain.

M is defined as

$$\begin{aligned} \frac{dN}{dM} &= N_0 \times \left(e^{-A(E_\mu)M} + B(E_\mu)e^{-C(E_\mu)M} \right), \\ A(E_\mu) &= 0.085 + 0.54e^{-0.075E_\mu}, \\ B(E_\mu) &= \frac{27.2}{1 + 7.3e^{-0.076E_\mu}}, \\ C(E_\mu) &= 0.67 + 1.4e^{-0.12E_\mu}, \end{aligned} \quad (2.13)$$

where N_0 is a normalization factor, and E_μ is muon energy. The angler dependence of fast neutron with respect to cosmic muon direction is defined as

$$\begin{aligned} \frac{dN}{d \cos \theta} &= \frac{N_0}{(1 - \cos \theta)^{0.6} + D(E_\mu)}, \\ D(E_\mu) &= 0.699E_\mu^{-0.136}, \end{aligned} \quad (2.14)$$

where $\cos \theta$ corresponds to angle between muon and fast neutron momentum. Figure 2.24 shows kinetic energy spectrum (top left), $\cos \theta$ distribution (top right), and multiplicity distribution (bottom left) of the generated neutrons, where θ is the zenith angle. The direction of cosmic muon is determined based on $\cos^2 \theta$ angular distribution, and muon energy is fixed at 4 GeV for approximation. The kinetic energy distribution of fast neutron is assumed as flat distribution, which is determined by comparing to the data obtained in the first run.

Because the detector is located in the MLF building, we assume that cosmic neutrons are generated in the concrete walls around the detector. For simulation, the walls are modeled in a simple squared U-shape with 1 m thickness as shown in Fig. 2.25. In addition, it is assumed that the interaction between muon and matter in concrete occurs uniformly. Figure 2.26 shows the vertex distribution where neutrons are generated in the simulation in XY plane (left) and in XZ plane whose origin is set to the detector center.

Cosmic-ray induced γ generator

The energy spectrum of cosmic-ray induced gamma ray is measured and modeled by the following empirical function:

$$\frac{dN}{dE} = \frac{A}{B}e^{-E/B} + \frac{C}{D}e^{-E/D}, \quad (2.15)$$

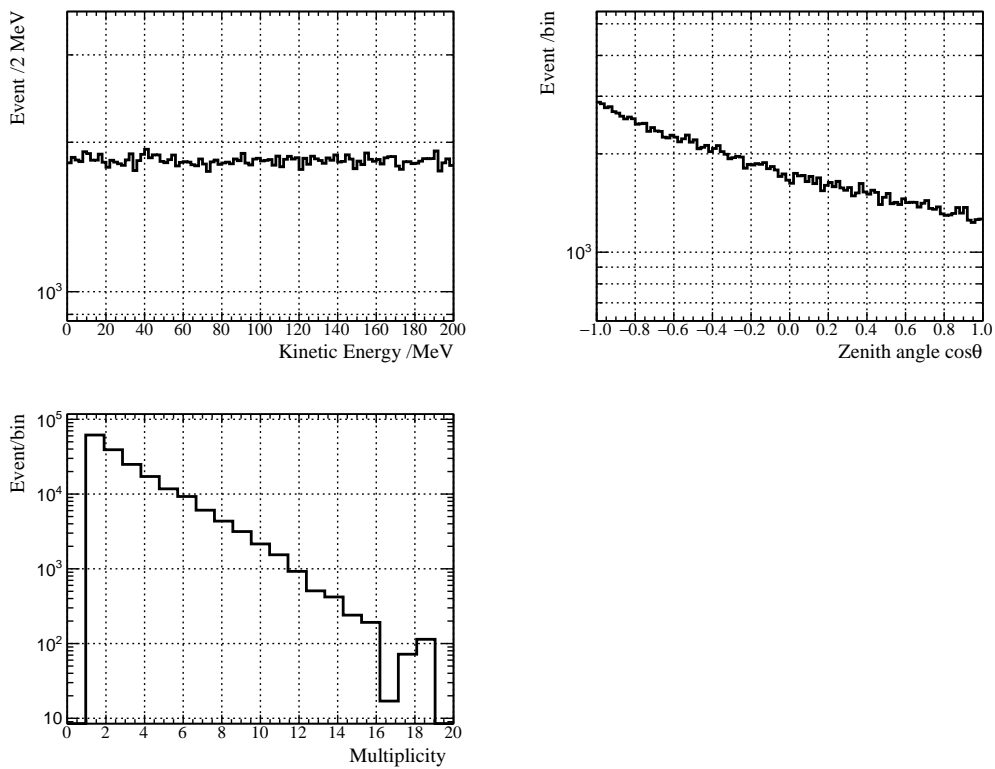


Figure 2.24: Generator information of cosmic fast neutron. Top left: kinetic energy distribution. Top center: $\cos\theta$ distribution for zenith angle θ . Top right: multiplicity. Bottom left: particle generation point in XY plain. Bottom center: particle generation point in XZ plain. The origin of XYZ coordinate is set to the detector center.

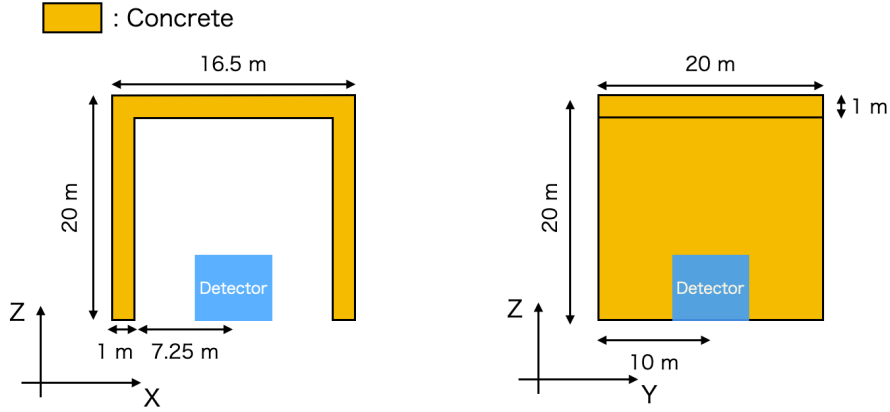


Figure 2.25: A model of concrete walls in the MLF third floor shows spatial relations to the detector in the XZ plane (left) and the YZ plane (right), respectively. We assume that cosmic ray induced fast neutron/gamma ray generated in the concrete volume as a result of an interaction between cosmic muon and matter in the concrete.

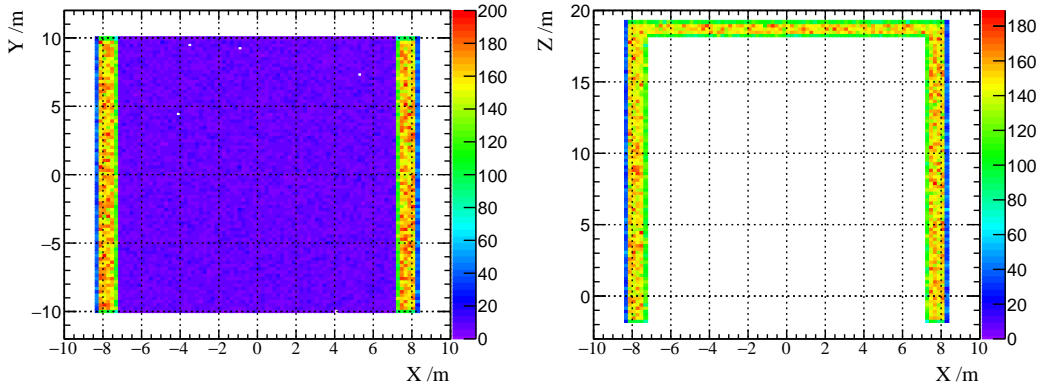


Figure 2.26: Neutron generated position distribution in XY plane (left) and in XZ plane (right). The origin of XYZ coordinate is set to the detector center.

where E is kinetic energy of gamma ray, A, B, C and D are parameters determined as $(A, B, C, D) = (3 \text{ Hz/m}^2, 26 \text{ MeV}, 25 \text{ Hz/m}^2), 150 \text{ MeV}$ [29]. The angler dependence and generation point is generated in the same way as the cosmic fast neutron generator. Figure 2.27 displays distributions of kinetic energy, $\cos \theta$ distribution for zenith angle θ in the top panels, and 2D histograms of the generation point in XY and XZ plain in the bottom panels, respectively.

Generator for γ from the surface on the hatch

The gamma rays coming from the surface on the hatch of the mercury target was observed and reported in the background measurement in 2014 [29]. It is modeled as gamma rays generated in thermal neutron capture on nuclei in concrete [30]. Figure 2.28 shows energy distribution of floor gamma. In MC simulation, we generate gamma ray following the energy distribution uniformly on the hatch surface (12.5 m

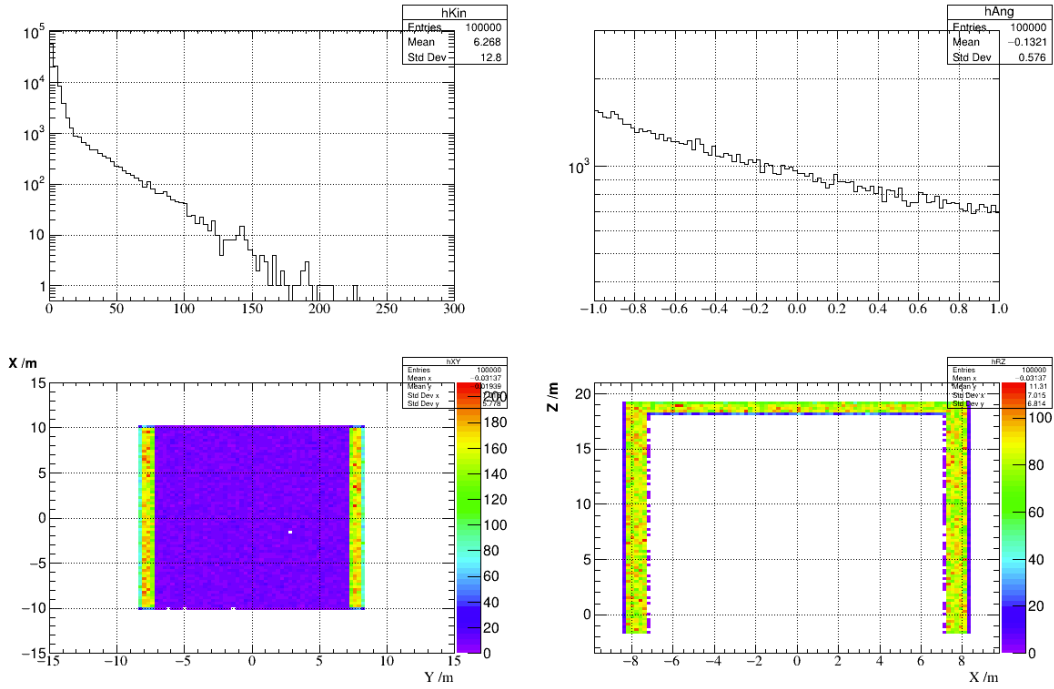


Figure 2.27: Generator information of cosmic fast neutron. Top left: kinetic energy distribution. Top right: $\cos \theta$ distribution for zenith angle θ . Bottom left: particle generation point in XY plain. Bottom right: particle generation point in XZ plain. The origin of XYZ coordinate is set to the detector center.

$\times 5.7$ m) in XY plain, and assumes the direction is fixed +z direction to reproduce the event vertex distribution in the data.

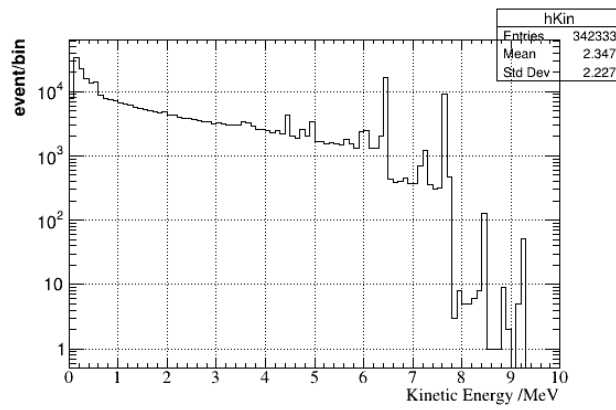


Figure 2.28: Kinetic energy distribution of floor gamma.

Chapter 3

Detector

As described in the previous chapter, the JSNS² detector is a movable detector to detect $\bar{\nu}_e$ using the IBD with Gd-LS. This chapter concentrates on detailed description of each detector components and their R&D to complete construction.

3.1 The stainless steel tank and the anti-oil-leak tanks

The stainless steel tank (s.s. tank) is an exoskeleton of the JSNS² detector made of 5 mm thick SUS304. Two anti oil-leak walls surround the s.s. tank which prevent liquid from spilling out in emergency case. The side view drawing and the photo of the entire tank are shown in figure 3.1 and figure 3.2, respectively. The construction of the stainless steel tank began on December 2017, and finished in the end of February 2018. Morimatsu was in charge of construction of the tank. All construction processes were done in J-PARC in the open air. The production of the components was done at the factory of Morimatsu in advance.

The inner dimensions of the cylindrical part of the s.s. tank are 4.6 m in diameter, 3.5 m in height, and the containable volume is 58 m³. There is a large flange structure along the circumference pointed in figure 3.1 to tightly enclose the lid. Herme-seal No.800, a oil-proof liquid gasket, is used as a sealing material for both LS and gas. We evaluated its sealing capability for gas using ~ 0.1 kPa relative high pressure with respect to atmospheric pressure, and concluded that it satisfied our requirement in order to keep nitrogen ambience with the nitrogen gas flow system (details are described in [31]). The shape of the top lid has a function to stabilize a liquid level change due to thermal expansion of Gd-LS/LS with a liquid level stabilization system (LLSS) described below.

The cylindrical (1st) anti oil-leak wall made of 6 mm thick steel (SS400) with 6.6 m diameter and 2.7 m height is capable of containing 80 m³, which adequately keep all liquid volume in the detector. The 2nd anti-oil-leak wall (1.5 m high and 4.5 mm thick) is also placed along the edge of the tank base as a backup prevention of liquid leak. The anti-oil-leak walls passed liquid penetrate test, which certify liquid sealing at welding points.

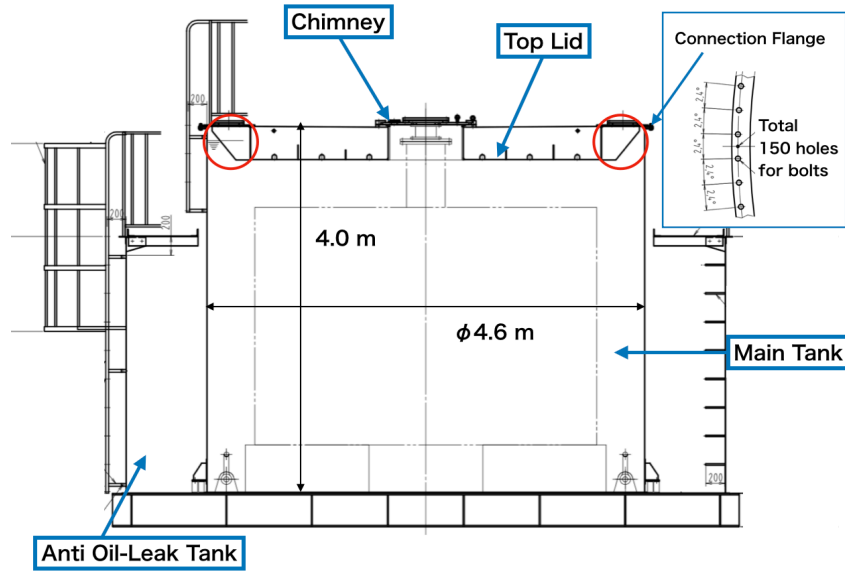


Figure 3.1: A side view of the tank and the anti oil-leak tank. The red circles correspond to the LS buffer space, which forms a large ring shape, to prevent a change of liquid level due to thermal expansion of LS. There are eight anti-sloshing blades in the buffer space to disturb the surface of LS from sloshing during crane work for detector installation to MLF, which is drawn as the trapezoid shapes in the red circles.



Figure 3.2: An entire viewing photo of the detector at HENDEL building. The red-painted square shape wall is anti-oil-leak wall welded on the edge of the tank base. The outer cylindrical structure with JSNS² logo on the surface is the 1-st anti-oil-leak wall. The most inner and highest structure is the s.s.tank of the detector. There are ladders and decks on the 1st anti-oil-leak tank for accessing to the detector.

3.2 The acrylic vessel

The acrylic vessel is a container for the Gd-LS forming neutrino target volume, which made from Plexiglas plates, ultra-violet transparent polymethyl methacrylate (PMMA). A drawing of the vessel is displayed in figure 3.3. The radius, height and volume of the vessel are 1.6 m, 2.4 m and 19.3 m^3 , respectively. The top and bottom part have 1.8 degree taper to avoid air trap in case liquid filling and nitrogen purging in the detector. 20 mm thick side wall has a robustness to pressure difference corresponding to 30 cm liquid level difference between inside and outside of the vessel. This allow us to quick operation about Gd-LS/LS filling and extraction process. Because the optical separator divides the outside volume of the vessel, support legs of the vessel consists of two separated structure (figure 3.4). The vessel was manufactured by Nakano Int'l Co. in Taiwan which is a company produced all inner acrylic vessels of Daya Bay experiment. Following measurements were done to check production quality of the vessel; optical quality, wall thickness and leakage. Details are described in following subsections.

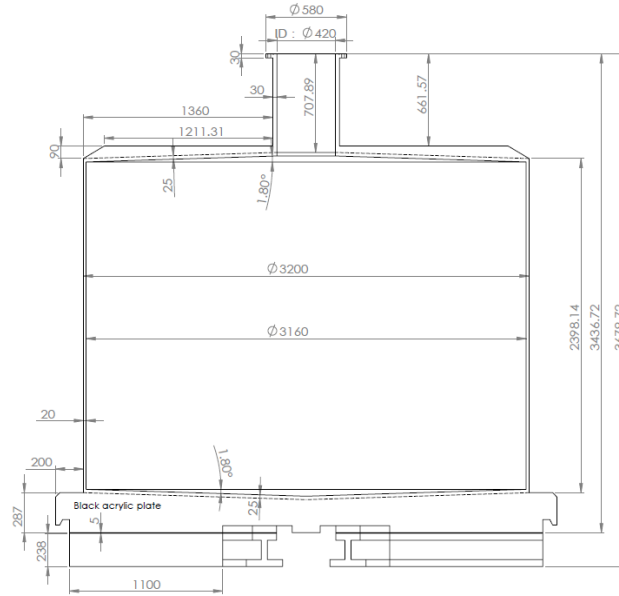


Figure 3.3: A drawing of entire vessel structure.

3.2.1 Optical quality test

As an important optical parameter of the acrylic, we measured transmittance spectrum of an acrylic sample quarried from a part of the vessel raw material. The sample was shaped in a rectangular solid with 5 cm optical path length for compatibility to a spectrophotometer U-3900 (Hitachi High-Tech). The result of transmittance spectrum in the air is shown in figure 3.5. 5 cm transmittance is $> 90 \%$ in the range of bis-MSB re-emission spectrum (400 - 600 nm) even it includes an effect of reflection at the boundary.

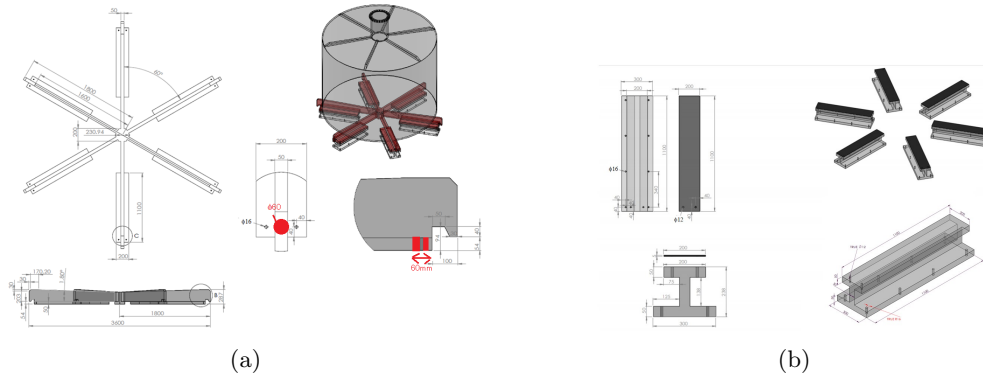


Figure 3.4: Drawings and 3D models of leg structure of the vessel. The leg structure above optical separator is glued on the bottom plate of the vessel, and has 6 beams with flat plate (left). I-shaped beam structures is placed below optical separator and fixed on the bottom of the s.s.tank with bolts.

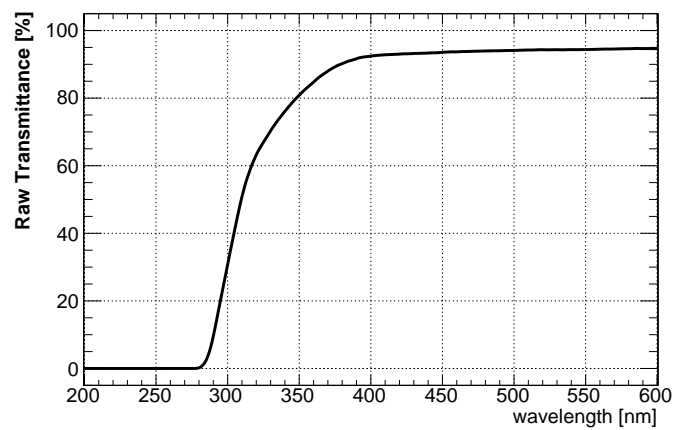


Figure 3.5: Measured 5 cm transmittance spectrum of the quarried acrylic sample. Note that the transmittance includes an effect of reflection at the boundary.

3.2.2 Thickness survey

Thickness of the vessel wall was surveyed after the vessel production. We utilized ultrasonic thickness meter which has an advantage in the way of non-destructive inspection. Calibration was performed using standard acrylic pieces measured with a micrometer in advance, and the precision reaches to 0.1 mm over the range (0 - 50 mm). Figure 3.6 shows the result of measurement. We measured around 100 points on the wall along the circumference at the center and found that the data show a periodic variation along the azimuth angle. This is because the vessel was made from 6 acrylic plates with polymerization gluing. However, the amplitude of variance is within 1 mm tolerance level.

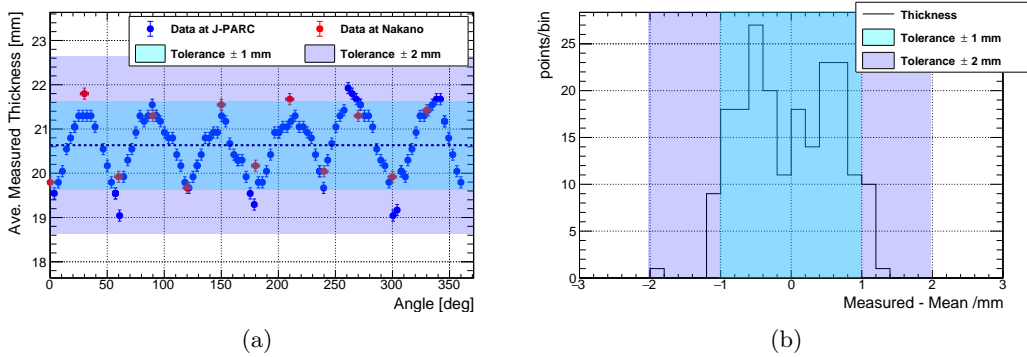


Figure 3.6: (a): Detailed thickness survey on the side wall. (b): A histogram of thickness difference from the mean value. The number of measured points is around 100 along the circumference at the center of the side wall. The measured data shows periodical fluctuation as a function of azimuth angle because of manufacturing process; however, the thickness fluctuation is within 1 mm displayed as light blue region.

3.2.3 Leakage survey

The sealing capability of the vessel was tested by applying nitrogen gas with ~ 0.9 kPa with respect to the atmospheric pressure. If there is significant leak around the vessel, the inner pressure will exponentially decrease as a function of time. We monitored the inner gas pressure and the environmental conditions, i.e., atmospheric temperature, pressure, and inner gas temperature, during the test. Figure 3.7 shows the obtained data about the inner gas temperature (green), the atmospheric temperature (red) and the atmospheric pressure (blue) in the left plot, and the inner gas pressure (black) in the right plot as a function of time. We developed a numerical calculation based on the equation of state for ideal gas to make a prediction of inner gas pressure behavior using the environmental condition data. It includes effects of leakage and acrylic thermal expansion in addition to gas state change. The prediction (blue) based on no leak assumption is overlaid on the right plot to compare it to the data, and shows that they are consistent within the uncertainty of the pressure sensor accuracy. It corresponds to leak rate $< 4 \mu\text{L}/\text{year}$.

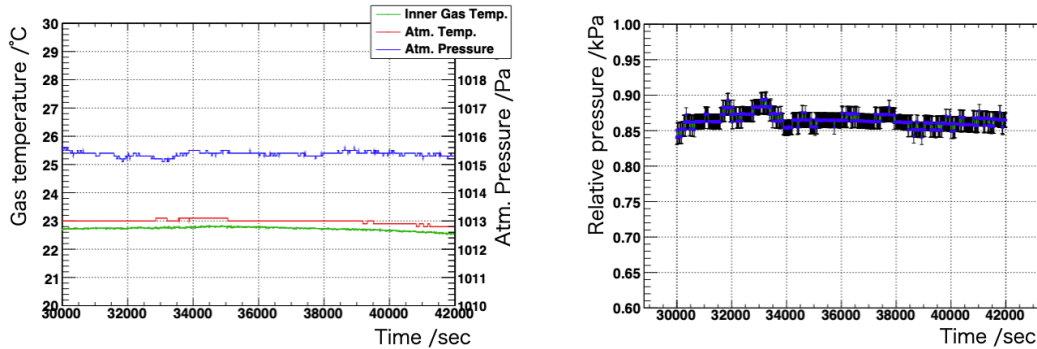


Figure 3.7: Left: Environmental conditions as a function of time. The left vertical axis is for the inner gas and atmospheric temperature data, and the right one is for the atmospheric pressure. Right: time evolution of the inner gas pressure with respect to atmospheric pressure. The black markers with error bar corresponds to the data points, and the blue line shows the prediction from no leak assumption. The horizontal axes show time. 30000 is the start time of the measurement.

3.2.4 Installation

The vessel was installed in the detector after all installation processes of detector components were done. Because clearance between the vessel and the installed components, such as PMTs and optical separators, is less than 10 cm, precise and careful crane operation was performed. During the installation, 3 m long guide rods were installed at the bolt holes for accurate hole matching. We finally fixed the vessel to the detector with 12 bolts from 3 m higher position after having settled the vessel. A 3 m long extension wrench with a magnet attachment at the edge was utilized to tighten bolts at the legs of the vessel because it is impossible to access to the bottom of the detector after the vessel installation. For this scheme we selected a bolt made of ferrite-austenite duplex stainless steel which has a magnetic property unlike usual SUS304.

3.3 Liquid Level Stabilization System

Liquid level control is a quite important system preventing the Gd-LS from spilling out from the acrylic vessel. The thermal expansion coefficient of LAB is $\Delta V/V \sim 9 \times 10^{-4} / ^\circ\text{C}$ [32]. Thus, temperature change leads to 12 cm/ $^\circ\text{C}$ in level change in the chimney of the vessel (42 cm radius). This change is quite large because the maximum temperature variation in the MLF is expected to be ± 10 $^\circ\text{C}$. In order to manage the phenomenon, we developed a liquid level stabilization system whose concept is shown in the top left of figure 3.9. It has 2 groups of 4 tanks (shown as the bottom left photo in figure 3.9) whose base area is ~ 2 m^2 in total, which contributes to a decrease in liquid level change. The Gd-LS in the stabilizer tanks is connected with the Gd-LS in the detector via an inverse siphon exchanging the liquid until reaching to an equilibrium state in level. There is a buffer tank helping establish the inverse siphon state, shown in the right photo of figure 3.9. Making vacuum in the buffer tank fills out the pipe lines for the inverse siphon system with

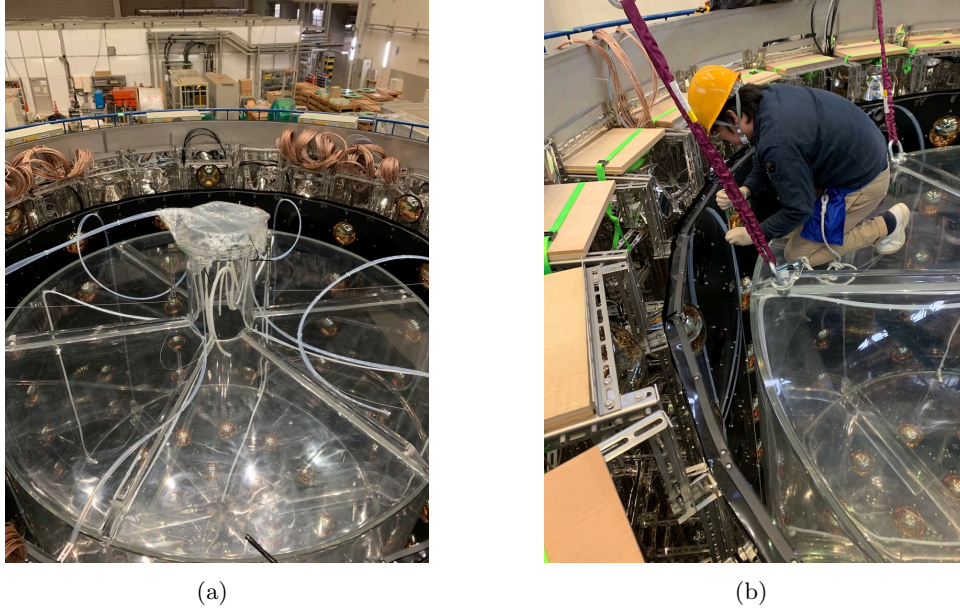


Figure 3.8: (a): The installed acrylic vessel. (b): A photo of work for fixing the vessel to the detector from the vessel lid.

the Gd-LS. We also utilize this system for filling the chimney of the vessel with the Gd-LS in order to match filling speed with the level of the LS out of the vessel.

3.4 Internal structures of the detector

For supporting detector components, such as PMT and optical separators, we designed support structure skeleton using L-shaped angle made of stainless steel (SUS304). There are L-angle bars welded on the inner surface of the s.s.tank, which are bases to fix the support skeletons and PMTs.

The support skeleton of the barrel part consists of 24 units of a box unit assembled with 40 mm width L-angle bars (figure 3.10). Each box unit were attached and fixed with the 2 vertical welded L-angles on the barrel wall. It had 5 horizontal L-angle bars in 600 mm step. The PMTs were fixed to the horizontal bars at their support jigs. Figure 3.10 (right) shows a design of main optical separator for the barrel part made of black-colored acrylic board with no-glare surface. The dimension of the board is 600 mm height, 486 mm width and 5 mm thickness, respectively, and each board has 256 mm diameter hole at the center to insert PMT. 5 black boards were vertically attached to each box unit; therefore, 120 boards in total were placed and formed 24-sides tube structure with 1.86 m radius and 3.0 m height. L-shaped black PET sheet made of Lumirror X30 (Toray) with 0.25 mm thickness as a supplemental optical separator (figure 3.10 right) is inserted together with each board to fill slight gaps among adjacent boards.

The structure for the lid is displayed in figure 3.11 (a), and the basic design for bottom part is similar to the lid part except for the part around the chimney. The PMTs were directly fixed to the base L-angle welded on the s.s. tank surface for lid part. Rectangle shapes consisting of L-angles were attached between the PMTs to enhance robustness of entire structure.

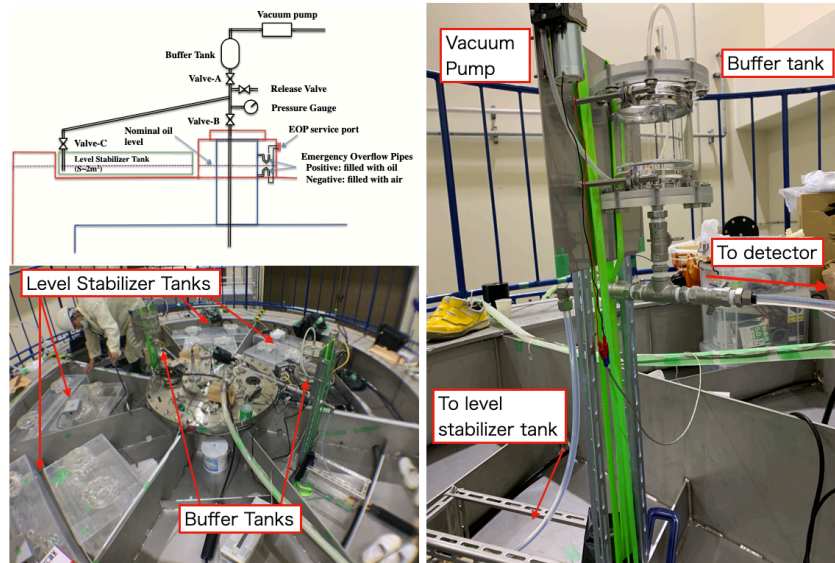


Figure 3.9: Top left: a conceptual diagram of the liquid level stabilization system. Bottom left: a photo of entire view of the system. Right: a photo of pipe lines for making inverse siphon.

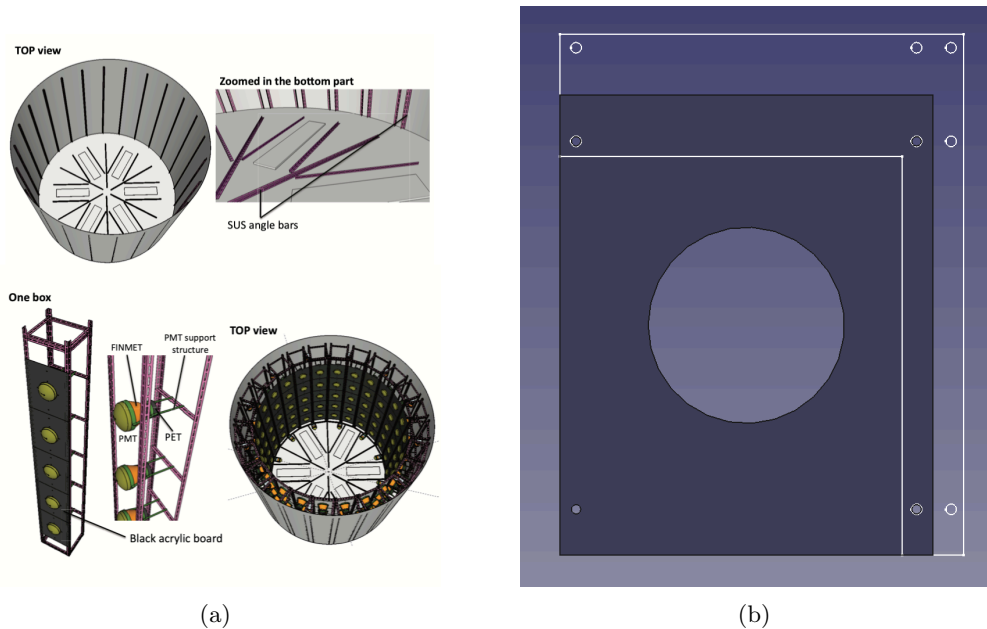


Figure 3.10: A design of support skeleton units for barrel part. Left shows the position of the base L-angles for fixing the skeleton structures. Right exhibits a box unit support structure and an image of installed status. Each unit contains 5 PMTs with 5 rectangle black boards.

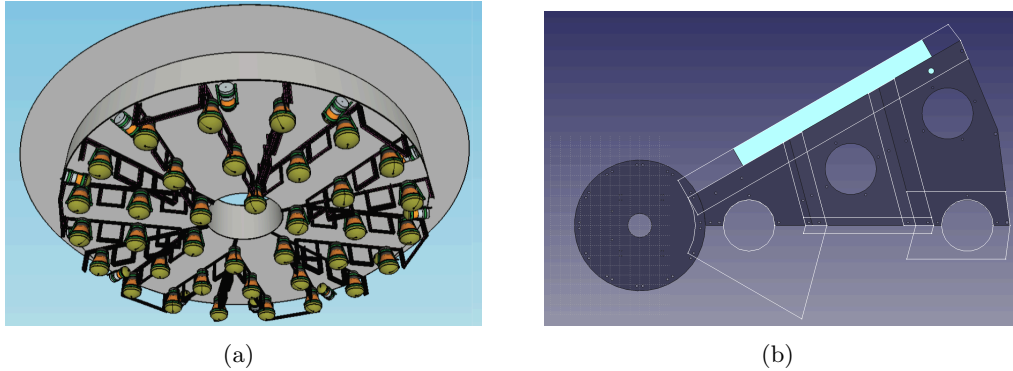


Figure 3.11: (a) A 3D model of the PMTs on the top lid and their support structures. (b) Drawings of the optical separators for the bottom part. The white lines show the drawings of supplemental optical separator for filling gaps among the boards.

The design of optical separator for top lid and bottom part is shown in figure 3.11 (b). Because of symmetry, 3 boards in one section out of 12 are only displayed. The white lines indicate drawings of supplemental optical separating sheets for filling gaps among the boards. In contrast with the barrel part, 6 differently designed sheets were used per one out of six sections by considering overlap region. Only for the bottom part, we placed a round shape board with 330 mm radius which had 120 mm diameter hole at the center. A switching open window was attached over the central hole used for smoothing liquid flow between the GC and the veto layer during LS filling and extraction.

Each PMT is to be assembled with a special ring connectable to the black board in order to achieve reinforcing PMT support and filling physical gap between black board and PMT simultaneously. The structures around PMTs are described in section 3.5.

3.4.1 Veto layer

The optical separator forms veto layer surrounding the inner detector, which is used to reject charged and neutral particles coming from outside the detector, and to detect energy leakage from the central volumes. The thickness of the veto layer is 25 cm at the top and bottom part and 43 cm in the barrel part, respectively. To enhance scintillation photon collection efficiency, we cover the surfaces of the veto layer with reflection sheets made of REIKO LUIREMIRROR, which has good reflectance above 380 nm wavelength and for wavelengths longer than 440 nm, the reflectance is more than 94 % [33]. The reflection sheets covering the surface of s.s. tank are fixed to the welded angles using 6,6-Nylon cable ties. For the optical separator surfaces, we cut and made reflection sheet in the same shape as each black board. When attaching the black boards, the reflection sheets are attached and fixed as well as the black PET sheets for filling gaps between boards (left picture in figure 3.12). In addition to the large area surfaces, PMT and LED modules are also covered with the reflection sheet. The installation complete appearance of a part of the veto layer in the top lid is shown in the right photo in figure 3.12.



Figure 3.12: (a) A photo of the reflection sheet attached to the black board. (b) A photo of the top lid veto layer after installation. One can find that most of the surfaces, such as the PMTs, the s.s.tank, and the optical separator, is covered with reflections sheet.

3.5 Photomultiplier tubes

As photosensors to observe scintillation photon in the JSNS² detector, an oil-proof photomultiplier tube (Hamamatsu R7081) is selected for both inner detector and veto layer. The diameter of the PMT envelop and its photocathode is 10 inch and at least 220 mm, respectively. Base circuit of PMT is molded in epoxy resin, and signal cable is fully coated by Teflon jacket as a oil-proof treatment. A drawing and photo of R7081 is shown in figure 3.13.

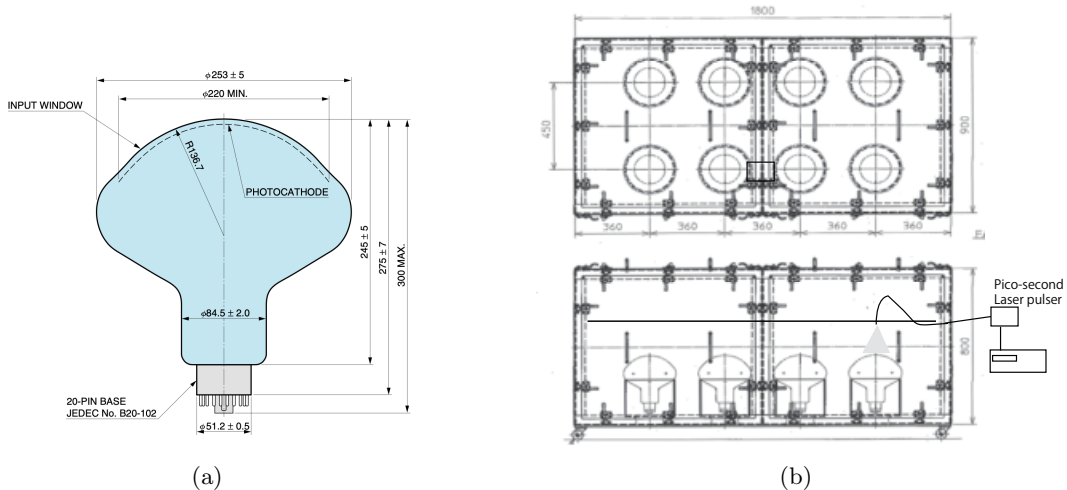


Figure 3.13: (a) A side view drawing of PMT R7081 [34]. (b) A drawing of the dark box used for the pre-calibration.

As described in the previous chapter, we decided to install 120 PMTs in total. 96 out of 120 PMTs were installed in the inner detector and remained 24 PMTs were mounted in the veto layer. The photocathode coverage of the inner detector is $\sim 5\%$. 67 and 24 PMTs were donated from RENO and Double Chooz experiment

respectively, and 39 PMTs were newly purchased.

3.5.1 Pre-calibration

Gain curve, peak-to-valley ratio and dark rate at a gain of 10^7 for all PMTs were measured before installation. We utilized the dark box, shown in figure 3.13 (b), designed to hold up to 8 PMTs at once for efficient work, which is originally used for the PMT performance measurement in Double Chooz experiment.

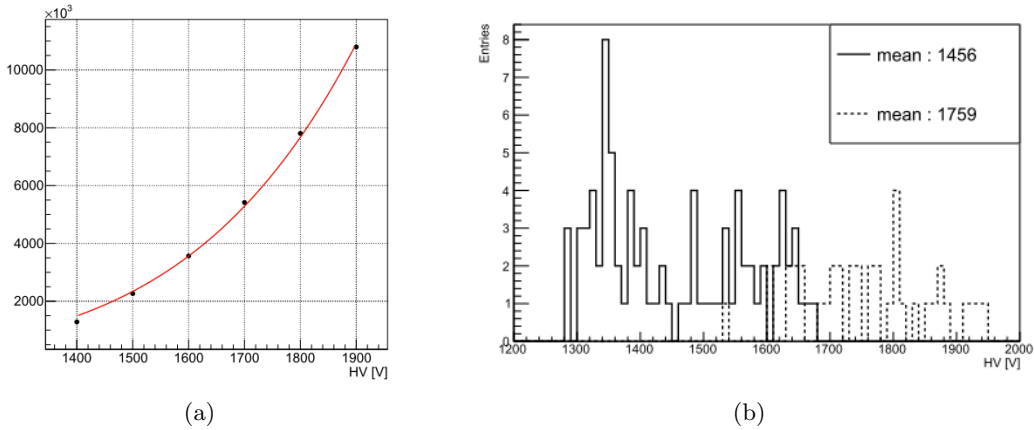


Figure 3.14: (a) An example of the result of gain curve measurement. The black dots shows the measured gain at each high voltage value, and the red line is a fitting result with the function defined in equation (3.1) [36]. (b) A distribution of high voltage values at a gain of 10^7 [36]. The dashed line shows a distribution of the newly purchased PMTs. The solid line is that of the donated PMTs.

Figure 3.14 shows one of the result of measured gain curve (left), and a distribution of high voltage values to obtain 10^7 gain (right). The fit function for the gain curve is described in [35] and given as a function of a high voltage value V by

$$gain = \alpha \times V^\beta, \quad (3.1)$$

where both α and β are fitting parameters. The measured gain curves were used for gain adjustment and matching in the detector. Details and further information about pre-calibration is described in [36]. As a result of the pre-calibration, we found all tested 123 PMTs were good for use in the JSNS² experiment. Finally, we chose 120 PMTs to be installed in the detector and saved 3 PMTs for backups.

3.5.2 Assembling and Installation

Each PMT is assembled with structures and covers before installation. As described above, we designed a special ring structure fitting to the surface of the black boards in the view point of light shielding and robust PMT support. Figure 3.15 (a) shows a drawing of the PMT ring. The ring has a slope part to make cone shape covers fit well to the ring for preventing light from passing through the optical separator boundary. The designed ring is mass-produced using a fused deposition modeling 3D printer MF2200D shown in figure 3.15 (b), and made of polylactic acid (PLA) resin, which has thermoplastic property with melting point 195 °C. It takes roughly 8

hours per one ring production; however, the raw material cost for one ring is around 500 yen. The total cost including infrastructure is amount to less than 600000 yen in case of 200 ring production. It is quite reasonable cost compared to typical plastic mass-production method, such as injection molding.

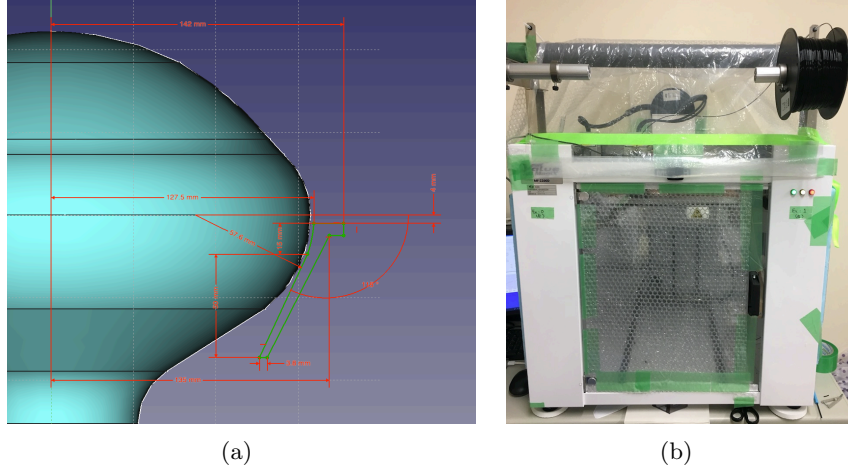


Figure 3.15: (a) A drawing of the PMT support ring. (b) A photo of fused deposition modeling 3D Printer for JSNS². The maximum printable size is 30 cm \times 30 cm \times 30 cm. It takes roughly 8 hours for printing out one ring.

All components assembled to PMT is shown in figure 3.16. The black sector and octangle cup shaped sheet is made of black PET (Lumirror X30: 0.1 mm thickness). The sector forms cone shape with the same slope as PMT ring to eliminate gap. The octangle cup covers the transparent potting part. FINEMET sheet, the second sector from the top in figure 3.16 (a), is a magnetic shield substituting for a μ -metal in order to eliminate interference from the geomagnetic field to electron in the PMT. We made a cone shape cover, and attached to PMT in the same way as the black PET sheet. The outermost cover of a PMT is a reflector made of LUIREMIRROR. We attached both the cone shape and an octangle cup cover likewise the black PET cover. In this sequence, the cone part of the reflection cover is attached over the PMT ring to maximize coverage of the reflector in the veto layer. PMT support jigs are finally attached after cover assembling process. The order of above assembling process is exhibited in figure 3.16 (b) to (e).

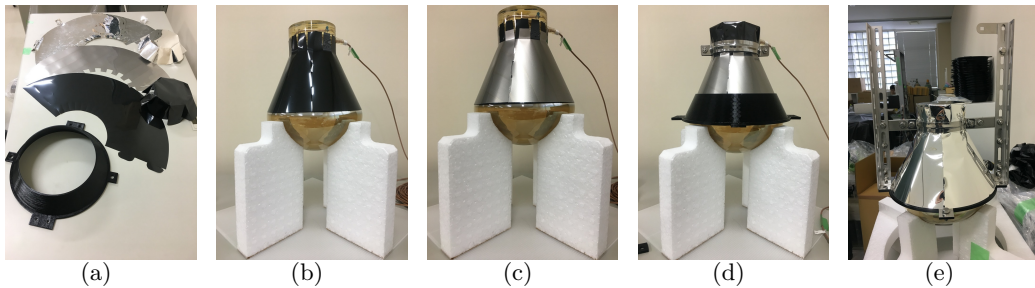


Figure 3.16: (a): The covers and support ring to be assembled to one PMT. (b) to (e) shows the order of assembling covers, ring and angle jigs.

The assembled PMTs are sequentially installed as well as the optical separators and the reflection sheets because they share the through holes for bolting on. The installation started from the barrel part, then moved to the lid, and finally bottom PMTs were installed. Figure 3.17 (a) and (b) show the photos of PMT installation work in the detector and PMTs before being covered with the optical separators, and their completed view can be found in (c).

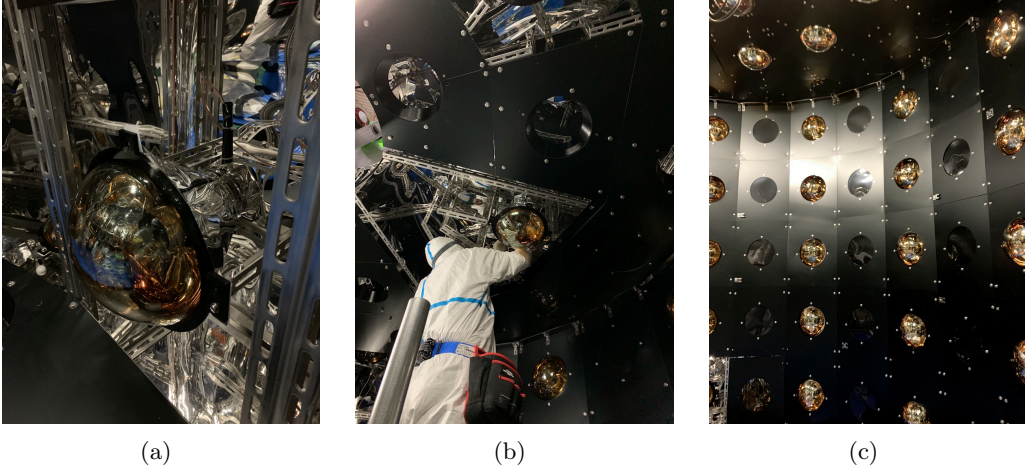


Figure 3.17: (a): A photo of an installed PMT before being covered with a black board. PMTs are eventually fixed at the angle jig and the black board via the PMT ring. (b) A photo of PMT installation work to the top lid. (c) A part view of complete installation of PMTs and optical separators.

3.5.3 Cable feed through

The cable feed through flange is designed in order to be compatible with a sealing capability of both gas and liquid. Its drawing is shown in figure 3.18. There is a space between the top and bottom part, where epoxy resin, ThreeBond TB3952D, is filled with. Each flange has 80 of ϕ 5.4 holes with counter sinks, which are compatible with not only the PMT cable but also the cables for LEDs and thermosensors. Figure 3.19 exhibits a series of photos in each sequence of the work. Before filling with epoxy resin, we fixed cables in straight as shown in figure 3.19 (left), and filling is conducted in this state (center). The right one shows the completed appearance of the flange after being tightly fixed to the 200 A flange port on the s.s. tank.

The sealing capability of the completed flange was examined in the laboratory by applying ~ 15 kPa with respect to the atmospheric pressure in the same method as [31]. The left photo in figure 3.20 shows the setup for the test, and its schematic view is in the central one. If we set a tolerance leak level to 100 mL/min, the corresponding time constant of an exponential decrease in the inner gas pressure is 0.5 min. The tolerance leakage level is equivalent to a flow rate to keep positive pressure in the gas phase of the detector. Because a typical nitrogen gas cylinder contains 7 m^3 , it can keep the flow rate for ~ 1.5 month. The right plot of figure 3.20 shows the measured result of time evolution of the inner gas pressure, and fitting with an exponential function leads to time constant $\tau = 3.3 \pm 0.2$ min. Thus, it is concluded that the sealing capability is good enough for our purpose.

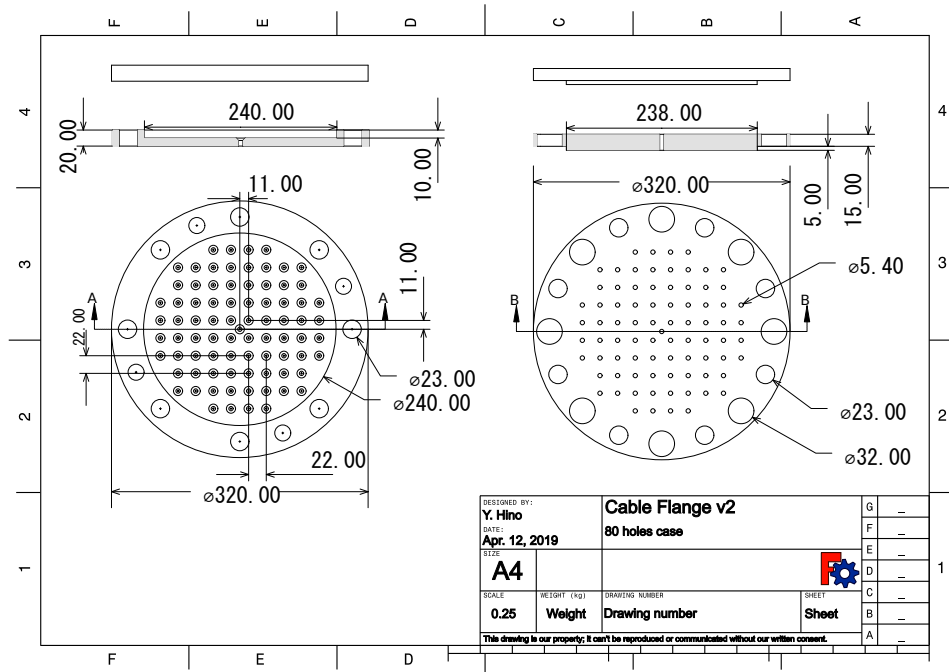


Figure 3.18: A drawing of cable feed through flange.

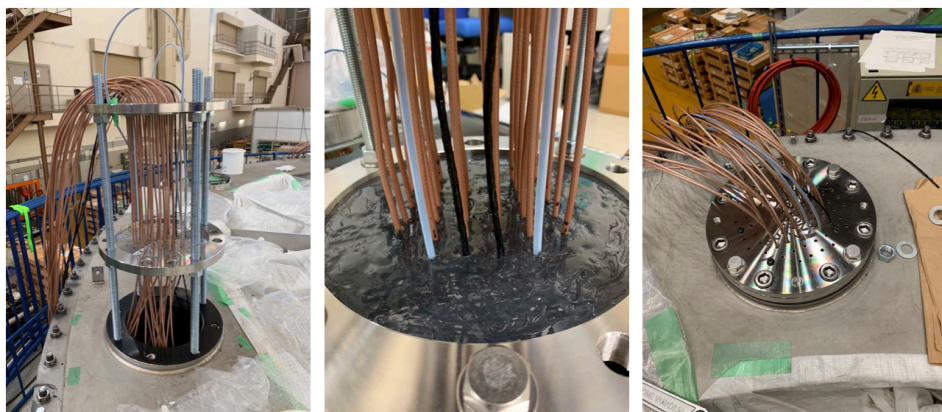


Figure 3.19: A series of photos of the sealing process. Left: preparation before filling epoxy. Center: after filling. Right: after being closed and fixed to the flange port on the s.s. tank.

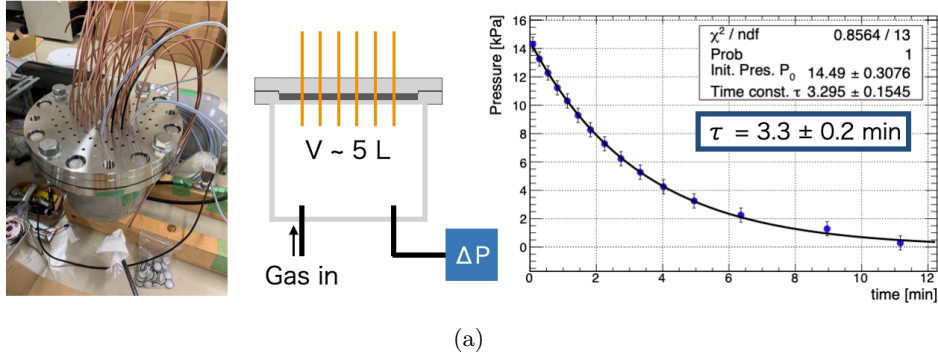


Figure 3.20: Left: A photo of sealing test setup. Center: A schematic view of the test setup. Right: Measured inner gas pressure with respect to the atmospheric pressure as a function of time (black marker). The blue line is the fit result with an exponential function.

3.5.4 High voltage supply and Signal-HV Splitter

Each PMT has a single cable which is used for both signal transfer and high voltage (HV) supply. PMT signals are separated from the HV bias at a splitter circuit, a kind of high pass filter, and then sent to front-end electronics (FEE). The FEE has functions to amplify the PMT signals and generate a summation of the amplified signals for generating a trigger. HV for the PMTs are supplied by HV crate SY1527LC and HV module A1535P product of CAEN. The HV module and crates and the splitter circuits are donated from the Double Chooz Experiment.

3.6 Liquid Scintillators

3.6.1 Gd-loaded liquid scintillator

The Gd-LS used in the JSNS² detector is donated from Daya Bay experiment. It consists of LAB (linear alkylbenzene) as the base solvent, 3 g/L PPO (2,5-diphenyloxazole) as the fluor, and 15 mg/L bis-MSB (1,4-bis(2-methylstyryl) benzene) as the wavelength shifter. Gd is solved as a Gd carboxylate complex with 3,5,5-trimethylhexanoic acid (TMHA) ligands with concentration 0.1 w%.

LAB ($C_nH_{2n+1}-C_6H_5$, $n = 10 \sim 13$) is a non-toxic material with a high flash point of 152 °C. It has a long attenuation length of >10 m at 430 nm, and produces a large light yield of ~ 10000 photons per MeV.

3.6.2 Gd-LS storage

As described in previous chapter, we extract the Gd-LS from the detector and store it in an ISO tank, based on International Organization of Standardization, in annual operation. Because Gd-LS stability exposed to stainless steel has been reported in [37], we decide to utilize normal ISO tank with SUS316 surface for Gd-LS storage. The donated Gd-LS had been stored in the ISO tank for about 10 months until the first run, and we performed sampling surveys during the storage period. The first survey was carried out on August 7th 2019, soon after the arrival of the ISO tank from Daya Bay site. The second sampling opportunity was on December 4th 2019.

The time interval between two surveys is 119 days. Two essential properties, Gd concentration and transmittance, of the Gd-LS were measured for stability check.

Gd concentration stability

Ethylene Diamine Tetra Acetic acid (EDTA) titration method widely used for quantitative analysis of metal concentration in chemistry field [40]. We used it in order to measure Gd concentration of the sampled Gd-LS. EDTA is one of the well-known chelating agents and forms a chelate complex with a variety of metal ions including Gd. In case of Gd, EDTA makes a chelating complex in the ratio of 1 to 1. Thus, Gd concentration can be determined by the total amount of EDTA which is computed from dropped volume of a EDTA solution and its certified concentration.

Xylenol Orange (XO), an indicator reagent for metal titration, was added in order to know the end point of the EDTA titration. XO gives red-violet color in $\text{pH} < 6$ when a metal ion exists. Otherwise, the color shows yellow. Because a chelating complex with EDTA is inactive to XO, the color changes red-violet into yellow gradually as EDTA is dropped. An equivalent point where the amount of EDTA is equal to that of Gd is determined as the point where the color (yellow) does not change any more (figure 3.21).

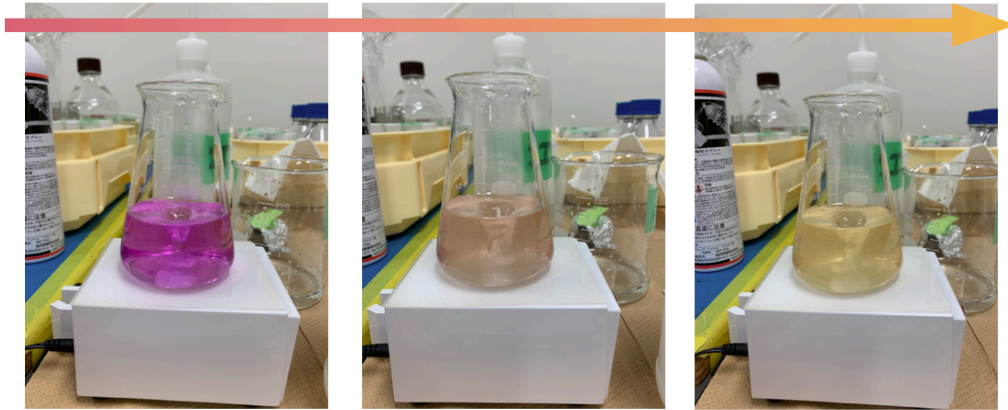


Figure 3.21: A series of photos exhibiting the procedure of the titration.

Table 3.1 shows the result of titration. The results of measured Gd concentration were consistent within uncertainty, and show no significant degradation on Gd concentration over 119 days exposure. Therefore, one can conclude that Gd concentration of the Gd-LS is stable in the ISO tank storage.

Table 3.1: The result of the EDTA titration to the Gd-LS.

Sampling date	EDTA Vol./mL	Gd Concentration /w%	Interval /day
August 7th, 2019	0.525 ± 0.006	0.096 ± 0.002	0
December 4th, 2019	0.539 ± 0.007	0.099 ± 0.002	119

transmittance stability

Transmittance spectrum of the sampled Gd-LS was measured using the spectrophotometer, which measures sample contained in quartz cell with 10 cm optical path

length. Using the same cell in each measurement allows us to directly compare the results without a uncertainty from transparency and reflectivity of the cell. Figure 3.22 shows the result of transmittance measurement. The left plots exhibits the entire range of the spectra, and indicates both spectra are identical over the measured wavelength range. The right plot is a zoomed plot to the region surrounded by the dashed box in the left plot. It also shows that the transmittance spectra are consistently identical each other within the uncertainty over the measured range.

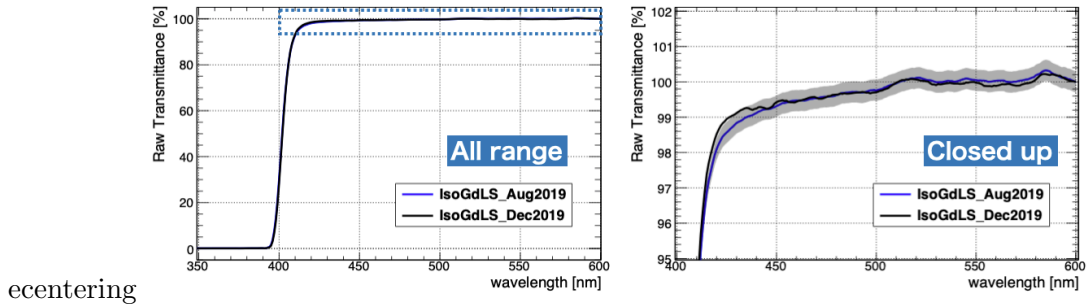


Figure 3.22: Left: Measured 10 cm transmittance spectra of the sampled Gd-LS in the entire range. Right; The spectra zoomed in the region surrounded by the dashed box in the left plot. The blue line indicates spectrum of the sample in the first survey with the expected uncertainty displayed as gray shaded region. The black line is that of the sample obtained in the second survey. Both spectra are identical within the uncertainty in the range of 350 to 600 nm.

The result of sampling survey shows no degradation on the both aspects of Gd concentration and transmittance over 119 days exposure to SUS316 surface. Therefore, one can conclude that the Gd-LS is stable and compatible with the inner surface of the ISO tank.

3.6.3 Unloaded Liquid Scintillator

The unloaded LS is made of the same components as the Gd-LS except for Gd complex. The base solvent of the LS is LAB, and 3 g/L of PPO as the fluor and 30 mg/L of bis-MSB as the wavelength shifter are contained in the LS. 38000 L of fresh LS was newly produced for JSNS² experiment using the facility of RENO experiment shown in the left photo of figure 3.23. A refurbishment including cleaning and new pipeline construction was done to reuse the facility. The produced LS was stored in two ISO tanks, and delivered to Japan. Figure 3.23 (right) shows a schematic diagram of the refurbished mass production system for the JSNS² LS. In mass production one batch of LS was made by diluting 200 L of enriched PPO and bis-MSB master LS solution with 1800 L of LAB. each batch of LS was transported into the ISO tank after nitrogen purging for water contamination removal. As a result, we produced 21 batch of the fresh LS.

Relative Light yield comparison with the Gd-LS

As a performance check for the produced LS, we measured light yield of the LS, and compared it to that of the Gd-LS which was measured in the identical setup.

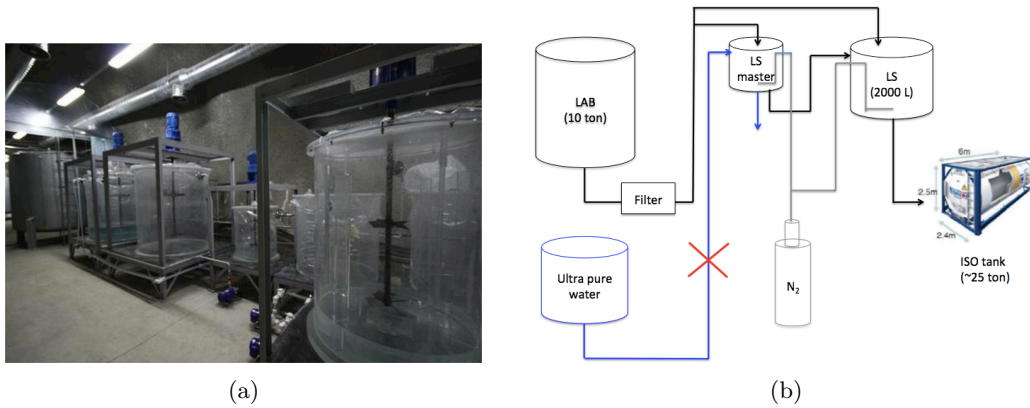


Figure 3.23: (a) A photo of LS production facility in RENO site. (b) A schematic diagram of the LS mass production system modified from the one that was used for the RENO experiment. The LAB goes through a micro-filter of $0.5 \mu\text{m}$ pore size. The black, blue and gray line correspond to the route of LAB (or LS) flow, ultra-pure water (not used), and nitrogen gas flow, respectively.

The left picture of figure 3.24 illustrates the setup for light yield measurement. We used 0.662 MeV monochromatic γ from ^{137}Cs source, and 2 inch NaI placed in the opposite side in order to tag the back scattered γ from electron in the LS so that the energy deposition to the LS can be almost monochromatic ($\sim 0.48 \text{ MeV}$). The size of LS sample is 2 inch diameter and 10 cm height, which corresponds to 100 mL in volume. The right plot of figure 3.24 shows the result of light yield measurement. The PMT charge distributions of the LS and Gd-LS are overlaid to compare them. They are in good agreement with each other; therefore, it can be concluded that the light yield of the JSNS² Gd-LS and LS is identical.

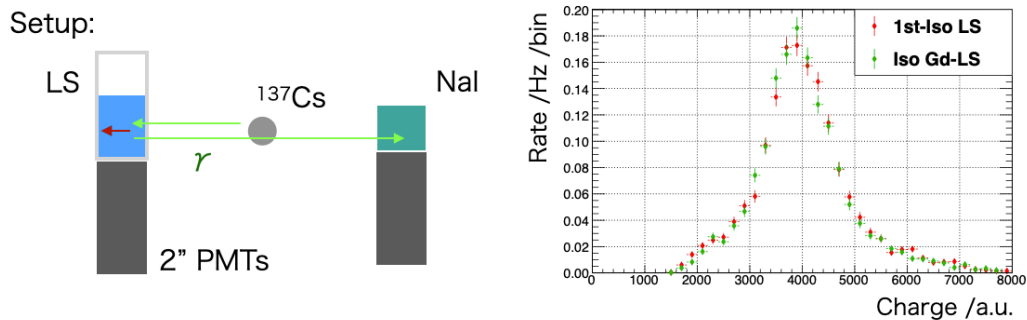


Figure 3.24: Left: a schematic of the setup for light yield measurement. Right: distributions of charge corresponding to scintillation light yield at $\sim 0.48 \text{ MeV}$ electron recoil. The red marker shows the measurement result of the LS, and the green one corresponds to that of the Gd-LS.

3.6.4 Gd-LS/LS Filling and Extraction

Figure 3.25 shows a schematic of the LS filling and extraction. The pipe line for the Gd-LS (light blue line) is connected to the bottom of the acrylic vessel and the level stabilizer tanks with a switchable valve. The line for the LS (light green line) is fixed along the s.s. tank wall in the veto layer. We chose 1 inch diameter pipe for liquid flow in order to reduce resistance of liquid flow and load to pumps. Each line is independent, and individually has a vortex pump (Nikuni 32NPD07Z) whose flow rate is controlled using an inverter.

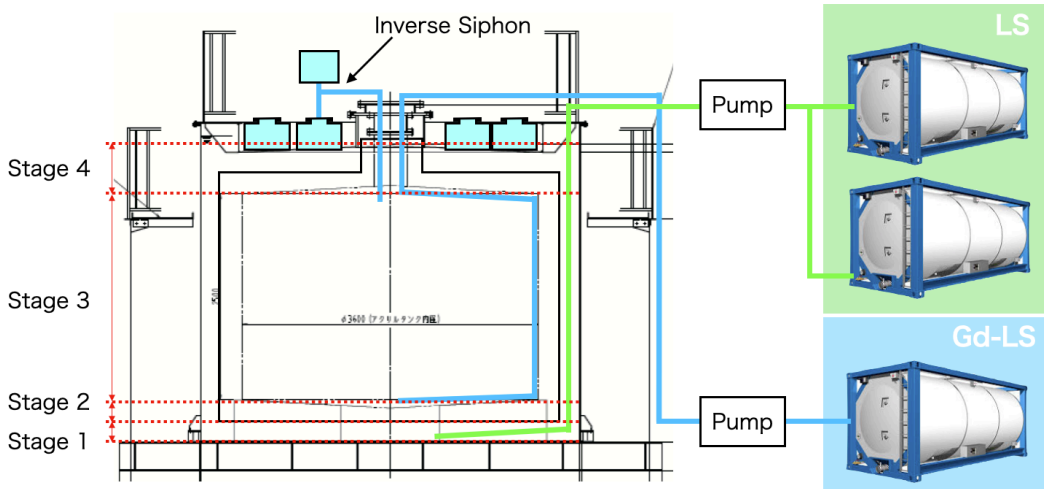


Figure 3.25: A schematic diagram of the LS filling and extraction. The light blue lines indicate pipe lines for the Gd-LS, and the light green one is for the LS. Sequences of filling and extraction operation is categorized into four stages corresponding to boundaries of the optical separator and the vessel for safe operation.

The sequences of filling and extraction is categorized into 4 stages for safe operation, which is also exhibited in figure 3.25. We finally set 36 L/min flow rate, and finished both filling and extraction within 4 days. Note that filling and extraction for the Gd-LS in stage 4 was done using the inverse siphon system because of the smaller area of base in the acrylic vessel chimney. Figure 3.26 shows the entire view of the filling and extraction setup in the left photo, and the central and right ones exhibit the moment in the veto layer and the inner detector, respectively. We sometimes monitored the internal view using a camera in addition to the sensors as shown in the photos. Figure 3.27 shows the history of liquid level during the filling, data-taking, and extraction in the first run. We kept the level of the Gd-LS higher than that of the LS to avoid stress on the acrylic vessel due to buoyancy. This also shows that the liquid level was stable during the entire data taking period of the first run.

3.7 Nano-pulsar optical calibration system

A LED calibration system is installed in the JSNS² detector for gain and timing calibration on each PMT. The system consists of six branches, and each branch has

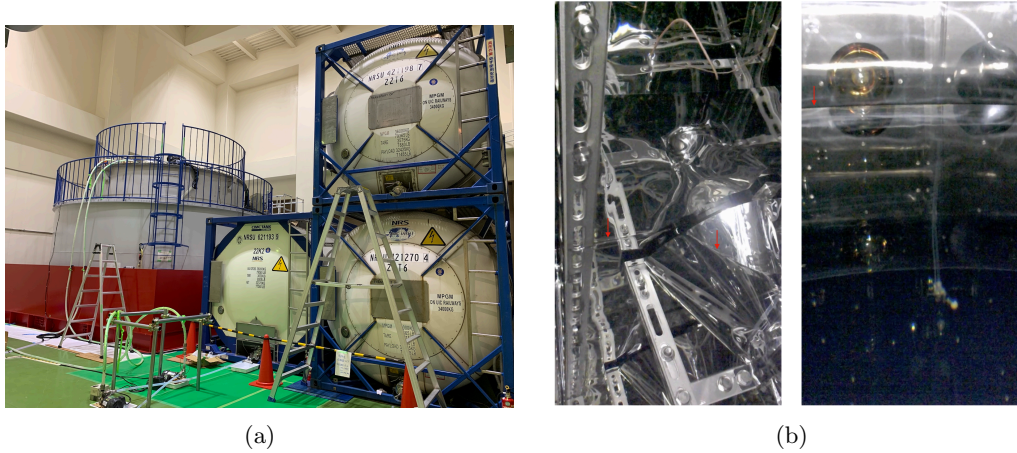


Figure 3.26: (a) A photo of the entire view of the setup for filling and extraction. The stacked ISO tanks contain the LS, and the other next to the detector is for the Gd-LS. (b) photos of the veto layer (left) and the inner detector region (right) during the filling. The red arrows point the liquid level at that time.

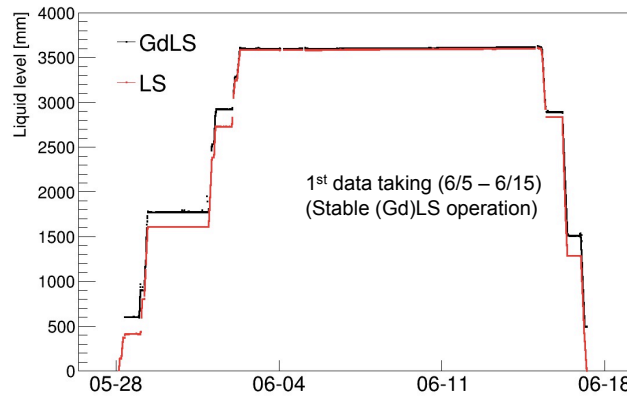


Figure 3.27: A history of liquid level height during the filling, data-taking, and extraction. The black and red line corresponds to the level of the Gd-LS and the LS, respectively.

either two or three pulserheads, an electronics board with digital logic and an ultra-fast LED pulser, with daisy chain connection. In total, there are 12 pulserheads with a visible blue LED (420 nm) and two pulserheads with a UV LED (355 nm) whose light will be absorbed almost immediately and emitted isotropically as a longer wavelength in the LS. Figure 3.28 exhibits the positions of each pulserhead and cable routing to the controller box. The color indicates a type of LED emission light, i.e., blue and violet markers correspond to the visible LEDs and the UV LEDs, respectively. The cables coated with teflon exit the cable feed through flanges for PMTs, and are then connected to a junction box relaying ethernet cables to the nanopulser control box. The controller box has following functions:

- Talking to the DAQ PC via ssh connection with the internal raspberry pi PC,
- Generating a trigger signal in-sync with the optical pulse.

LED illumination can be controlled by linux command based interface in the raspberry pi PC, which can designate channel, intensity and delay as arguments. The intensity of illumination can be adjusted by 14 bit integer in the range of 10^1 to 10^6 photons per pulse.

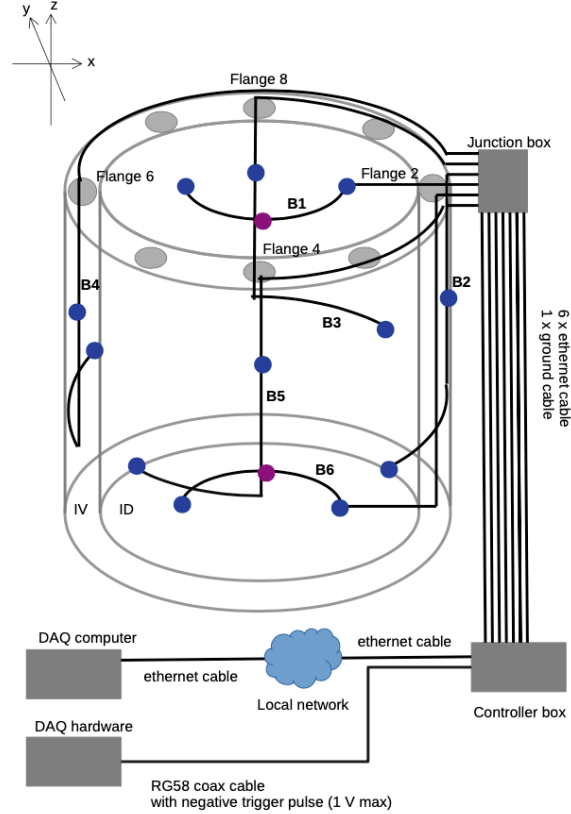


Figure 3.28: A schematic view of the pulserhead positions and cable routing to the controller box. The blue and violet markers correspond to the visible and UV LEDs, respectively.

The angular dependence of light emission from the LED (in air) is close to a Lambertian distribution. This typically corresponds to approximately 30 degree opening angle. The emission spectra of the LEDs is reasonably well described by a double Gaussian, with a mean of either 355 nm or 420 nm, and a lower sigma of 10 nm and a higher sigma of 15 nm as shown in figure 3.29. The timing structure of the emitted light pulse is shown in figure 3.30. The fall time of each LED is ~ 2 ns, which is quite similar to the fast component of scintillation light.

Each pulserhead is contained in the transparent acrylic housing, and mounted on the black board. Therefore, we developed a specially designed cover to prevent light from cross talking between the inner detector and the veto layer. Figure 3.31 (a) shows a 3D model of the cover consisting of a front and a back parts. The separated design is due to the property of the 3D printer; however, they have overlap region with each other preventing light from coming in and going out. The photo of the installed pulserhead is displayed in figure 3.31 (b), and one can find that the reflection sheet covers the cylindrical part occupying the most of surface of the cover.

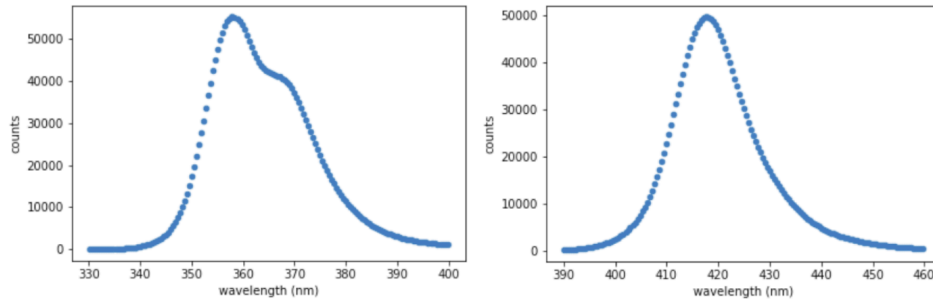


Figure 3.29: The emission spectrum of the UV LEDs (left) and the visible LEDs (right).

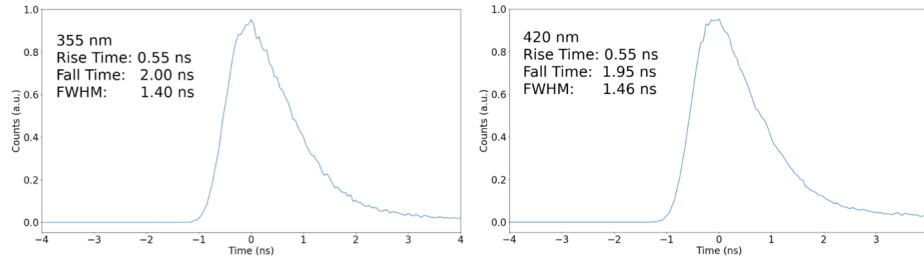


Figure 3.30: The timing structure of emitted light pulse of the UV LEDs (left) and the visible LEDs (right).

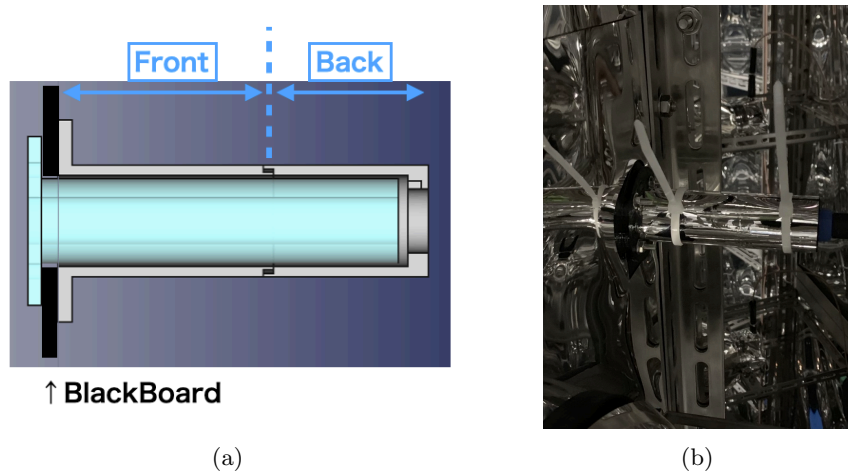


Figure 3.31: (a): A drawing of covers for the pulser head made using 3D printer. In order to avoid cable connector interference the cover separately consists of front and back part. (b): A photo of the LED module installed in the detector. The module and cover are tightly fixed with a bolt and a nut on to the black board, and finally surrounded by reflector sheet.

3.8 Monitoring system

Monitoring the detector status is quite crucial in performing the experiment at the experimental position in terms of the radioactive control area of the MLF. We developed a LabView-based system, called slow control monitor (SCM), to monitor the detector status, i.e., liquid level, temperature, and so on, being observed by sensors with an analog output. Figure 3.32 shows the schematic view of position of each sensor, and table 3.2 summarizes a list of the mounted sensors.

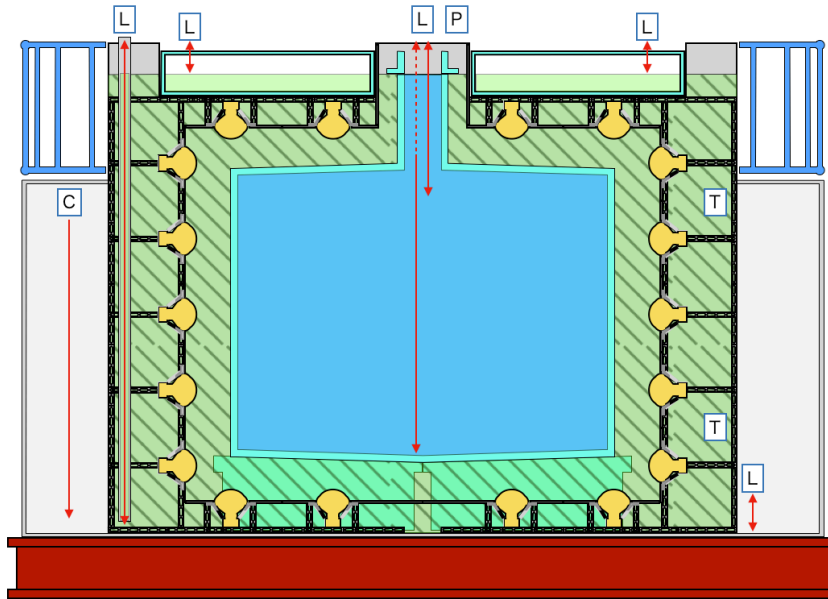


Figure 3.32: A schematic view of the positions of devices for monitoring. The red arrows indicates the range of each level sensor or the direction which the web camera looks towards.

Table 3.2: List of devices for monitoring.

Device	Symbol	Purpose
US-015 + Arduino	L	Liquid level monitoring in the LLST.
US-015 + Arduino	L	Oil leak monitoring in the 1st anti-oil-leak wall.
Sick (Long range)	L	Liquid level of the LS (veto layer).
Sick (Short range)	L	Liquid level of the LS (veto layer).
Sick (Long range)	L	Liquid level of the Gd-LS.
Sick (Short range)	L	Liquid level of the Gd-LS.
GC-31	P	Pressure difference between in- and outside.
PT100 RTD	T	LS temperature.
TR-73U	-	Atm. temperature, pressure, and humidity.
Web Camera	C	Oil leak monitoring in the 1st anti-oil-leak wall.
FM3104	-	Flow rate monitor during filling and extraction.

We utilizes two ultra sonic distance sensors (Sick UM30) for measuring the liquid level in the detector. One of them is sensitive to long distance range, and mainly used during the Gd-LS/LS filling and extraction. In the stage 4 of filling and extraction

operation or during data taking periods, it is replaced with short range one. A ultrasonic sensor module is developed using US-015, sensor mounted circuit, controlled by Arduino for a liquid level monitor in the liquid level stabilization tank and oil leak monitor in the 1st anti-oil-leak wall. Liquid temperature is measured at 8 positions in the veto layer using a RTD sensor. TR-73U, a logger for atmospheric pressure, temperature and humidity, is placed on the top of the detector. The data acquisition scheme of each sensor output is illustrated in figure 3.33, as shown, the system integrates a monitoring scheme provided from the CAEN HV supplier to monitor the time variation of supplied HV value to each PMT as well, which is called high voltage control monitor (HVCM).

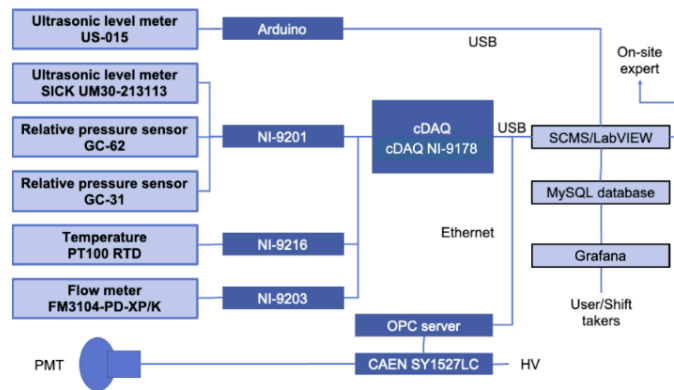


Figure 3.33: A block diagram of data acquisition system for sensors and HV [38].

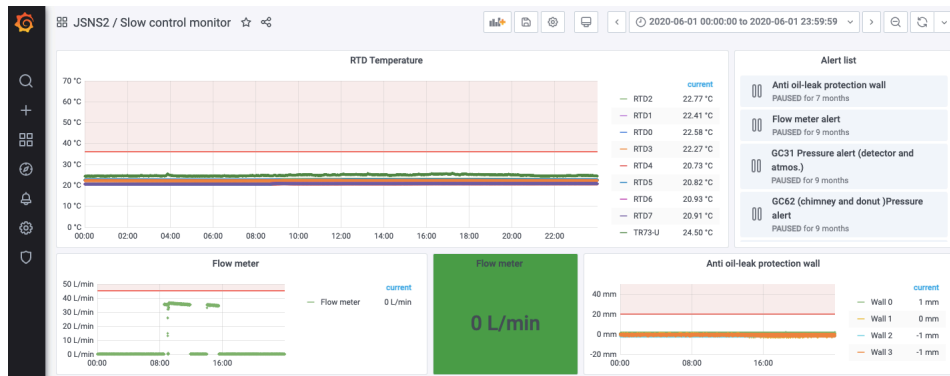


Figure 3.34: A screenshot of the grafana page for sensor log.

The acquired data is stored in MySQL database and displayed in real-time using Grafana which is a web-based tool for data plotting and alert generation. Figure 3.34 and 3.35 shows an example of display of grafana for the SCM and HVCM. The grafana system allow users to set threshold to each value (shown as the red lines in the plots) for alarm generation which informs registered users of the situation via e-mail, and the alarm setting is individually turned on/off.

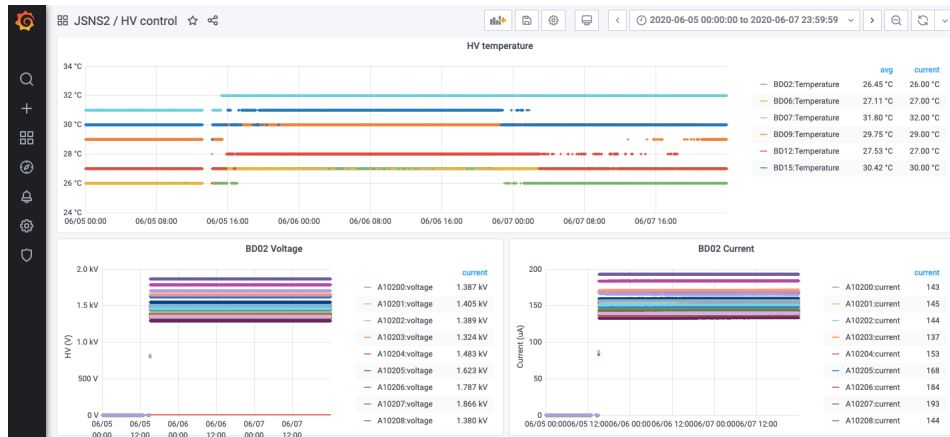


Figure 3.35: A screenshot of the grafana page for HV log.

3.8.1 Camera system for oil leak alert [41]

In addition to the ultra sonic level sensors for the 1st anti-oil-leak wall, we set 4 web cameras (symbolized as "C" in figure 3.32) continuously monitoring the floor by taking a photo regularly. Oil leakage detection is automated using an image analysis to the taken photo, which discriminates color (RGB) intensity change at a pixel by pixel. Figure 3.36 shows an example of taken photo by the camera system comparing before and after oil exposure. The tiny blue paper in the red circle is a oil test paper which turns its color to deep blue when it contacts with oil so that it helps the system with color change detection.

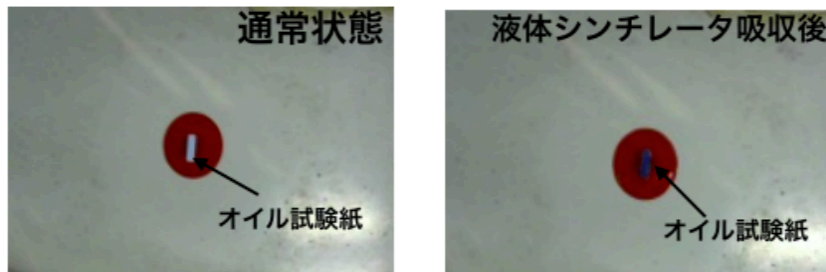


Figure 3.36: A photo of the oil test paper before (left) and after oil exposure (right).

Chapter 4

Background Measurement

JSNS² experiment launched the first data taking in June 2020. The duration was from the evening on June 5th to the early morning on 15th, amount to about 10 days. During this period, the proton beam transported to the mercury target in the MLF was operated at 600 kW power for about 9 days, and there was 24 hours beam off period due to a biweekly facility maintenance, as shown in Fig. 4.1(a). The beam intensity information is retrieved from the database of the MLF. The accuracy of the provided beam information is $\sim 1\%$ caused by deviation from the beam monitors [42]. The integrated number of proton-on-target (POT) corresponds to a milestone of neutrino production in the target. The history of POT recorded in the JSNS² data is displayed in Fig. 4.1(b) as a function of time. The recorded POT is amount to 8.9×10^{20} which is 1.0 % of the accepted POT by J-PARC [9], and the expected number of the IBD event in the first run is ~ 1 based on the estimation in reference [9]. Therefore, this obtained data can be used for background estimation.

In this chapter, background measurement using the first run data is described in the following steps. First, trigger condition and data acquisition system using waveform digitizers are described as well as methods of defining event and variables used in analysis from the obtained waveform. Second, we explain calibration, energy and vertex reconstruction method. The calibration of charge and timing on each channel is done using the nano-pulsar LED system, and ²⁵²Cf source is used for understanding detector response for the reconstruction. Finally, estimations of each background component are described. The measured background rate is compared to the expectation in reference [9] to discuss an effect on sensitivity of sterile neutrino search.

4.1 Triggers and DAQ for the first run

In order to obtain non-biased data, we utilized simple data acquisition (DAQ) and triggers in the first run, such as kicker and self trigger for physics data, and external trigger for calibration using LED. Figure 4.2 illustrates a schematic diagram DAQ system for the first run. The amplified PMT signals are inserted into 28 flash analog-to-digital converters (FADCs) and digitized there. The digitized waveform data are stored and stacked temporarily in the ring buffer when trigger is generated. The FADC sends the data to the DAQ PC via optical link much before the buffer reaches to full. In case of high trigger rate, buffer full status can happen before data transfer

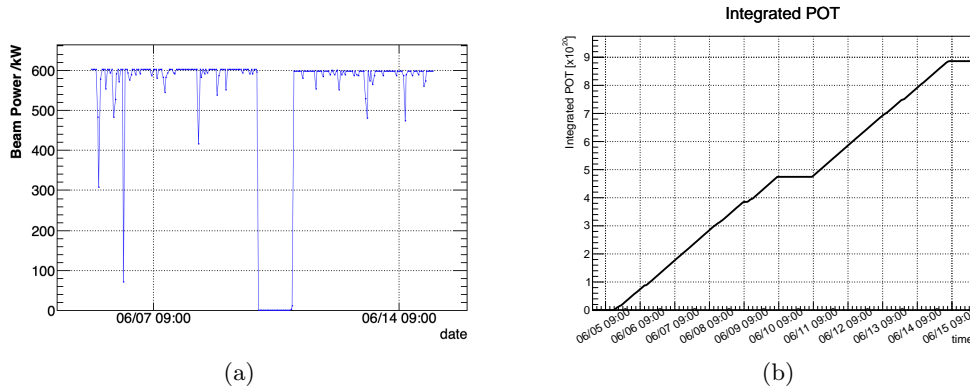


Figure 4.1: (a) History of beam power at MLF in the data taking period. Averaged beam power over a hour is plotted as a function of time in date. Sudden decreases in power were caused by short time beam stop for some reason in the facility side. Note that there was facility maintenance beam off period for 24 hours on June 10. (b) The integrated POT recorded in data.

to the DAQ PC is done. DAQ is stopped in that situation, and wait for transfer completion in order to avoid overwriting, and then restarts. The FADC used in the JSNS² DAQ is a waveform digitizer, CAEN VX1721, with 1 Vpp/8 bits resolution in 500 MHz sampling rate, which is donated from the Double Chooz experiment. The front-end electronics (FEE) receives PMT signal and outputs two different gain signals to the FADC: amplified signal with a factor of 16 in high gain (HG) channel, attenuated signal with a factor of 0.6 in low gain (LG). Data quality monitor (DQM) PC receives the data from the DAQ PC and performs data file compression in gzip format in order to reduce the size for data transfer to KEKCC through the internet. The detailed analysis is performed in KEKCC. The DQM PC has a function to show a waveform display of the acquired data for real-time data quality monitoring. The trigger pulses are inserted into signal input channels on the trigger board FADC to discriminate types of trigger and generate an underlying output for distribution to each FADC board. This scheme allow us to record the trigger pulses as well as PMT signals.

Kicker trigger is the main trigger to collect beam related events in the signal timing window in 25 Hz repetition. Figure 4.3 shows timing structure of the trigger pulses and beam related signals. The kicker trigger pulse is generated from the timing information logic pulse from the kicker magnet which ejects 3 GeV proton beam in the RCS to the beam-line towards MLF, and then applied $\sim 100 \mu\text{s}$ delay using gate generator. The delayed gate pulse is set $\sim 2 \mu\text{s}$ before the timing of proton beam collision on the mercury target. The waveform acquisition width by FADC is set to 10 or 25 μs . In case of 10 μs width, one more additional trigger pulse with variable delay from the kicker trigger is inputted in the range from 11 μs to the next kicker trigger (40 ms later) so that data about the intermediate situation between the kicker triggers can be taken.

The other trigger for physics data acquisition is the self trigger using the detector activity. Figure 4.4(a) shows the block diagram of the self trigger logic. The signals of the inner detector PMTs are summed up using the FEE and several analog fan in/fan out (FI/FO) modules. The analog sum outputs from the FEEs are attenuated

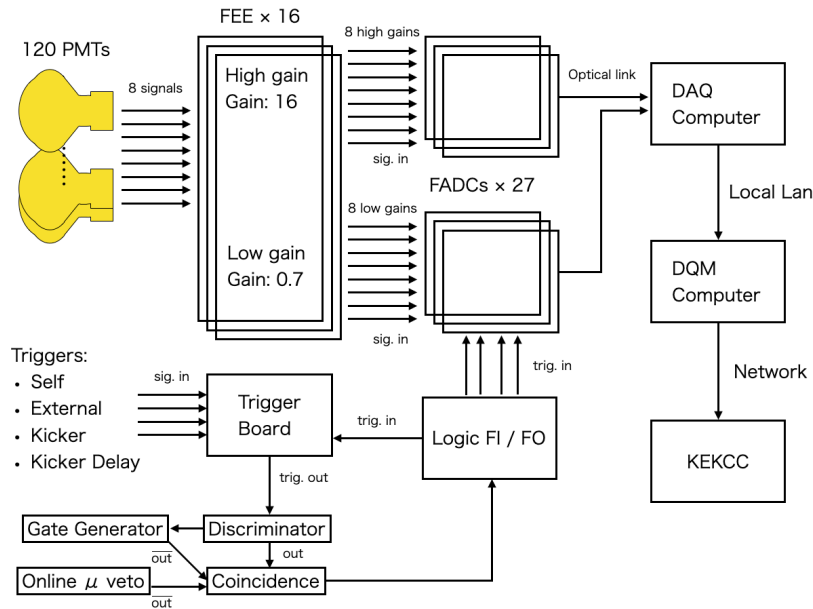


Figure 4.2: A schematic diagram of DAQ and data flow for the first run.

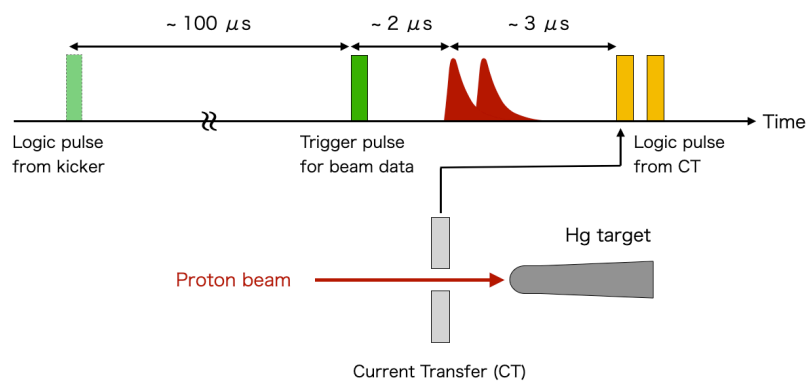


Figure 4.3: A schematic diagram of timing structure of the kicker trigger. The red pulse illustrates activity in the detector caused by beam spill to the target, which can be a signal of IBD interaction and so on.

with a factor of $1/6$ in order to match the dynamic range of the analog FI/FO module. Further 2dB attenuation is applied to 3 lines out of 4 so as to compensate an amplification effect at the FI/FO module. Timing of each lines is adjusted to the line for PMTs with 25 m cable length by applying certain delay values to the other lines before total summation of all the analog sum signals. We applied 80 mV threshold to the total analog sum signal, which is equivalent to ~ 2 MeV which is less than total γ energy of nGd events.

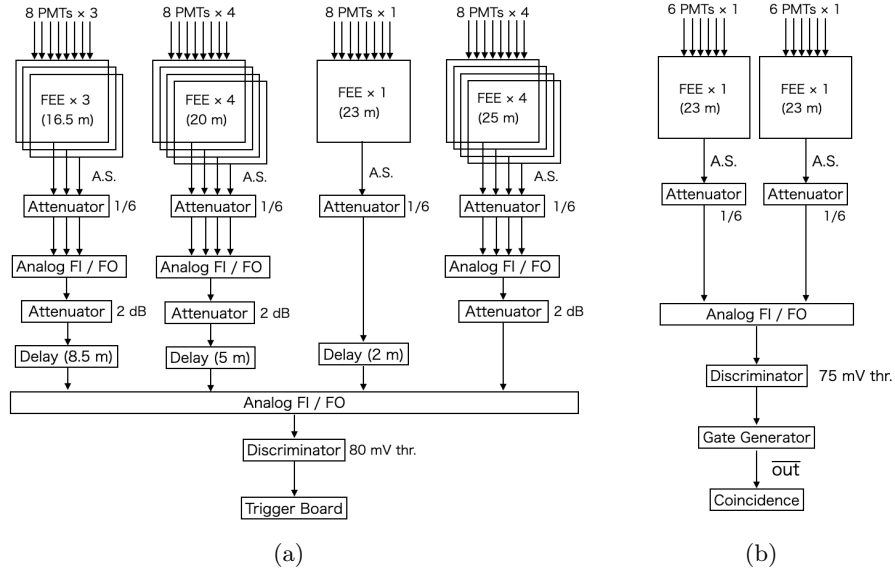


Figure 4.4: (a) A block diagram of trigger logic for the self trigger. (b) A block diagram of logic for the online muon veto.

Online cosmic muon veto logic for trigger rate reduction is constructed using FEEs analog summation signal of PMTs in the veto layer. Figure 4.4(b) shows the diagram of the online μ veto for the self trigger. 12 PMTs installed on the top of the veto layer are summed at 2 FEEs and an analog FI/FO module with $1/6$ attenuation for muon discrimination. We set 75 mV threshold at the discriminator. Its output is converted into an inverted NIM pulse with $1 \mu\text{s}$ width without delay at a gate generator and sent to the coincidence module. The online veto is only applied to the self trigger runs if necessary, e.g., checking source calibration run. Note that the analog sum waveforms are also inputted to the trigger board FADC and recorded. The trigger efficiency of the self trigger is estimated using the recorded analog sum waveforms in section 4.2.2.

External trigger comes from output clock signal from the Nano pulser driver system when LED calibration is performed. Figure 4.5 displays timing structure of the trigger and the applied veto logic. Overlap veto is mandatory to avoid overlapped trigger causes malfunction in FADC event synchronization. It vetos 300 ns after any triggers; however, it effectively works in case of the self trigger.

Table 4.1 summarizes trigger menus and their conditions. Figure 4.6 shows the history of DAQ efficiency during the entire first run. The long time run using the kicker trigger had almost 100 % efficiency. The efficiency losses were mainly caused by setup or configuration changes and a trouble on the HV crate. The total average efficiency is 94.5 % including these efficiency losses.

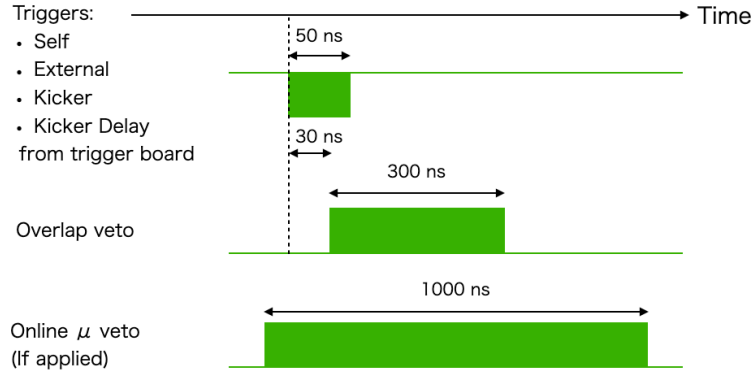


Figure 4.5: A schematic diagram of timing structure of the trigger pulse (top one) and the associated veto logic pulses illustrated in inverse of the trigger pulse.

Table 4.1: Trigger menu for the first run.

Type	FADC window size	Trigger Rate
Kicker ($25 \mu\text{s}$)	$25 \mu\text{s}$	25 Hz
Kicker ($10 \mu\text{s} + 10 \mu\text{s}$)	$10 \mu\text{s}$	$25 + 25$ Hz
Self	500 ns	8 kHz (beam on typical)
External (LED)	$2 \mu\text{s}$	up to 200 Hz

4.2 Waveform Analysis

4.2.1 Event extraction from wide range waveform

In contrast to data acquired using the self trigger, it is necessary to define and extract a physics-like event from tens μs wide waveform obtained by the kicker trigger. A scintillation event makes hit on multiple PMTs in the inner detector so that the number of hit based event definition is developed for a physics event discrimination.

Hit discrimination

Hit discrimination using differential waveform has an advantage on skipping baseline definition in contrast to a usual pulse-height-based discrimination applying a certain threshold level. The differential waveform can eliminate the low frequency noise component observed during the dry-run commissioning as shown in Fig. 4.7 for instance. It causes of a baseline shift as a function of time.

The differential waveform for digitized waveform array is defined as

$$\text{Diff}[i] = \text{FADC}[i] - \text{FADC}[i - 1] \quad (i = 1, 2, \dots, n - 1), \quad (4.1)$$

where $\text{FADC}[i]$ is FADC count at the i -th sampled point, n is the number of sampling, e.g., 4992 for $10 \mu\text{s}$ window and 12480 for $25 \mu\text{s}$ window. Figure 4.8 shows an example of single photoelectron (p.e.) level waveform in high gain channel (top) and its differential waveform (bottom). One can find that a sharp bi-polar like spike around the origin of the vertical axis in the same timing of pulse in the raw

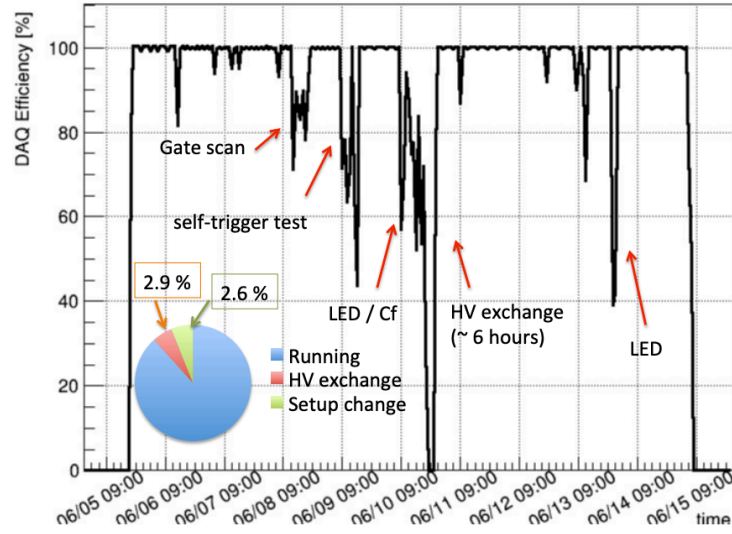


Figure 4.6: A history of DAQ efficiency in the first run. The total efficiency was 94.5%. The efficiency loss is caused by setup change and HV crate exchange.

waveform. A hit is defined as single p.e. observation at a PMT so that we apply -3 FADC count threshold to the differential waveform.

A correlation between pulse height of differential waveform (Dif. PH) and that of raw waveform (PH) shows a linearity as displayed in Fig. 4.9 (left), where the red dashed line corresponds to the threshold level for the hit discrimination. Note that it is obtained from the data by LED illumination with low intensity. Figure 4.9 (right) shows PH distributions before (black markers) and after the hit discrimination (red markers), respectively. It demonstrates that the condition discriminates the pedestal component ($PH \lesssim 1$ mV) from single (or multiple) p.e. hit by comparing them. A summation of an exponential and gaussian function is used as a model function for single p.e. distribution. The single p.e. detection efficiency is computed as a ratio of the integral of the model function above the threshold to that of all range. Figure 4.10 shows single p.e. detection efficiency of each PMT (left) and its projected histogram to the vertical axis (right). They indicate that the hit discrimination ensures more than 60 % single p.e. detection efficiency for all ID PMTs.

Event definition

The algorithm for event definition in wide range waveform is listed below in the order of process.

- Make a differential waveform of raw waveform in high gain channel at each PMT.
- Perform hit discrimination in each differential waveform, and accumulate hit timing information with 50 ns coincidence width in order to construct a number of hit waveform (NHWF). The timing of hit information at each PMT is corrected with a relative timing offset measured using the nano-pulsar LED system explained later.

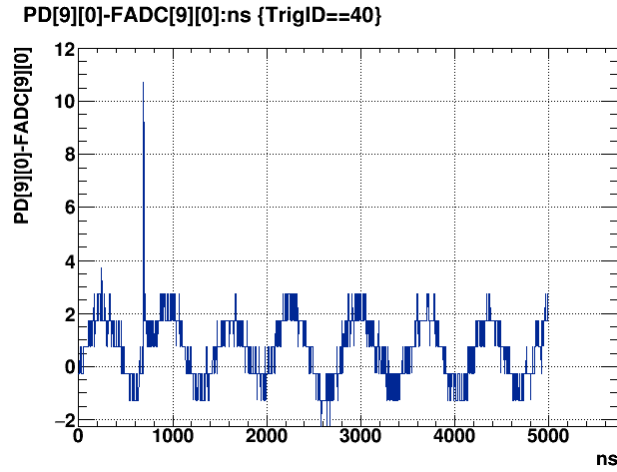


Figure 4.7: An example of waveform with low frequency noise observed during the dry-run commissioning. The vertical axis indicates pulse height in a unit of FADC count. The sharp peak around 700 ns corresponds to a pulse from the LED illumination.

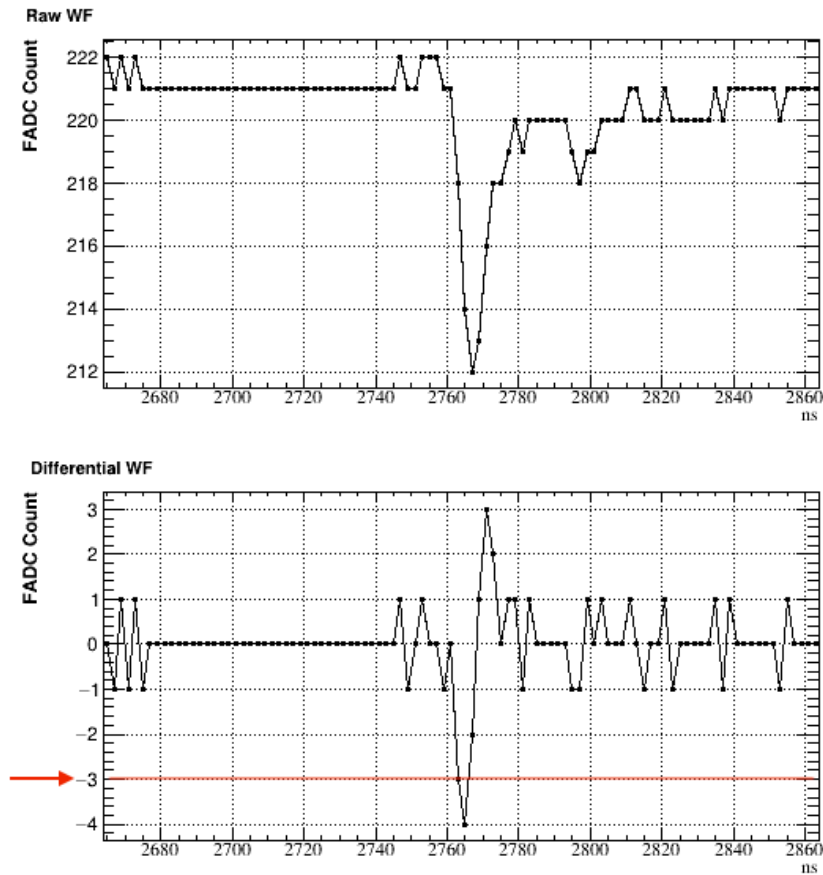


Figure 4.8: An example of hit discrimination using differential waveform. the top panel shows a raw waveform recorded at the FADC. Its differential waveform is displayed in the bottom panel. The red line in the bottom panel exhibits threshold level to discriminate single p.e. hit.

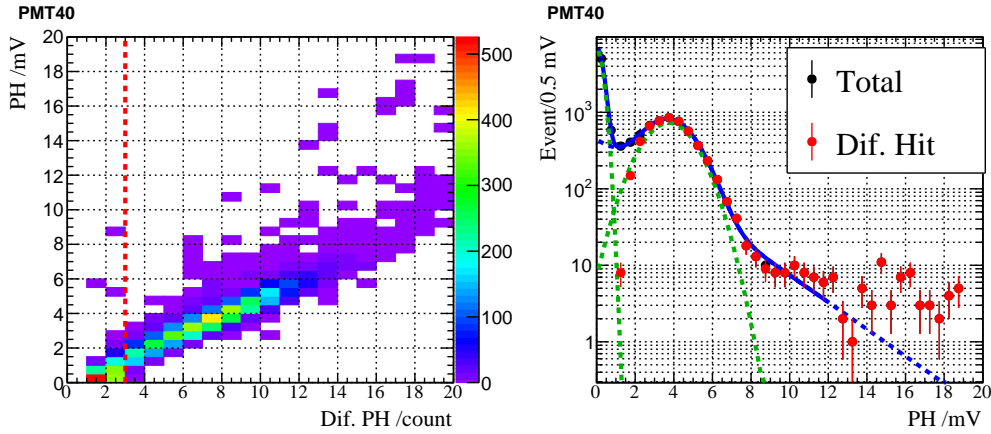


Figure 4.9: Left: a correlation between pulse height of differential waveform (horizontal axis) and that of raw waveform (vertical axis). The red dashed line corresponds to the threshold level for the single p.e. hit discrimination. Right: pulse height distributions of all events (black markers) and events with hit (red markers). The blue line shows a fit result with an exponential and gaussian function as a model for single p.e..

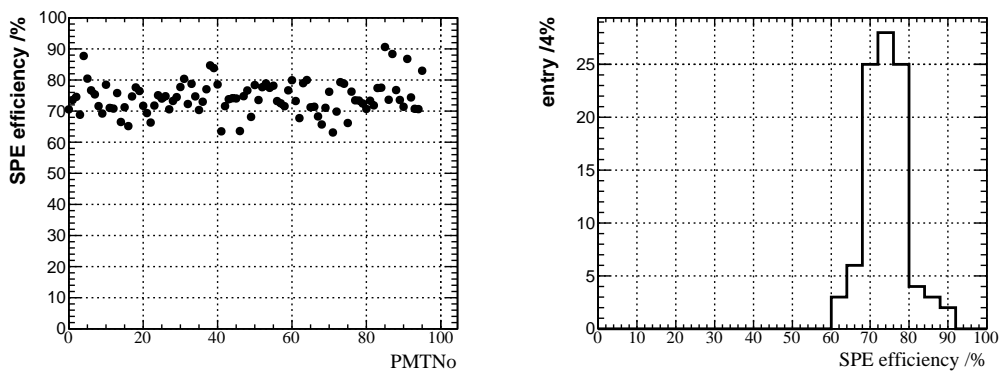


Figure 4.10: Left: single p.e. detection efficiency of the hit discrimination condition for each ID PMT. Right: the distribution of the single p.e. detection efficiency. It indicates that the condition can ensure at least 60 % efficiency for single p.e. detection over the PMTs.

- Define 500 ns event window around the cluster which has over 20 hits in the NHWF.

Taken the detection efficiency of the hit discrimination into account, the threshold level for the event selection (> 20 hits) corresponds to 20 to 40 p.e. equivalent to ~ 0.3 MeV. An efficiency of the event definition is estimated using the MC simulation with neutron capture events generated uniformly in the detector. Figure 4.11 (top) shows the total number of p.e. distributions of all generate events (red) and the events with more than 20 hit (blue). We conservatively assumed that the hit discrimination efficiency is 60 % for each PMT in the simulation. The event definition efficiency defined as a ratio of the blue spectrum to the red one at each bin is shown in Fig. 4.11 (bottom). The efficiency reaches to > 99 % at 100 p.e. (equivalent to ~ 1 MeV).

Figure 4.12 shows an example of the NHWF with defined event windows for 25 μ s waveform. 3 events which have over 20 hits within 500 ns window are discriminated in the whole range of the waveform. The defined event windows are used for variable calculation at each channel. Note that the same event window is used in the low gain channel as well.

This event definition process is skipped for the data obtained using the self trigger such that all triggered events are regarded as physics-like event because it has 500 ns window and triggered by activity in the inner detector.

4.2.2 Trigger efficiency of the self trigger

The trigger efficiency of the self trigger can be estimated using the data obtained by the kicker trigger and DAQ because the inner analog sum waveform is recorded in the trigger board FADC. Figure 4.13 (top) shows the total number of p.e. distributions of all defined events (red) and the events in case analog sum pulse height (A.S.PH) is more than 80 mV. The trigger efficiency defined as a ratio of the blue spectrum to the red one at each bin is shown in Fig. 4.13 (bottom) as the black line as well as the gray shaded area corresponding to the statistic uncertainty. As shown that the event definition efficiency is > 99 % above 100 p.e., a valid range for this self trigger efficiency estimation is from 100 p.e.. It indicates that the efficiency is consistent with 100 % within the statistic uncertainty above 450 p.e. which corresponds to 4 MeV. Therefore, nGd events are sufficiently obtained by the self trigger with the set threshold level.

The same calculations are conducted for the events in the top half and the bottom half of the detector volume separately. They are overlaid in Fig. 4.13 (bottom) as the red markers (top half) and the blue markers (bottom markers). There is a discrepancy between the efficiencies between the top half and the bottom half volume in the range 200 to 400 p.e.. It will appear on the neutron capture event energy spectrum as a difference on the peak height of nH event. Nevertheless, both efficiencies reach to 100 % within the statistic uncertainty above 4 MeV equivalent charge.

4.2.3 Variable definition

Variables, such as charge, timing and so on, are computed at each channel in each defined event. Figure 4.14(a) illustrates definitions of the variables computed from a

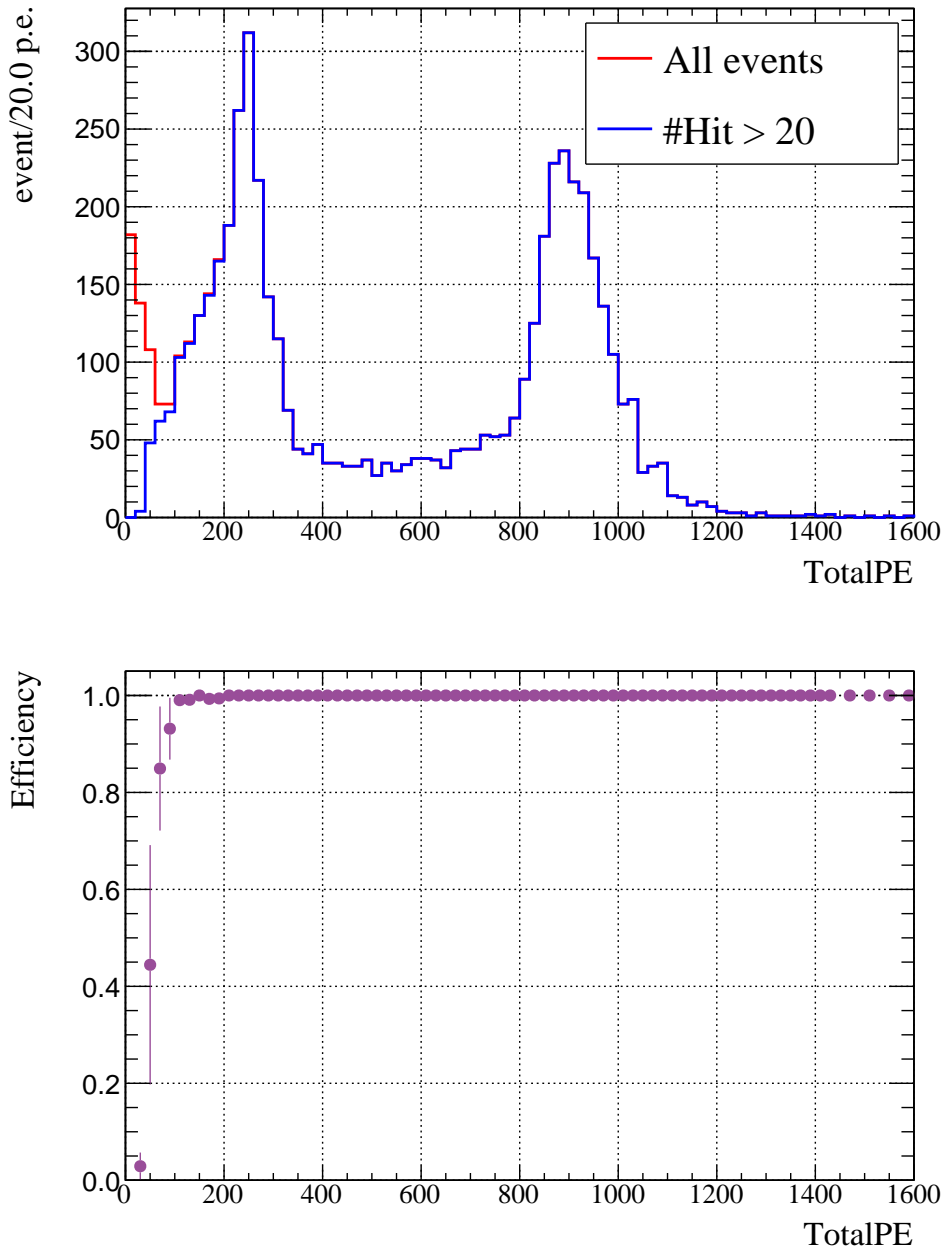


Figure 4.11: Top: the total number of p.e. distributions of all generate events (red) and the events with more than 20 hit. Note that they are obtained from the MC simulation of neutron capture events. The peaks at ~ 250 and ~ 900 p.e. correspond to $n\text{H}$ and $n\text{Gd}$ peak, respectively. Bottom: the efficiency of the event definition condition (the number of hit > 20) as a function of the total number of p.e.. The efficiency reaches to 99 % at 100 p.e. equivalent to 1 MeV.

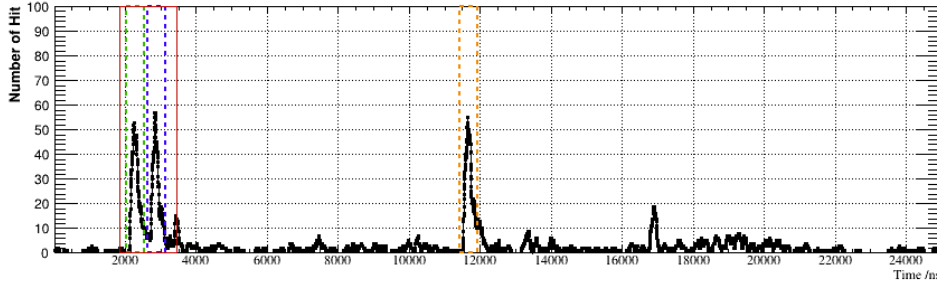


Figure 4.12: An example of number of hit waveform. The dashed rectangles colored green, blue and orange indicate the defined event windows. The red solid box shows beam on-bunch timing region.

waveform in an event range. First, local baseline of the waveform is computed as an average of the first 30 ns from the beginning edge of the event corresponding to the green region in the figure, and find peak position of the waveform in the event range. Then, the charge of the waveform, Q^{raw} , is defined as an integral (= summation in digitized waveform)

$$Q^{raw} = \sum_{i=sbin}^{ebin} (baseline - FADC[i]), \quad (4.2)$$

where the beginning of the range is set to 20 ns before peak timing, and to 200 ns after the peak timing displayed as the blue area in the figure. Pulse height is also defined as height at peak position with respect to the baseline.

For timing calculation, a method of constant fraction discriminator (CFD) is utilized in order to obtain timing resolution narrower than the sampling width (2 ns). CFD is a electric circuit used for timing discrimination suppressing charge-timing correlation effect in contrast to simple threshold triggering. In addition, this method is robust against waveform saturation due to the vertical dynamic range of FADC. Following CFD circuit principle we constructed CFD waveform from the digitized waveform expressed in

$$\begin{aligned} \text{CFD}[i] = & (baseline - FADC[i + n_{\text{delay}}]) \\ & - c \times (baseline - FADC[i]) \quad (i = 0, 1, \dots, n - n_{\text{delay}}), \end{aligned} \quad (4.3)$$

where $n_{\text{delay}} = 10$ sampling corresponding to 20 ns, and the factor c is set to 0.5. Figure 4.14(b) shows an example of CFD waveform from a digitized waveform. Timing is defined as the zero-crossing point of the CFD waveform, which is searched for with linear interpolation. In this sequence, high gain and low gain channels are separately dealt with. However, the hit timing at each PMT is defined as the timing calculated in high gain channel. Timing of event is defined as a arithmetic mean of all hit PMT.

4.2.4 Beam information identification

The logic pulse from the kicker magnet is generated regardless of beam injection toward the MLF target. Beam spill to the MLF can be judged from signals from current transformers (CTs), beam intensity measurement module using the induced

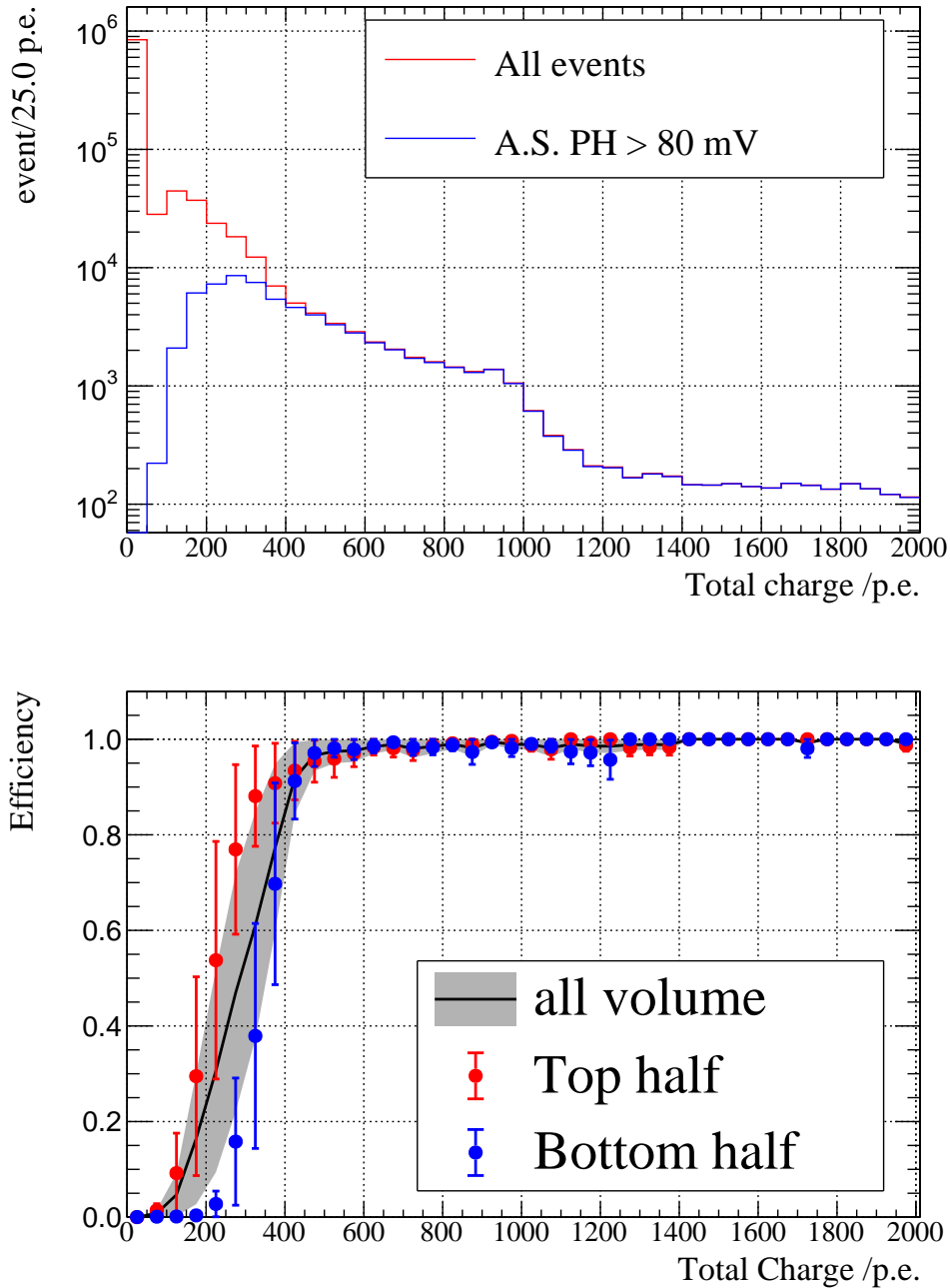


Figure 4.13: Top: the total number of p.e. distributions of all events (red) and the events with more than 80 mV A.S.PH (blue). Bottom: the trigger efficiencies of all events (black line), events in the top half volume (red) and events in the bottom half volume (blue) as a function of the total number of p.e.. The efficiencies are consistent with 100 % above 450 p.e. equivalent to 4 MeV.

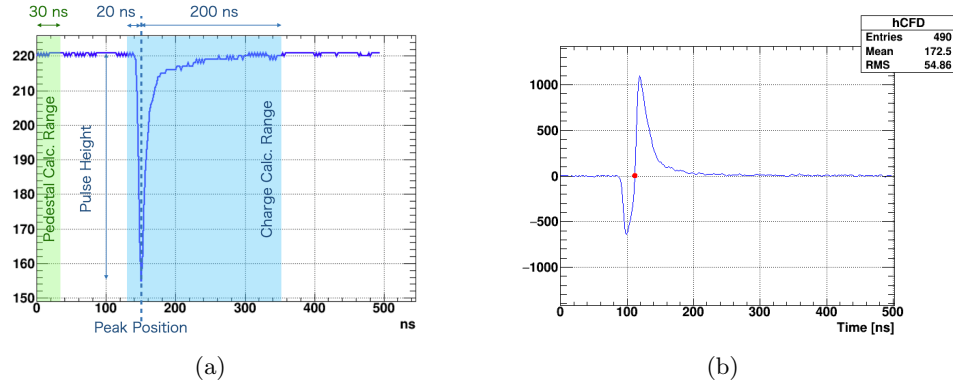


Figure 4.14: (a) The definition of variables computed from a waveform. (b) an example of CFD waveform. The red point indicates zero crossing point used as timing.

current of the coil, located in the beamline between the RCS and the mercury target [50]. The discriminated CT pulse is available for the MLF users, and the timing of the CT signal is $\sim 2.7 \mu\text{s}$ after the actual beam collision due to delay from the electronics (Fig. 4.3). The CT pulse is recorded at the trigger board FADC in order to discriminate beam spill existence in offline analysis. Figure 4.15 shows an example of trigger pulse waveform when CT pulse exists. The beam timing is determined from the kicker pulse (blue) using the CFD method, and beam spill is discriminated using the CT pulse (red) in the FADC window.

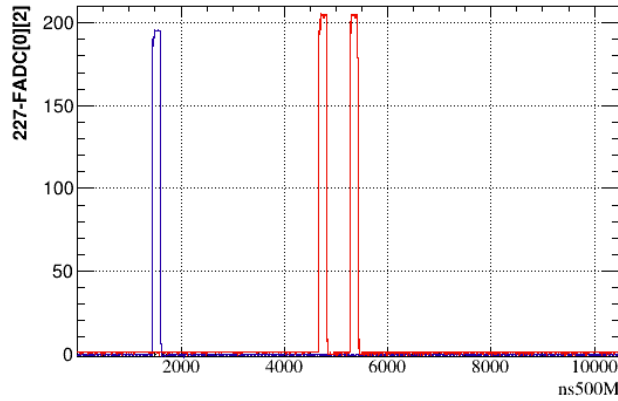


Figure 4.15: An example waveform of kicker (blue) and CT (red) pulses. The vertical axis corresponds to pulse height in a unit of FADC count, and the horizontal axis shows time in a unit of nano second. The CT pulse has 2 bunch structure reflecting the proton beam spill.

4.3 Calibration

For event vertex and energy reconstruction, it is essential to convert Q^{raw} into observed number of p.e. (NPE) at each PMT in the inner detector. Low gain channel is quite important in the energy range of the JSNS² experiment target above 20 MeV.

The calibration items are listed below.

- PMT gain ... as a conversion factor of $Q_{\text{HG}}^{\text{raw}}$ to NPE including gain of FEE HG.
- Relative FEE Gain ... low gain charge correction high energy events.
- Relative timing offset ... timing correction for event timing definition and event extraction from wide range waveform

4.3.1 PMT Gain

In order to perform PMT gain calibration without multi-p.e. contamination, we optimized light intensity of LED illumination. Occupancy is an observable as a quantitative criterion for optimization. Occupancy at i -th PMT O_i is defined as

$$\begin{aligned}
 O_i &\equiv \frac{N_i^{\text{hit}}}{N_{\text{event}}} \\
 &= \frac{P_h(\mu_i)N_{\text{event}}}{N_{\text{event}}} \\
 &= 1 - e^{-\mu_i} \\
 &\sim \mu_i \quad (\mu_i \ll 1)
 \end{aligned} \tag{4.4}$$

where N_i^{hit} is the number of hit on i -th PMT, and N_{event} is total number of LED illumination equivalent to that of generated trigger from the nano-pulsar system. The hit threshold is set to 0.3 p.e. level. Given Poisson distribution, the hit probability is $P_h(\mu_i) = 1 - e^{-\mu_i}$. Therefore, occupancy can be denoted as mean value μ_i of Poisson distribution in case the mean is much less than 1. Multi-p.e. contamination can be written down as a function of occupancy as a fraction of s.p.e. event in total hit $F_{\text{s.p.e.}}$.

$$\begin{aligned}
 F_{\text{s.p.e.}} &= \frac{P(n=1; \mu_i)}{P_h(\mu_i)} \\
 &= \frac{\mu_i e^{-\mu_i}}{1 - e^{-\mu_i}} \\
 &\sim 1 - \frac{\mu_i}{2} = 1 - \frac{O_i}{2} \quad (\mu_i \ll 1).
 \end{aligned} \tag{4.5}$$

If we set occupancy to 5 %, a purity of single p.e. in the observed charge distribution reaches to 97.5 %. Table 4.2 shows the optimized intensity at each LED and target PMT number, which is measured in the dry-run commissioning. Because LED No.8, 9 and 13 did not work temporarily at that time, they are not used in gain calibration runs. The light intensity is controlled by a 14 bits integer as an argument of the LED control software. The digits listed in the table are equivalent to 10^1 to 10^2 photons per pulse at each LED channel.

Figure 4.16 (left) shows the distribution of the observed charge converted into relative gain with respect to 1×10^7 , such that,

$$Q^{\text{rel}} = Q^{\text{raw}} \times \frac{3.9[\text{mV}] \times 2[\text{ns}]}{50[\Omega]} \times \frac{1}{16} \times \frac{1}{1.6 \times 10^{-10}[\text{pC}]}, \tag{4.6}$$

Table 4.2: Table of LED intensity for gain calibration.

LED ch	Intensity	Target PMT
1	9010	28, 29, 40, 47, 48, 49, 50, 51, 52, 54, 62
2	7850	5, 59
3	9790	26, 39, 72, 76
4	8330	2, 14, 23, 41, 45, 53, 55, 56, 65, 77, 78, 82, 91
5	8300	13, 17, 66, 68, 69, 70, 71, 94
6	9050	3, 8, 12, 16, 20, 25, 30, 31, 32, 42, 73
7	8800	27, 37, 46, 61, 63, 64, 87, 88, 89
8	-	
9	-	
10	9160	7, 19, 24, 36, 38, 44, 57, 74, 75, 84, 85, 95
11	7920	11, 18, 33, 43, 58, 60, 67, 79, 83, 86, 92
12	9450	0, 1, 4, 6, 15, 22, 35, 80
13	-	
14	8700	9, 10, 21, 34, 81, 90, 93

obtained in gain calibration run with optimized LED intensities assuming gain of FEE high gain is uniformly 16 over channels. It was applied 1 mV threshold equivalent to 0.3 p.e. level in offline analysis. One can find that multi-p.e. contamination is well suppressed due to low intensity light illumination. Thus, single gaussian is used for fitting to extract gain at each PMT.

Because there is no light source, such as LED, in the veto layer, gain calibration is done using dark hit. Figure 4.16 (right) shows relative gain distribution, which applied 1 mV threshold equivalent to 0.3 p.e. level in offline. Gain value is estimated by fitting with single gaussian, accordingly. The result of gain calibration is summarized in Fig. 4.17 and table 4.3. Note that the PMT gain calibration is performed together with gain of FEE high gain channel per channel simultaneously.

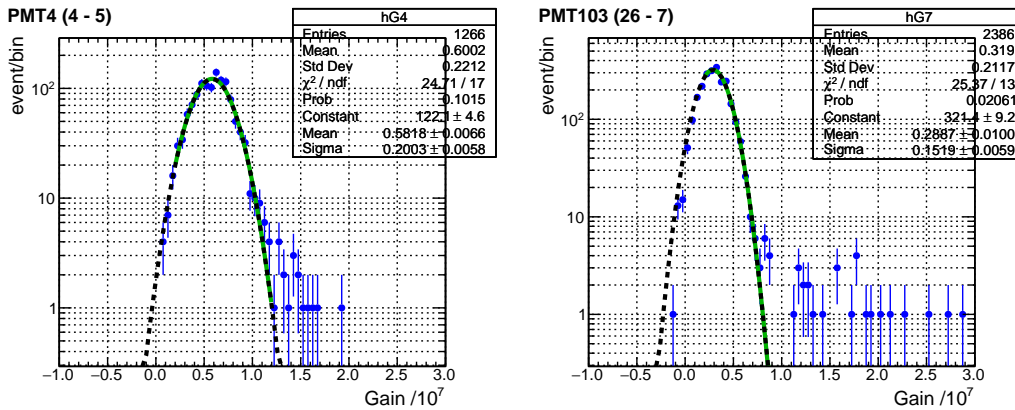


Figure 4.16: Left: Charge distribution of PMT No.4 in the inner detector as a result of gain calibration run using LED 12. Right: Charge distributions PMT No.103 in the veto layer. The blue marker shows data, and green line represents fitting result with single gaussian.

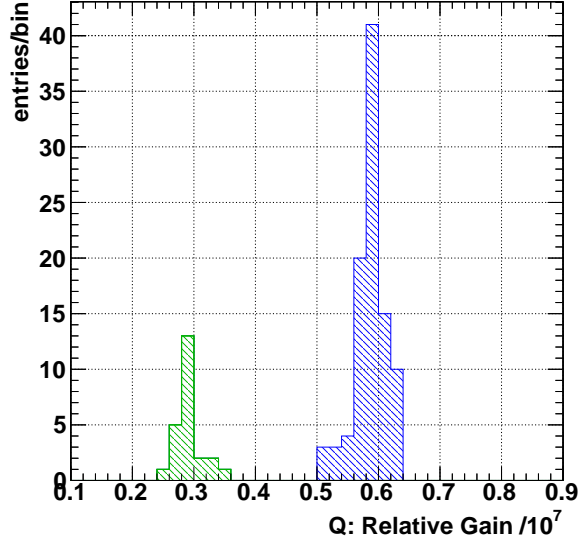


Figure 4.17: Gain distribution for all PMTs. The blue shaded one shows gain distribution of the inner PMTs, and the green one is for veto PMTs.

Table 4.3: Table of LED intensity for gain calibration.

Region	Target gain	Measured Gain Mean	Measured Gain Std. Dev.
Inner	6×10^6	5.88×10^6	0.25×10^6
Veto	3×10^6	2.91×10^6	0.22×10^6

4.3.2 Relative FEE Gain

Gain calibration is performed using only high gain channels because typical single p.e. pulse height in low gain is around 2 mV which is less than vertical digitization resolution of 8 bit FADC. Therefore, calibration for low gain charge is relatively conducted with respect to high gain charge. Raw charge to NPE conversion in LG channel is defined using the measured PMT gain as

$$Q_{\text{LG}}^{\text{NPE}} = Q_{\text{LG}}^{\text{raw}} \times \frac{3.9[\text{mV}] \times 2[\text{ns}]}{50[\Omega]} \times \frac{1}{0.6} \times \frac{1}{1.6 \times 10^{-10}[\text{pC}]} \times \frac{1}{\text{gain}}, \quad (4.7)$$

where 0.6 is a typical gain value of FEE low gain channel. Figure 4.18 (a) shows 2D histogram of low gain NPE ratio with respect to NPE in high gain as a function of HG NPE. The red marker indicates mean value along the vertical axis at each bin in the horizontal axis, and it converges to a constant above 15 p.e., which is used as a correction factor for NPE in low gain. The range from 17 to 35 p.e. in HG (green dashed line) is selected for computing correction factor of gain ratio in order to avoid HG saturation due to FADC dynamic range and small pulse height in low gain channel compared to FADC digitization resolution. Finally, the correction factor for charge of LG channel is computed as an average of the mean over the range. Figure 4.18 (b) shows the correction factor as a function of PMT ID, and its mean value is 0.82.

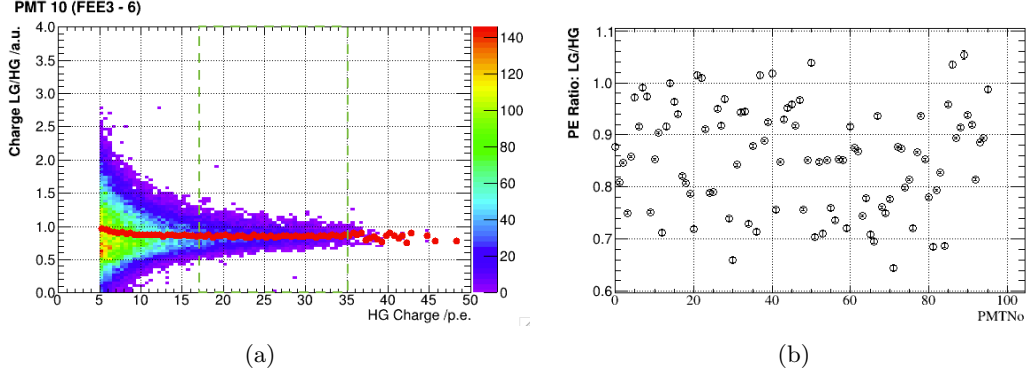


Figure 4.18: Correlation between NPE ratio of LG to HG and NPE in high gain channel assuming that the typical gain of FEE is 0.7 and 16 for low gain and high gain, respectively. The dashed green line exhibits the selection region for correction factor computation.

4.3.3 Relative Timing Offset

Relative timing offset of each PMT is important for event definition in the data obtained using the kicker trigger. It is calibrated using the nano-pulsar LED system which can perform several nano second pulsed light illumination on each LED. Fig-

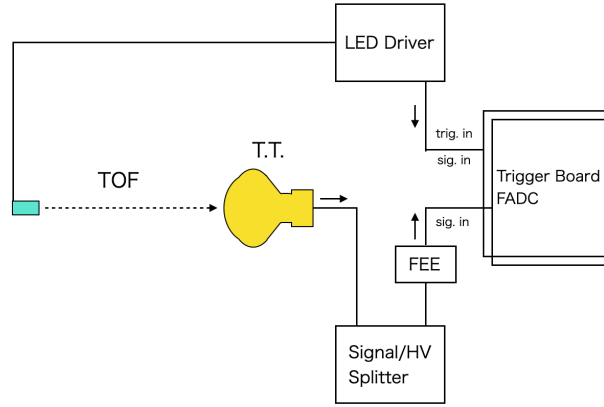


Figure 4.19: A schematic diagram of timing calibration using the nano-pulsar LED system.

Figure 4.19 shows a schematic diagram of relative timing calibration using the nano-pulsar system. The observable, timing difference between LED trigger and PMT signal can be written down as

$$\Delta t_{\text{LED-PMT}} = t_{\text{TOF}} + (t_{\text{TT}} + t_{\text{SD}}) + t_{\text{LED}}, \quad (4.8)$$

where TOF, TT and SD stands for time of flight of photon from LED to PMT surface, transit time in PMT, and signal delay caused by electronics circuit, respectively. t_{TT} and t_{SD} uniquely depend on each PMT (channel). There is timing difference between actual light emission on LED and trigger signal timing recorded in FADC, t_{LED} , because of differences of cable length from LED modules in the detector to the LED driver module. Given the angular property of light emission, PMT grouping

with respect to each LED is performed, whose position is simply in the opposite side of each LED. High intensity illumination allow to obtain large pulse, and helps lowering an effect of transit time spread in PMT. Table 4.4 summarizes intensities and PMT group for each LED. Note that there are overlapped PMTs among the groups. They can be used for t_{LED} correction between the LEDs. LED No. 2 and 13 are not used as they are UV LEDs.

Table 4.4: Table of LED intensity for relative timing calibration.

LED ch	Intensity	Target PMT
1	11000	78, 79, 80, 84, 85, 86, 87, 88, 95, 81, 83, 94
2	-	
3	12000	81, 82, 83, 89, 90, 91, 92, 93, 94, 78, 80, 88
4	12000	6, 7, 8, 18, 19, 20, 30, 31, 32, 72, 73, 74
5	12000	31, 32, 33, 43, 44, 45, 55, 56, 57, 91, 92, 93
6	12000	3, 4, 5, 15, 16, 17, 27, 28, 29, 69, 70, 71
7	12000	28, 29, 30, 40, 41, 42, 52, 53, 54, 88, 89, 90
8	12000	0, 1, 2, 12, 13, 14, 24, 25, 26, 66, 67, 68
9	12000	25, 26, 27, 37, 38, 39, 49, 50, 51, 85, 86, 87
10	12000	9, 10, 11, 21, 22, 23, 33, 34, 35, 75, 76, 77
11	12000	34, 35, 24, 46, 47, 36, 58, 59, 48, 94, 95, 84
12	12000	60, 61, 62, 66, 67, 68, 69, 70, 77, 63, 65, 76
13	-	
14	12000	63, 64, 65, 71, 72, 73, 74, 75, 76, 60, 62, 70

Figure 4.20(a) shows an example histogram of timing difference $t_{\text{LED-PMT}}$ after TOF subtraction about PMT7 in LED4 illumination. Mean of the histogram is used as relative timing offset before t_{LED} matching. Figure 4.20(b) shows relative timing offset of each PMT as a function of PMT ID after t_{LED} matching is performed using the overlapped PMTs. One can find that there is clear correlation between the offset value and cable length of PMT, which indicates that timing difference follows 5 ns/m similar with a usual LEMO cable.

4.3.4 Monte Carlo simulation tuning

Tuning the JSNS² RAT simulator to reproduce detector response was performed based on the calibration data using ²⁵²Cf source deployed at several position along z axis in the detector. The deployed positions are 0, ± 50 , ± 75 , ± 100 cm in the z axis whose origin is set to the detector center. The responses in the source calibration data are made by selecting 7 - 9 MeV equivalent charge to include the peak of nGd demonstrated in Fig. 4.21(a). The same condition is applied to the MC output accordingly as shown in Fig. 4.21(b). In addition, given the symmetry of PMT position with respect to the z axis, we make 9 groups with PMTs which have the same acceptance as shown in Fig. 4.22. Figure 4.23 shows the result of MC tuning and compares MC response (red dashed line) with the data (black marker) in case the ²⁵²Cf source is at the center. Scintillation light yield of the liquid scintillators in the MC simulator is adjusted to reproduce the observed NPE at each PMT in the data. One can find that the tuned MC responses of each PMT group are in good agreement with that of the data. Note that inconsistency in low p.e. region is caused

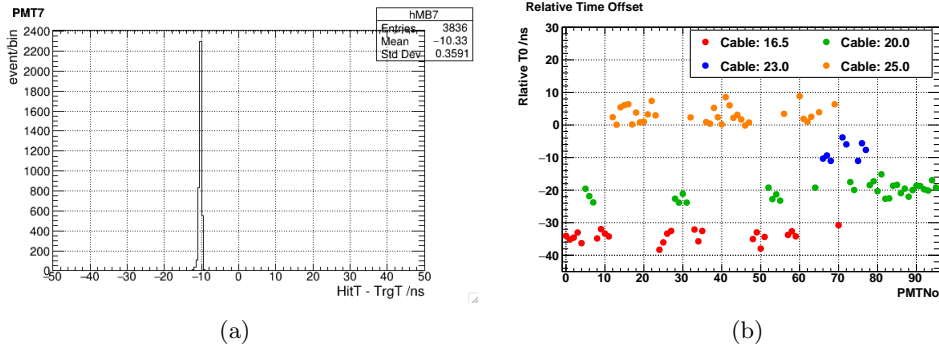


Figure 4.20: (a) A histogram of timing difference between signal on PMT 7 and external trigger pulse from LED 4. (b) Relative timing difference for all PMTs. Trigger timing difference unique to each LED are corrected using timing of the overlapped PMTs. The origin in the vertical axis is arbitrary; however, the relative values among PMTs are calibrated. The colors of marker classify cable length of PMT.

by impurity of nGd event in the data. Comparisons between MC and data in the other source positions are shown in Figs. 4.24 to 4.26. They also show a consistency with the data.

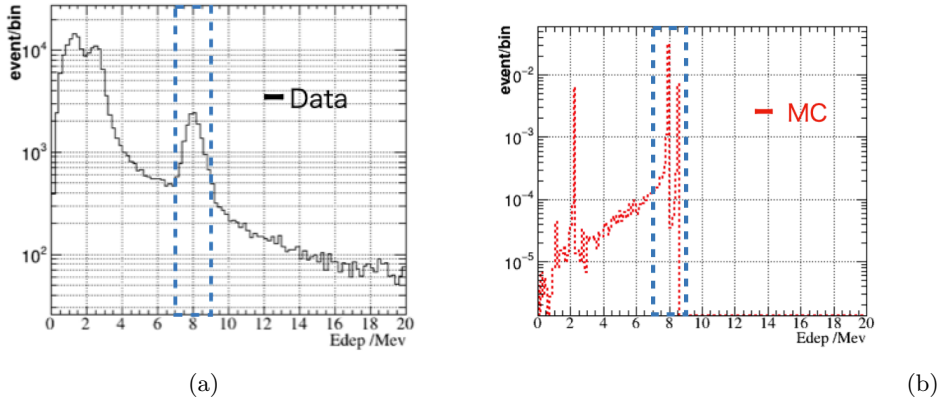


Figure 4.21: Event selection criterion displayed by blue dashed box for the data (a) and the MC (b), respectively.

4.4 Event Vertex and Energy Reconstruction

An event vertex and energy simultaneous reconstruction is developed based on a maximum likelihood algorithm using charge response on PMTs. Technically, it is identical as minimizing negative logarithm of the likelihood, which is much more convenient to compute instead of maximum search. The negative log likelihood (NLL) to be minimized is characterized with a vector of parameters $\vec{\alpha} = (E, x, y, z)$ consists of deposit energy and a vertex position in the inner detector. Thus, it is

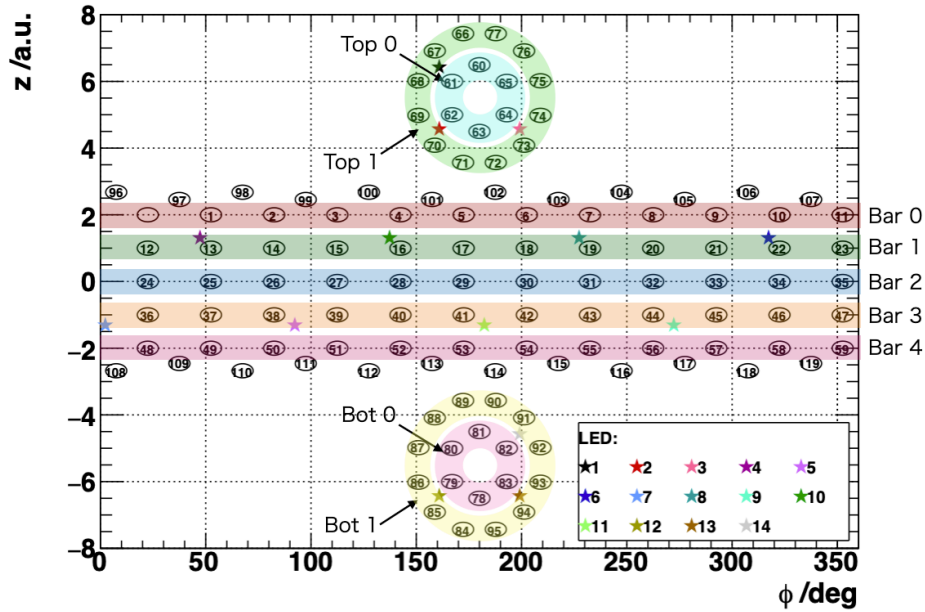
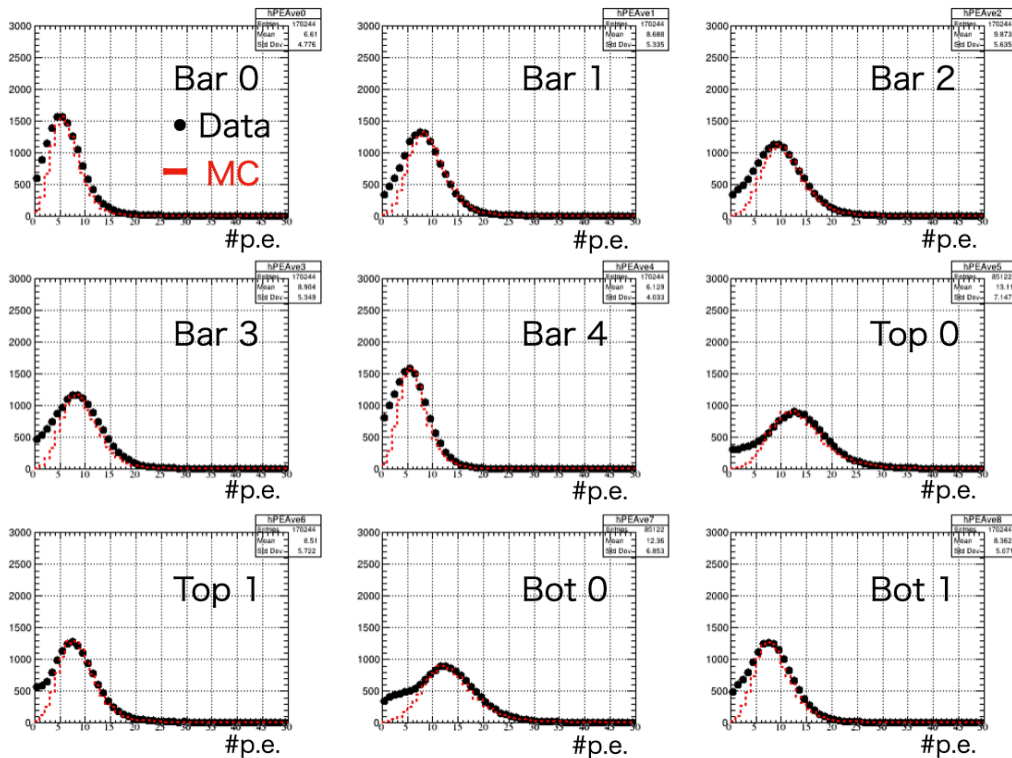


Figure 4.22: A map of the PMT groups.

Figure 4.23: The observed NPE response of each PMT group when the ^{252}Cf source is deployed at the center ($z = 0$ cm). Both response of the data (black dots) and the MC (red dashed line) are overlaid to compare them.

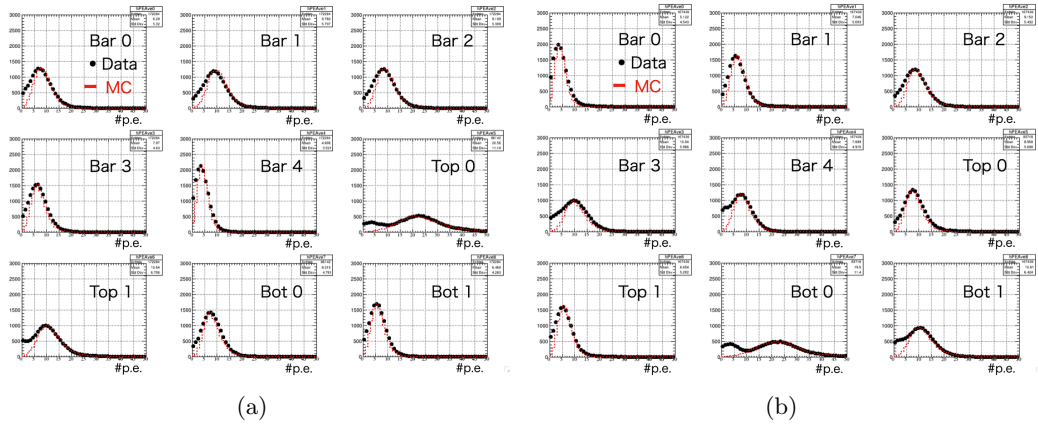


Figure 4.24: The observed NPE response of each PMT group when the ^{252}Cf source deployed at $z = 50$ cm (left) and -50 cm (right). Both response of the data (black dots) and the MC (red dashed line) are overlaid to compare them.

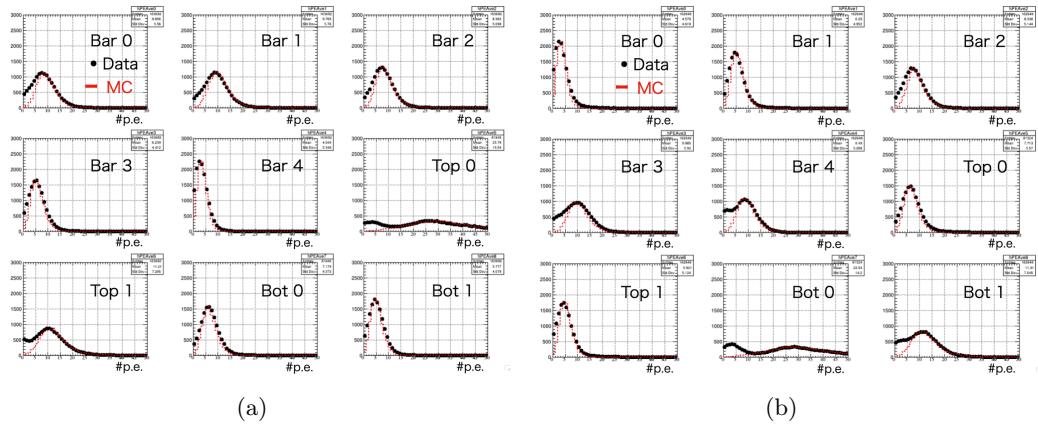


Figure 4.25: The observed NPE response of each PMT group when the ^{252}Cf source deployed at $z = +75$ cm (left) and -75 cm (right). Both response of the data (black dots) and the MC (red dashed line) are overlaid to compare them.

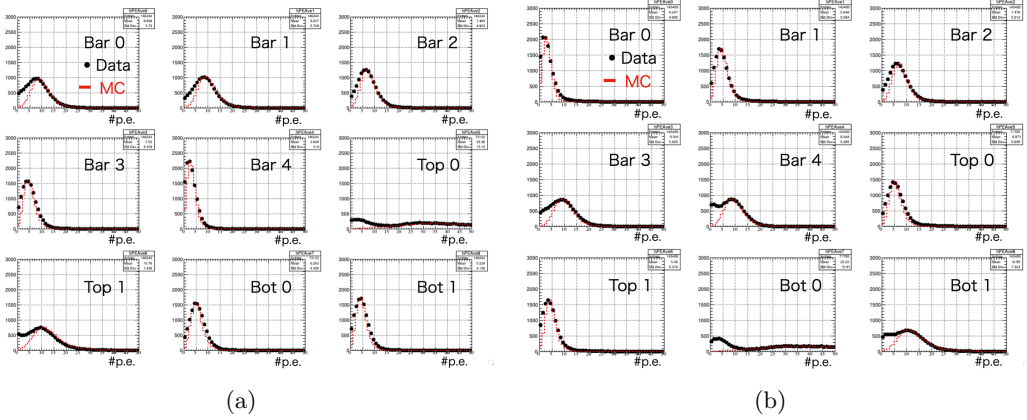


Figure 4.26: The observed NPE response of each PMT group when the ^{252}Cf source deployed at $z = +100$ cm (left) and -100 cm (right). Both response of the data (black dots) and the MC (red dashed line) are overlaid to compare them.

denoted as

$$NLL = -\log \mathcal{L} = -\sum_{i=1}^{N_{\text{PMT}}} \log \mathcal{L}_q(q_i; \vec{\alpha}), \quad (4.9)$$

where q_i is the observed charge on i -th PMT, and \mathcal{L}_q is a charge likelihood for i -th PMT as a function of parameter $\vec{\alpha}$ with respect to the observed charge. In particular, the charge likelihood is Poisson likelihood approximated by Stirling's approximation, such that

$$-\log \mathcal{L}_q(q_i; \vec{\alpha}) = (\mu_i(\vec{\alpha}) - q_i) + q_i \log \left(\frac{q_i}{\mu_i(\vec{\alpha})} \right) \quad (\text{if hit}) \quad (4.10)$$

and

$$-\log \mathcal{L}_q(q_i; \vec{\alpha}) = \mu_i(\vec{\alpha}) \quad (\text{if no hit}), \quad (4.11)$$

where $\mu_i(\vec{\alpha})$ is the expected charge as a function of parameters. Note that hit/no hit treatment is taken into account with hit discrimination by applying 0.3 p.e. equivalent threshold to pulse height of signal as following the methods above. The expected charge response is generated using the JSNS² RAT simulator with tuning at 8 MeV so that it can include a realistic effect caused by the geometry of the detector, such as shape of PMT surface, on the prediction. Figure 4.27 shows response maps for each PMT group as a function of $\cos \theta$ and r whose definition is shown in figure 4.28. The PMT grouping classification is same as the group displayed in figure 4.22.

A correction for the expected charge is applied in order to take a saturation effect of PMT into consideration. Figure 4.29 shows the measured saturation effect of R7081 in the laboratory. The data is well modeled by an equation

$$Q^{\text{obs}} = p_0 \times Q^{\text{exp}} + p_1 \left[1 - \exp \left(-\frac{Q^{\text{exp}}}{p_2} \right) \right], \quad (4.12)$$

where Q^{obs} is a observed charge, Q^{exp} is an expected charge at PMT and three parameters p_i ($i = 0, 1, 2$), displayed as the black line in the figure.

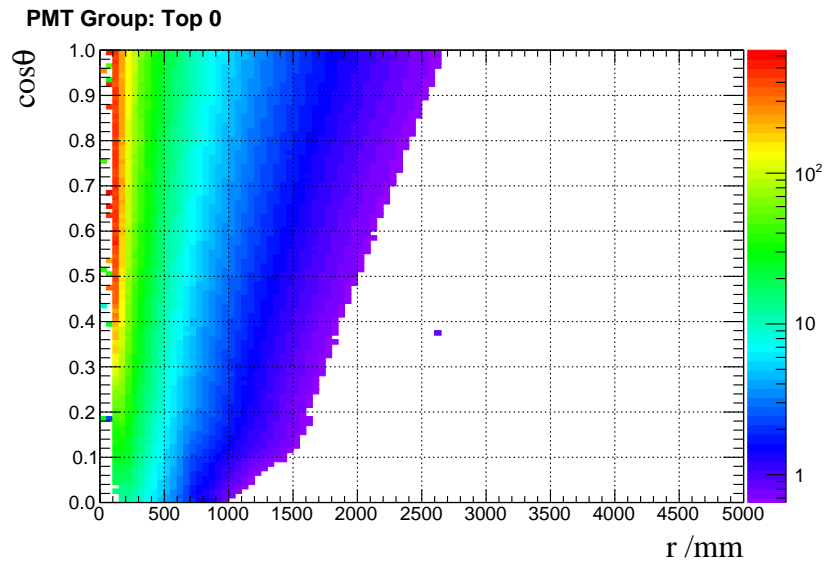


Figure 4.27: An example of the response map of the group top 0. The vertical and horizontal axes correspond to a distance between a vertex and PMT r and $\cos\theta$ of a zenith angle to the vertex θ . The z axis exhibited as color graduation represents expected number of p.e. per MeV at each vertex.

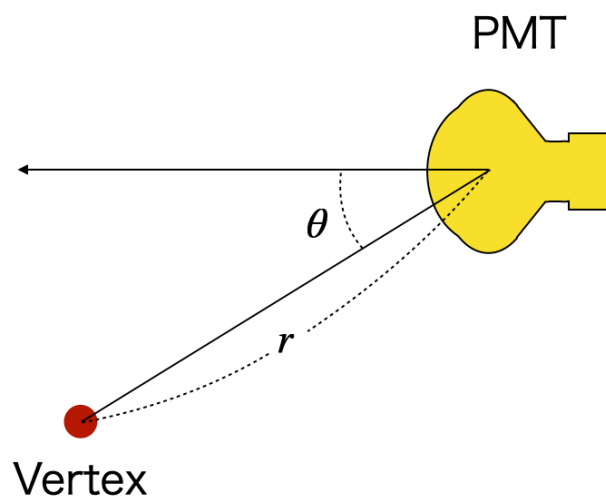


Figure 4.28: A schematics of the coordinate in the response map.

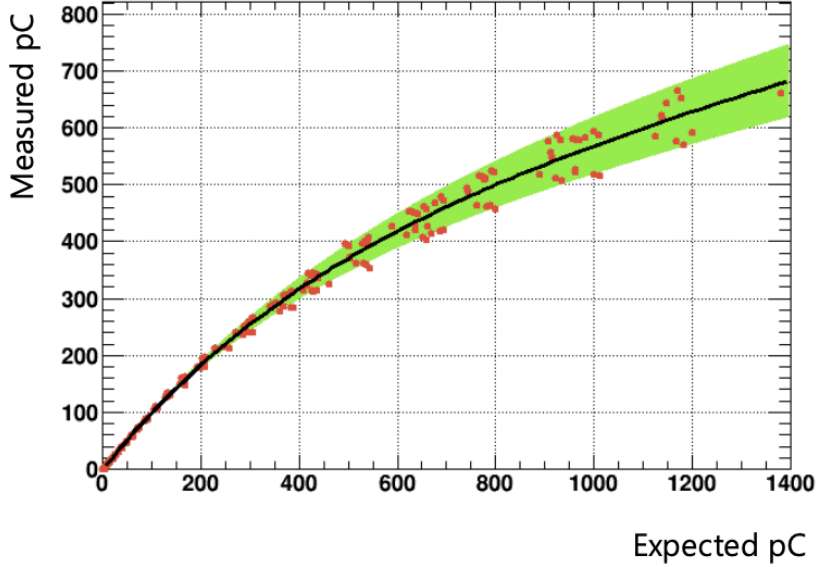


Figure 4.29: The measured PMT response representing a saturation effect in 10 inch PMT R7081 at the gain of the inner PMT [46]. The red points are the measured data, the black line indicates the fitting result based on the model function given by Eq. (4.12), respectively. The uncertainty of the fitting is displayed as the green area.

As there are high and low gain channel for each PMT in the inner detector, the input observed charge q_i is selected in the below condition in order to avoid HG signal saturation due to FADC dynamic range;

- If the pulse height is below 90% of FADC vertical range, $q_i = Q_i^{\text{HG}}$ [p.e.].
- Else $q_i = Q_i^{\text{LG}}$ [p.e.].

Q_i^{HG} and Q_i^{LG} is charge equivalent to the number of photoelectron computed in high gain and low gain channel of i -th PMT, respectively. In case Q_i^{LG} reaches 1000 p.e. which is equivalent to pulse height saturation due to the vertical limit of FADC in low gain channel, the PMT is eliminated from the likelihood calculation.

The performance of the reconstruction and consistency between data and MC simulation are to be demonstrated using the source calibration data and Michel electron events in the following sections.

4.5 Measurement of Background Rate of each component

There exists various background sources in the environment of JSNS² experiment. The components of the background is listed below;

- Cosmic muon
- Michel electron from stopped muon decay

4.5. MEASUREMENT OF BACKGROUND RATE OF EACH COMPONENT 83

- Cosmic ray induced fast neutron
- Cosmic ray induced gamma ray
- gamma ray from the surface of the hatch

In this section, the event rate in the signal window is being measured based on the data in the first run.

4.5.1 Cosmic muon tagging (offline muon veto)

Cosmic muons can be a source of accidental background for both prompt and delayed signal of IBD in case it deposits the appropriate energy in the inner detector. In addition, a Michel electron generated in stopped muon decay in the detector has the same energy spectrum as $\bar{\nu}_\mu$ from the mercury target so that it can be an accidental background source for the IBD prompt region. It is possible to eliminate the backgrounds using correlation between the parent muon and Michel electron; therefore, tagging cosmic muon plays a crucial roll. For cosmic muon veto in offline analysis, the following selections are used;

- Veto layer activity: $Q_{\text{total}}^{\text{Veto}} < 100$ p.e.
- Inner detector activity: $E_{\text{vis}}^{\text{ID}} < 400$ MeV

where $Q_{\text{Total}}^{\text{Veto}}$ is charge summation over all PMTs in the veto layer. Otherwise, the events are judged to be caused by cosmic muons. The left plot of Fig. 4.30 shows the correlation between the ID visible energy $E_{\text{vis}}^{\text{ID}}$ (the horizontal axis) and the total charge in the veto layer $Q_{\text{total}}^{\text{Veto}}$ (the vertical axis), and the selection criteria is displayed as the red dashed box in the figure. There are events whose activity in the veto layer is below the criterion because of muons intruding from the chimney and stopping in the detector. That is, the criterion on the inner detector activity is applied.

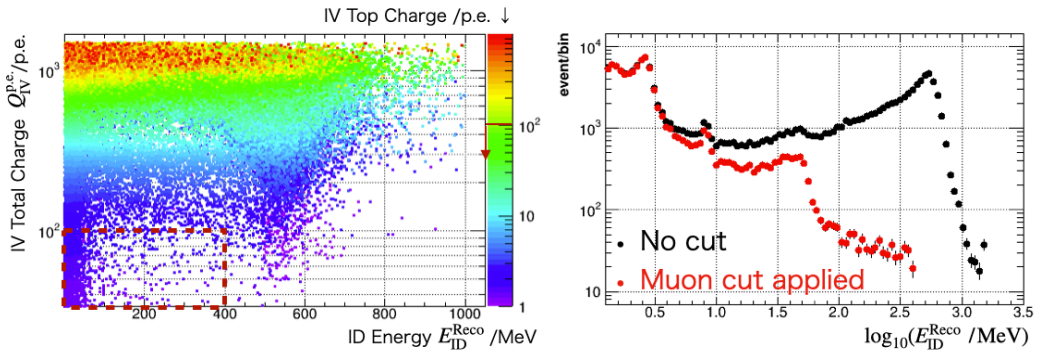


Figure 4.30: Left: selection criteria for cosmic muon tagging. Events in the outside of the red dashed box are defined as activities caused by cosmic muon. Right: Energy distribution in common logarithm scale before (black) and after muon veto (red) in the horizontal axis.

The right plot of Fig. 4.30 demonstrates the muon selection in the ID visible energy distribution in log scale. As a result of the offline veto, sufficient reduction

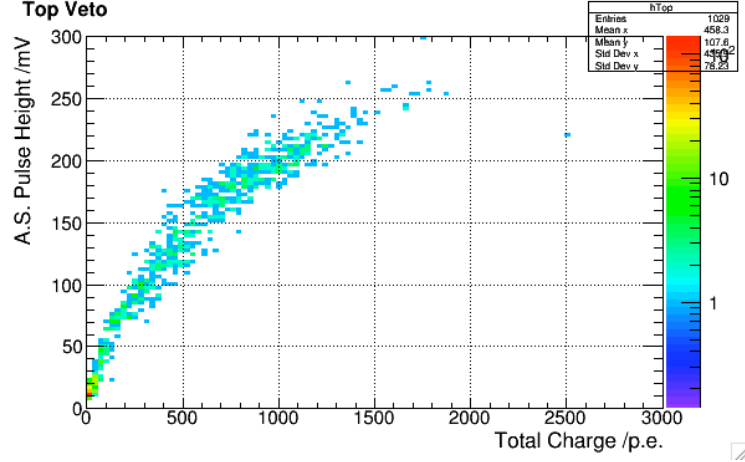


Figure 4.31: Correlation between pulse height of the veto top analog sum signal (vertical) and total charge in the veto layer $Q_{\text{total}}^{\text{Veto}}$ (horizontal). The former is used for online muon veto by applying 75 mV threshold equivalent to 200 p.e..

of muon events after the selection and clear Michel electron excess appear around 1.8 in the horizontal axis.

Figure 4.31 show a correlation between pulse height of the veto top analog sum signal and total charge in the veto layer. The threshold level to the analog sum pulse height for the online veto is 75 mV, which corresponds to 200 p.e. in the total charge $Q_{\text{total}}^{\text{Veto}}$. Thus, the offline veto condition gives severer selection to events.

4.5.2 ^{252}Cf data for validation

As a demonstration of the reconstruction and MC tuning, the source calibration data are described here as well as their MC. It is needed to perform delayed coincidence for extraction of events caused by ^{252}Cf , especially neutron capture on Gd (nGd). The following selection criteria are applied to select nGd events from fission in the source:

- Offline muon veto for both prompt and delayed signals,
- Prompt signal
 - Signal isolation: $\Delta t > 200 \mu\text{s}$ from the last event,
 - Visible energy: $4 < E_{\text{vis}}^{\text{ID}} < 20 \text{ MeV}$,
- Delayed visible energy: $7 < E_{\text{vis}}^{\text{ID}} < 12 \text{ MeV}$,
- Timing correlation between prompt and delayed: $\Delta t_{\text{p-d}} < 100 \mu\text{s}$,
- Spatial correlation between prompt and delayed: $\Delta VTX_{\text{p-d}} < 150 \text{ cm}$.

Because ^{252}Cf emits multiple neutrons in a decay (3.75 ± 0.01 per fission [47]), the signal isolation cut is applied in order to avoid nGd-nGd pairing. The selection criteria of the time correlation cut and the delayed energy cut are set to the identical condition as that of the IBD selection in order to estimate neutron detection efficiency. Figure 4.32 shows distributions of each variable to which all selections

4.5. MEASUREMENT OF BACKGROUND RATE OF EACH COMPONENT 85

except for the selection to itself are applied. The correlated and accidental event candidates are displayed together with the correlated event excess with respect to the accidental events (green, blue, and black, respectively). The accidental coincident events are estimated by pairing events in the off-timing, e.g., from 1000 μs to 2000 μs after the prompt candidate with prompt candidates (off timing method illustrated in Fig. 4.33).

The time constant of neutron capture on Gd can be estimated by fitting exponential function to the $\Delta t_{\text{p-d}}$ distribution. The orange line in the middle left plot in Fig. 4.34 displays the fit result with an exponential function. It gives time constant $\tau = 30.84 \pm 0.37 \mu\text{s}$ in case the source position is at the center of the detector ($Z = 0 \text{ cm}$). Figure 4.34 shows the estimated time constants at each source position. The average of the time constant is 30.27 μs , and they are identical within 2 % difference over the positions.

Neutron detection efficiency is expressed as a product of three components:

$$\epsilon_{\text{neutron}} \equiv \epsilon_{\Delta t_{\text{p-d}}} \times \epsilon_{E_{\text{delayed}}} \times \epsilon_{\text{Gd}}, \quad (4.13)$$

where $\epsilon_{\Delta t_{\text{p-d}}}$ and $\epsilon_{E_{\text{delayed}}}$ are efficiencies of the time correlation and the delayed energy cuts respectively, and ϵ_{Gd} is a fraction of nGd with respect to total neutron capture. As shown in the middle left plot in Fig. 4.34, almost all neutron capture on Gd with $7 < E_{\text{vis}}^{\text{ID}} < 12 \text{ MeV}$ occur within 300 μs . Thus, a time correlation cut efficiency is defined as a ratio the number of events in $\Delta t_{\text{p-d}} < 100 \mu\text{s}$ to that of events in $\Delta t_{\text{p-d}} < 300 \mu\text{s}$:

$$\epsilon_{\Delta t_{\text{p-d}}} = \frac{N(\Delta t_{\text{p-d}} < 100 \mu\text{s})}{N(\Delta t_{\text{p-d}} < 300 \mu\text{s})}, \quad (4.14)$$

where N stands for an integrated value of the $\Delta t_{\text{p-d}}$ distribution over the condition shown in the parentheses. Accordingly, because almost all nGd events give $E_{\text{vis}}^{\text{ID}} > 4 \text{ MeV}$, the definition of an efficiency of delayed energy cut is

$$\epsilon_{E_{\text{delayed}}} = \frac{N(7 < E_{\text{vis}}^{\text{ID}} < 12 \text{ MeV})}{N(4 < E_{\text{vis}}^{\text{ID}} < 12 \text{ MeV})}, \quad (4.15)$$

where N is an integrated value of the delayed energy distribution over the range designated in the parentheses. Based on the top right and the middle left plots in Fig. 4.32, $\epsilon_{E_{\text{delayed}}} = 95.5 \%$ and $\epsilon_{\Delta t_{\text{p-d}}} = 95.4 \%$ at $Z = 0 \text{ cm}$, respectively. The Gd fraction is estimated to be $\epsilon_{\text{Gd}} = 86.0 \%$ based on the MC simulation. Therefore, the neutron detection efficiency at the center of the detector is 78.4 %. The bottom left plot in Fig. 4.32 shows the histogram of delayed signal multiplicity, whose mean value is 2.9. This is consistent with the average neutron multiplicity from ^{252}Cf by taking the neutron detection efficiency into consideration, i.e., $3.75 \times 0.784 = 2.93$.

Energy resolution as a function of visible energy can be computed using the peaks of neutron capture on H (nH) and Gd. Due to low trigger efficiency around 2 MeV in the bottom half of the detector, the data obtained in case the source position at $Z = 0$ to 100 cm was used. Figure 4.35 shows the result of peak fitting using single gaussian for the nH peak and double gaussian for the nGd peak consisting of ^{155}Gd and ^{157}Gd with 0.6 MeV difference (left), and the computed energy resolution at each position (right). The dashed lines in the right plot show the result of fitting

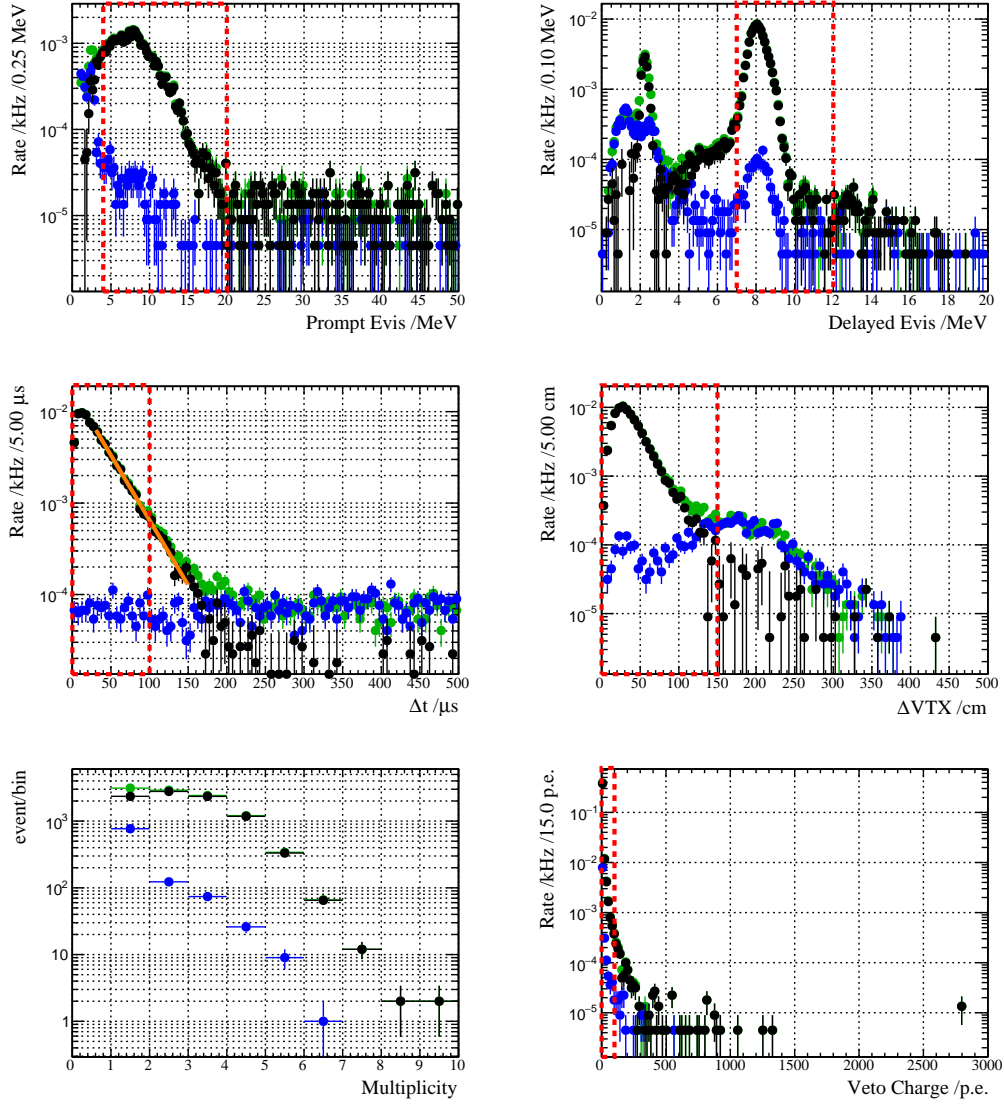


Figure 4.32: Delayed coincidence for the data with the ^{252}Cf source positioned at $z = 0$ cm along the z axis. Top left: prompt visible energy. Top right: delayed visible energy. Middle left: Δt_{p-d} . Middle right: ΔVTX_{p-d} . Bottom left: multiplicity of delayed signal. Bottom right: total charge in the veto layer. Each distribution of variable is applied all selections except for the selection to itself. The red boxes show the selection criterion to each variable. The green marker corresponds to correlated event candidates, and the blue one shows the estimated accidental coincidence events. The accidental subtracted distribution is displayed as the black marker in the plots.

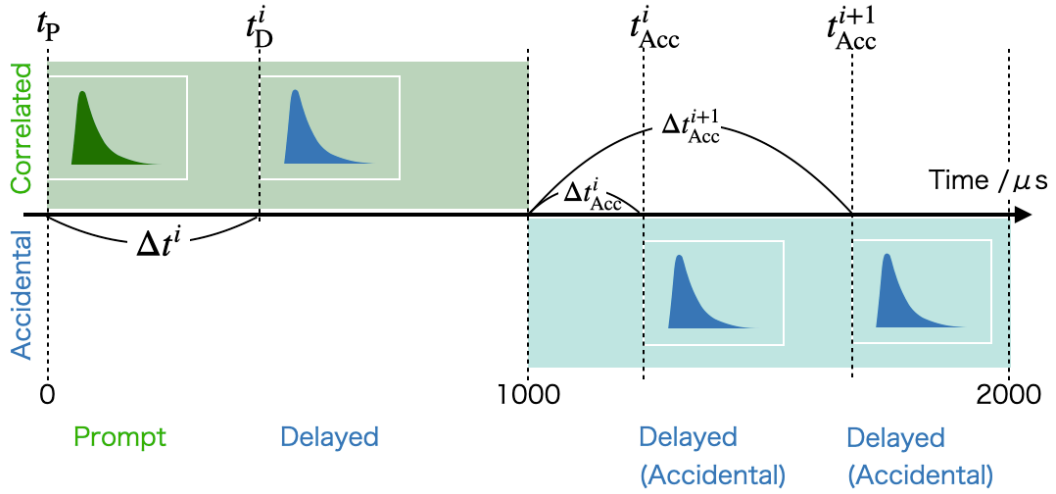


Figure 4.33: A schematic of delayed coincidence for correlated events. Accidental coincidence is estimated using off timing window.

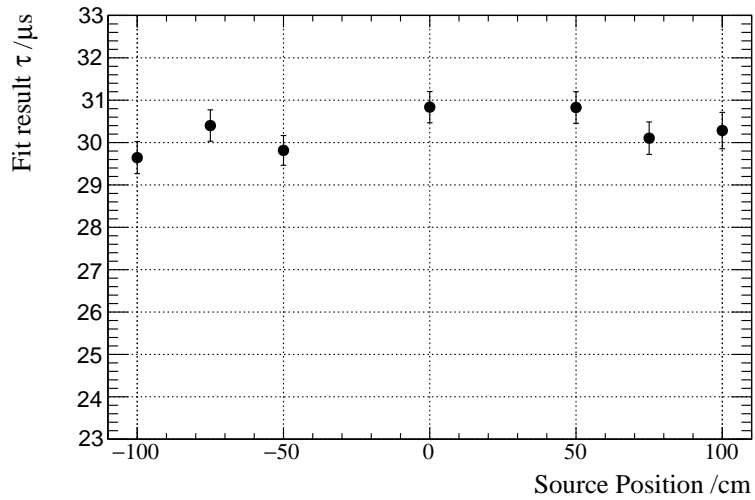


Figure 4.34: Time constant τ as a result of the fitting to the Δt_{p-d} distribution with an exponential function at each source position. They are in agreement within 2 % each other.

with an equation used in [48, 49] as

$$\text{resolution} \equiv \frac{\sigma_E}{E_{\text{vis}}^{\text{ID}}} = \sqrt{\frac{p_0^2}{E_{\text{vis}}^{\text{ID}}} + p_1^2 + \left(\frac{p_2}{E_{\text{vis}}^{\text{ID}}}\right)^2}, \quad (4.16)$$

where p_0 , p_1 and p_2 are fit parameters. The parameter p_1 represents a constant term which limits resolution in high photon statistics because of an integrated effect from electronics. The estimated constant terms at each position are listed in table 4.5. These values will be compared to a constant term estimation from Michel electron spectrum in order to investigate a consistency between the different energy ranges, i.e., around 8 MeV and from 20 to 60 MeV.

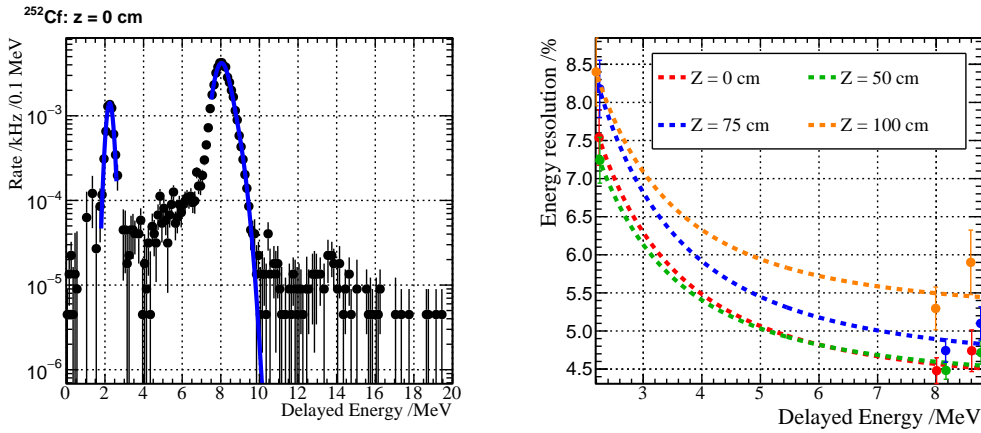


Figure 4.35: Left: the delayed energy spectrum with the nGd and nH peak fittings in case the source is at $Z = 0$ cm. Right: the energy resolution at each position as a function of the visible energy.

Table 4.5: The estimated constant term from the ^{252}Cf data.

^{252}Cf Source Position /cm	Constant term from fit /%
0	4.25 ± 0.12 %
50	4.29 ± 0.11 %
75	4.50 ± 0.16 %
100	5.19 ± 0.27 %

Data and MC comparison

The plots in Figs. 4.36 to 4.38 show comparisons between the data (black point) and the ^{252}Cf MC simulation (blue shaded area) about delayed visible energy (left) and $\Delta t_{\text{p-d}}$ (right) at each source position. The distributions of the data are accidental event subtracted spectra. The visible energy distributions show good agreement in the data and the MC simulation in each condition over the displayed range, except for the nH peak in case the source position is below the center (Fig. 4.38). This obviously shows an effect of low trigger efficiency around 2 MeV in the bottom half of the detector.

In order to investigate reproducibility of the MC simulation, the selection efficiency of delayed visible energy and that of Δt selection were compared between the

4.5. MEASUREMENT OF BACKGROUND RATE OF EACH COMPONENT 89

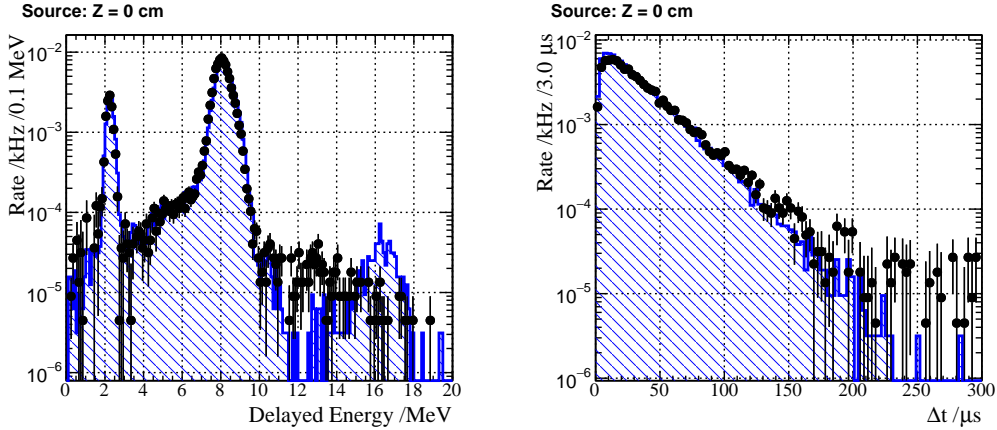


Figure 4.36: Delayed visible energy (left) and Δt distribution (right) at $z = 0$ cm. The black marker shows the data points after accidental subtraction. The blue shaded histogram is the MC simulation output.

data and the MC simulation. The left plot in Fig. 4.39 shows a comparison between delayed energy selection efficiencies estimated from the data (black) and from the MC simulation (blue) at each source position. The efficiency of the delayed energy selection decrease as approaching to the boundary due to nGd gamma ray escape from the inner detector. The efficiencies agree within at most 4 % each other at each position so that the MC simulation reproduce the delayed energy spectra including the gamma ray escape effect. The right plot in Fig. 4.39 shows a comparison between timing correlation selection efficiencies displayed in the same manner as the left plot. Both the data and the MC simulation shows that timing correlation selection efficiency is flat over the source position as indicated by the position dependence of the time constant in Fig. 4.34. The difference between the data and the MC is within ~ 1 % at each position so that giving a correction to the efficiency computed from the MC output makes this effect negligibly small.

The vertex reconstruction performance is to be examined by comparing the data and the MC simulation. Figure 4.40 separately exhibits distributions of x , y and z of the reconstructed vertex. Their black points correspond to histograms of the data, and the overlaid blue shaded histogram indicates that of the MC simulation in case of the source at $z = 0$ cm. All the three plots support reproducibility of the MC simulation to the data at $z = 0$ cm. In addition, z values of the reconstructed vertex in the data are compared to the MC output as a difference of mean value as a result of fitting with a gaussian distribution at each source position. The result is shown in Fig. 4.41 which displays the mean differences (vertical axis) as a function of the source position (horizontal axis), and it lead to an consistency between data and MC within ± 5 cm over the source positions.

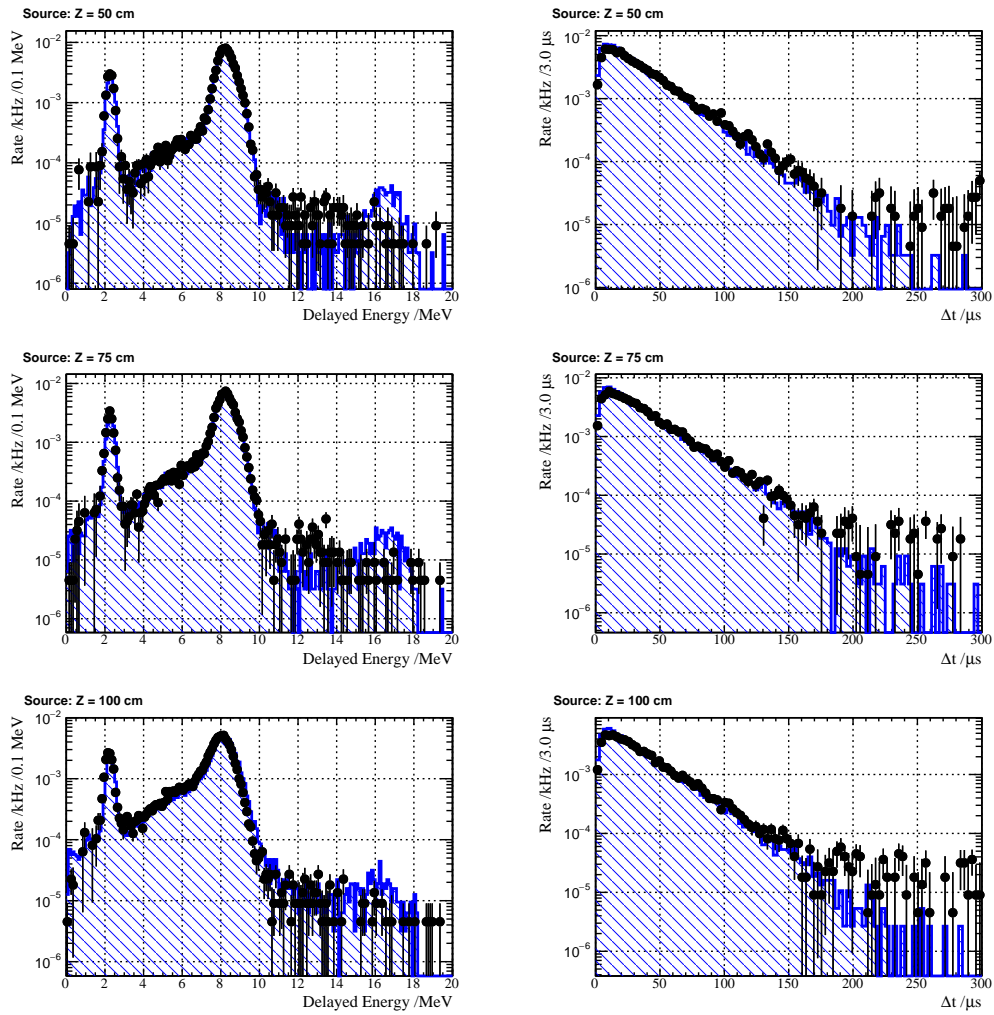


Figure 4.37: Delayed visible energy (left) and Δt distribution (right) at $z = +50$, $+75$, $+100$ cm from the top. The black marker shows the data, and the blue shaded area corresponds to the MC simulation output, respectively.

4.5. MEASUREMENT OF BACKGROUND RATE OF EACH COMPONENT 91

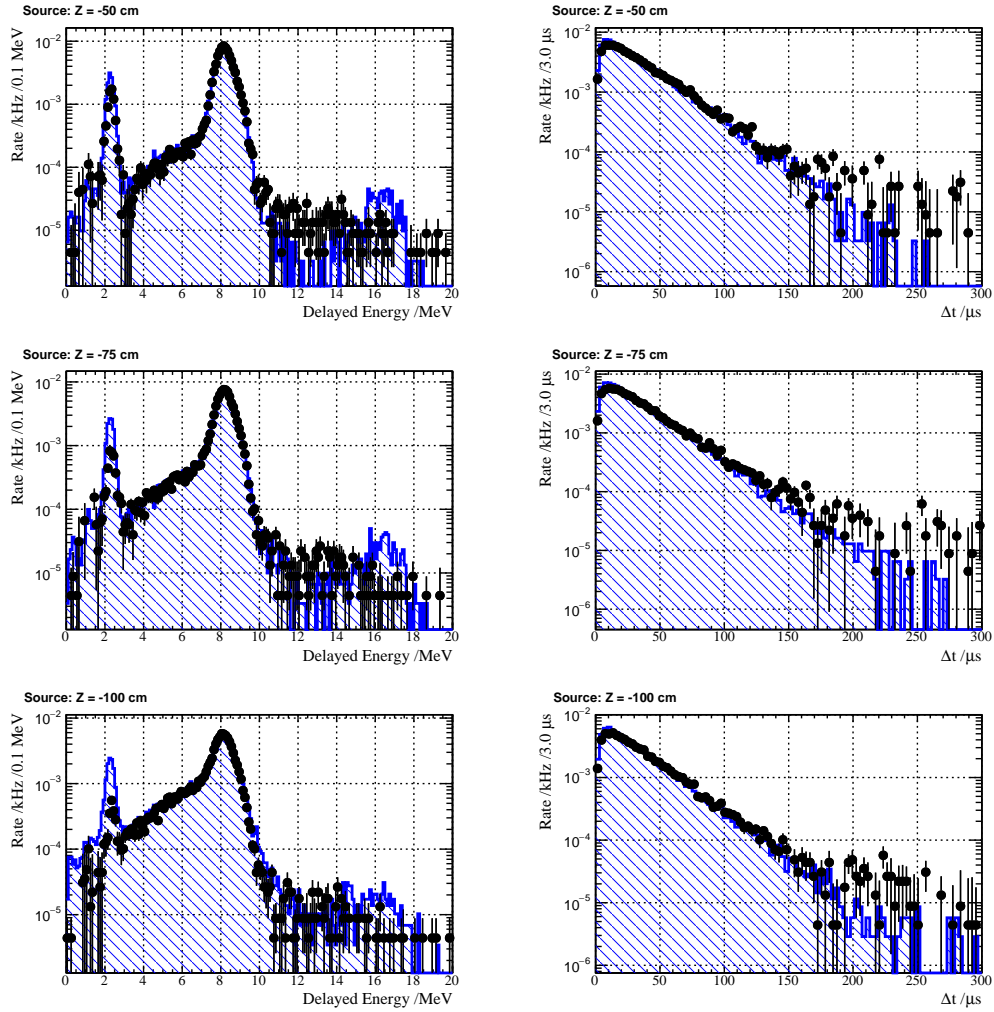


Figure 4.38: Delayed visible energy (left) and Δt distribution (right) at $z = -50, -75, -100$ cm from the top. The black marker shows the data, and the blue shaded area corresponds to the MC simulation output, respectively.

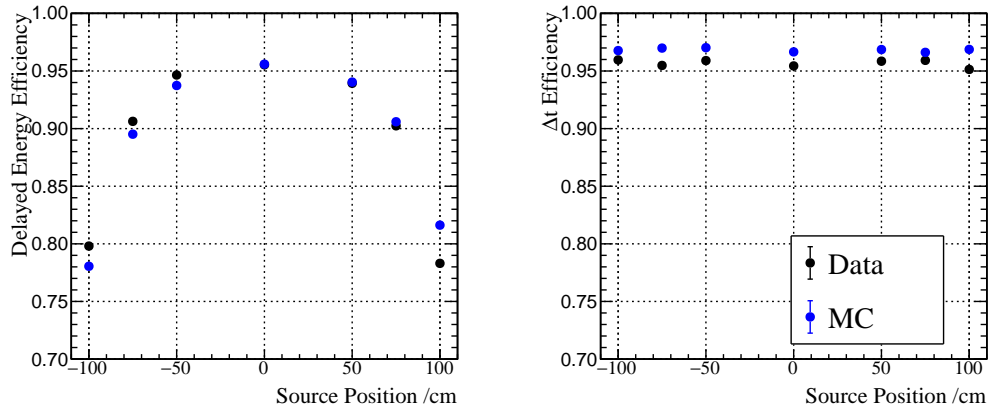


Figure 4.39: The selection efficiency of delayed visible energy (left) and that of Δt selection (right) at each source position. The efficiencies estimated based on the data (black) and the MC simulation (blue) are displayed simultaneously.

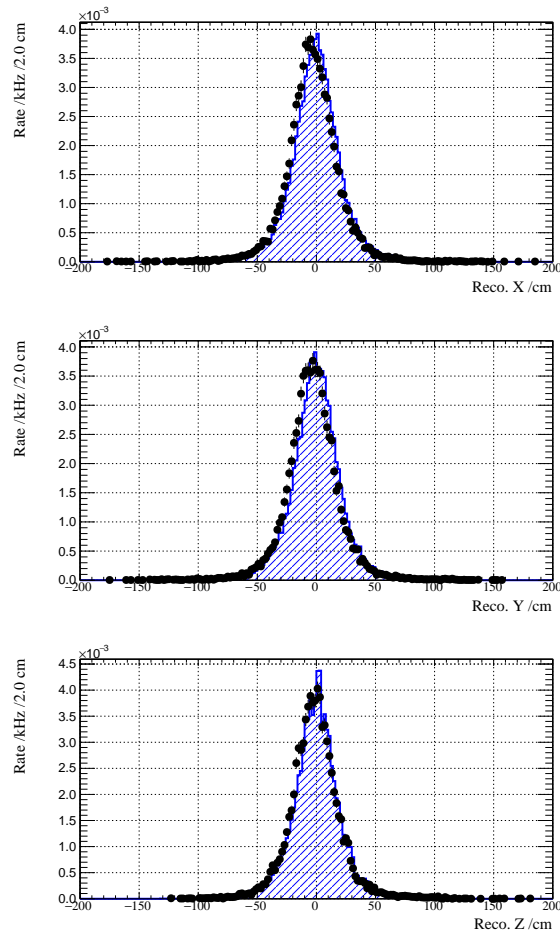


Figure 4.40: Comparisons of the reconstructed vertex between data and MC at $z = 0$ cm. Top: x, middle: y, bottom: z of the reconstructed vertex, respectively.

4.5. MEASUREMENT OF BACKGROUND RATE OF EACH COMPONENT 93

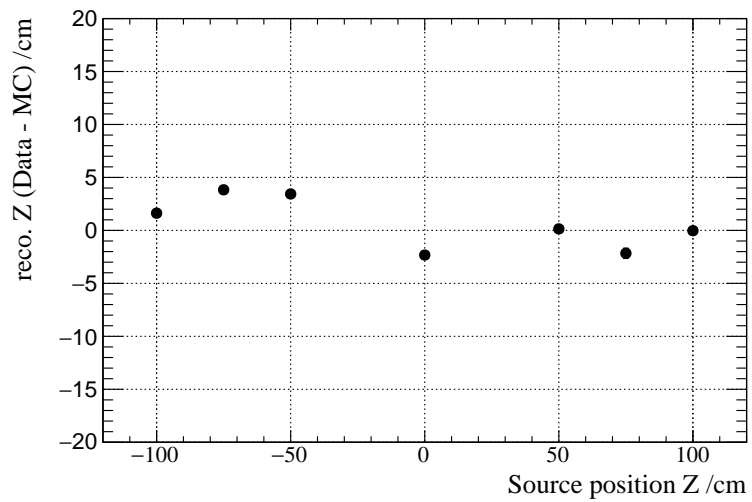


Figure 4.41: Difference of reconstructed vertex between data and MC about z at various source positions. They agreed with each other within \pm cm difference over the range.

4.5.3 Michel electron

As described above, Michel electron is one of the accidental background components in the IBD prompt region. Thus, an event rate of Michel electron in the detector has to be estimated. The following selection criteria are applied for Michel electron events;

- Prompt signal
 - visible energy: $10 < E_{\text{vis}}^{\text{ID}} < 800$ MeV,
- Delayed signal
 - Offline muon veto: $Q_{\text{total}}^{\text{Veto}} < 100$ p.e. & $E_{\text{vis}}^{\text{ID}} < 400$ MeV
 - visible energy: $20 < E_{\text{vis}}^{\text{ID}} < 60$ MeV,
- Timing correlation between prompt and delayed signals: $\Delta t_{\text{p-d}} < 10$ μs ,
- Spacial correlation between prompt and delayed signals: $\Delta VTX_{\text{p-d}} < 150$ cm.

Figure 4.42 shows distributions of each variable to which all selections are applied except for the selection to itself in the same manner as Fig. 4.32. The ranges of each selection are displayed as the red dashed boxes. Because cosmic muon intruding from the chimney gives no activity in the veto layer, the muon tagging condition is insufficient to identify such a muon if it stopped in the detector. Therefore, $10 < E_{\text{vis}}^{\text{ID}} < 800$ MeV was selected for the prompt signal to be independent of the veto activity. The diameter of the inner detector is 3.9 m so that the range can cover muons stopped with long traversing path in the detector. The spacial and timing correlation cuts were applied loosely enough to obtain more than 99 % efficiency. As a result of the selections, the event rate in the energy range of 20 - 60 MeV is measured to be 93.5 ± 0.8 Hz, which is estimated from the delayed visible energy spectrum after accidental background subtraction (black histogram of the top right plot).

There are 3 peaks in the veto charge spectrum (bottom right) corresponding to structures caused by minimum ionizing particle (MIP). The central (around ~ 500 p.e.) and right ones (around ~ 1000 p.e.) correspond to energy loss in the top layer with 25 cm thickness and in the barrel layer with 45 cm thickness, respectively. The left one at ~ 250 p.e. appears due to the saturation effect at dynamic range of the FADC as we only recorded high gain waveforms for the veto PMTs. Despite the saturation effect the offline veto threshold (100 p.e.) can tag 95.3 % of muons which generate Michel electron in 20 - 60 MeV range. It is possible to improve the tagging efficiency by covering the chimney with plastic scintillator plates.

Figure 4.43 shows Δt distribution interpreted as a time constant of muon decay in the scintillator. The fitting result with exponential function (blue line) lead to the time constant $\tau_{\mu} = 2.09 \pm 0.02$ μs . The shorter time constant compared to muon lifetime in vacuum is because of a matter effect on negative muon. The observed lifetime of muon in matter can be written down in

$$\tau_{\text{obs}} = (1 + \rho) \frac{\tau^{-} \tau^{+}}{\tau^{+} + \rho \tau^{-}}, \quad (4.17)$$

4.5. MEASUREMENT OF BACKGROUND RATE OF EACH COMPONENT 95

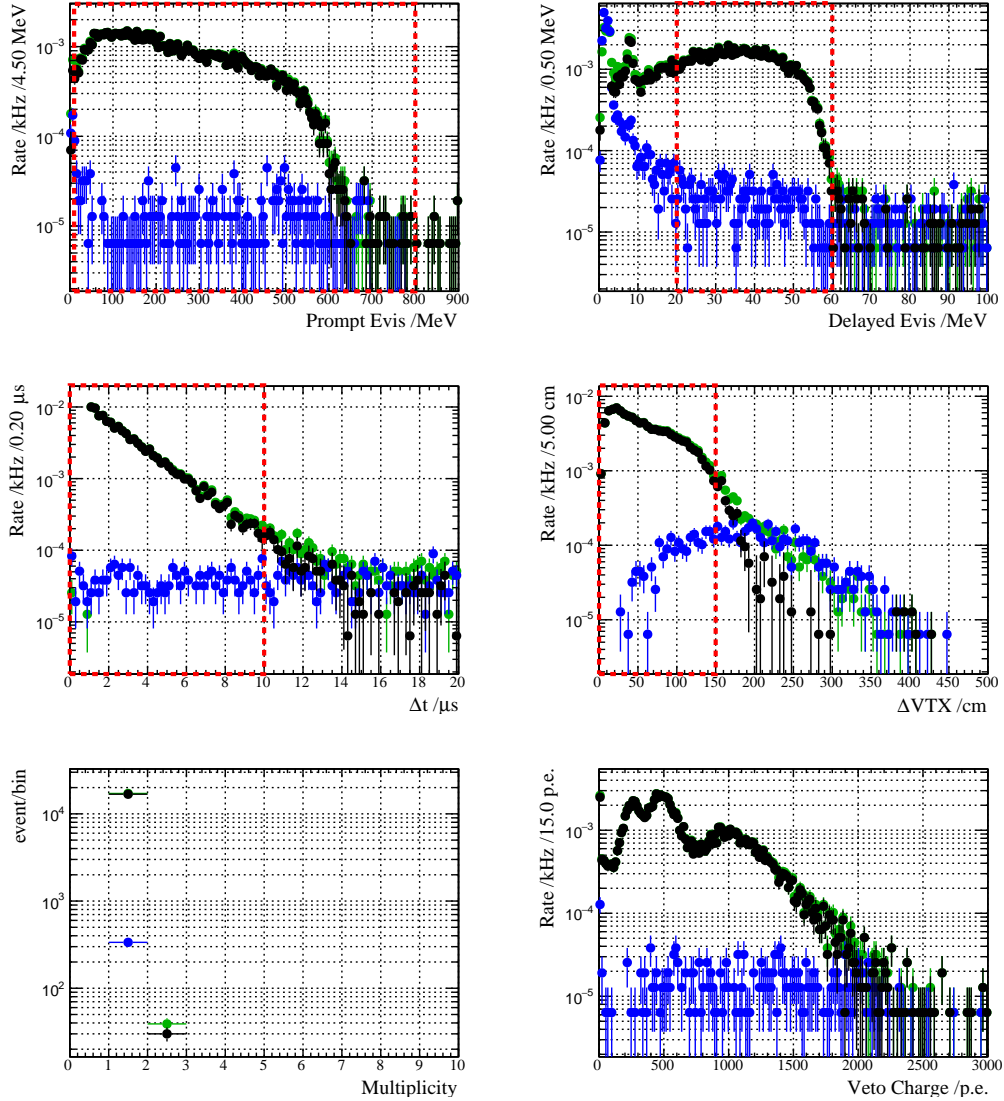


Figure 4.42: Delayed coincidence for Michel electron selection. Top left: prompt visible energy. Top right: delayed visible energy. Middle left: Δt_{p-d} . Middle right: ΔVTX_{p-d} . Bottom left: multiplicity of delayed signal. Bottom right: total charge in the veto layer. Each distribution of variable is applied all selections except for the selection to itself. The red boxes show the selection criterion to each variable. The green marker corresponds to correlated event candidates, and the blue one shows the estimated accidental coincidence events. The accidental subtracted distribution is displayed as the black marker in the plots.

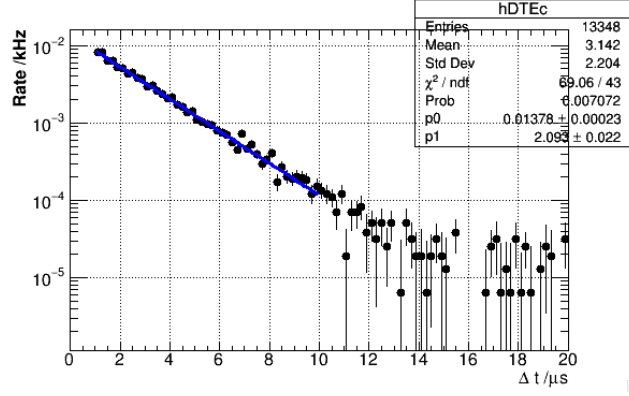


Figure 4.43: Fitting result to Δt_{p-d} distribution with an exponential function exhibited as the blue line. The black marker shows the accidental-subtracted histogram identical with the middle left plot in Fig. 4.42.

where ρ is the charge ratio of cosmic muon, and τ^\pm is the lifetime of positive and negative muon in matter. Using the effective lifetime of negative muon in carbon $\tau_G^- = 2.043 \mu\text{s}$ [51] instead and assuming the lifetime of positive muon is same as the free space lifetime value $\tau_\mu = 2.2 \mu\text{s}$, the observed lifetime is $\tau_{\text{obs}} \sim 2.1 \mu\text{s}$ by hand calculation, where $\rho = 1.28$ [52] is assumed.

Data and MC comparison

Reproducibility of the MC simulation to the data is also checked with Michel electron. The constant term of energy resolution was independently estimated in data-MC comparison of the Michel electron energy spectrum. Fiducialization is done by applying $|z| < 100 \text{ cm}$ and $r < 120 \text{ cm}$ in addition to the Michel electron selection in order to avoid energy spectrum distortion due to energy deposition to the acrylic vessel. The spectrum of the MC simulation is folded with a gaussian distribution with $\sigma = c \times E_{\text{vis}}$ where c represents a constant term. χ^2 fitting with the range from 20 to 60 MeV was done to explore the best fit value. Figure 4.44 shows the best fit spectrum (blue line) compared to the data (black markers) at constant term $c = 4.61 \%$ with $\chi^2/\text{n.d.f.} = 1.14$ (left) and the $\Delta\chi^2$ curve for error estimation. The estimated constant term from the Michel electron spectrum is $4.61^{+0.20}_{-0.18} \%$. The result shows an intermediate value between the constant terms estimated from ^{252}Cf data in table 4.5 so that it can be interpreted as the averaged value over the target volume.

Figure 4.45 shows comparisons between the data and the MC simulation of Michel electron about visible energy (top left), vertex Z (top right), $\rho = \sqrt{x^2 + y^2}$ (bottom left) and $R = \sqrt{x^2 + y^2 + z^2}$ (bottom right). The sharp edge in the z and the ρ distribution represents the fiducialization cut. Note that the peak around 8 MeV appears in the energy spectrum because the selection can contain correlated events caused by fast neutron which is thermalized and captured within $10 \mu\text{s}$. One can find that the vertex distributions of the data and that of the MC simulation shows a good agreement with each other as well as the visible energy distribution.

4.5. MEASUREMENT OF BACKGROUND RATE OF EACH COMPONENT 97

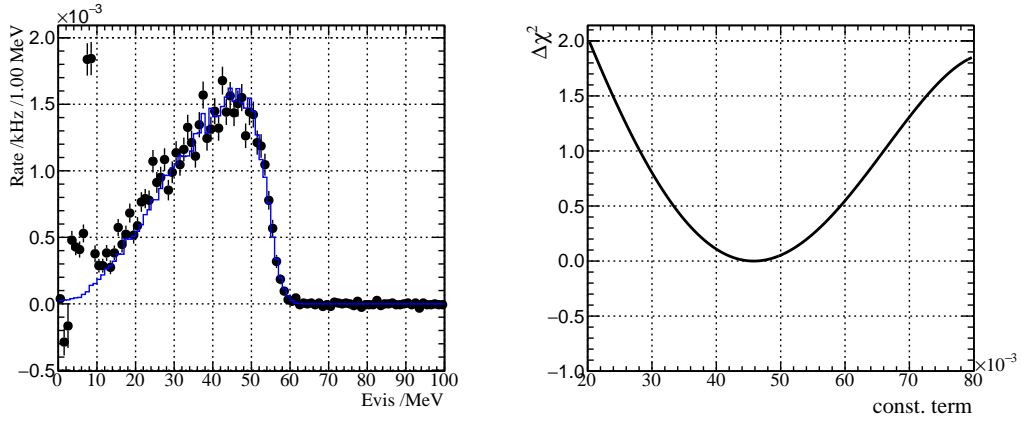


Figure 4.44: Left: the fitting result (blue line) to the Michel electron spectrum obtained from the data (black markers). Right: $\Delta\chi^2$ curve of the fitting. The estimated constant term is $4.61^{+0.20}_{-0.18}$ %, which can be interpreted as an averaged value over the target volume.

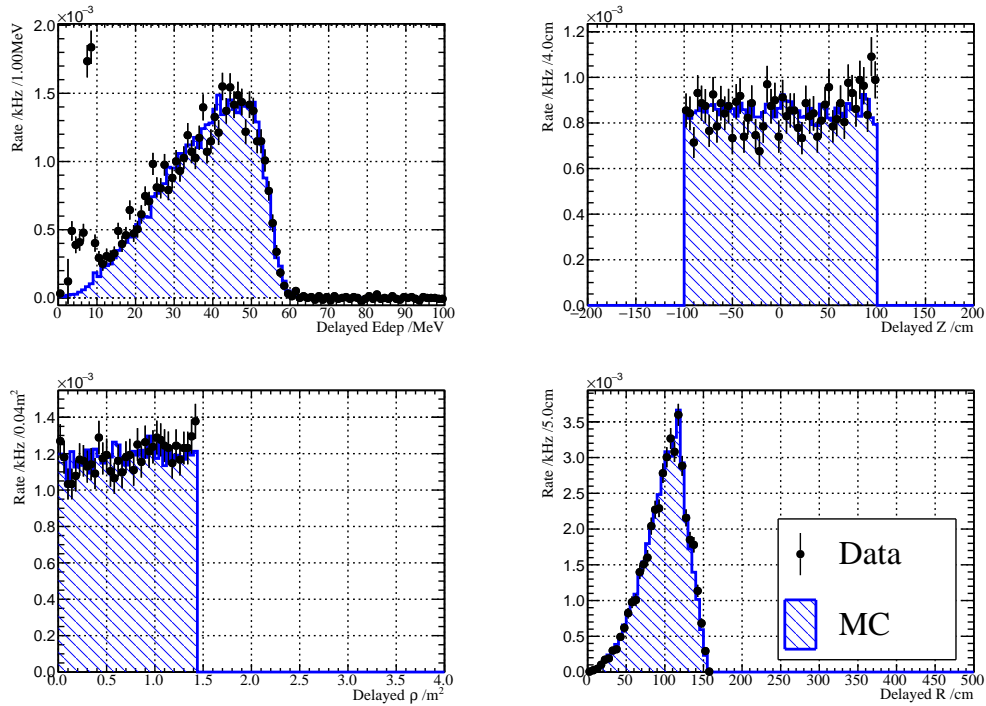


Figure 4.45: Comparative plots of Michel electron events between data and MC simulation. Top left: the visible energy spectrum. Top right: Z distribution. Bottom left: $\rho = \sqrt{x^2 + y^2}$ distribution. Bottom right: $R = \sqrt{x^2 + y^2 + z^2}$ distribution. The black marker shows spectrum of the accidental-subtracted data, and the blue shaded area is that of the MC simulation.

4.5.4 Cosmic-ray induced fast neutron

Cosmic fast neutron is the major correlated background which directly mimics IBD reaction in delayed coincidence. The event rate of fast neutron in the IBD selection is estimated in the following selection criteria;

- Offline muon veto for both prompt and delayed signals,
- Prompt visible energy: $20 < E_{\text{vis}}^{\text{ID}} < 60$ MeV,
- Delayed visible energy: $7 < E_{\text{vis}}^{\text{ID}} < 12$ MeV,
- Timing correlation between prompt and delayed signals: $\Delta t_{\text{p-d}} < 100$ μs ,
- Spacial correlation between prompt and delayed signals: $\Delta VTX_{\text{p-d}} < 60$ cm.

Figure 4.46 and Fig. 4.47 show distributions of each variable to which all selections are applied except for the selection to itself in the same manner as Fig. 4.32 in case of the online applied or not, respectively. The former was obtained using the self trigger without the online muon veto, the later was applied the online muon veto in contrast. The estimated event rates in the selection condition are 3.04 ± 0.14 Hz (without the online veto) and 3.18 ± 0.06 Hz (with the online veto), and therefore, they are consistent within the statistic error. The estimated rate $(2.70 \pm 0.05) \times 10^{-5}$ /spill is quite large compared to the expectation 1.4×10^{-6} /spill in reference [9, 30]. Lifetime cut, likelihood based selection using correlation with beam timing described in the next chapter, can reduce it in a factor of ~ 0.5 ; however, there still remains ~ 10 times larger. We have to deal with this background increase by hardware countermeasure in order to avoid signal detection efficiency reduction which directly affects sensitivity due to decrease in statistical significance of signal with respect to backgrounds.

The behavior of the cosmic fast neutron model as described in section 2.4.2 is tested by comparing with cosmic fast neutron MC simulation to the data. Figure 4.48 shows comparisons between the data (black marker) and the MC simulation output (blue shaded area) about prompt visible energy (top left), delayed visible energy (top right), timing correlation $\Delta t_{\text{p-d}}$ (middle left), spacial correlation $\Delta VTX_{\text{p-d}}$ (middle right), and multiplicity of the delayed signal (bottom left). The red dashed box in the plots display the IBD selection regions of each variable. One can find that the MC simulation consistently reproduced the prompt energy, the delayed energy, $\Delta t_{\text{p-d}}$ and $\Delta VTX_{\text{p-d}}$ distribution within the IBD selection region, respectively. A fitting with an exponential function to the $\Delta t_{\text{p-d}}$ distribution was performed for both the data and the MC simulation. The time constant as a result of the fit is 29.45 ± 0.99 μs for the data and 29.37 ± 0.76 μs for the MC simulation. They are consistent with each other as well as the time constant measured based on the ^{252}Cf data.

In addition to them, event vertex distributions are compared in the way of z (top), $\rho = \sqrt{x^2 + y^2}$ (middle) and $R = \sqrt{x^2 + y^2 + z^2}$ (bottom) in Fig. 4.49. The plots in the left hand side corresponds to the prompt signal, and ones in the right hand side shows the vertex distributions of the delayed signals. The MC simulation reproduces a behavior of the event vertex inclination towards $+z$ direction for both the prompt and the delayed signal, and thus, it indicates that the angular distribution assumed in the generator is well-modeled.

4.5. MEASUREMENT OF BACKGROUND RATE OF EACH COMPONENT 99

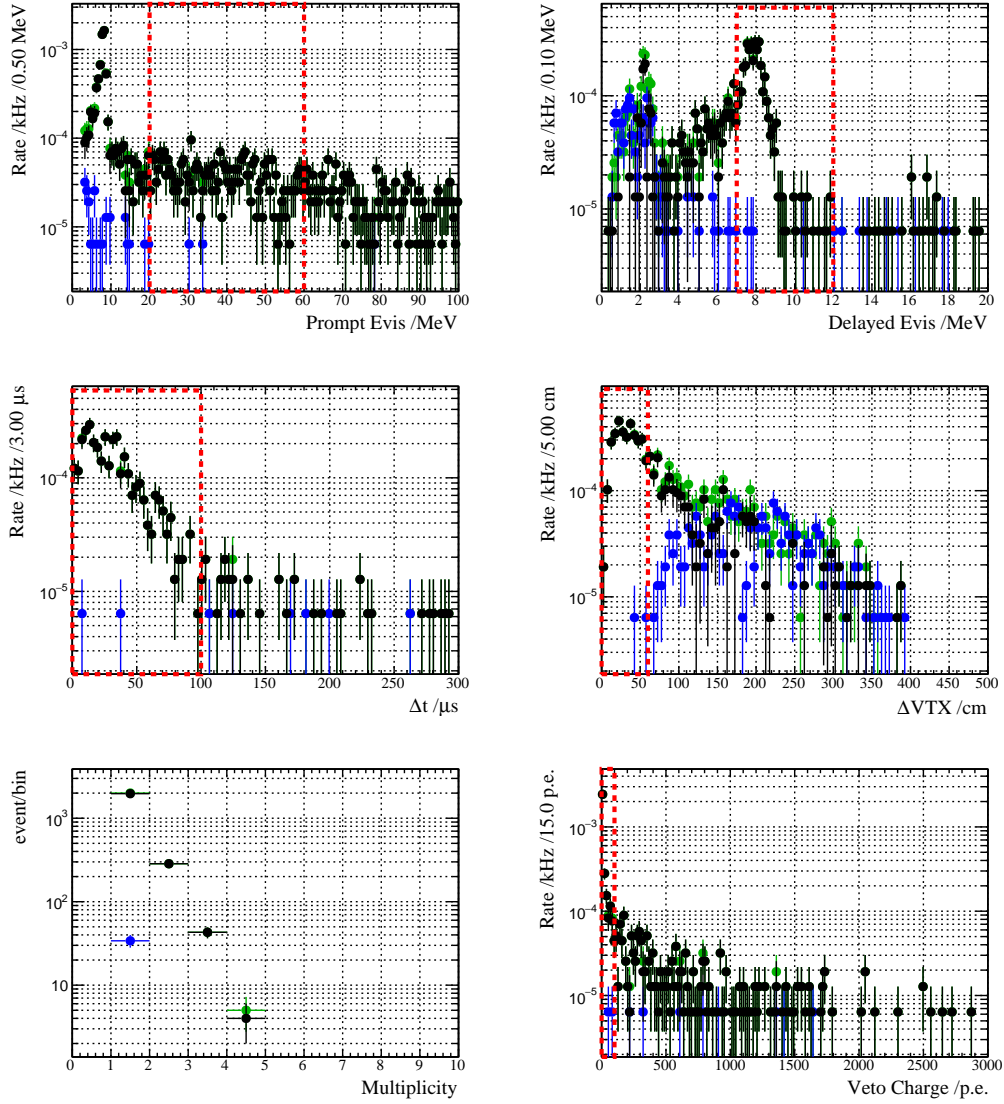


Figure 4.46: Delayed coincidence for cosmic fast neutron selection to the data obtained using the self trigger without the online veto. Top left: prompt visible energy. Top right: delayed visible energy. Middle left: Δt_{p-d} . Middle right: ΔVTX_{p-d} . Bottom left: multiplicity of delayed signal. Bottom right: total charge in the veto layer. Each distribution of variable is applied all selections except for the selection to itself. The red boxes show the selection criterion to each variable. The green marker corresponds to correlated event candidates, and the blue one shows the estimated accidental coincidence events. The accidental subtracted distribution is displayed as the black marker in the plots.

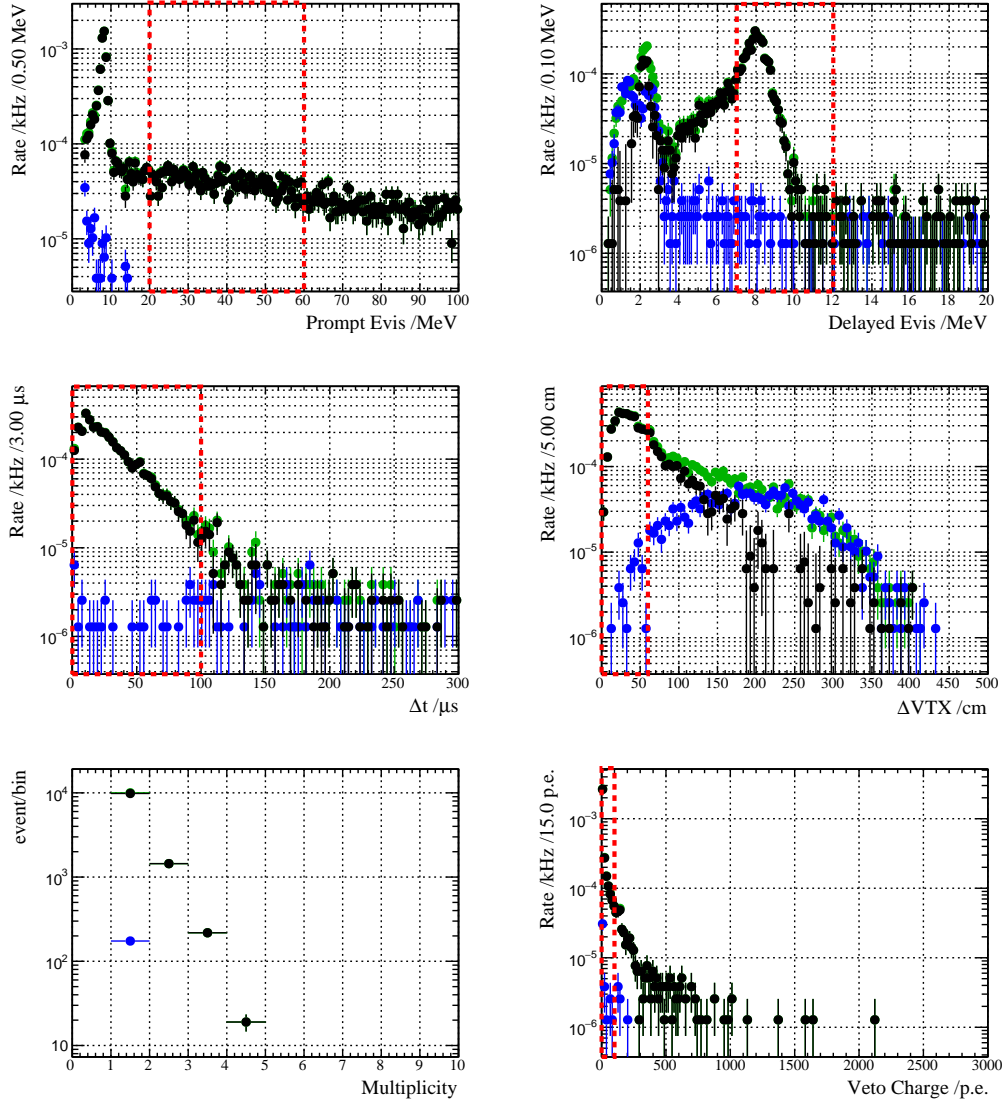


Figure 4.47: Delayed coincidence for cosmic fast neutron selection to the data obtained using the self trigger with the online veto. Top left: prompt visible energy. Top right: delayed visible energy. Middle left: Δt_{p-d} . Middle right: ΔVTX_{p-d} . Bottom left: multiplicity of delayed signal. Bottom right: total charge in the veto layer. Each distribution of variable is applied all selections except for the selection to itself. The red boxes show the selection criterion to each variable. The green marker corresponds to correlated event candidates, and the blue one shows the estimated accidental coincidence events. The accidental subtracted distribution is displayed as the black marker in the plots.

4.5. MEASUREMENT OF BACKGROUND RATE OF EACH COMPONENT 101

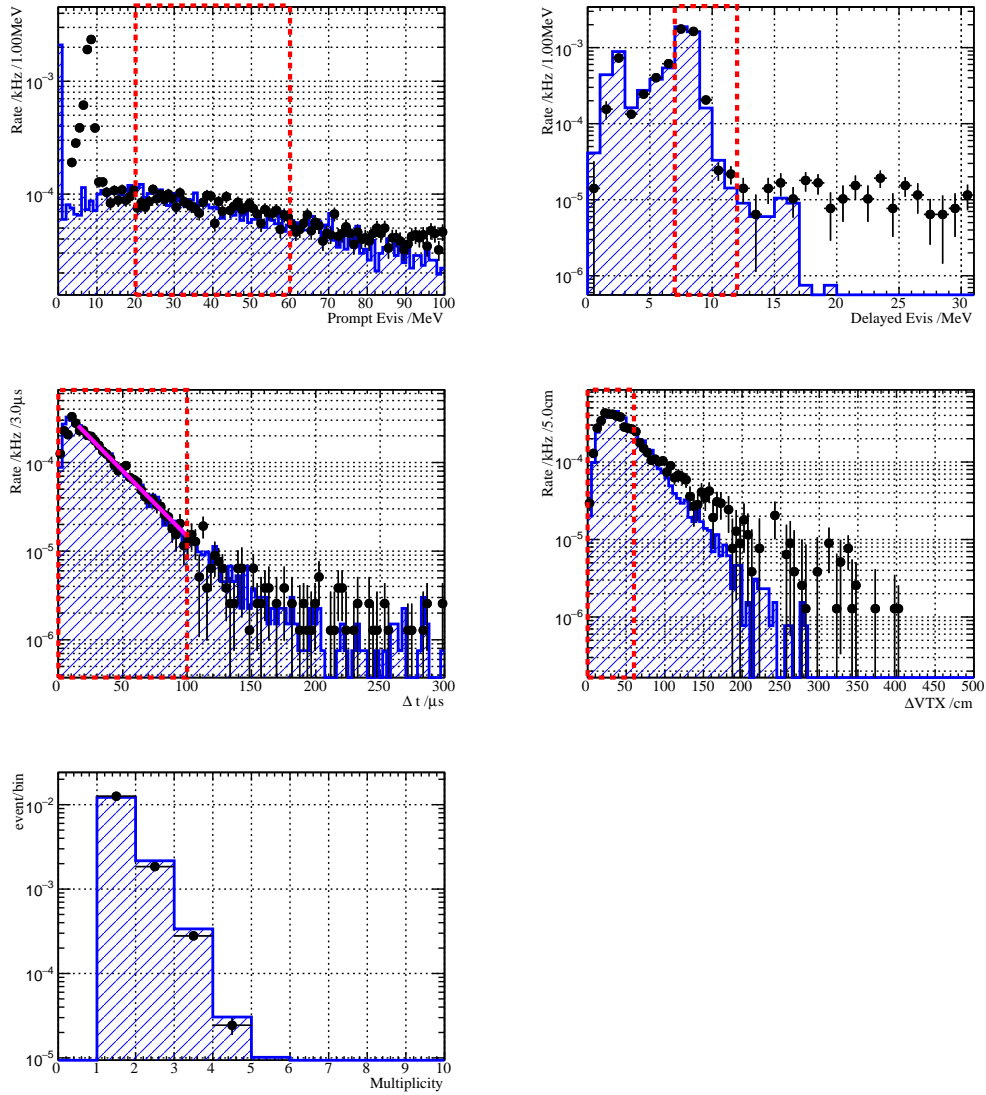


Figure 4.48: Distributions of prompt visible energy (top left), delayed visible energy (top right), Δt (bottom left), and ΔVTX (bottom right). The blue shaded area shows MC output of each variable overlaid with the data (black marker) in order to compare them.

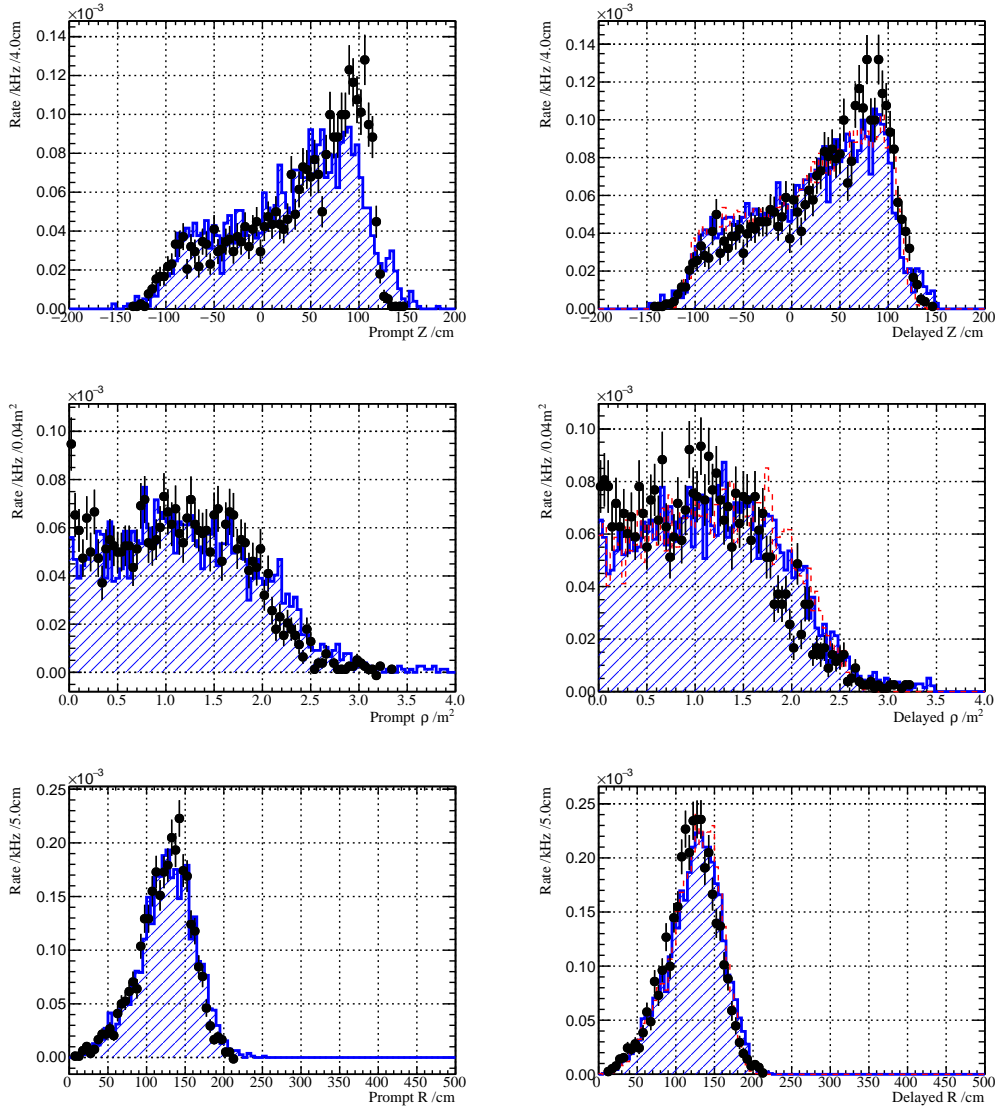


Figure 4.49: The event vertex distribution in the detector. The histograms of z , $\rho = \sqrt{x^2 + y^2}$ and $R = \sqrt{x^2 + y^2 + z^2}$ are placed in the order of the top to the bottom. The plots in the left hand side corresponds to the histogram of the prompt signal, and the plots in the right hand side shows that of the delayed signals, respectively. The blue shaded area shows MC output of each variable overlaid with the data (black marker) in order to compare them.

4.5.5 Cosmic ray induced gamma ray

Cosmic ray induced gamma ray (cosmic gamma) is one of the major accidental background component for both prompt and delayed signal of IBD. Its energy spectrum consists of two exponential components according to the background measurement in 2014 as described in section 2.4.2. The spectrum and event rate of cosmic gamma in the detector is measured by subtracting correlated events and cosmic muons from the single rate spectrum. The left plot of Fig. 4.50 shows the single rate spectrum (black marker) with each component. Cosmic muon (red shaded area) is selected by the inverted condition of the offline muon veto. For energy spectra of Michel electron (blue shaded area) and both prompt (magenta) and delayed signal (violet) of cosmic fast neutron, the accidental subtracted spectra of them in the same delayed coincidence condition except for $\Delta VTX_{p-d} < 150$ cm are used. $\Delta VTX_{p-d} < 150$ cm are applied to avoid selection inefficiency. In addition, there exists nGd from cosmic fast neutron whose prompt signal is classified as cosmic muon due to sufficient energy deposition to the veto layer. The delayed energy spectrum selected in below criteria is considered (orange area labeled as "Cosmic $\mu \rightarrow$ nGd") for the subtraction.

- Prompt signal
 - Cosmic muon tag: $Q_{\text{total}}^{\text{Veto}} > 100$ p.e. or $E_{\text{vis}}^{\text{ID}} > 400$ MeV,
- Delayed signal
 - Offline muon veto,
- Timing correlation between prompt and delayed: $10 < \Delta t_{p-d} < 100$ μ s,
- Spatial correlation between prompt and delayed: $\Delta VTX_{p-d} < 150$ cm.

The residual spectrum after the correlated and cosmic muon event subtraction is displayed in Fig. 4.50 (right) as light green markers. It is compared to the spectrum obtained using the MC simulation (blue shaded area). The MC spectrum was scaled to fit to the data spectrum based on χ^2 minimization. The definition of χ^2 is

$$\chi^2 = \left(\frac{R_i^{\text{Data}} - c \times R_i^{\text{MC}}}{\sigma_i^{\text{Data}}} \right)^2, \quad (4.18)$$

where R_i^{Data} and σ_i^{Data} are an event rate and an statistic error at i -th bin of the data spectrum respectively, and $c \times R_i^{\text{MC}}$ represents scaled entry at i -th bin of the MC spectrum. As a result of the fit, $\chi^2/\text{n.d.f.} = 1.48$ in the range of 5 to 60 MeV. Therefore, they show good agreement with each other above 5 MeV region which is appropriate energy range for the JSNS² signal. The event rates of cosmic gamma in the prompt and the delayed region were estimated from the residual spectrum as 51.8 ± 0.6 Hz and 82.4 ± 0.7 Hz, respectively. Compared to the expectation in reference [9], contribution to the prompt and delayed signal selection region is a factor of 1.2 and 1.9 times larger. Therefore, an effect of the increase in cosmic gamma contribution to the accidental background is relatively small in contrast to other accidental source, e.g., floor gamma described later.

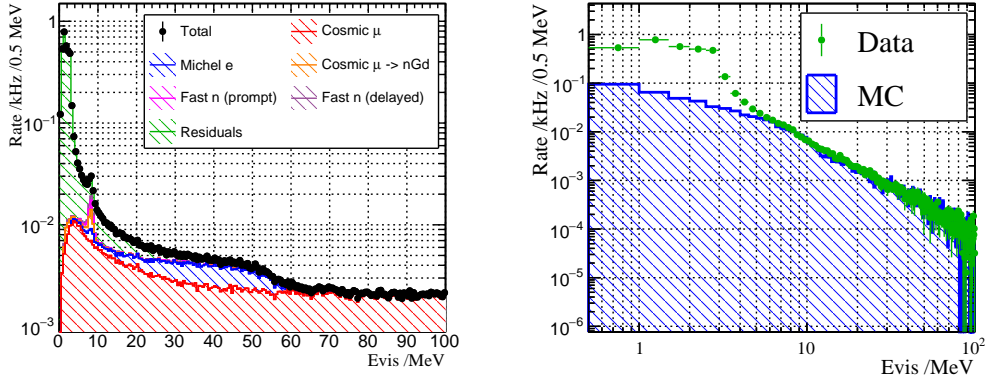


Figure 4.50: Left: the single rate energy spectrum in the beam off period (black marker) with its components classified by color. Right: the residual energy spectrum after subtraction (green marker) corresponding to the green shaded area in the left plot. The overlaid spectrum (blue shaded area) shows the MC simulation of cosmic gamma, and consistently agree with the residual spectrum from the data above 5 MeV.

4.5.6 Gamma ray from the surface of the hatch

As mentioned before, gamma ray from the surface of the hatch (floor gamma) is a source of accidental background for the IBD delayed signal, which is generated beneath the detector. The event rate of it in the IBD delayed signal window is estimated based on the data obtained using the kicker trigger because floor gamma exists in beam operation period. We had special runs to scan event rate in the time window of the delayed signal of the JSNS² signal using the kicker $10 \mu\text{s} + 10 \mu\text{s}$ DAQ. The run list to be used in following analysis is summarized in table 4.6.

Table 4.6: Run list for floor gamma estimation.

Run No.	Run Type	Gate Delay	$\Delta t / \mu\text{s}$
1416	Kicker ($10 \mu\text{s} + 10 \mu\text{s}$)	$0 \mu\text{s}$	3 - 7
1416	Kicker ($10 \mu\text{s} + 10 \mu\text{s}$)	$11 \mu\text{s}$	9 - 17
1405	Kicker ($10 \mu\text{s} + 10 \mu\text{s}$)	$30 \mu\text{s}$	29 - 37
1408	Kicker ($10 \mu\text{s} + 10 \mu\text{s}$)	$50 \mu\text{s}$	48 - 57
1409	Kicker ($10 \mu\text{s} + 10 \mu\text{s}$)	$70 \mu\text{s}$	68 - 77
1410	Kicker ($10 \mu\text{s} + 10 \mu\text{s}$)	$90 \mu\text{s}$	88 - 97

Beam-related neutron coming into the detector in the on-bunch timing makes nGd event if it is thermalized in the detector. Therefore, nGd event subtraction is performed in order to estimate floor gamma event rate. It can be extracted using delayed coincidence selection with an event in the on-bunch timing:

- Prompt signal as the on-bunch activities
 - Timing from beam: $0 < \Delta t_{\text{beam-p}} < 1.6 \mu\text{s}$,
 - Visible energy: $1 < E_{\text{vis}}^{\text{ID}} < 200 \text{ MeV}$,
- Delayed signal

4.5. MEASUREMENT OF BACKGROUND RATE OF EACH COMPONENT 105

- Offline muon veto same as above,
- Visible energy: $7 < E_{\text{vis}}^{\text{ID}} < 12$ MeV,
- Timing correlation between on-bunch and delayed: listed in table 4.6,
- Spacial correlation between on-bunch and delayed: $\Delta VTX_{\text{p-d}} < 110$ cm.

In contrast to the delayed coincidence selection to the natural background, e.g., cosmic fast neutron, the selection to correlation with beam timing is applied as well. Figure 4.51 shows correlations between event timing and energy of the prompt signal (left) and delayed signal (right). The prompt timing and energy correlation shows a double bunch cluster in the beam on-bunch region ($\approx 2 \mu\text{s}$), which reflects double bunch structure of proton beam. Tagging inefficiency of on-bunch neutron leads to an increase in the nGd events contributing to the accidental background in the IBD delayed signal region. Thus, the energy threshold to the prompt energy is set to 1 MeV. The selection criteria to the prompt signal and the delayed signal are displayed as a red dashed boxes in each plot, respectively.

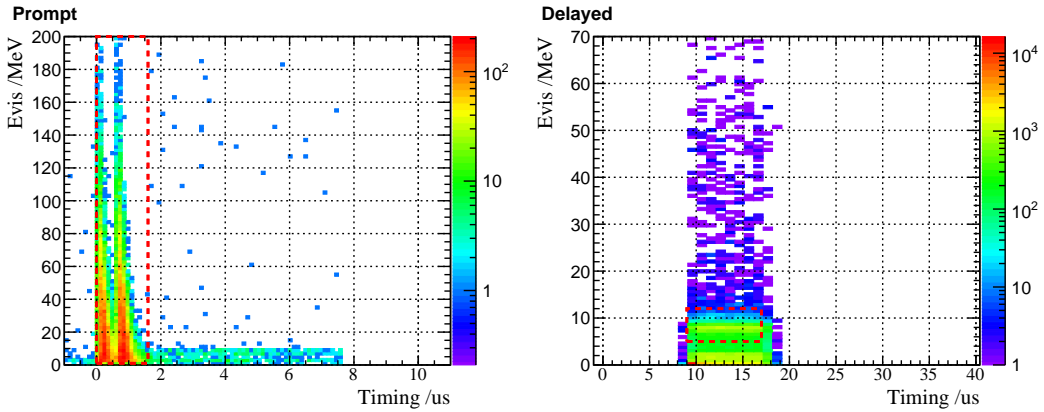


Figure 4.51: Left: Correlation between visible energy and event timing of the prompt signal. Right: Correlation between visible energy and event timing of the delayed signal. The origin of the horizontal axes in each plot are set to the beam timing. The red dashed boxes show the selection criteria to the prompt and the delayed signal, respectively.

Figure 4.52 shows distributions of each variable: the prompt visible energy (top left), the delayed visible energy (top right), timing correlation $\Delta t_{\text{p-d}}$ (middle left), spacial correlation $\Delta VTX_{\text{p-d}}$ (middle right), multiplicity of the delayed signal (bottom left) and total veto charge (bottom right). The ranges of each selection are displayed as the red dashed boxes. As shown in table 4.6, the selection criteria to the $\Delta t_{\text{p-d}}$ is set to the range corresponds to the second $10 \mu\text{s}$ FADC window. The $\Delta VTX_{\text{p-d}}$ selection criteria is determined according to the reference [9].

Figure 4.53 shows the prompt vertex (left) and the delayed vertex distribution (right) in the XY plane. Both prompt and delayed vertex locally distributes in $Y \approx 0$ cm region. This reflects the fact that the mercury target exists in the +Y direction.

The delayed visible energy spectrum is used for nGd event subtraction from a single rate spectrum in the later $10 \mu\text{s}$ window with the same timing width as the

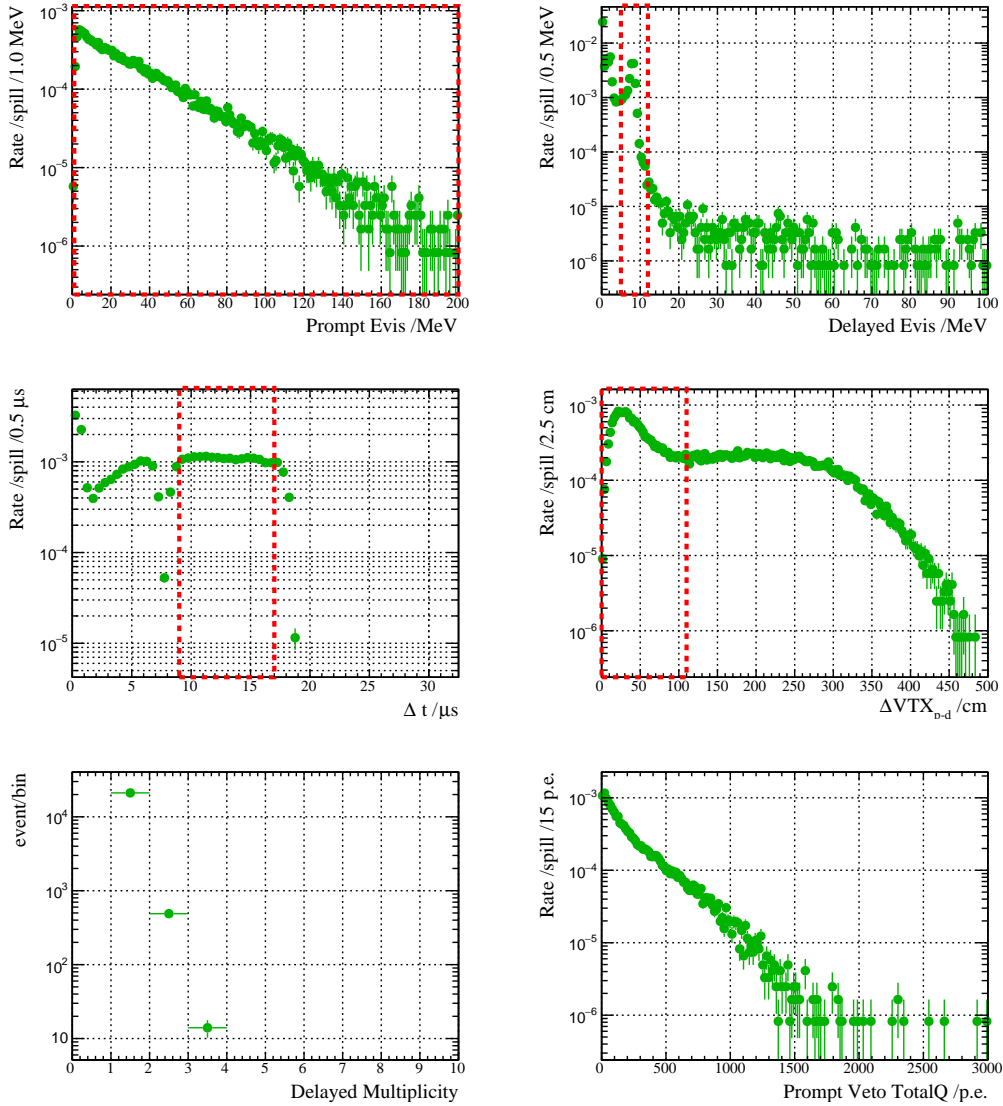


Figure 4.52: Delayed coincidence for nGd events correlated to on-bunch neutron in run 1416. Top left: prompt visible energy. Top right: delayed visible energy. Middle left: Δt_{p-d} . Middle right: ΔVTX_{p-d} . Bottom left: multiplicity of delayed signal. Bottom right: total charge in the veto layer. Each distribution of variable is applied all selections except for the selection to itself. The red boxes show the selection criterion to each variable. The green marker corresponds to correlated event candidates, and the blue one shows the estimated accidental coincidence events. The accidental subtracted distribution is displayed as the black marker in the plots.

4.5. MEASUREMENT OF BACKGROUND RATE OF EACH COMPONENT 107

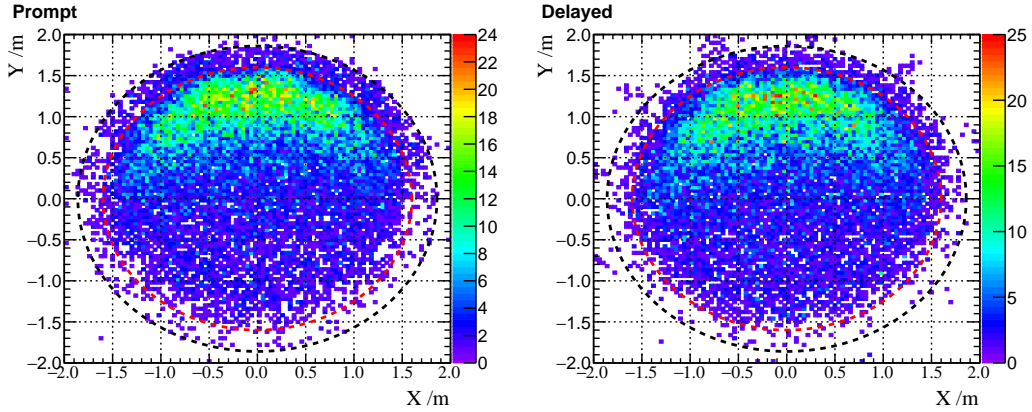


Figure 4.53: The prompt vertex (left) and the delayed vertex distribution (right) in the XY plane. The biased vertex distributions in $y > 0$ cm region reflects the incoming direction of beam on-bunch fast neutron. The mercury target exists in the $+y$ direction in the detector coordinate.

Δt selection. Figure 4.54 shows nGd event subtraction from single rate spectrum in run 1416. The left plot displays full range of the histograms where the black marker shows the single rate spectrum, the green one corresponds to the delayed energy spectrum in Fig. 4.52. The result of the subtraction is shown as the blue histogram. One can find that the peak at 8 MeV in the single rate spectrum disappeared after the subtraction. The right plot shows the zoomed spectrum of the left one in 0 to 30 MeV range.

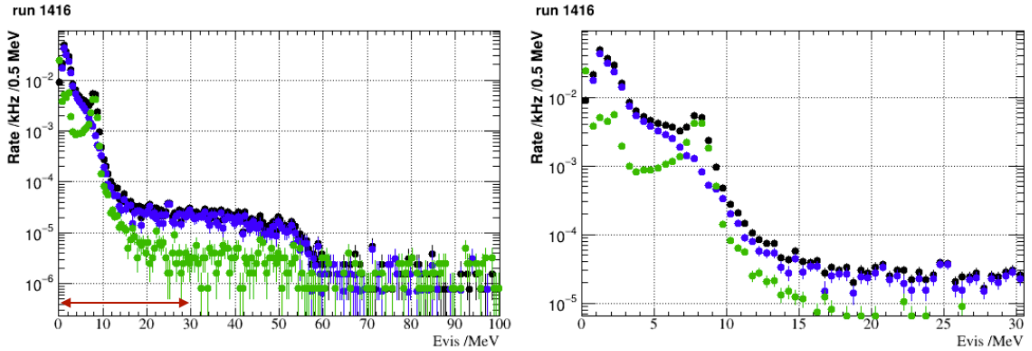


Figure 4.54: The nGd event subtraction from single rate spectrum in run 1416 for example. Left: all range. Right: zoomed into the red arrow region in the left plot.

The same analysis is applied to the other runs listed in table 4.6, and the obtained spectra for all runs after subtraction are shown in Fig. 4.55 as the black marker histogram in each plot. The blue, green and red shaded spectra overlaid in each plot correspond to the MC simulation output of floor gamma, Michel electron and cosmic gamma, respectively. Normalization of the MC spectra about Michel electron and cosmic gamma are done using the measured event rate in 20 - 60 MeV, and it demonstrates reproducibility in the kicker trigger data. The floor gamma spectrum of the MC simulation also agrees with that of the data.

The event rate in 7 to 12 MeV for each runs are summarized in table 4.7. Be-

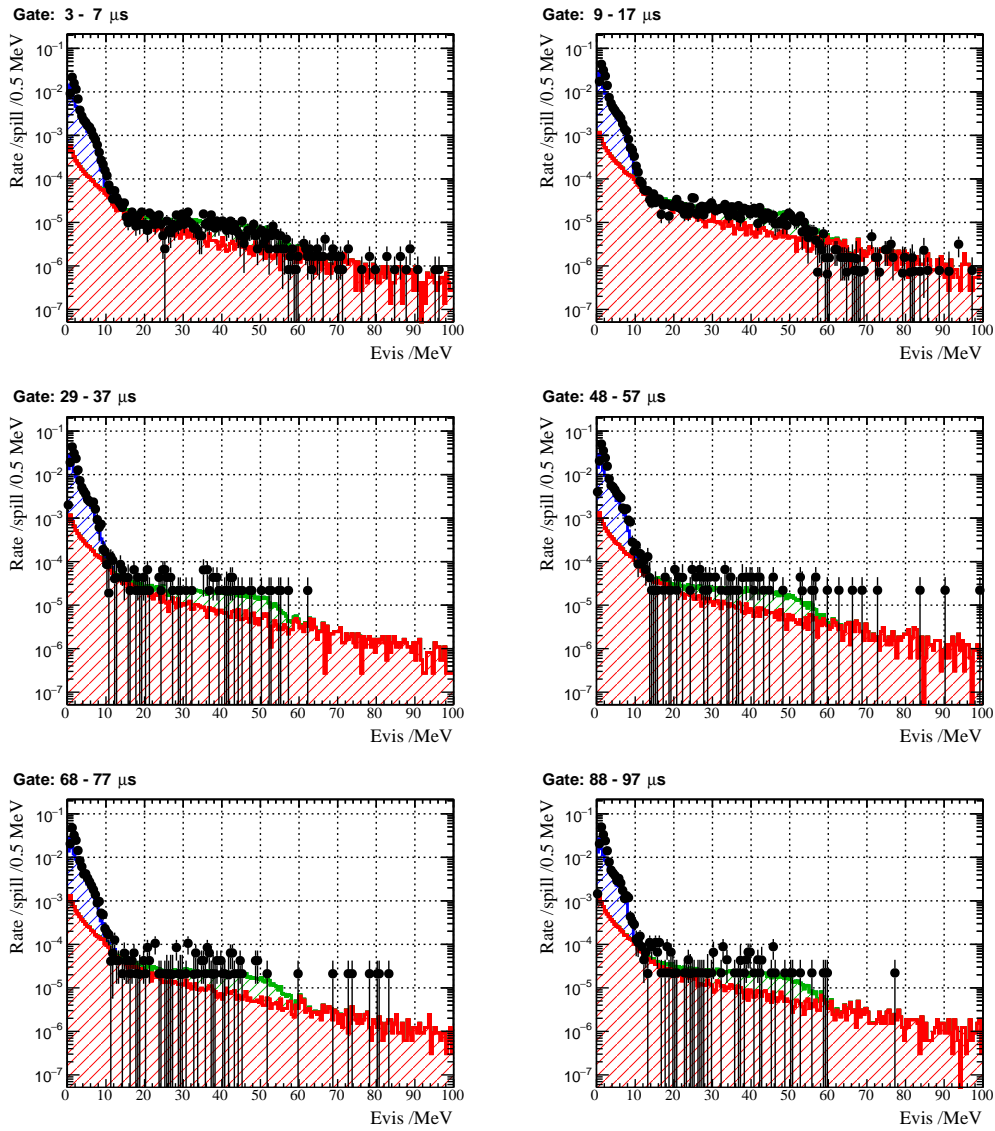


Figure 4.55: The nGd event subtracted spectrum (black marker) for all runs listed in table 4.6. The spectrum shape is described by floor gamma (blue shaded area), cosmic gamma (red shaded area) and Michel electron (green shaded area) in the range of 4 to 100 MeV.

cause cosmic gamma event contributes to the rate, the event rate of floor gamma is estimated as $(5.35 \pm 0.22) \times 10^{-2}$ /spill/100 μ s equivalent to 0.535 ± 0.022 kHz, and is 44.5 times as large as 1.2×10^{-3} /spill/100 μ s in reference [9]. It indicates that the capability of the shield in the current configuration is insufficient compared to the configuration in the reference, covering entire area of the hatch with 12.5 cm lead. Therefore, we need to consider an efficient way of reinforcing the shield capability.

Table 4.7: The results of floor gamma estimation for each run.

Run No.	Event rate in 7 -12 MeV /spill/100 μ s	Gate range
1416	$(6.85 \pm 0.26) \times 10^{-2}$	3 - 7
1416	$(6.62 \pm 0.20) \times 10^{-2}$	9 - 17
1405	$(5.72 \pm 0.82) \times 10^{-2}$	29 - 37
1408	$(6.60 \pm 0.60) \times 10^{-2}$	48 - 57
1409	$(5.50 \pm 0.55) \times 10^{-2}$	68 - 77
1410	$(5.74 \pm 0.48) \times 10^{-2}$	88 - 97
ave.	$(6.17 \pm 0.22) \times 10^{-2}$	-

4.6 Event rate in the signal window

The background rates uncorrelated to beam timing, e.g., cosmic ray induced component and floor γ , were estimated in the previous section. In this section, the actual background rate in the signal window corresponding to the region in 1.5 to 10 μ s from beam timing is estimated based on the full dataset taken using the kicker 25 μ s (as listed in table 4.8). The total number of beam spill is amount to 8092503 corresponding to 3.5 days.

Table 4.8: Run list for event rate estimation.

Run No.	Run Type	Total spill
1427	Kicker (25 μ s)	1516628
1458	Kicker (25 μ s)	3069861
1461	Kicker (25 μ s)	954803
1479	Kicker (25 μ s)	2551211
Total	-	8092503

4.6.1 Estimation of Event rate in the signal window

The selection shown below is applied to the beam data as following the IBD selection described above.

- Prompt signal
 - Offline muon veto,
 - No muon 5 μ s before prompt signal,
 - timing from beam: $1.5 < \Delta t_{\text{beam-p}} < 10$ μ s,
 - visible energy: $20 < E_{\text{vis}}^{\text{ID}} < 60$ MeV.

- Delayed signal
 - Offline muon veto,
 - visible energy: $7 < E_{\text{vis}}^{\text{ID}} < 12$ MeV,
 - Correlation between delayed and on-bunch if exists: $\Delta VTX_{\text{OB-d}} > 110$ cm.
- Timing correlation between prompt and delayed: $\Delta t_{\text{p-d}} < 25$ μs ,
- Spacial correlation between prompt and delayed: $\Delta VTX_{\text{p-d}} < 60$ cm.

There are two conditions newly applied. The first condition is to eliminate Michel electron events in the prompt signal region by applying 5 μs veto time after muon events. On-bunch fast neutrons cause mis-identification of cosmic muon so that no muon discrimination is performed in the on-bunch timing window (0 - 1.5 μs after the beam timing). The veto time width overlapping with the signal window can be written down as a function of muon event timing t_μ ;

$$W^{\text{veto}}(t_\mu) = \begin{cases} (t_\mu + 5) - 1.5 & (-2 < t_\mu < 0 \text{ } \mu\text{s}), \\ 0 & (0 < t_\mu < 1.5 \text{ } \mu\text{s}), \\ 5 & (1.5 < t_\mu < 5 \text{ } \mu\text{s}), \\ 10 - t_\mu & (5 < t_\mu < 10 \text{ } \mu\text{s}). \end{cases} \quad (4.19)$$

Then, the signal inefficiency is 1.1 % because of the veto time, which can be computed by an equation

$$\bar{\epsilon}_{\text{veto}} = \int dt_\mu R_\mu \frac{W^{\text{veto}}(t_\mu)}{8.5\mu\text{s}}, \quad (4.20)$$

where the cosmic muon rate R_μ is 2373 Hz. The second condition is added to delayed signal in order to reject nGd events using space correlation between on-bunch and delayed candidate if there is an event in the on-bunch timing window. It corresponds to the subtraction method used in the floor γ estimation. The criteria for on-bunch event is

- On-bunch event
 - timing from beam: $0 < t_{\text{beam-event}} < 1.5$ μs ,
 - number of hit > 30 ,

and its rate is 0.475 ± 0.001 /spill over the runs. Figure 4.56 shows $\Delta VTX_{\text{OB-d}}$ distribution in the condition $7 < E_{\text{vis}}^{\text{ID}} < 12$ MeV when on-bunch event exists. The green histogram shows coincidence events with on-bunch event, and blue one is estimated accidental events. An accidental coincidence evaluation is done by combining a prompt candidate with delayed events in the next beam window (figure 4.57). Because the signal has no correlation with on-bunch event, nGd events of IBD delayed signal are supposed to belong to the accidental histogram. As shown above, we set $\Delta VTX_{\text{OB-d}} > 110$ cm to eliminate nGd correlated with on-bunch neutron, and its signal efficiency is 92.1% computed from the accidental histogram. The remained nGd events correlated with the beam on-bunch activities can be estimated as the events in the subtracted histogram (black markers) in > 110 cm. The measured event rate is $(8.62 \pm 2.07) \times 10^{-4}$ /spill/100 μs . The expected event rate is

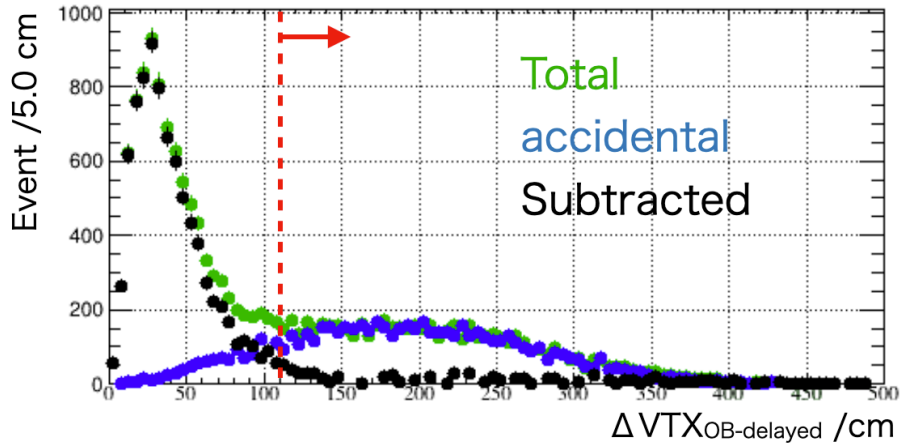


Figure 4.56: ΔVTX_{OB-d} distribution in the condition $7 < E_{vis}^{ID} < 12$ MeV when on-bunch event exists. The beam unrelated events, e.g., IBD and cosmic fast neutron, belongs to the accidental distribution (blue markers). The black marker distribution shows nGd events correlated with beam on-bunch neutron.

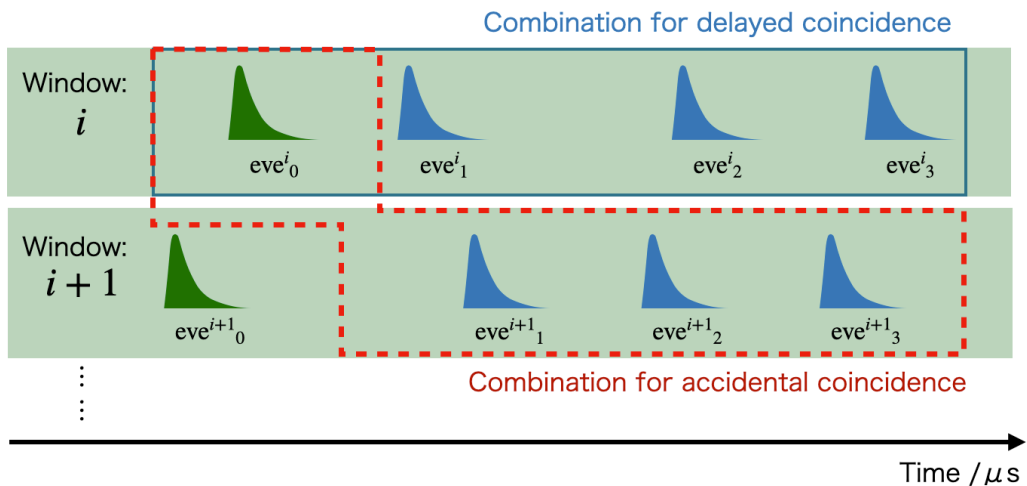


Figure 4.57: A schematic of algorithm for accidental coincidence estimation.

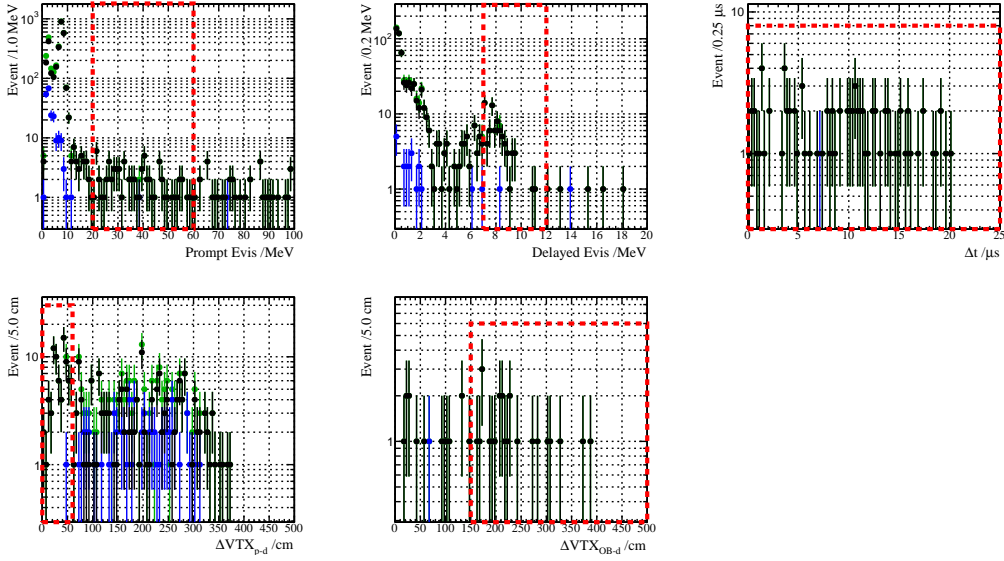


Figure 4.58: Delayed coincidence for the IBD event selection. Top left: prompt visible energy. Top right: delayed visible energy. Middle left: Δt_{p-d} . Middle right: ΔVTX_{p-d} . Bottom left: ΔVTX_{OB-d} . Each distribution of variable is applied all selections except for the selection to itself. The red boxes show the selection criterion to each variable. The green marker corresponds to correlated event candidates, and the blue one shows the estimated accidental coincidence events. The accidental subtracted distribution is displayed as the black marker in the plots.

4×10^{-4} /spill/100 μs in reference [9]. Therefore, they agrees with each other within a factor of 1.5 to 2.5.

As a result of the full selection performed with the same selection criteria as IBD, the prompt and the delayed signal candidate spectra are obtained shown in figure 4.58. The remained number of events in the signal region is 74 events, and that of estimated accidental coincidence events is 1 event. That is, the correlated event excess is 73 ± 9 events. Cosmic fast neutron can be a source of the remained events in the full IBD selection.

In order to compare the obtained number of events in the IBD selection with the measured event rate of cosmic fast neutron, inefficiency of selections unique in the IBD selection to the beam data has to be taken into consideration and applied to the cosmic fast neutron rate. One of them comes from an effect of FADC window size as shown in figure 4.59. Because cosmic ray induced events has no correlation with beam timing, they uniformly distribute along the vertical axis. Therefore, the inefficiency for cosmic fast neutron event can be computed based on a following formula;

$$\left\{ \begin{array}{l} \epsilon_{\text{window}} = \frac{\int_{1.5}^{10} dt_v \int_0^{t'} dt_h \exp\left(-\frac{t_h}{\tau_{Gd}}\right)}{\int_{1.5}^{10} dt_v \int_0^{100} dt_h \exp\left(-\frac{t_h}{\tau_{Gd}}\right)}, \\ t' = -\frac{21}{23.5}t_v + 21, \end{array} \right. \quad (4.21)$$

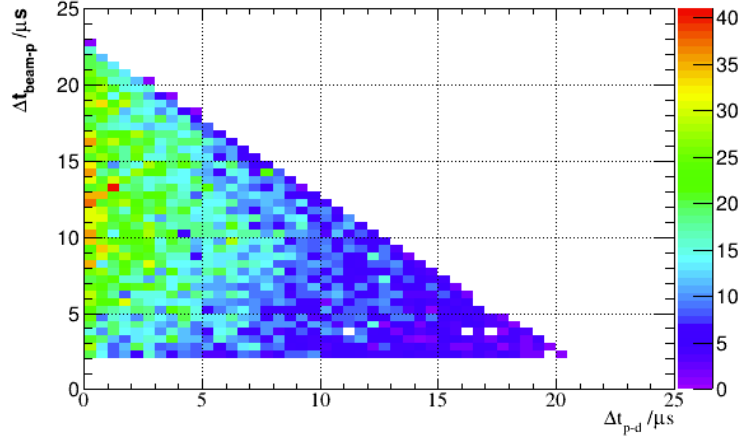


Figure 4.59: Correlation between $\Delta t_{\text{beam-p}}$ (vertical axis) and $\Delta t_{\text{p-d}}$ (horizontal axis). The FADC window size ($25 \mu\text{s}$) naturally limits timing information used in the selection.

where t_v represents $\Delta t_{\text{beam-p}}$, t_h corresponds to $\Delta t_{\text{p-d}}$. Thus, $\epsilon_{\text{window}} = 0.377$ using the measured capture time $\tau_{\text{Gd}} = 29.4 \mu\text{s}$ obtained from the Δt distribution of the cosmic fast neutron. Finally, the expected cosmic fast neutron rate of the kicker data in the IBD selection is

$$\begin{aligned}
 R_{\text{fastn}}^{\text{kicker}} &= R_{\text{fastn}}^{\text{self}} \times \text{num. of spill} \times (1 - \bar{\epsilon}_{\text{veto}}) \times \epsilon_{\text{window}} \times \epsilon_{\Delta VTX_{\text{OB-d}}} \\
 &= (2.70 \pm 0.05) \times 10^{-5} / \text{spill} \times 8092503 \text{ spill} \times 0.989 \times 0.377 \times 0.921 \\
 &= 75.1 \pm 1.4 \text{ events,}
 \end{aligned} \tag{4.22}$$

which is consistent with the remained number of events 73 ± 9 events in the IBD selection. Therefore, one can conclude that the remained background in the full IBD selection can be described by cosmic fast neutron events.

4.7 Summary of Background Measurement

The measured event rate of each component are summarized in table 4.9 as well as the expectations in references [9, 30] for convenience. The signal windows for prompt and delayed signal are set to $8.5 \mu\text{s}$ and $100 \mu\text{s}$, respectively. Note that the rate of cosmic fast neutron is after the IBD selection without particle identification using pulse shape discrimination (PSD). As studied in [9], the neutron rejection factor of PSD selection is 100.

The measured fast neutron rate $(2.70 \pm 0.05) \times 10^{-5} / \text{spill}$ before applying lifetime cut (described in the next chapter) corresponding to 19 times larger than the expected rate $1.4 \times 10^{-6} / \text{spill}$ in the reference. The fast neutron rate will reduce in a factor of ~ 0.5 by lifetime cut (described in the next chapter); thus, the remained rate is still ~ 10 times larger. The Michel electron rate $(8.42 \pm 0.07) \times 10^{-4} / \text{spill}$ can be reduced to $0.77 \times 10^{-4} / \text{spill}$ by applying $5 \mu\text{s}$ veto time after cosmic muon event. Thus, the total accidental rate in the prompt region has a factor of 1.4 with respect to the expectation.

Because of poor shield capability, there is a quite large event rate of floor gamma-ray

Table 4.9: A summary of background measurement for each component.

Component	Measured Rate /spill	Ref. /spill [9, 30]	Type
Cosmic n (self)	$(2.70 \pm 0.05) \times 10^{-5}$	1.4×10^{-6}	Correlated
Cosmic n (kicker)	$(2.60 \pm 0.32) \times 10^{-5}$	1.4×10^{-6}	Correlated
Michel electron	$(8.42 \pm 0.07) \times 10^{-4}$	-	Prompt accidental
Cosmic γ	$(4.66 \pm 0.13) \times 10^{-4}$	3.8×10^{-4}	Prompt accidental
Cosmic γ	$(8.24 \pm 0.07) \times 10^{-3}$	4.4×10^{-3}	Delayed accidental
nGd from beam n	$(8.62 \pm 2.07) \times 10^{-4}$	4×10^{-4}	Delayed accidental
Floor γ	$(5.35 \pm 0.22) \times 10^{-2}$	1.2×10^{-3}	Delayed accidental

in the IBD delayed region, and it makes the total accidental in the delayed energy range 10 times larger.

Assuming rejection efficiency of the selections, e.g., ΔVTX_{p-d} etc, is identical with one in the reference, the significance of signal with respect to background should be 0.38 times smaller compared to the expectation in the reference at oscillation parameter $(\Delta m^2, \sin^2 2\theta) = (2.5 \text{ eV}^2, 3 \times 10^{-3})$, which is equivalent to sensitivity degradation as well.

In order to recover sensitivity, optimization of the neutrino selection criteria and hardware countermeasure are desired as an immediately possible solution. An effect of these recovery efforts are discussed and examined in the next chapter.

Chapter 5

Sensitivity Study for Sterile Neutrino Search

As described in the previous chapter, background rate of each component has been measured based on the data taken in the first run. Therefore, sensitivity of JSNS² experiment can be studied based on the real data. In this chapter, the method to compute sensitivity for sterile neutrino search and its result are described. For the computation, estimation of signal efficiency using both the first run data and the tuned MC simulation of neutrino events is done. As mentioned in the previous chapter, signal selection criteria are optimized to enhance significance of signal with respect to background. The number of events for each component used in the sensitivity calculation is calculated in the optimized selection criteria. In addition to it, hardware countermeasure to reduce cosmic fast neutron and floor gamma is explained respectively. We finally compare estimated sensitivities before and after the countermeasure to the expectation in reference [9].

5.1 Fit Method

The binned maximum likelihood method is used for a shape analysis to energy spectrum of signal in order to extract neutrino oscillation parameters ($\Delta m^2, \sin^2 2\theta$). The number of events in each bin in the spectrum is statistically small so that maximum likelihood instead of the usual minimum χ^2 method based fit is used. For this analysis, the following equation is used to compute Poisson likelihoods:

$$\begin{aligned}\mathcal{L} &= \prod_i P(N_{\text{exp}}^i | N_{\text{obs}}^i) \\ &= \prod_i \frac{e^{-N_{\text{exp}}^i} (N_{\text{exp}}^i)^{N_{\text{obs}}^i}}{N_{\text{obs}}^i!},\end{aligned}\tag{5.1}$$

where N_{exp}^i is the expected number of events in i -th bin, N_{obs}^i is the observed number of events in i -th bin corresponding to measured data. The range of bin number i corresponds to the fitting range set to 20 to 60 MeV, e.g., 10 bins in total in case of 4 MeV/bin binning. The expected number of events N_{exp} consists of

$$N_{\text{exp}} = N_{\text{Signal}}(\Delta m^2, \sin^2 2\theta) + \sum N_{\text{BG}},\tag{5.2}$$

where $N_{\text{Signal}}(\Delta m^2, \sin^2 2\theta)$ is computed based on the oscillation probability expressed in Eq. (1.14), and $\sum N_{\text{BG}}$ is a summation of background events about all components. In addition, both $N_{\text{Signal}}(\Delta m^2, \sin^2 2\theta)$ and $\sum N_{\text{BG}}$ must include an effect of detector response to fit to obtained data.

The maximum likelihood point gives the best fit parameters, and $2\Delta \log \mathcal{L}$ provides the uncertainty of the fit parameters. Two parameters are required to determine the uncertainties from the fit as shown in [54].

5.1.1 Systematic Uncertainty

In addition to statistical uncertainty, systematic uncertainties should be incorporated into Eq. (5.1). Because the energy spectra of oscillated signal and background are well known; thus, a covariance matrix of energy is not needed. Uncertainties on the overall normalization of each component have to be taken into account in this case, and the assumption can be a good approximation in this sequence of experiment. As a treatment of systematic uncertainties in likelihood, constraint terms are introduced to the likelihood equation following [53]. That is,

$$\mathcal{L} = \prod_i P(N'_{\text{exp}} | N_{\text{obs}}) \times \exp\left(-\frac{(1-f_1)^2}{2\Delta\sigma_1^2}\right) \times \exp\left(-\frac{(1-f_2)^2}{2\Delta\sigma_2^2}\right), \quad (5.3)$$

where

$$N'_{\text{exp}} = f_1 \times N_{\text{Signal}}(\Delta m^2, \sin^2 2\theta) + (f_2 \times N_{\text{BG}}^{\text{IBD}} + \sum N_{\text{BG}}^{\text{others}}), \quad (5.4)$$

and $\Delta\sigma_i$ gives uncertainty on the normalization factor of the i -th component.

The profiling fitting method is used to treat the systematic uncertainties, which is widely known as a correct fitting method, and it fits all nuisance parameters as well as the oscillation parameters. For systematic uncertainties for JSNS², the uncertainty on the flux of $\bar{\nu}_e$ from μ^- decay at the mercury target of MLF and that of $\bar{\nu}_\mu$ are taken into consideration. 10 % uncertainty is set to the former one, which comes from the uncertainty on cross section of $\nu_e + {}^{12}\text{C} \rightarrow e^- + {}^{12}\text{N}_{\text{g.s.}}$ used for $\bar{\nu}_\mu$ flux normalization in JSNS² [5]. We assigns 50 % uncertainty on the later one due to model dependence of charged pion production. In this study, we assumes that other uncertainties are negligibly small compared to the uncertainties described above.

5.2 Optimization of Signal Efficiency

Signal selection efficiency has to be estimated for a sensitivity study. The selection criteria in the background measurement is determined to follow the selections used in the references for comparison. Therefore, optimization of selection criteria is performed based on the real data in order to maximize sensitivity.

In this section, signal efficiency of the selection criteria about the following variables are estimated:

- Prompt signal timing from beam: $\Delta t_{\text{beam-p}}$,
- Lifetime cut,
- Neutron detection efficiency,

- Gd fraction,
- Delayed visible energy: $E_{\text{vis}}^{\text{ID}}$,
- Timing correlation between prompt and delayed: $\Delta t_{\text{p-d}}$,
- Prompt visible energy: $E_{\text{vis}}^{\text{ID}}$.
- Spacial correlation between delayed and on-bunch: $\Delta VTX_{\text{OB-d}}$,
- Spacial correlation between prompt and delayed: $\Delta VTX_{\text{p-d}}$.

For optimization, Enhance is defined as

$$\text{Enhance} = \frac{\epsilon_{\text{signal}}}{\sqrt{\epsilon_{\text{BG}}}}, \quad (5.5)$$

where ϵ_{signal} and ϵ_{BG} are signal and background efficiencies of the selection, respectively. The enhance corresponds to statistical significance of the signal with respect to the background. Thus, maximizing the enhance value of each selection criterion leads to optimization to obtain better sensitivity in the current situation. The optimization is performed to some of the selections if necessary.

PSD capability can not be estimated using the first run data because it was impossible to perform nitrogen purging to the Gd-LS and LS. However, it has been investigated using MC simulation based on the measured waveform data of LAB-based Gd-LS so that we can use the value in reference [9].

Prompt signal timing from beam: $\Delta t_{\text{beam-p}}$

The signal efficiency of selection to prompt signal timing with respect to beam timing $\Delta t_{\text{beam-p}}$ is estimated from the timing profile of μ DAR ($P_{\text{beam}}(t)$). It is generated from a convolution of the measured timing profile of proton beam at the MLF shown in Fig. 5.1 with μ decay (an exponential distribution with lifetime $\tau_{\mu} = 2.2 \mu\text{s}$). Figure 5.2 shows the generated profile of $\Delta t_{\text{beam-p}}$ (left) and the estimated signal efficiency, $\epsilon(t_e)$, which is defined in

$$\epsilon(t_e) = \frac{\int_{1.5 \mu\text{s}}^{t_e} dt P_{\text{beam}}(t)}{\int_{1.5 \mu\text{s}}^{10 \mu\text{s}} dt P_{\text{beam}}(t)}, \quad (5.6)$$

where t_e is an end point of the selection criterion. If we set $1.5 < \Delta t_{\text{beam-p}} < 10 \mu\text{s}$, the efficiency is 72.7% from the right plot.

Lifetime cut

The lifetime cut is a selection to value of the negative log likelihood NLL based on $\Delta t_{\text{beam-p}}$ and $\Delta t_{\text{p-d}}$, that is,

$$NLL = -2 \log \mathcal{L}_{\text{Lifetime}} = (-2 \log \mathcal{L}_{\text{prompt}}) + (-2 \log \mathcal{L}_{\text{delayed}}) \quad (5.7)$$

where $\mathcal{L}_{\text{prompt}}$ is likelihood of the probability density function (PDF) of the prompt signal timing from beam $\Delta t_{\text{beam-p}}$, and $\mathcal{L}_{\text{delayed}}$ is that of $\Delta t_{\text{p-d}}$ PDF. The prompt

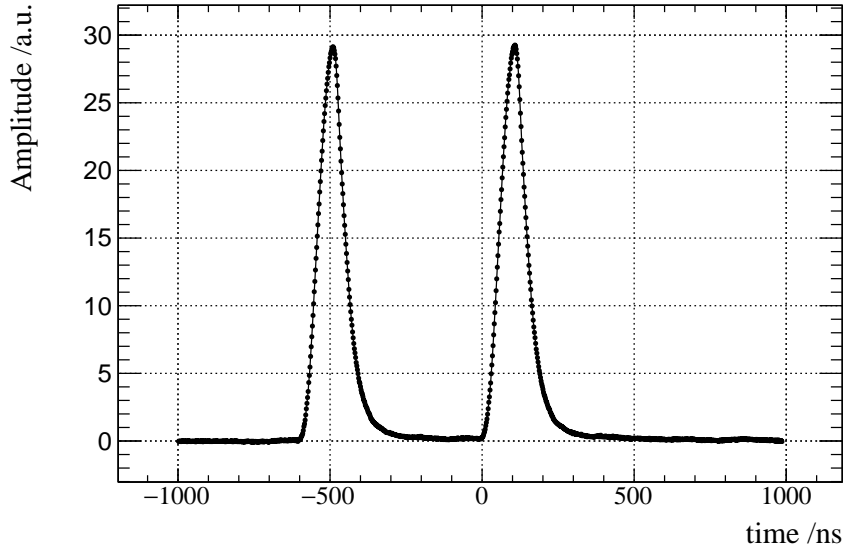


Figure 5.1: The measured timing profile of the proton beam to the mercury target [55].

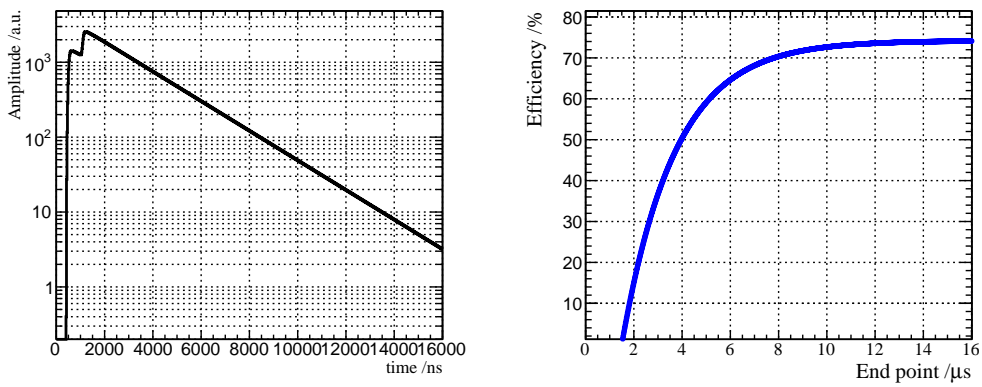


Figure 5.2: Left: The timing profile of signal as a function of signal timing with respect to beam timing. Right: The estimated signal efficiency as a function of end point of the selection criterion. The red line indicates the efficiency value in case of $1.5 < \Delta t_{\text{beam-p}} < 10 \mu\text{s}$.

timing PDF is represented by an exponential distribution with the neutron capture time on Gd as a time constant. The likelihood value is computed in the range of the prompt signal timing cut ($1.5 < \Delta t_{\text{beam-p}} < 10 \mu\text{s}$) and that of the timing correlation cut ($\Delta t_{\text{p-d}} < 100 \mu\text{s}$). Figure 5.3 shows correlations between $\Delta t_{\text{beam-p}}$ and $\Delta t_{\text{p-d}}$ for the signal (top), the accidental backgrounds (middle), and cosmic fast neutron events (bottom), respectively. For the timing

Figure 5.4 exhibit distributions of likelihood value for each component and their efficiencies classified with color as follows: signal in red, cosmic fast neutron in blue and accidentals in green. The PDFs of each component are summarized in table 5.1.

Table 5.1: Component classification in lifetime.

Component	Prompt PDF	Delayed PDF	Color in Fig. 5.4
Signal	$P_{\text{beam}}(t)$	$P_{\Delta t_{\text{p-d}}}(t)$	Red
Cosmic fast n	Flat	$P_{\Delta t_{\text{p-d}}}(t)$	Blue
Accidentals	Flat	Flat	Green

The efficiency is defined as

$$\epsilon(x) = \frac{N(10 < NLL < x)}{N(10 < NLL < 40)}, \quad (5.8)$$

where x is an end point of the selection criterion, and N stands for the total number of events in the designated range. The signal enhance curves with respect to cosmic fast neutron (blue) and accidentals (green) are shown in the bottom plot in Fig. 5.4. The results of optimization to the lifetime cut are listed in table 5.2. The enhance reaches maximum value at endpoint of the selection depending on the component focused on. In this study, we choose the selection criterion $NLL < 22$ as the best one in order to reinforce sensitivity with respect to cosmic fast neutron background.

Table 5.2: Efficiencies of lifetime cut.

Case	Cut NLL	Signal eff./%	Fast n eff./%	Accidental eff./%
Ref. [30, 9]	-	91.6	50	64
Opt. (Fast n)	22	78.8	47.2	25.5
Opt. (Acci.)	20	53.6	23.5	10.1

Neutron detection efficiency

Neutron detection efficiency is expressed as a product of three components:

$$\epsilon_{\text{neutron}} \equiv \epsilon_{\Delta t_{\text{p-d}}} \times \epsilon_{E_{\text{delayed}}} \times \epsilon_{\text{Gd}}, \quad (5.9)$$

where $\epsilon_{\Delta t_{\text{p-d}}}$ and $\epsilon_{E_{\text{delayed}}}$ are efficiencies of the time correlation and the delayed energy cuts respectively, and ϵ_{Gd} is a fraction of nGd with respect to total neutron capture. The Gd fraction is estimated from the MC simulation. A ratio of the number of Gd capture events to that of all IBD interactions uniformly generated in the Gd-LS volume is 82.3 % It indicates 4.3 % reduction in the Gd fraction compared to the estimation based on the ^{252}Cf simulation at the center of the detector due to

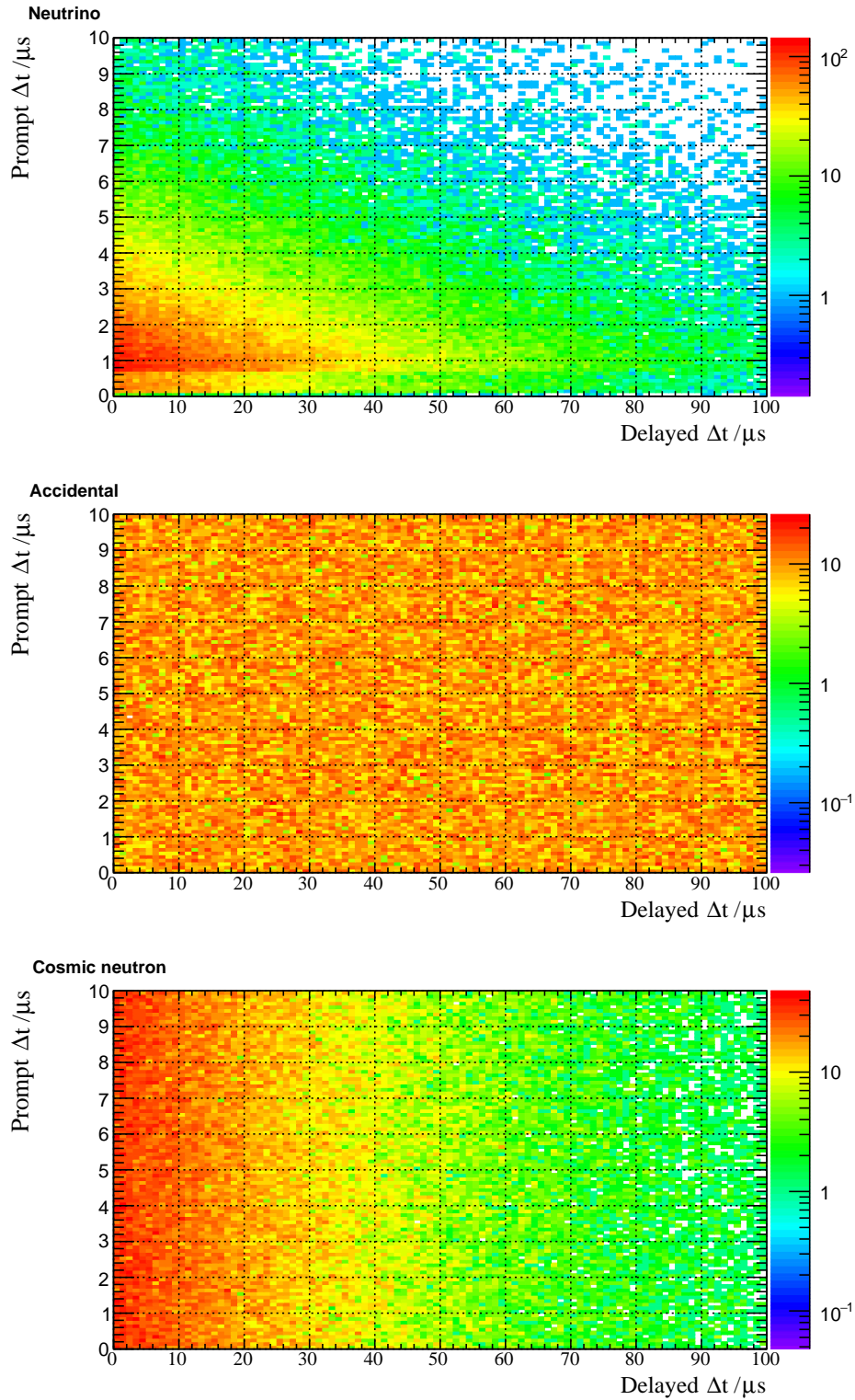


Figure 5.3: Correlations between $\Delta t_{\text{beam-p}}$ (vertical axis) and $\Delta t_{\text{p-d}}$ (horizontal axis) of the signal (top), the accidental backgrounds (middle), and cosmic fast neutron events (bottom).

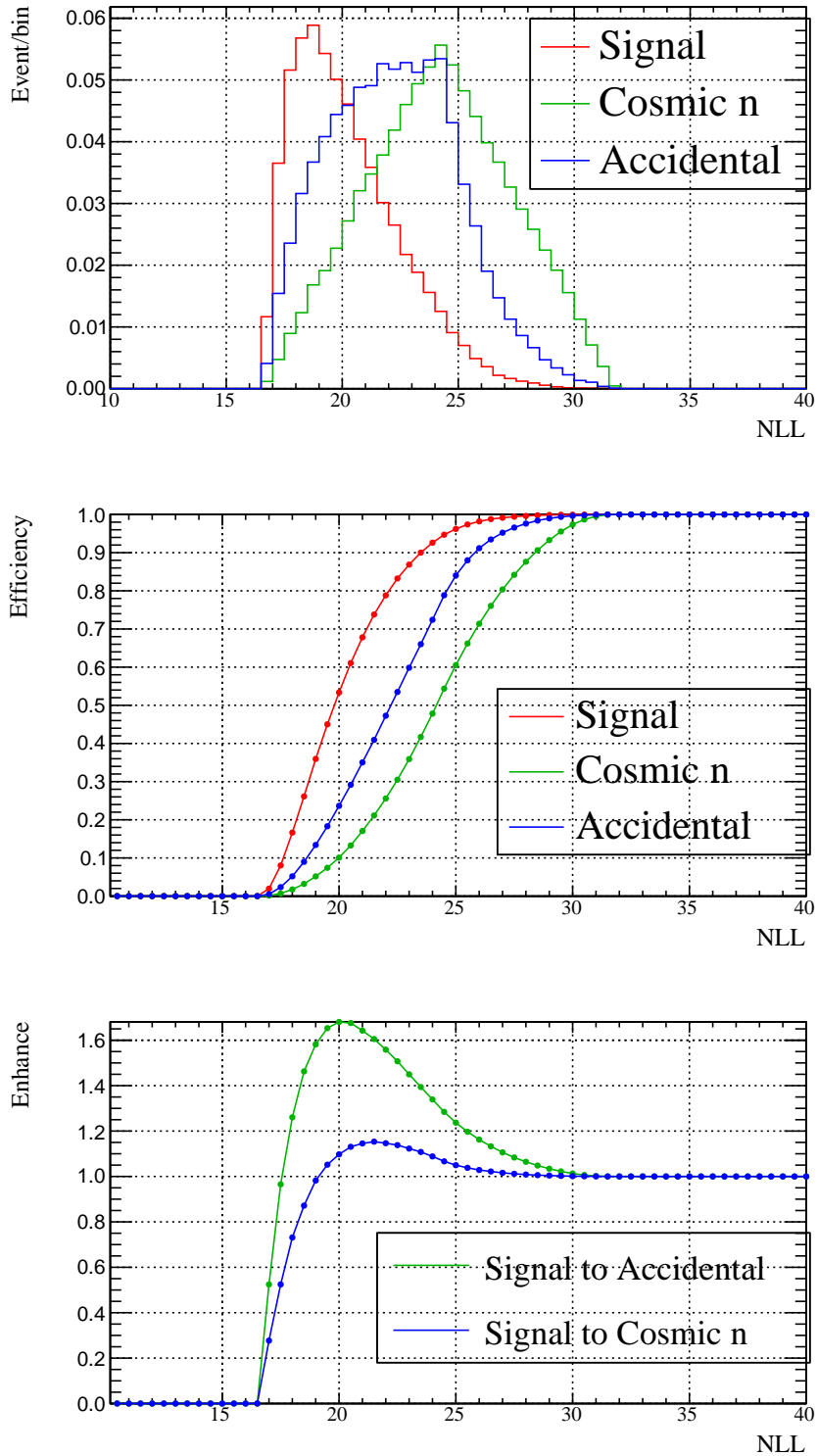


Figure 5.4: Top: distributions of log-likelihood value, middle: selection efficiency as a function of selection value of log-likelihood for the signal (red), the accidental events (green) and cosmic fast neutron (blue). Bottom: the enhance curves of signal to accidental (green) and signal to fast neutron (blue).

an effect of IBD neutron spilling out of the acrylic vessel. On the other hand, there also exists a process that neutron from IBD interaction out of the Gd-LS boundary comes into the Gd-LS volume and is captured on Gd (spill-in). As a result of an integration of both spill-in/out effect, 86.5 % is used as an effective Gd fraction for computing the expected number of IBD events.

Delayed visible energy: E_{delayed}

In order to reflect an effect of energy leak of nGd events, an efficiency of the delayed signal energy selection based on the delayed energy spectrum of the IBD simulation uniformly generated in the detector. It is shown in the top plot in Fig. 5.5 as the black histogram with the spectrum of the accidental backgrounds (green markers). The efficiencies of them as a function of endpoint of the energy selection are displayed in the middle plot, and the enhance curve (bottom) shows that significance reaches to maximum at 9 MeV. The optimization result is summarized in table 5.3 to compare it with the old selection criterion. The definition of the signal efficiency for delayed signal selection is

$$\epsilon_{\text{signal}}(x) = \frac{N(7 < E_{\text{vis}}^{\text{ID}} < x \text{ MeV})}{N(4 < E_{\text{vis}}^{\text{ID}} < 12 \text{ MeV})}, \quad (5.10)$$

where x is an end point of the selection criterion, and N stands for the total number of events in the designated range as following above. The background efficiency is defined as a ratio of the number of events in the delayed signal range with respect to the case in the original selection:

$$\epsilon_{\text{BG}}(x) = \frac{N(7 < E_{\text{vis}}^{\text{ID}} < x \text{ MeV})}{N(7 < E_{\text{vis}}^{\text{ID}} < 12 \text{ MeV})}. \quad (5.11)$$

Table 5.3: Efficiencies of delayed energy selection.

Case	Selection Range	Signal eff./%	Accidental eff./%
Original	7 - 12 MeV	80.0	100
Optimized	7 - 9 MeV	75.6	75.5

Timing correlation between prompt and delayed: $\Delta t_{\text{p-d}}$

To estimate a selection efficiency of $\Delta t_{\text{p-d}}$, the ^{252}Cf data and MC, and the IBD MC simulation are compared. Figure 5.6 shows the histogram of $\Delta t_{\text{p-d}}$ obtained from the data when we deployed the ^{252}Cf source at the center of the detector as black markers. It is overlaid with MC simulation output of the signal IBD generated uniformly in the detector, and one can find that they are in good agreement. For the signal MC simulation, the following selections are applied in order to follow the real signal selection condition;

- Prompt visible energy: $20 < E_{\text{vis}}^{\text{ID}} < 60 \text{ MeV}$.
- Delayed visible energy: $7 < E_{\text{vis}}^{\text{ID}} < 9 \text{ MeV}$,
- Spacial correlation between prompt and delayed: $\Delta VTX_{\text{p-d}} < 60 \text{ cm}$.

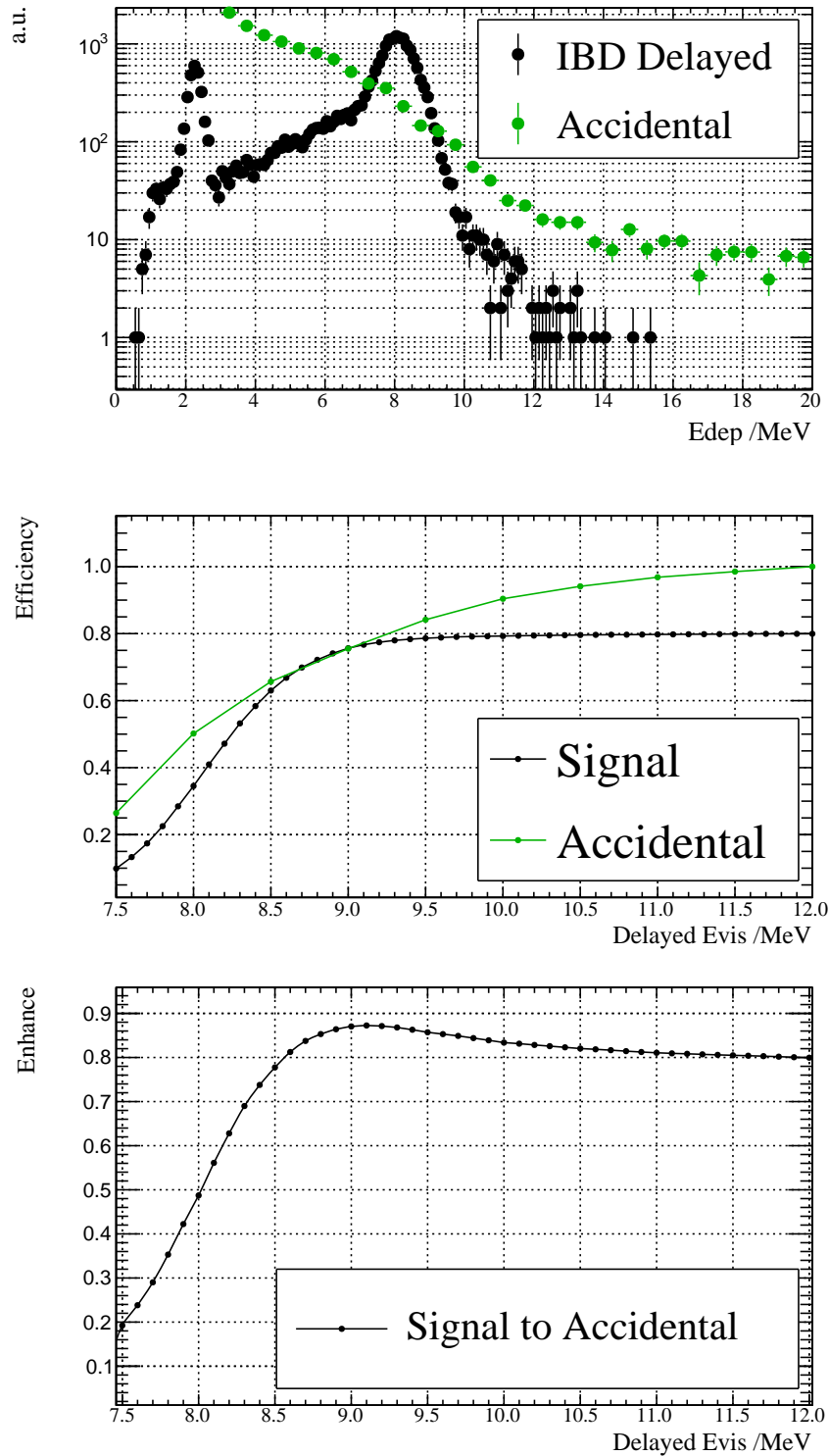


Figure 5.5: Top: The delayed energy distribution of the IBD simulation (black) and the accidental events during beam operation (green). Middle: selection efficiency as a function of the endpoint of the delayed energy selection of signal (black) and background (green). Bottom: The enhance curve of signal to accidental background efficiency.

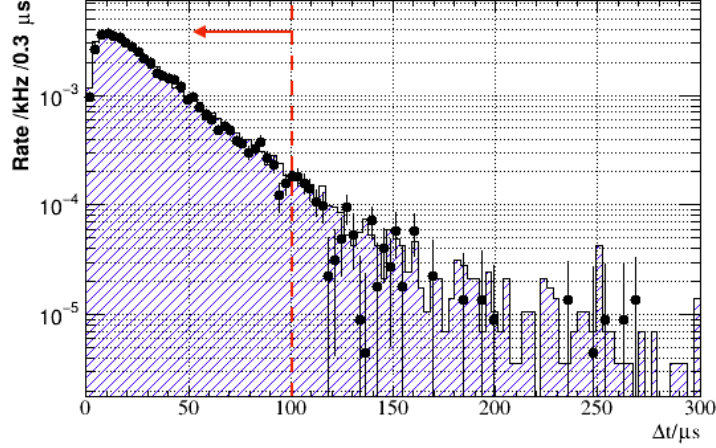


Figure 5.6: Δt_{p-d} distribution of the data with ^{252}Cf at the $Z = 0$ cm (black marker) and the signal MC output.

The efficiency is estimated from the Δt_{p-d} distribution of the ^{252}Cf data based on the following definition;

$$\epsilon = \frac{N(\Delta t_{p-d} < 100)}{N(\Delta t_{p-d} < 300)} \quad (5.12)$$

where N stands for the total number of events in the designated range. As a result, the efficiency computed from the IBD simulation is 96.2 %. It is consistent with the ^{252}Cf MC simulations shown in Fig. 4.39 (right). Therefore, it indicates that an effect of uniform vertex on the Δt_{p-d} selection efficiency is negligibly small. Taken the discrepancy of the calculated efficiency between the data and the MC result in ^{252}Cf into consideration, we finally adopt the average value of the efficiency of the ^{252}Cf data. Thus, it is computed as 95.4 %.

Prompt visible energy: E_{prompt}

The efficiency for the prompt energy selection can only be estimated from the signal MC simulation result. Figure 5.7 shows the visible energy spectrum of IBD prompt signal of $\bar{\nu}_\mu \rightarrow \bar{\nu}_e$ in 100 % oscillation case as well as that of $\mu^- \rightarrow \bar{\nu}_e$ in the following conditions:

- Delayed visible energy: $7 < E_{\text{vis}}^{\text{ID}} < 9$ MeV,
- Timing correlation between prompt and delayed: $\Delta t_{p-d} < 100$ μs ,
- Spacial correlation between prompt and delayed: $\Delta VTX_{p-d} < 60$ cm.

The selection criterion to it is the same range of the fitting rage, i.e., 20 to 60 MeV. The efficiency for the signal is 95.5 % in a definition

$$\epsilon = \frac{N(20 < E_{\text{vis}}^{\text{ID}} < 60 \text{ MeV})}{N(1 < E_{\text{vis}}^{\text{ID}} < 60 \text{ MeV})}, \quad (5.13)$$

where N stands for the total number of events in the designated range. The efficiency for the background IBD is computed as 93.4 % accordingly.

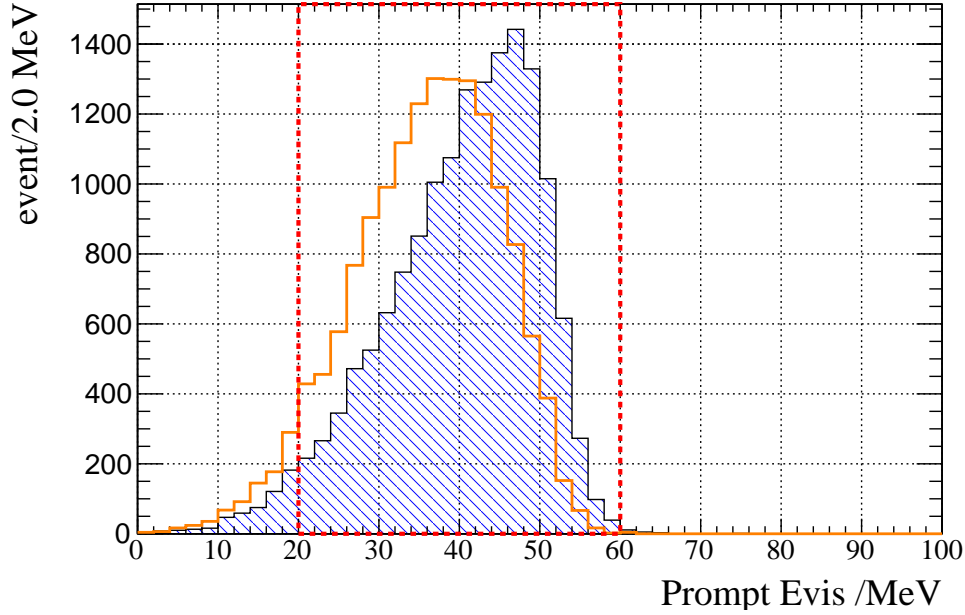


Figure 5.7: Prompt visible energy spectra of the signal (blue shaded area) and the background IBD events (orange line). The red dashed box corresponds to the selection criterion. The selection efficiencies are 95.5 % for the signal and 93.4 % for the background IBD, respectively. Note that the signal spectrum shows the 100 % oscillation case.

Spatial correlation between delayed and on-bunch: $\Delta VT X_{\text{OB-d}}$

The top left plot in Fig. 5.8 is the distribution of spacial correlation delayed and on-bunch: $\Delta VT X_{\text{OB-d}}$, which is already shown in Fig. 4.56. The signal and background efficiencies is computed from the distributions on the definition

$$\epsilon(x) = 1 - R_{\text{OB}} \times \left(\frac{N(\Delta VT X_{\text{OB-d}} > x \text{ cm})}{N(\Delta VT X_{\text{OB-d}} > 0 \text{ cm})} \right), \quad (5.14)$$

where x is an beginning point of the selection criterion, and N stands for the total number of events in the designated range shown between the parentheses. In the right hand side of Fig. 5.8, the efficiencies and signal enhance are shown on the top and bottom, respectively. One can find that the enhance is maximized at $\Delta VT X_{\text{OB-d}} > 150 \text{ cm}$. Table 5.4 shows a summary of the optimization, and it also exhibits the remained accidental background rate after this selection (defined as $R_{\text{OB-nGd}}$) in each selection case.

Table 5.4: Efficiencies of $\Delta VT X_{\text{OB-d}}$ selection.

Case	Selection Range	Signal eff./%	BG eff./%	$R_{\text{OB-nGd}}/\text{spill}/100\mu\text{s}$
Original	$> 110 \text{ cm}$	92.1	6.3	$(8.62 \pm 2.07) \times 10^{-4}$
Optimized	$> 150 \text{ cm}$	84.6	3.9	$(4.38 \pm 1.85) \times 10^{-4}$

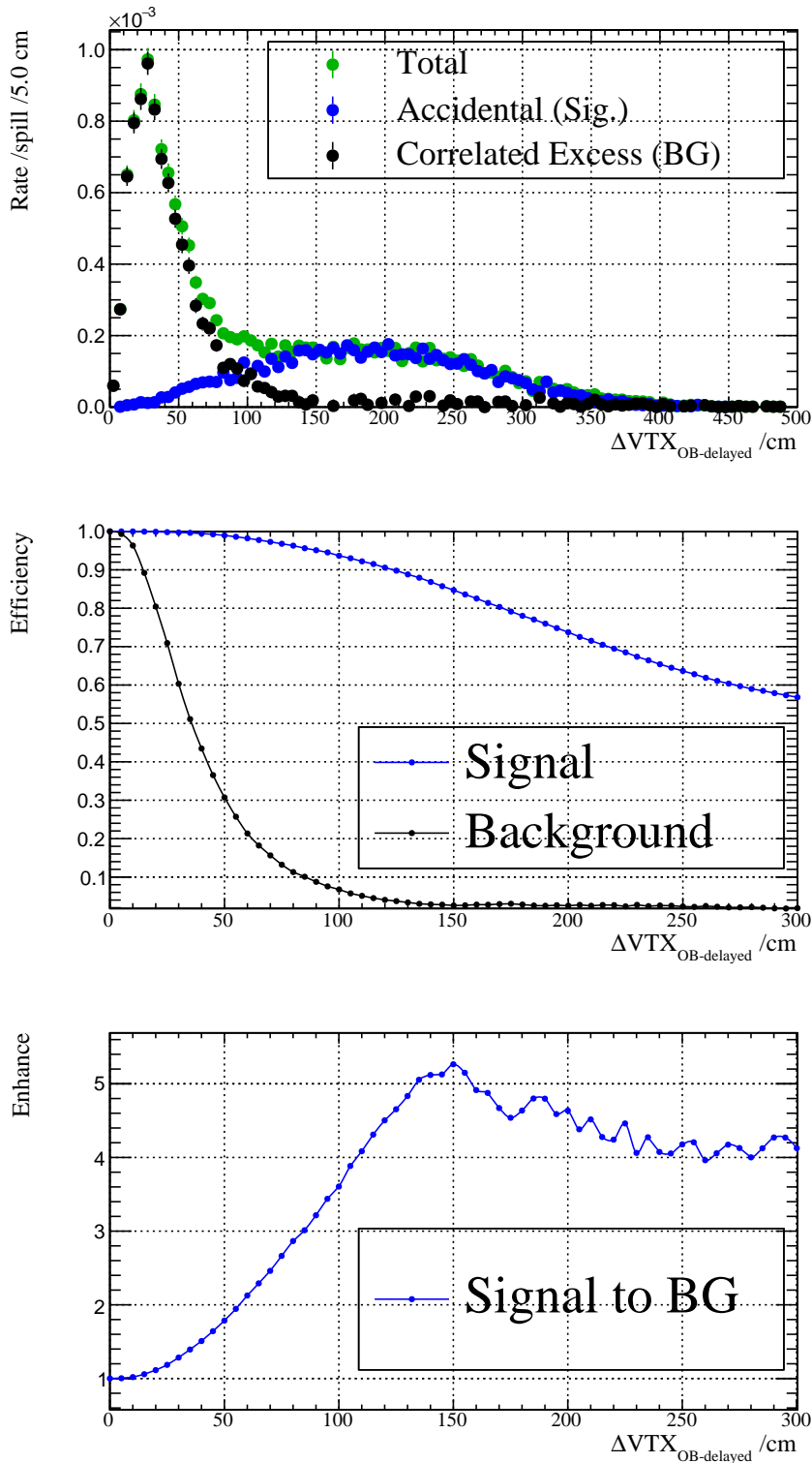


Figure 5.8: Top: Distributions of $\Delta VTX_{OB\text{-d}}$ for the correlated delayed event with on-bunch activity (black) and the events accidentally coincided with on-bunch activity (blue). Note that the signal IBD will be accidental in this case. Middle: efficiency curves as a function of cut line of the selection to the signal (blue) and the on-bunch correlated event (black). Bottom: enhance curve of signal to on-bunch correlated delayed event.

Spacial correlation between prompt and delayed: ΔVTX_{p-d}

Efficiency of ΔVTX_{p-d} for signal is estimated from the MC simulation result. Figure 5.9 shows ΔVTX_{p-d} distribution (top left) and efficiencies as a function of cut value (top right) of the signal MC output (blue), cosmic fast neutron (red) and accidentals (green) of the data. For the signal MC, the following conditions are applied;

- Prompt visible energy: $20 < E_{\text{vis}}^{\text{ID}} < 60$ MeV.
- Delayed visible energy: $7 < E_{\text{vis}}^{\text{ID}} < 9$ MeV,
- Timing correlation between prompt and delayed: $\Delta t_{p-d} < 100 \mu\text{s}$.

The efficiency is defined as following formula:

$$\epsilon(x) = \frac{N(\Delta VTX_{p-d} < x \text{ cm})}{N(\Delta VTX_{p-d} < 500 \text{ cm})}. \quad (5.15)$$

Enhance curves (bottom right in Fig. 5.9) are obtained using the efficiency curves in three case: signal MC to fast neutron data (red), signal MC to accidental data and fast data to accidental data (green). Because of short statistics in the accidental histogram, the large fluctuation appears on the blue and green lines. Therefore, the optimization is performed based on the signal to fast neutron enhance value. The result is summarized in table 5.5.

Table 5.5: Efficiencies of ΔVTX_{p-d} cut.

Case	Selection Range	Signal eff./%	Fast n eff./%	Accidental eff./%
Optimized	< 60 cm	86.3	65.9	2.5

5.2.1 Summary of Signal Efficiency

Table 5.6 summarizes the signal efficiency after optimization based on the signal enhance method. The total selection efficiency results in 24.7 % corresponding to 65 % less than the expected value 38 % in refrence [9]. This indicates that we need additional 1.6 years to collect the same statistics as the reference. Both an increase in the background and efficiency reduction is supposed to affect on sensitivity. Therefore, it is highly crucial to reduce the background rate without an signal efficiency loss. The total efficiency is used to compute the expected number of signal event for sensitivity calculation. In addition, the effects of selection criteria optimization on the background event rate are estimated as well, and these modification will be considered in calculation of the number of background events in the next section.

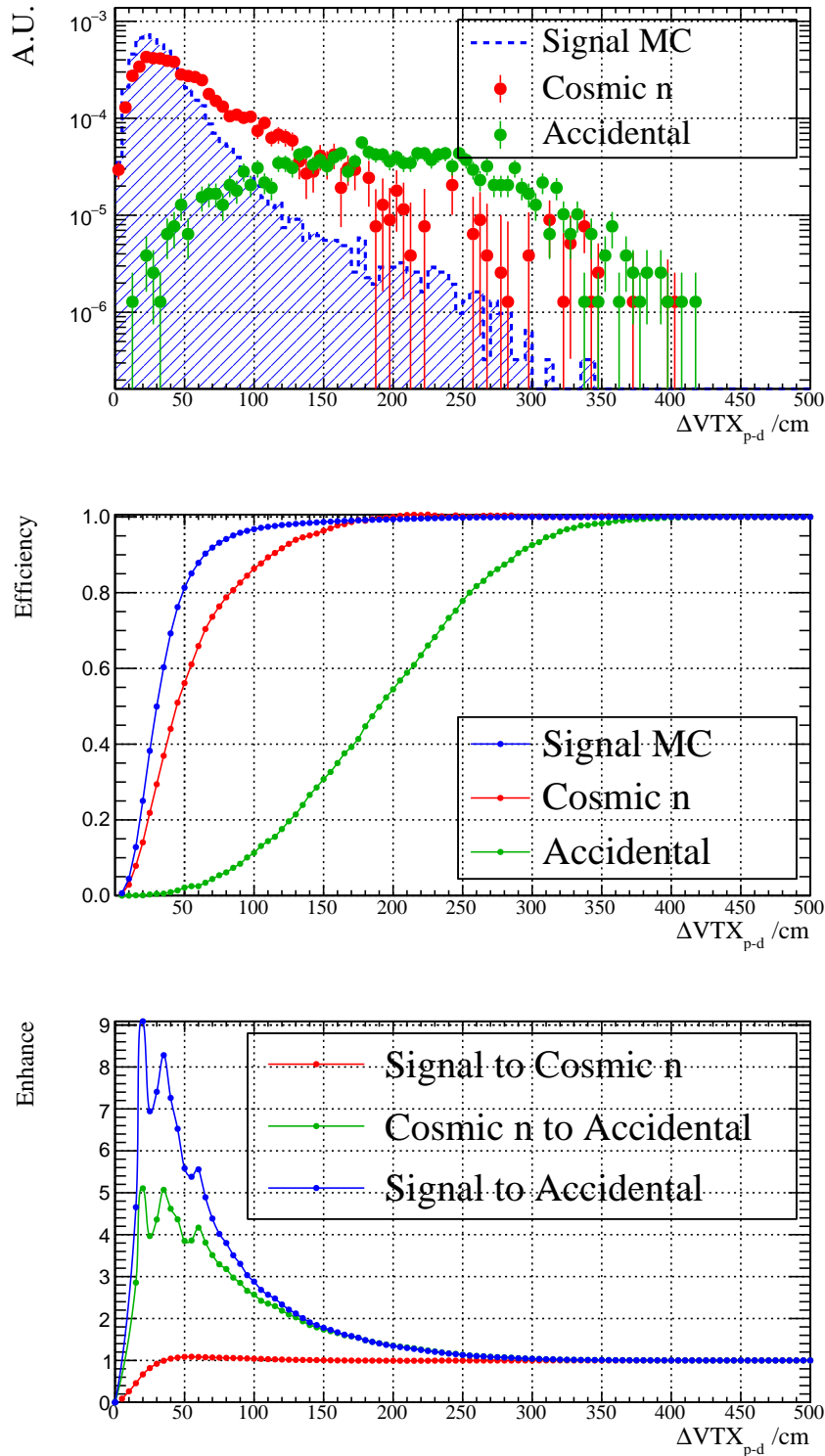


Figure 5.9: Top: ΔVTX_{p-d} distribution of the fast neutron sample (red marker) and the accidental sample (green) in the data, respectively. The blue dashed line shows that of the IBD from the signal MC simulation. Middle: efficiency curves as a function of cut line of the selection in the same color classification. Bottom: enhance curves: signal to fast neutron (red), signal to accidental (blue) and fast neutron to accidental (green). Spike on the curves is due to poor statistics below 80 cm.

Table 5.6: A summary of signal efficiency estimation.

Selection Condition	Efficiency/%
$1.5 < \Delta t_{\text{beam-p}} < 10 \mu\text{s}$	72.7
Lifetime $NLL < 22$	78.8
Gd fraction	86.5
$7 < E_{\text{delayed}} < 9 \text{ MeV}$	75.6
$\Delta t_{\text{p-d}} < 100 \mu\text{s}$	95.4
$20 < E_{\text{prompt}} < 60 \text{ MeV}$	95.5
$\Delta VTX_{\text{OB-d}} > 150 \text{ cm}$	84.6
$\Delta VTX_{\text{p-d}} < 60 \text{ cm}$	86.3
PSD cut	~ 99
Total (this work)	24.7
Total (reference [9])	38

5.3 Possible Hardware Upgrade

The result of background measurement indicates the larger number of background events compared to the expectation in reference [9, 30]. Therefore, hardware upgrade as a countermeasure is highly desired for background reduction without efficiency loss. The following upgrades are immediately feasible:

- Shield upgrade and optimization,
- Reinforcement of PSD capability for neutron rejection.

The first countermeasure is to directly reduce the event rate of floor γ , which leads to total accidental rate reduction. The second one can be realized by adding DIN (2,7-diisopropylnaphthalene) to the JSNS² Gd-LS and LS. In this section, investigation and studies to implement them are described, and their background rejection capabilities is estimated.

5.3.1 Shield Upgrade

Investigation for shield upgrade is done using MC simulation tuned based on the data. In order to perform a quick implementation, we concentrates on optimizing configuration of lead shield. Because the data indicate floor γ is almost vertically emitted from the surface of the detector, it could be effective to enlarge double layer coverage. The floor γ simulations are performed in the following configuration to estimate shielding capability:

- the current JSNS² shield: Lead R1.6 m (5 cm thickness) + R2.5 m (5 cm thickness), and Iron 6 m \times 9 m (4.4 cm thickness),
- upgraded configuration: Lead R2.3 m (10 cm thickness), and Iron 6 m \times 9 m (6.6 cm thickness).

The point of the upgrade is that it is possible for us to implement the upgrade with the current number of lead blocks.

Figure 5.10 and 5.11 show the results of the MC simulation in the current shield configuration and in the upgraded configuration, respectively. The plots in the left hand side shows energy spectrum of floor γ events, and their red dashed boxes correspond to the delayed signal range. The number of event in the delayed signal region is 124 and 21, respectively; therefore, it is concluded that the rejection power of the upgraded shield configuration for floor γ is $21/124 \sim 1/6$. The plots in the right hand side display event vertex distribution in $r^2 - z$ plain just for demonstration. By comparing them, enlarging double layer coverage below the detector works sufficiently.

5.3.2 Reinforcing PSD Capability

As mentioned above, DIN is a candidate material for PSD reinforcement. It is already used in several neutrino experiments, and shows good PSD capability [56, 58]. Thus, we investigated PSD capability and stability of DIN-mixed Gd-LS sample in order to show feasibility.

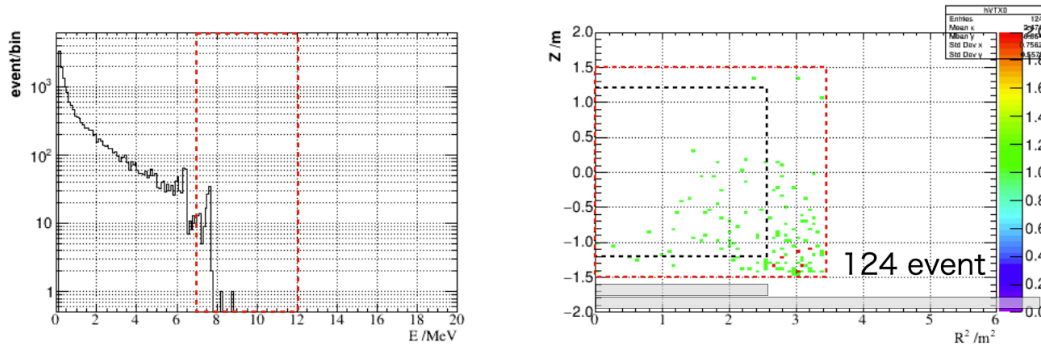


Figure 5.10: MC simulation result in the current JSNS² shield configuration. Left: True deposited energy in the detector. Right: Event vertex distribution in the detector. The horizontal axis shows r^2 of the vertex, and the vertical axis corresponds to z of the vertex. The gray rectangles illustrate the lead shield coverage.

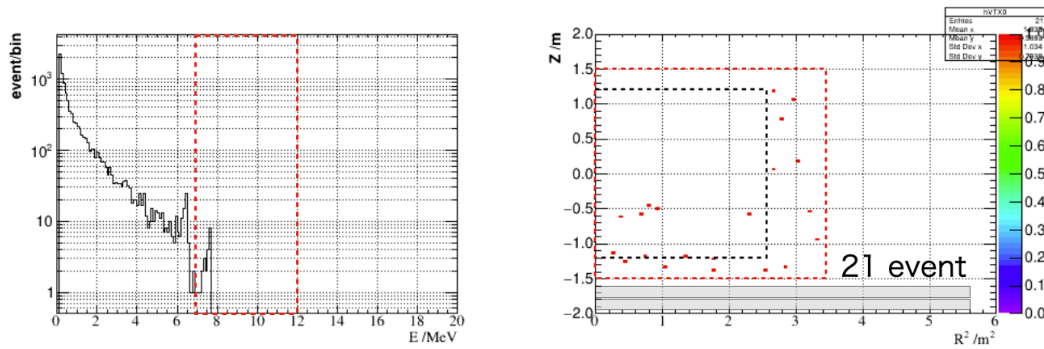


Figure 5.11: MC simulation result in the upgraded shield configuration. Left: True deposited energy in the detector. Right: Event vertex distribution in the detector. The horizontal axis shows r^2 of the vertex, and the vertical axis corresponds to z of the vertex. The gray rectangles illustrate the lead shield coverage.

PSD Capability

PSD capability of the DIN mixed Gd-LS was measured in the setup shown in figure 5.12 (a). ^{252}Cf source was used as a neutron source, and R7081 10 inch PMT observed scintillation light from the sample. The sample was sufficiently exposed to nitrogen flow as nitrogen purging. This measurement was performed using the identical electronics configuration with the JSNS² detector, such as splitter, FEE and FADC.

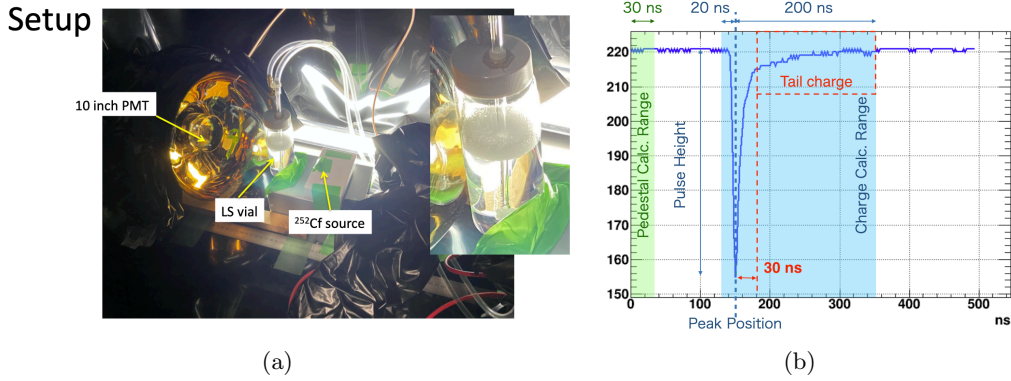


Figure 5.12: (a) A photo of the setup for PSD capability measurement. 100 mL of each DIN mixed Gd-LS sample contained in the 2 inch vial was exposed to ^{252}Cf source, and 10 inch PMT (R7081) observed scintillation light from the sample. (b) Definition of variables especially Q_{tail} . The integration range is from 30 ns to 200 ns after the peak.

Figure 5.13 shows the result of PSD capability of each sample whose DIN concentration is 0% (left), 5% (center) and 10% (right) in volume, respectively. The top panel is a 2D histogram of $Q_{\text{tail}}/Q_{\text{total}}$ (vertical axis) and Q_{total} converted to the number of p.e. (horizontal axis) for each sample. The definition of Q_{tail} is visualized in figure 5.12 (b). The bottom one corresponds to $Q_{\text{tail}}/Q_{\text{total}}$ distribution in the selection region (600 - 1200 p.e.) shown in the top panel. One can find that DIN mixed samples show better PSD capability compared to the DIN 0% (= JSNS² Gd-LS) sample. Note that the resolution of $Q_{\text{tail}}/Q_{\text{total}}$ distribution gets better as a function of photo statistics, and 10 times larger number of p.e. will be available for events in the IBD prompt region in the JSNS² detector. The neutron rejection efficiency was estimated based this data as follows [9], and we found that DIN 10% mixture gave 1/200 rejection with keeping the current signal efficiency (figure 5.14).

Stability

Because the Gd-LS and LS are annually exposed to the air in the filling and extraction sequence of experiment, stability of the DIN mixed Gd-LS to air exposure was checked by monitoring transmittance spectrum of the sample. Figure 5.15 shows comparison of the measured transmittance spectra in two different days (top panel), and their ratio at each wavelength (bottom panel). They indicate that the spectrum of the sample has been stable against air exposure for 23 days. Therefore, there is no problem in the annual operation of JSNS² experiment.

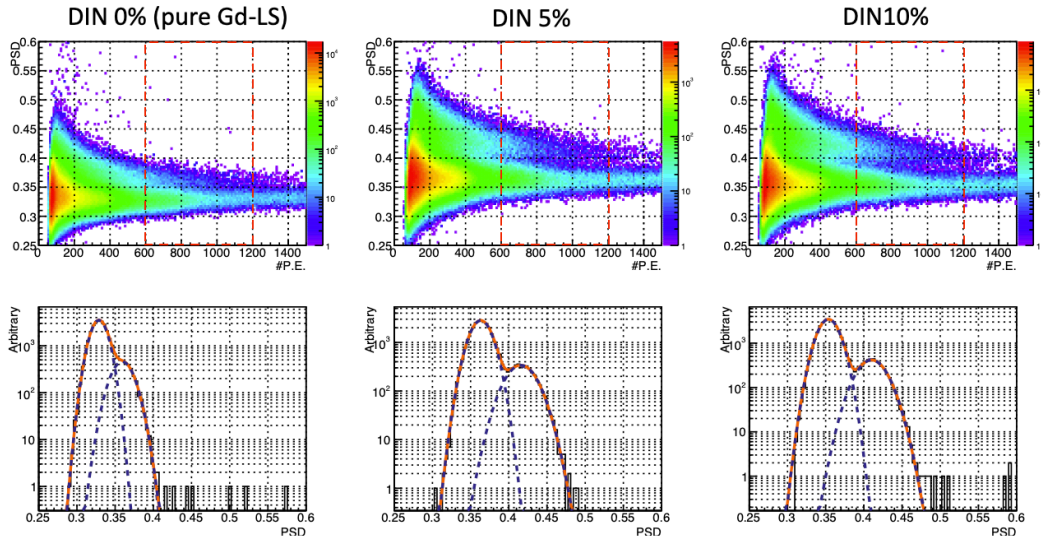


Figure 5.13: The results of PSD capability measurement for each sample. Top panel shows a correlation of $Q_{\text{tail}}/Q_{\text{total}}$ (vertical axis) and Q_{total} (horizontal axis). The bottom panel displays $Q_{\text{tail}}/Q_{\text{total}}$ distribution in the selection region (600 - 1200 p.e.) shown in the top panel.

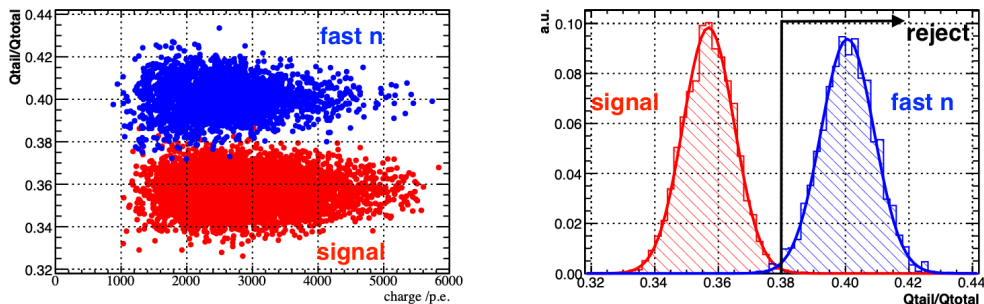


Figure 5.14: The estimated PSD capability of the DIN mixed Gd-LS in the JSNS² detector. Left: $Q_{\text{tail}}/Q_{\text{total}}$ versus Q_{total} in the unit of the number of p.e.. Right: $Q_{\text{tail}}/Q_{\text{total}}$ distribution in the prompt signal region. The black line shows the criterion at neutron rejection power 200.

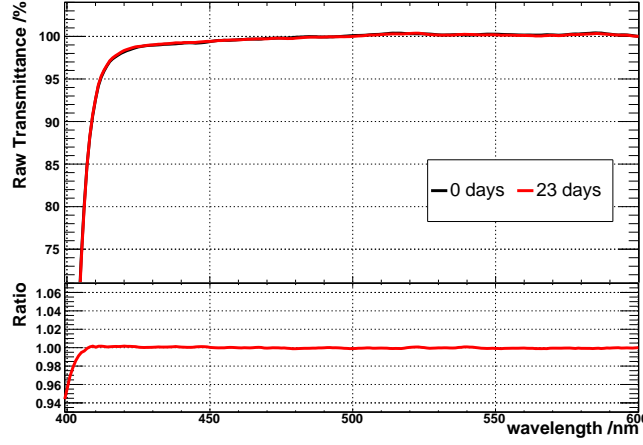


Figure 5.15: The measured transmittance spectrum. The top panel shows raw transmittance spectra of the DIN mixed sample measured in the first day (black) and 23 day later (red). The bottom panel displays the ratio spectrum of the red one to the black one as a function of wavelength. The drop below 410 nm is because of divergence of the ratio.

5.4 Sensitivity for Sterile Neutrino Search

In this section, expected sensitivity of sterile neutrino search is calculated based on the event rate measured in the first run and the signal efficiency estimated above. The calculation is done in the binned maximum likelihood method with the systematic uncertainty treatment described in section 5.1. To perform it, we first estimate the number of events of each component taking the optimization of selection criteria and the hardware countermeasure into account: $\bar{\nu}_\mu \rightarrow \bar{\nu}_e$, $\bar{\nu}_e$ from μ^- , $\nu_e + {}^{12}\text{C} \rightarrow e^- + {}^{12}\text{N}_{\text{g.s.}}$, cosmic fast neutron and total accidental background.

5.4.1 Expected Number of Event Estimation

Signal IBD

The expected number of signal event N_{signal} can be computed from

$$\begin{aligned} N_{\text{signal}} &= \epsilon_{\text{signal}} \times n_p^{\text{GdLS}} \cdot V^{\text{GdLS}} \cdot T_{\text{beam}} \times \int dE f_{\bar{\nu}_\mu}(E) \sigma(E) P_{\bar{\nu}_\mu \rightarrow \bar{\nu}_e}(E) \\ &= \epsilon_{\text{signal}} \times n_p^{\text{GdLS}} \cdot V^{\text{GdLS}} \cdot T_{\text{beam}} \times 9.3 \times 10^{-48} \int dE f_{\bar{\nu}_\mu}(E) E^2 P_{\bar{\nu}_\mu \rightarrow \bar{\nu}_e}(E), \end{aligned} \quad (5.16)$$

where ϵ_{signal} is the signal efficiency, n_p^{LS} is the number of proton in the Gd-LS, and T_{beam} is total beam time. The flux $f(E)$ can be written down using the normalized flux $\Phi_{\bar{\nu}_\mu}$ as

$$f_{\bar{\nu}_\mu}(E) = n_{\text{POT}} \times \frac{R_{\bar{\nu}_\mu/p} \Phi_{\bar{\nu}_\mu}(E)}{4\pi L^2}, \quad (5.17)$$

where n_{POT} is the number of proton on target in a year, $R_{\bar{\nu}_\mu/p}$ is the number of $\bar{\nu}_\mu$ per proton on target, and L is the baseline. Each input value is listed as follows:

- $\epsilon_{\text{signal}} = 0.247$
- $n_p^{\text{GdLS}} = 6.48 \times 10^{28} \text{ m}^{-3}$,
- $V^{\text{GdLS}} = 19.3 \text{ m}^3$,
- $T_{\text{beam}} = 3 \text{ years}$,
- $n_{\text{POT}} = 3 \times 10^{22} \text{ /year}$ ($3.6 \times 10^8 \text{ spill/year}$),
- $R_{\bar{\nu}_\mu/p} = 0.344$,
- $L = 24 \text{ m}$.

In case the oscillation parameters are $(\Delta m^2, \sin^2 2\theta) = (2.5, 3 \times 10^{-3})$, for example, the expected number of event will be 59 events.

IBD of $\bar{\nu}_e$ from μ^-

The selection efficiency of $\bar{\nu}_e$ from μ^- is basically same as the signal efficiency, except for the selection to prompt energy due to the difference of spectrum shape. The energy spectrum of the MC simulation for $\bar{\nu}_e$ from μ^- events is shown in figure 5.7 as an orange line histogram. Following the efficiency definition for the signal, the selection efficiency for $\bar{\nu}_e$ from μ^- events is 93.4 %. Thus, the total efficiency for the IBD selection to $\bar{\nu}_e$ from μ^- is finally %.

The flux of $\bar{\nu}_e$ from μ^- is denoted as

$$f_{\bar{\nu}_e}(E) = n_{\text{POT}} \times \frac{R_{\bar{\nu}_e/p} \Phi_{\bar{\nu}_e}(E)}{4\pi L^2}, \quad (5.18)$$

where the number of $\bar{\nu}_e$ per proton on target $R_{\bar{\nu}_e/p}$ is 1.7×10^{-3} smaller compared to the signal case due to π^- and μ^- absorption on mercury nucleus according to table 2.2.

Series of reaction: $^{12}\text{C}(\nu_e, e^-)^{12}\text{N}_{\text{g.s.}}$ and β^+ decay of $^{12}\text{N}_{\text{g.s.}}$

For computing the number of event of $\nu_e + ^{12}\text{C} \rightarrow e^- + ^{12}\text{N}_{\text{g.s.}}$, the number density of target $n_{^{12}\text{C}}$ and cross section are needed. The number of target can be calculated as $n_p^{\text{GdLS}} \times R_{\text{C/H}} = 1.06 \times 10^{29} \text{ m}^{-3}$ according to the C/H ratio of the Daya Bay Gd-LS [59]. The cross section value $\sigma = 9.4 \times 10^{-42} \text{ cm}^2$ is used in this study, which was measured in KARMEN using μDAR electron neutrino identical to JSNS². In addition to them, the efficiency of $\nu_e + ^{12}\text{C} \rightarrow e^- + ^{12}\text{N}_{\text{g.s.}}$ in the signal selection criteria need to be considered. The event rate is significantly limited by the condition $\Delta t_{\text{p-d}} < 100 \mu\text{s}$ because the life time of $^{12}\text{N}_{\text{g.s.}}$ decay is 15.9 ms, and therefore, the efficiency is computed as 0.6 % based on exponential function. The selection efficiencies to prompt energy, delayed energy and $\Delta VTX_{\text{p-d}}$ are estimated based on MC simulation as following the signal case. Figure 5.16 shows distributions of them, and the red dashed boxes indicate the selection region to each variables. As following the signal case, the efficiencies are 61.2 % for prompt energy, 17.2 % for delayed energy, and 98.7 % for $\Delta VTX_{\text{p-d}}$, respectively. Therefore, the total efficiency for the IBD selection to $^{12}\text{C}(\nu_e, e^-)^{12}\text{N}_{\text{g.s.}}$ is finally 0.065 %.

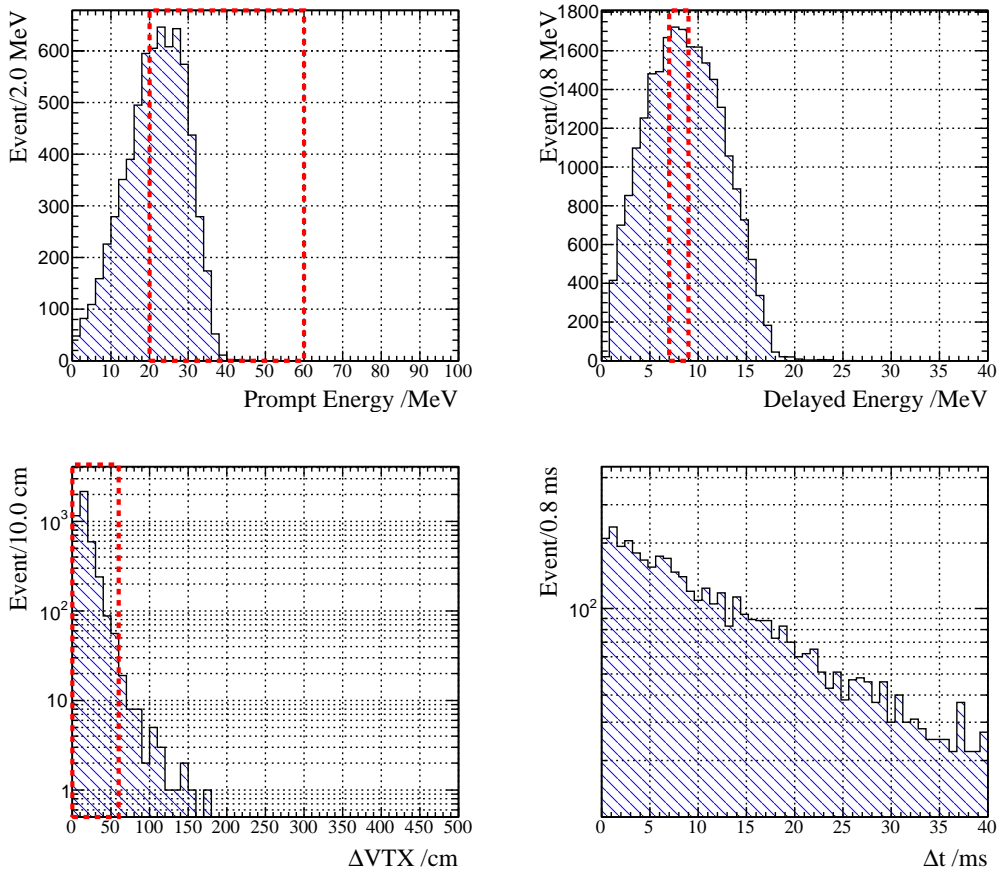


Figure 5.16: The delayed coincidence of $\nu_e + {}^{12}\text{C} \rightarrow e^- + {}^{12}\text{N}_{\text{g.s.}}$. Top left: prompt energy spectrum. Top right: delayed energy spectrum. Bottom left: ΔVTX_{p-d} distribution. Bottom right: Δt distribution. The red dashed boxes on each plot show selection criteria to each variable.

Cosmic fast neutron

The event rate of cosmic fast neutron should be revised based on the selection optimization result. For fast neutron, PSD and Life time cut are newly added to selections used in the background measurement, and the efficiencies of $\Delta VTX_{\text{OB-d}}$ and E_{delayed} is to be modified according to the result of the selection optimization. The cosmic fast neutron rate after the delayed energy selection modification is 2.54×10^{-5} /spill. Therefore, the revised rate $R_{\text{fastn}}^{\text{rev}}$ is computed from the measured rate R_{fastn} as follows:

$$\begin{aligned} R_{\text{fastn}}^{\text{rev}} &= R_{\text{fastn}} \times \epsilon_{\text{PSD}}^n \times \epsilon_{\text{Lifetime}}^n \times \rho_{\Delta VTX_{\text{OB-d}}} \\ &= R_{\text{fastn}} \times \epsilon_{\text{PSD}}^n \times 0.472 \times \frac{0.846}{0.921} \text{ /spill,} \end{aligned} \quad (5.19)$$

where ϵ^n indicates an efficiency of each selection to fast neutron event, and ρ is a ratio of efficiencies between before and after the optimization for each variable. After liquid scintillator upgrade, the rejection efficiency of PSD will be 1/200 with keeping the signal efficiency value.

Total accidental background

The total accidental rate R_{acc} is calculated in the following formula

$$R_{\text{acc}} = \sum \left(\sum R_i^{\text{prompt}} \times R_i^{\text{delayed}} \times \epsilon_i^{\text{Lifetime}} \times \epsilon_i^{\Delta VTX} \right) \text{ /spill,} \quad (5.20)$$

where R_i^{prompt} is the rate of i -th prompt accidental component, R_i^{delayed} is the rate of i -th delayed accidental component, and $\epsilon_i^{\text{Lifetime}}$ and $\epsilon_i^{\Delta VTX}$ are selection efficiencies of Lifetime cut and ΔVTX cut, respectively. Therefore, it is computed using the estimated values as

$$\begin{aligned} R_{\text{acc}} &= (R_{\text{cosmic } \gamma}^{\text{prompt}} + R_{\text{Michele}}) \times (R_{\text{floor } \gamma} \times \epsilon_{\text{shield}} + R_{\text{OB-nGd}} + R_{\text{cosmic } \gamma}^{\text{delayed}}) \\ &\quad \times \epsilon_{\Delta VTX_{\text{p-d}}}^{\text{acc}} \times \epsilon_{\text{Lifetime}}^{\text{acc}} \times \epsilon_{E_{\text{delayed}}}^{\text{acc}} \times \epsilon_{\text{PSD}}, \\ &= (4.66 + 0.77) \times 10^{-4} \times \left\{ (5.34 \times \epsilon_{\text{shield}} + 0.0438) \times \frac{1}{0.6} + 0.824 \right\} \times 10^{-2} \\ &\quad \times 0.025 \times 0.255 \times 0.755 \times 0.99 \text{ /spill,} \end{aligned} \quad (5.21)$$

where ϵ^{acc} indicates the selection efficiency of each variable estimated above, except for ϵ_{shield} , and ϵ_{shield} is the rejection factor of the shield configuration compared to the current one. If we upgrade the shield, ϵ_{shield} will be 21/124. Note that R_{Michele} already includes the effect of muon veto time, and the factor of 1/0.6 is applied to $R_{\text{floor } \gamma}$ and $R_{\text{OB-nGd}}$ in order to take beam power dependence of them into account.

5.4.2 Sensitivity

Table 5.7 summarizes the expected number of event estimation for signal and each background. The baseline of the detector from the target is 24 m, and the operation period is 5000 hours \times 3 years for one detector. The column of "Reference" shows the values from the reference [9]. The "Current" and "Upgrade" column compares

Table 5.7: Summary of the expected number of events for 5000 hours \times 3 years.

	Components	Reference [9]	Current	Upgrade
Signal	$\sin^2 2\theta = 3.0 \times 10^{-3}$ $\Delta m^2 = 2.5 \text{ eV}^2$ (MLF Best fit)	87	59	59
	$\sin^2 2\theta = 3.0 \times 10^{-3}$ $\Delta m^2 = 1.2 \text{ eV}^2$ (LSND Best fit)	62	38	38
Background	$\bar{\nu}_e$ from μ^-	43	27	27
	$^{12}\text{C}(\nu_e, e^-)^{12}\text{N}_{g.s.}$	3	2	2
	Cosmic fast n	negligible	117	58
	Total accidental events	20	278	68

the expected number of events before and after the upgrade as a countermeasure to cosmic fast neutron and accidental backgrounds described above.

Figure 5.17 displays an example of the prompt energy spectrum at oscillation parameter $(\Delta m^2, \sin^2 2\theta) = (2.5 \text{ eV}^2, 3.0 \times 10^{-3})$, and compares the cases before (top) and after the upgrade (bottom). Note that we assume the energy spectrum of the signal $\bar{\nu}_\mu \rightarrow \bar{\nu}_e$ (brown area), $\bar{\nu}_e$ from μ^- (red line) and $^{12}\text{C}(\nu_e, e^-)^{12}\text{N}_{g.s.}$ (green line) are from the MC simulation output including the reconstruction. We used the spectrum of cosmic fast neutron and accidental background measured in the first run data. In comparing the spectra, one can find the large improvement on signal to background ratio because of the upgrade. Figure 5.18 is the prompt energy spectrum at oscillation parameter $(\Delta m^2, \sin^2 2\theta) = (1.2 \text{ eV}^2, 3.0 \times 10^{-3})$ corresponding to the best fit parameters from the LSND experiment, and compares the cases before (top) and after the upgrade (bottom) in the same manner as figure 5.17.

Figure 5.19 shows sensitivity of sterile neutrino search. 90 % C.L. exclusion line of the reference [9] (black), before (green) and after the upgrade (red) are shown and overlaid with the allowed parameter space from the LSND experiment [3]. The configuration assumed here is matched to the reference: 3 years experimental duration with 1 MW beam power using a single 17 tons detector. It turns out that the 90% C.L. exclusion limit at $\Delta m^2 = 1.2 \text{ eV}^2$ (LSND best-fit) in the current configuration (without the upgrades) shows 80 % degradation with respect to the expected sensitivity in the reference, and the best-fit parameter $\sin^2 2\theta = 3.0 \times 10^{-3}$ is out of the exclusion limit. In contrast, the sensitivity recovers to 38 % degradation compared to the expectation if we conduct the upgrade as countermeasure. It is possible to give a conclusion on the oscillation parameter $(\Delta m^2, \sin^2 2\theta) = (1.2 \text{ eV}^2, 3.0 \times 10^{-3})$ at 90% C.L.. The degradation on the sensitivity can be recovered by extending the experimental duration. Sensitivity in case of twice of the experimental duration, 6 years, is shown as the green line in figure 5.20 and approaches to the designed performance on sensitivity in the reference. The difference between the 6 years sensitivity and the designed one is 19 %. It can explore most of the parameter space indicated by LSND experiment except for a part of the region $\Delta m^2 < 2 \text{ eV}^2$.

Figure 5.21 shows a comparison between the global fit result (99 % C.L.) [4] and 90 % C.L. (orange) and 99 % C.L. exclusion limits of the JSNS² (magenta) in 3 years experimental duration configuration. Although the sensitivity reaches to the current exclusion limitation from KARMEN experiment, the global fit preferred region (red

colored area) is out of the sensitivity. Extending the experimental duration from 3 to 6 years is also inadequate for exploring the preferred region as shown in figure 5.22.

To explore the entire allowed parameter space especially low Δm^2 region favored in the global fit, not only extending experimental duration, the following future extension are highly desired: Reducing the dominant systematic uncertainty, flux of $\bar{\nu}_e$ from μ^- , by an external experiment measuring π production in mercury, and an additional detector at longer baseline to obtain sensitivity at the low Δm^2 region. These are discussed in the next chapter.

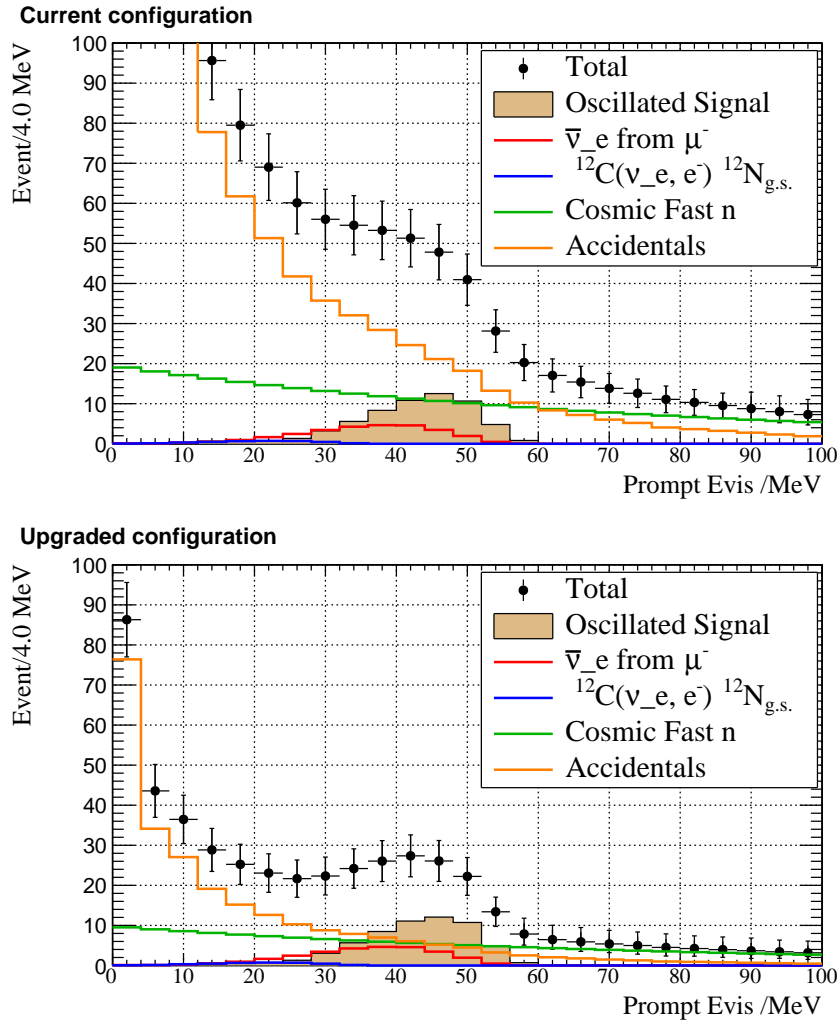


Figure 5.17: Top: Expected energy spectrum of prompt signal in the current configuration. Bottom: that of the upgraded configuration in the condition of $1 \text{ MW} \times 3 \text{ years} \times 1 \text{ detector}$. The oscillated signal in case of $(\Delta m^2, \sin^2 2\theta) = (2.5 \text{ eV}^2, 3.0 \times 10^{-3})$ (brown shaded area), the IBD of $\bar{\nu}_e$ from μ^- (red), $\nu_e + ^{12}\text{C} \rightarrow e^- + ^{12}\text{N}_{\text{g.s.}}$ (blue), cosmic fast neutron (green) and total accidental background (orange) are displayed together. The spectrum shown in the black points corresponds to the summation of all spectra.

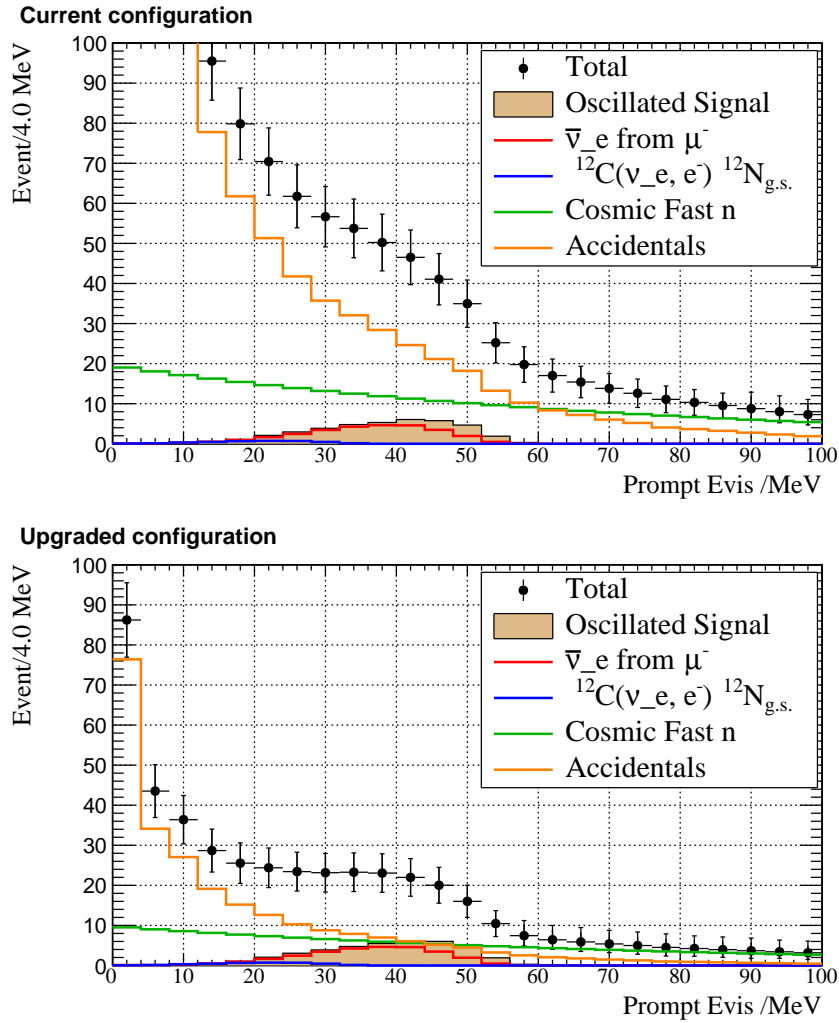


Figure 5.18: Top: Expected energy spectrum of prompt signal in the current configuration. Bottom: that of the upgraded configuration in the condition of $1 \text{ MW} \times 3 \text{ years} \times 1 \text{ detector}$. The oscillated signal in case of $(\Delta m^2, \sin^2 2\theta) = (1.2 \text{ eV}^2, 3.0 \times 10^{-3})$ (brown shaded area), the IBD of $\bar{\nu}_e$ from μ^- (red), $\nu_e + ^{12}\text{C} \rightarrow e^- + ^{12}\text{N}_{\text{g.s.}}$ (blue), cosmic fast neutron (green) and total accidental background (orange) are displayed together. The spectrum shown in the black points corresponds to the summation of all spectra.

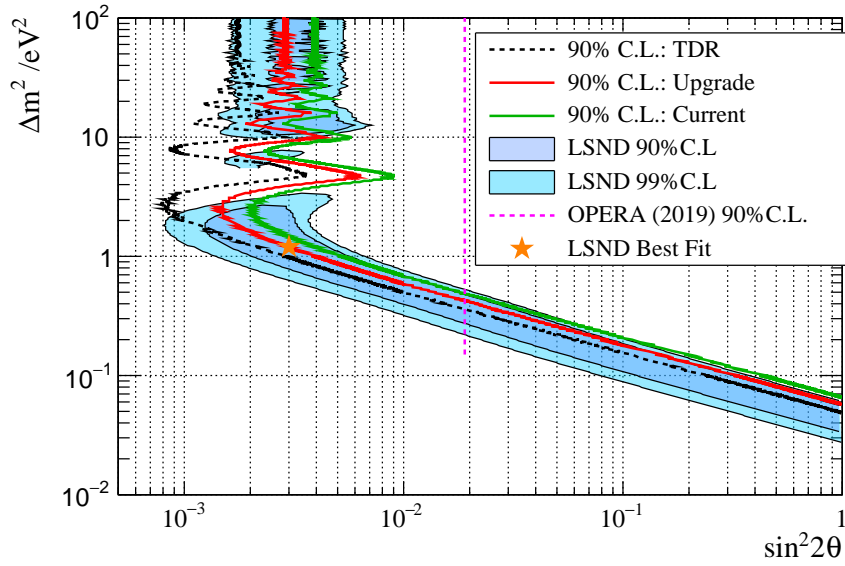


Figure 5.19: Sensitivity of JSNS² experiment based on the real data. 90% C.L. exclusion lines of the expectation in reference [9] (black), the upgraded configuration (red) and the current configuration (green) are displayed. The star points at the parameters of LSND best-fit. The exclusion line of the OPERA experiment is also shown [60].

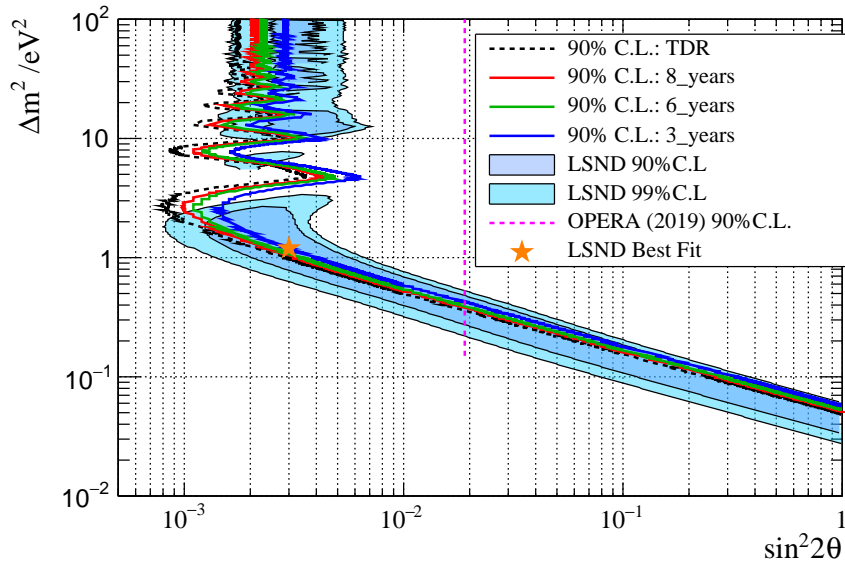


Figure 5.20: 90% C.L. exclusion to 3 + 1 sterile oscillation from JSNS² experiment in case of 3 years (blue), 6 years (green) and 8 years experimental duration (red) after the upgrade. It is turned out that 6 years experimental duration improves the sensitivity within 19 % loss with respect to the designed performance on sensitivity in reference [9] (black).

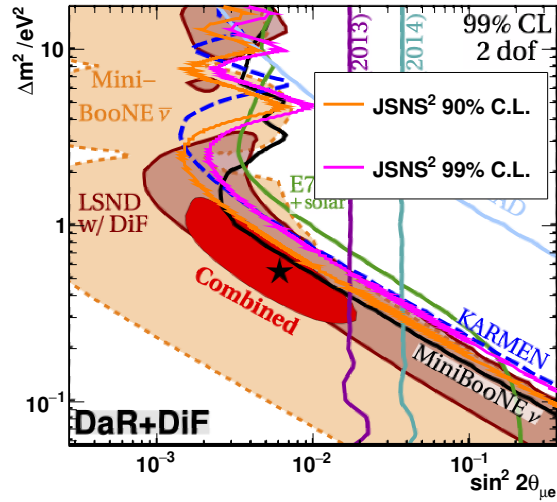


Figure 5.21: A comparison between the global fit result (red region) and 90% C.L. (orange), 99 % C.L. sensitivities of JSNS² experiment in case of 3 years experimental duration after the upgrade. It is shown that the sensitivity is insufficient to cover the global fit favored region even it can reach to the KARMEN exclusion limit [5].

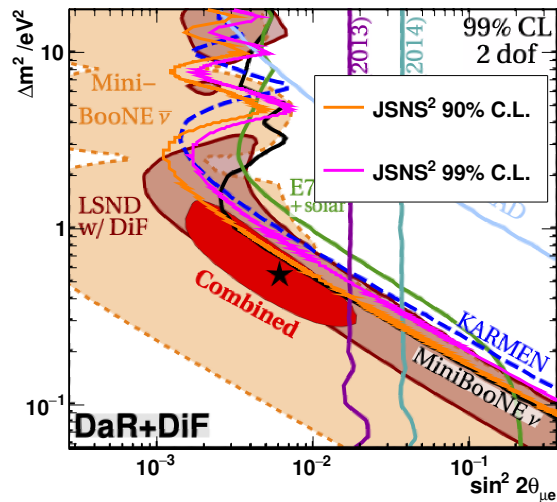


Figure 5.22: A comparison between the global fit result (red region) and 90% C.L. (orange), 99 % C.L. sensitivities of JSNS² experiment in case of 6 years experimental duration after the upgrade. Extending the experimental duration from 3 to 6 years gives a slight improvement.

Chapter 6

Future extension

In the previous chapter, the sensitivity to the sterile neutrino search with the single detector for the first 3 year was shown. It indicates that the majority of the region in $\Delta m^2 > 2 \text{ eV}^2$ within 3 to 6 years is a result of the hardware countermeasure. To explore the entire allowed parameter space, especially low Δm^2 region favored in the global fit [4], the following future extension are highly desired:

- Reducing the dominant systematic uncertainty on flux of $\bar{\nu}_e$ from μ^- by measurement of π production in mercury,
- An additional detector at longer baseline to obtain sensitivity at the low Δm^2 region.

In this chapter, prospects of these extensions are described.

6.1 Pion production measurement

Currently, JSNS² experiment has a large uncertainty on the $\bar{\nu}_e$ flux from μ^- -DAR. We assign 50 % as a systematic uncertainty on it from the discrepancy between the simulation models used in the neutrino flux estimation as described in chapter 2. According to ENDF [61], the evaluated nuclear reaction data library, the evaluated value in ENDF also heavily depends on nuclear model due to a lack of experimental data for nucleon reactions on mercury. In particular, there is no experimental data on pion production cross section on mercury with 3 GeV proton. Therefore, it is crucial to perform a cross section measurement in order to reduce the dominant systematic uncertainty of the JSNS² experiment.

6.1.1 NA61/SHINE

The NA61/SHINE is an experiment for measurement of hadron and nuclear fragment production properties in fixed-target reactions induced by hadron and ion beams. There are extensions for measurements of hadron-production for neutrino experiments. For example, T2K experiment joined to them and conducted a measurement of the production of charged pions and kaons on their carbon target for precise prediction calculation of the neutrino beam components and fluxes [63].

Figure 6.1 shows the experimental setup of the NA61/SHINE detectors. The momentum of the proton beam provided to there is several tens of GeV/c in present.

However, low energy beamline providing 1 to 10 GeV/c proton is being planned aiming at launching data taking in 3 years [64]. The members of JSNS² collaboration have launched an investigation for the experiment opportunity with the mercury target group in J-PARC.

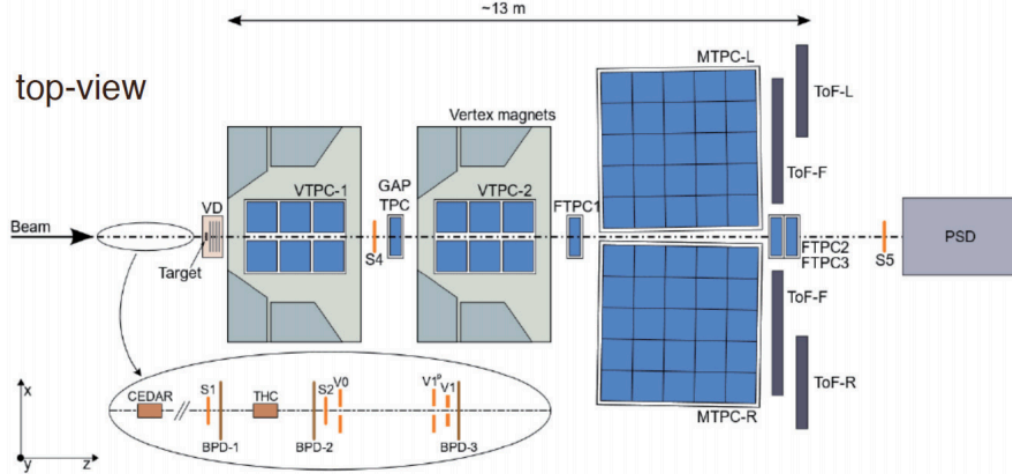


Figure 6.1: A schematic view of the detectors in NA61/SHINE experiment [62].

6.2 JSNS² - II

The JSNS²-II is the second phase of the JSNS² experiment with an additional detector placed at 48 m away from the mercury target as well as the current detector at 24 m baseline [65]. The detector located farther site (far detector) can contribute to large improvement on the sensitivity of the sterile neutrino search in the low Δm^2 region favored in the global fit [4]. The measurement with both the current detector (near detector) and the far detector has a potential to give a rigid conclusion on the LSND anomaly.

Figure 6.2 shows the planned location for the far detector. It is outside of the MLF building. Therefore, the detector has no exposure to the floor gamma ray which is a severe source of the accidental background. The detector design is shown in Fig. 6.3. It consists of 35 tons of Gd-LS and 65 tons of LS, where the target mass is twice as much as the near detector. In addition to the target mass, the thickness of gamma catcher and veto layer increase. The former will lead to improvement on the neutron detection efficiency of IBD. It also reinforces shield effect to the cosmic ray induced background, e.g., fast neutron. 240 of 10 inch PMTs are mounted in the far detector to keep the identical photo coverage with the near detector.

6.2.1 Background estimation

In order to estimate a performance of the far detector, the expected background rate is to be estimated based on the MC simulation. For the far detector, the following background are expected:

- cosmic ray induced fast neutron,



Figure 6.2: The planned detector location for the far detector with 48 m baseline.

- cosmic ray induced gamma ray.

The background models developed based on the first run data is used for the far detector case. Figure 6.4 shows a spatial relationship between the modeled concrete wall and the far detector. According to the location of the detector in Fig. 6.2, only one concrete volume with 20 m height, 20 m width and 1 m thickness is assumed. The dimension of the detector geometry follows the specification shown in Fig. 6.3.

Based on the MC result, FD-ND ratio for each component is estimated as a ratio of the number of events in the far detector to that of events in the near detector. It will be used for a normalization factor to scale the expected number of events in the near detector estimated in the previous chapter to that of events in the far detector for sensitivity calculation.

Figure 6.5 shows the prompt energy spectra (top left), delayed energy spectra (top right), Δt distributions (bottom left), ΔVTX distributions (bottom right) of the near detector (black line) and the far detector (blue line) as results of the MC simulation for cosmic fast neutron. The FD-ND ratio for cosmic neutron is computed as a ratio of the remained number of events in the IBD selection criteria in each detector. As a result, the FD-ND ratio for cosmic neutron is estimated to be 0.32.

Accordingly, the ND-FD ratio for cosmic gamma ray is estimated. The energy spectra in the prompt energy range (left) and in the delayed energy spectra (right) of the near detector (black line) and the far detector (blue line) are shown in Fig. 6.6. The FD-ND ratio for cosmic gamma ray is computed as a ratio of the number of events in the selection criteria in each detector. As a result, the FD-ND ratio for cosmic gamma ray is estimated to be 0.58 for the prompt signal region and 0.44 for the delayed signal region, respectively.

6.2.2 Sensitivity

For the sensitivity calculation, the binned maximum likelihood method is used. In order to combine the near and the far detector contribution, the likelihood in

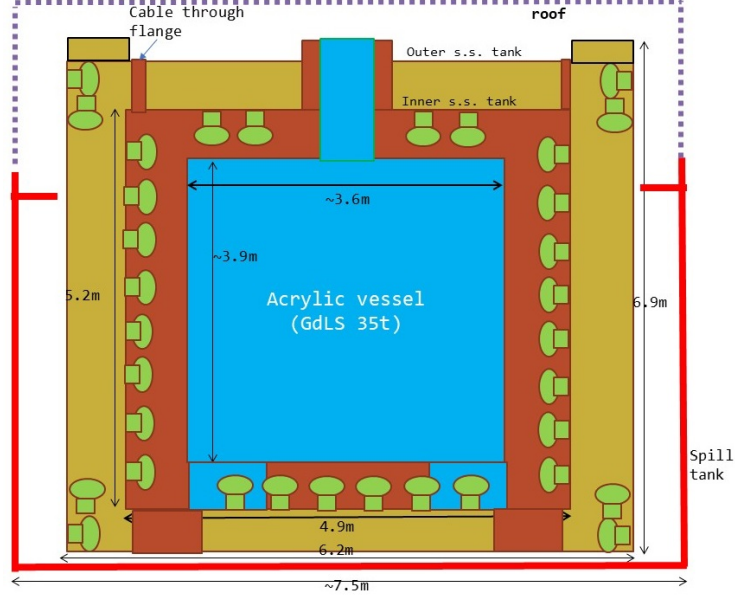


Figure 6.3: A schematic design of the far detector. The basic design is identical with the near detector.

Eq. (5.1) is modified as follows:

$$\begin{aligned} \mathcal{L} &= \mathcal{L}_1 \times \mathcal{L}_2 \\ &= \left[\prod_i P_1(N_{\text{exp}}^i | N_{\text{obs}}^i) \right]_1 \times \left[\prod_i P_2(N_{\text{exp}}^i | N_{\text{obs}}^i) \right]_2, \end{aligned} \quad (6.1)$$

where \mathcal{L}_1 and \mathcal{L}_2 are the likelihood of the near and the far detector. Note that the definition of each likelihood component is same as Eq. (5.1). The systematic uncertainties are also considered in the same method used in the previous chapter. That is,

$$\mathcal{L} = \mathcal{L} \times \exp\left(-\frac{(1-f_1)^2}{2\Delta\sigma_1^2}\right) \times \exp\left(-\frac{(1-f_2)^2}{2\Delta\sigma_2^2}\right), \quad (6.2)$$

where

$$N'_{\text{exp}} = f_1 \times N_{\text{Signal}}(\Delta m^2, \sin^2 2\theta) + (f_2 \times N_{\text{BG}}^{\text{IBD}} + \sum N_{\text{BG}}^{\text{others}}), \quad (6.3)$$

and $\Delta\sigma_i$ gives uncertainty on the normalization factor of the i -th component.

Table 5.7 summarizes the expected number of event estimation for signal and each background. The baselines of the detectors from the target are set to 24 m and 48 m, respectively. The operation period is 5000 hours \times 8 years for the near detector and 5 years for the far detector. In the event rate estimation, the FD-ND ratios are used for the cosmic ray induced backgrounds. Note that it is assumed that the neutron rejection power of PSD in the far detector is 100 in contrast with the near detector. We conservatively assume that the far detector has the same signal detection efficiency as the near detector.

Figure 5.17 displays an example of the prompt energy spectrum of the near detector (top) and that of the far detector (bottom) at oscillation parameter $(\Delta m^2, \sin^2 2\theta) =$

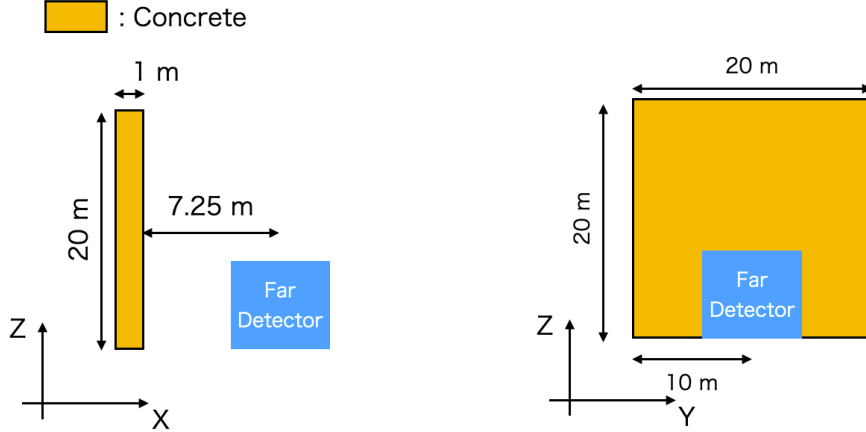


Figure 6.4: A model of concrete walls around the far detector site shows spatial relations to the far detector in the XZ plane (left) and the YZ plane (right), respectively. We assume that cosmic ray induced fast neutron/gamma ray generated in the concrete volume as a result of an interaction between cosmic muon and matter in the concrete.

Table 6.1: Summary of the expected number of events for 5000 hours \times 8 years for the near detector and 5 years for the far detector, respectively.

	Components	Near Detector (17 t)	Far Detector (35 t)
Signal	$\sin^2 2\theta = 3.0 \times 10^{-3}$ $\Delta m^2 = 2.5 \text{ eV}^2$ (MLF Best fit)	157	16
	$\sin^2 2\theta = 3.0 \times 10^{-3}$ $\Delta m^2 = 1.2 \text{ eV}^2$ (LSND Best fit)	100	48
Background	$\bar{\nu}_e$ from μ^-	72	22
	$^{12}\text{C}(\nu_e, e^-)^{12}\text{N}_{g.s.}$	5	2
	Cosmic fast n	145	58
	Total accidental events	177	10

(2.5 eV^2 , 3.0×10^{-3}). Note that we assume the energy spectrum of the signal $\bar{\nu}_\mu \rightarrow \bar{\nu}_e$ (brown area), $\bar{\nu}_e$ from μ^- (red line) and $^{12}\text{C}(\nu_e, e^-)^{12}\text{N}_{g.s.}$ (green line) are from the MC simulation output including the reconstruction. For the far detector, the same energy resolution is assumed because of the identical photo coverage. Figure 5.17 shows the other example of the prompt energy spectrum of the near detector (top) and that of the far detector (bottom) at oscillation parameter $(\Delta m^2, \sin^2 2\theta) = (1.2 \text{ eV}^2, 3.0 \times 10^{-3})$. It is clear that the double detector configuration has a complementary function to the sensitivity of sterile neutrino oscillation search.

Figure 6.9 shows a comparison between the global fit result (99 % C.L.) [4] and 90 % C.L. exclusion limits of the JSNS²-II configuration in case the uncertainty on $\bar{\nu}_e$ from μ^- flux are 50 % (green dashed line), 20 % (light blue dashed line) and 10 % (magenta line), respectively. The orange dashed line is 90 % C.L. sensitivity of the first 3 year for comparison. It is obvious that the global fit favored region

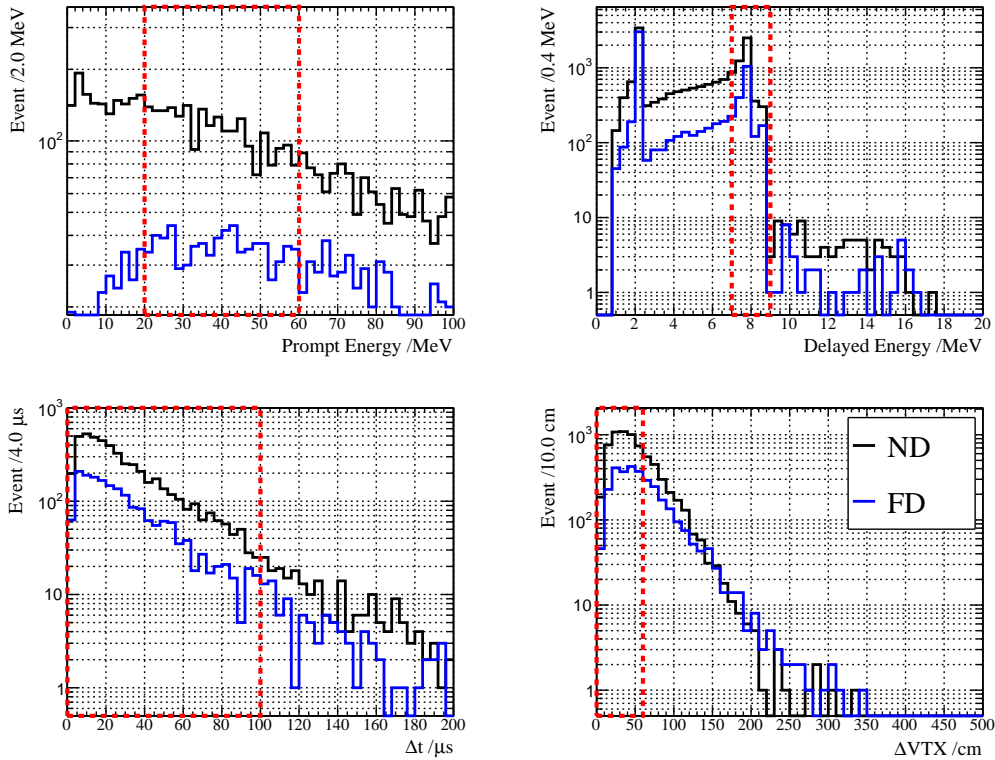


Figure 6.5: The MC simulation results of the cosmic fast neutron. Prompt energy spectra (top left), delayed energy spectra (top right), Δt distributions (bottom left), ΔVTX distributions (bottom right) of the near detector (black line) and the far detector (blue line), respectively. The red dashed boxes show the selection criteria for each variables.

(red region) is fully cover by 90 % C.L. exclusion limit even we leave the dominant systematic uncertainty 50 %. If the uncertainty is reduced to 10 % by the pion production cross section measurement at NA61/SHINE, the entire region of the LSND allowed oscillation parameter space will be concluded at > 90 % C.L..

Accordingly, Fig. 6.10 shows a comparison between the global fit result (99 % C.L.) [4] and 3σ C.L. exclusion limits of the JSNS²-II configuration in the same manner as Fig. 6.9. The 3σ sensitivity with 50 % $\bar{\nu}_e$ flux uncertainty can exclude most of the global fit favored region and the LSND allowed region. The coverage of the 3σ sensitivity highly depends on the amount of the $\bar{\nu}_e$ flux uncertainty. Almost all of the global fit favored region can be concluded at 3σ C.L. if we reach to 10 % $\bar{\nu}_e$ flux uncertainty.

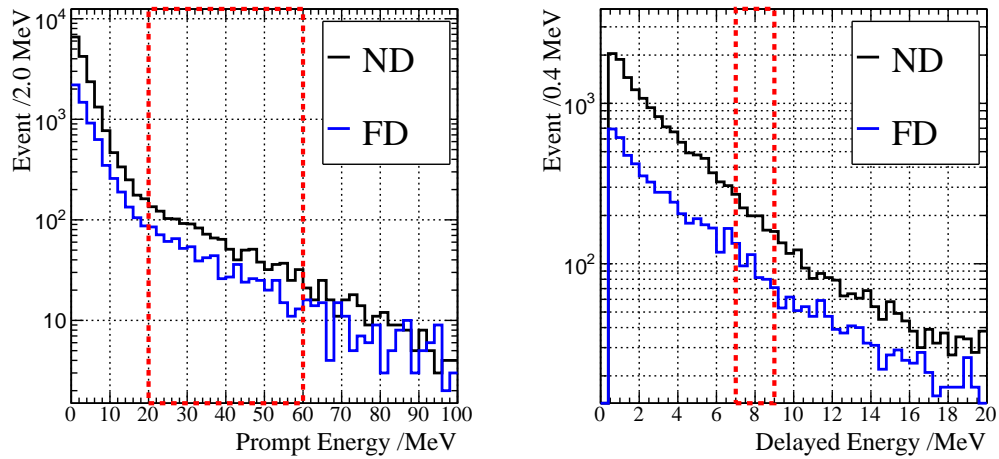


Figure 6.6: The MC simulation result of the cosmic gamma ray. The energy spectra in the prompt energy range (left) and in the delayed energy (right) of the near detector (black line) and the far detector (blue line) are shown, respectively. The red dashed boxes show the selection criteria for each variables.

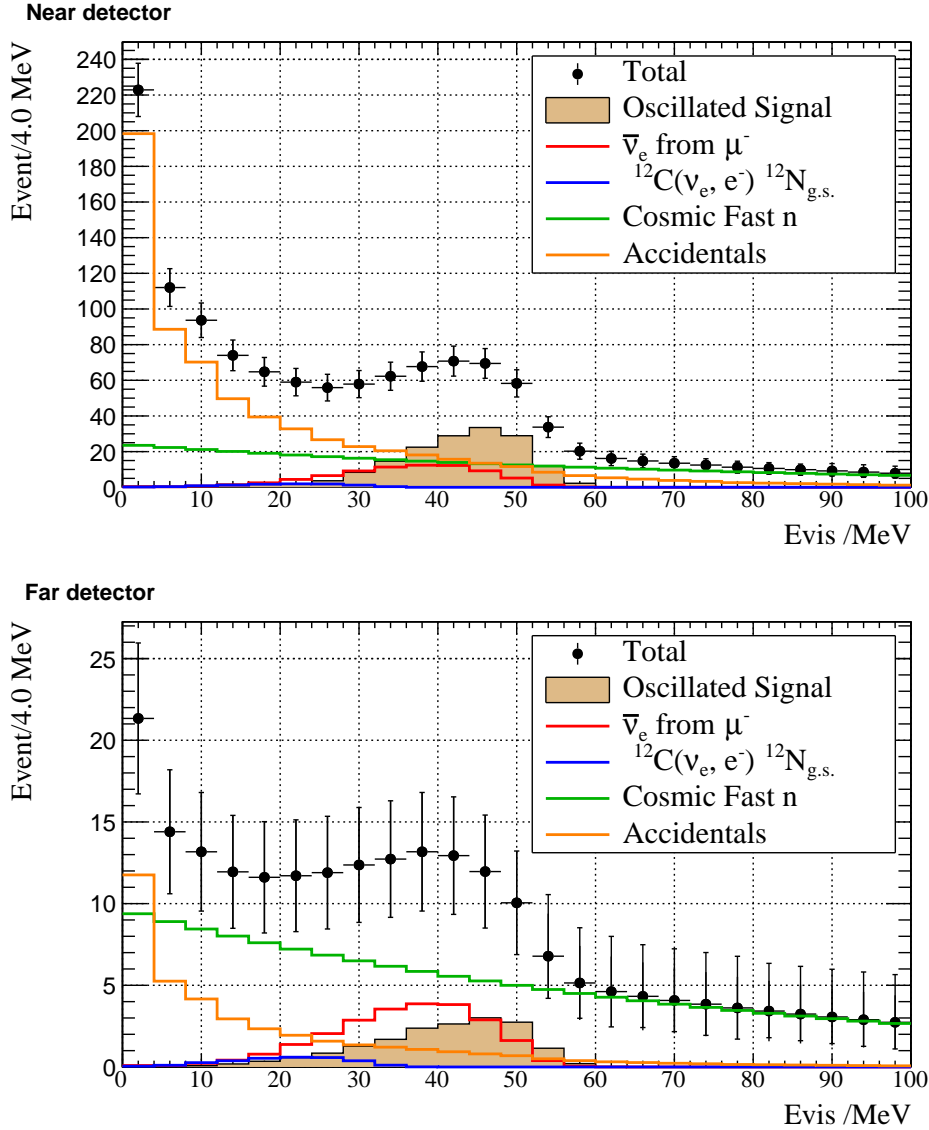


Figure 6.7: Top: Expected prompt energy spectrum of the near detector for 8 years. Right: that of the far detector for 5 years. The oscillated signal in case of $(\Delta m^2, \sin^2 2\theta) = (2.5 \text{ eV}^2, 3.0 \times 10^{-3})$ (brown shaded area), the IBD of $\bar{\nu}_e$ from μ^- (red), $\nu_e + ^{12}\text{C} \rightarrow e^- + ^{12}\text{N}_{\text{g.s.}}$ (blue), cosmic fast neutron (green) and total accidental background (orange) are displayed together. The spectrum shown in the black points corresponds to the summation of all spectra.

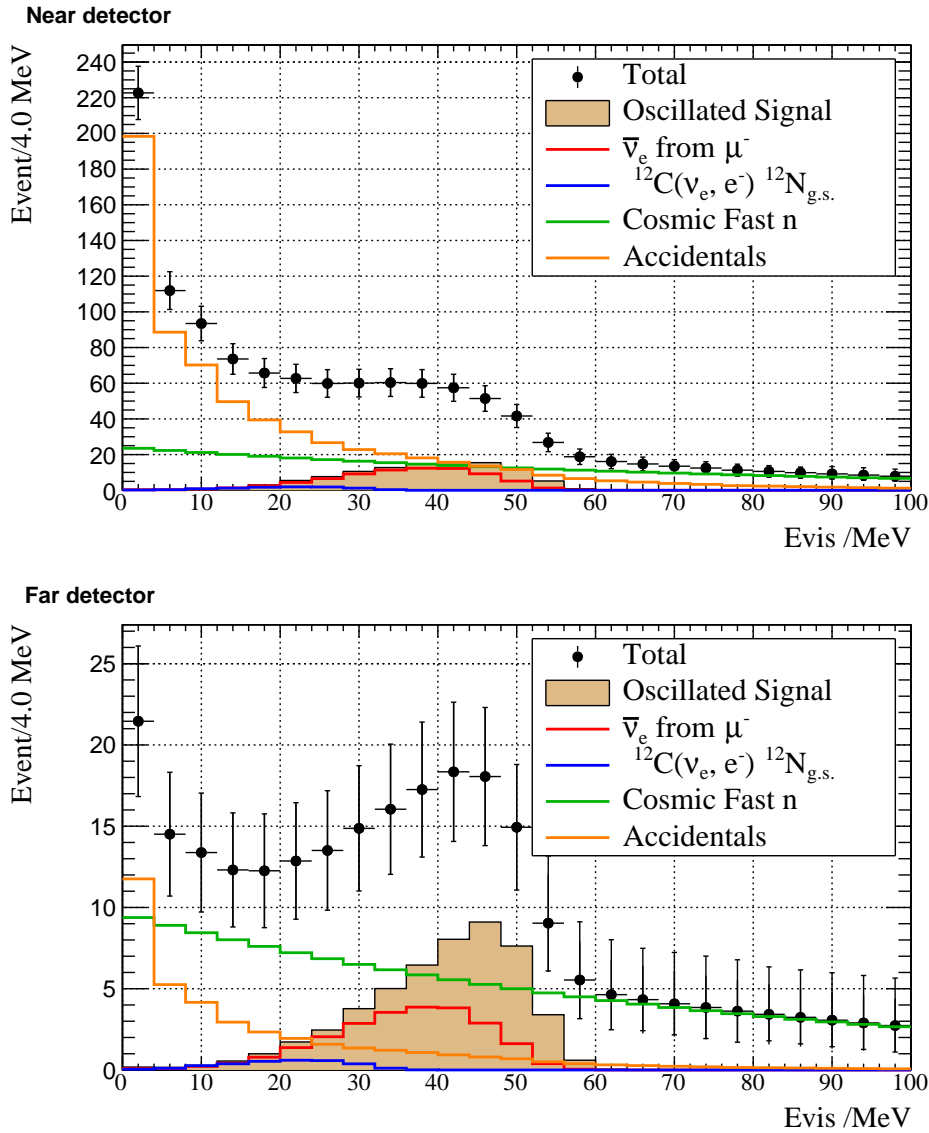


Figure 6.8: Top: Expected prompt energy spectrum of the near detector for 8 years. Right: that of the far detector for 5 years. The oscillated signal in case of $(\Delta m^2, \sin^2 2\theta) = (1.2 \text{ eV}^2, 3.0 \times 10^{-3})$ (brown shaded area), the IBD of $\bar{\nu}_e$ from μ^- (red), $\nu_e + ^{12}\text{C} \rightarrow e^- + ^{12}\text{N}_{\text{g.s.}}$ (blue), cosmic fast neutron (green) and total accidental background (orange) are displayed together. The spectrum shown in the black points corresponds to the summation of all spectra.

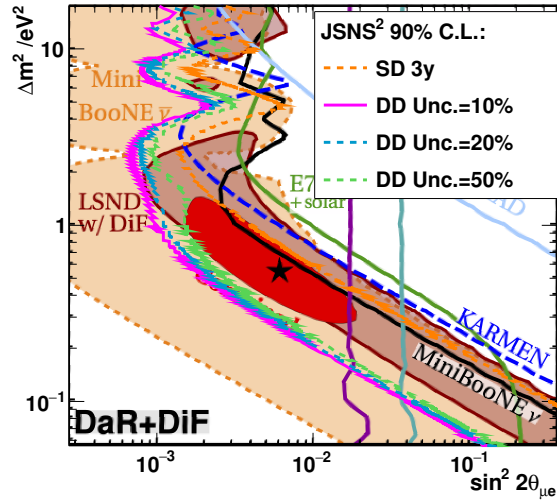


Figure 6.9: A comparison between the global fit result (red region) and 90% C.L. sensitivities of the JSNS²-II configuration in case the uncertainty on $\bar{\nu}_e$ from μ^- flux are 50 % (green dashed line), 20 % (light blue dashed line) and 10 % (magenta line) are shown.

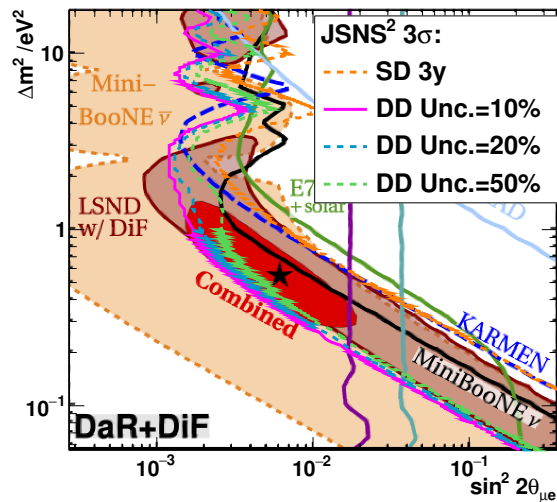


Figure 6.10: A comparison between the global fit result (red region) and 3σ C.L. sensitivities of the JSNS²-II configuration in case the uncertainty on $\bar{\nu}_e$ from μ^- flux are 50 % (green dashed line), 20 % (light blue dashed line) and 10 % (magenta line) are shown.

Chapter 7

Conclusion

The JSNS² experiment is a sterile neutrino search experiment aiming at a direct test to LSND experiment using the neutrino beam in the MLF and Gd-LS detector. As a first phase of the experiment, we start with single detector with 17 tons of fiducial volume and 3 years experimental period. The detector development and construction began in 2016, and it was completed on February 2020. We obtained the first opportunity to perform data taking for 10 days beam time, and it was successfully completed without severe efficiency loss. The obtained data provides us understanding of detector response, background event behavior and event rate of backgrounds in the neutrino selection criteria.

As a result of the first run, we measured the event rates of each background component, and found that some of them are quite large, and affects sensitivity for sterile neutrino search. In particular, we observed $(1.27 \pm 0.02) \times 10^{-5}$ /spill of cosmic fast neutron (after the lifetime cut) in the IBD selection region corresponding to 9.1 times larger compared to the expected rate in reference [9]. It was also found that the total accidental background in the IBD delayed region has 10.3 times as large as the expectation in reference [9] because of relatively poor shield capability against the floor γ . Thus, we concluded that it is necessary to give countermeasures against them for the coming long term physics run. Based on the behavior of accidental background, dominated by the floor γ , it was found that changing layout of lead shield without any additional lead blocks reduces it to 1/6. For fast neutron, PSD performance upgrade by mixing DIN is examined with respect to the PSD capability. It gives 2 times larger rejection power.

Sensitivity for sterile neutrino search for 3 years experimental period was estimated based on the estimated background rate and neutrino selection efficiency from the data. It turns out that the 90% C.L. exclusion limit without the upgrades shows 80 % degradation with respect to the expected sensitivity in reference. In contrast, the sensitivity recovers to 38 % degradation compared to the expectation if we apply the upgrade as countermeasure. In case we extend experimental period from 3 to 6 years with the upgraded configuration, the sensitivity reaches to almost identical sensitivity to the designed performance within 19 %.

To explore the entire allowed parameter space, especially the low Δm^2 region favored in the global fit [4], a prospect of JSNS²-II configuration which consists of the first detector and an far detector at 48 m baseline is investigated. The background rate in the far detector is estimated using the model developed based on the first data. As a result of the sensitivity study with the double detector configuration,

the entire global fit favored region can be concluded at 90 % C.L. even with 50 % systematic uncertainty on the flux of $\bar{\nu}_e$ from μ^- -DAR background. In case we reduce the uncertainty to 10 % by a measurement of pion production cross section on mercury with 3 GeV proton, it is possible to cover the entire region of the LSND allowed parameter space at 90 % C.L.. Furthermore, the systematic uncertainty reduction leads to the 3σ C.L. sensitivity in the almost all region of the global fit indication.

Bibliography

- [1] Z.Maki, M.Nakagawa, S.Sakata, Prog. [Theor. Phys. 28, 820] (1962).
- [2] E., Ivan et al., J. High Energ. Phys. 2020, 09, 178 (2020).
- [3] A. Aguilar et al., Phys. Rev. D64, 112007 (2001)
- [4] M., Dentler et al., J. High Energ. Phys. 2018, 10 (2018).
- [5] KARMEN collaboration, B. Armbruster et al., Phys. Rev. D 65 (2002) 112001
- [6] OPERA collaboration, N. Agafonova et al., JHEP 07 (2013) 004
- [7] A. A. Aguilar-Arevalo et al. [MiniBooNE Collaboration], Phys. Rev. Lett.110.161801, 2013
- [8] A. P., Serebrov et al., JETP Letters, 112, 199-212 (2020).
- [9] M. Harada, et al, arXiv:1705.08629 [physics.ins-det]
- [10] M. Harada, et al, arXiv:1310.1437 [physics.ins-det]
- [11] <https://j-parc.jp/researcher/MatLife/ja/facilities/building.html#03>
- [12] JAEA-Technology 2011-035, (2011),
- [13] P. Vogel and J. F. Beacom. Phys. Rev. D 60, 053003, (1999),
- [14] <http://n-concept.co.jp/service/tank/>
- [15] Y. Shingo, Hiroshima University, Master Thesis (2019)
- [16] K. Yamamoto, JPS Conf. Proc. 8, 012004 (2015)
- [17] D. Nagao, PoS(FPCP2015)062
- [18] A. Ferrari et al, CERN-2005-10 (2005), INFN/TC_05/11, SLAC-R-773
- [19] S. Agostinelli et al., Nucl. Instr. Meth. A 506, 250 (2003).
- [20] T.Suzuki et.al., Phys. Rev. C 35 (1986) 2212.
- [21] M. Fukugita and T. Yanagita, Physics of Neutrinos (Springer).
- [22] <https://rat.readthedocs.io/en/latest/index.html>

- [23] <https://www.phys.ksu.edu/personal/gahs/GLG4sim/>
- [24] J. B. Birks, *The Theory and Practice of Scintillation Counting*. London: Pergamon (1964)
- [25] J. S. Park et al., *NIM A*, 707 (2013) 45–53.
- [26] E. Kolbe, *Phys. Rev. C* 54, 1741 (1996).
- [27] T. Konno, Tokyo Tech. Ph.D. Thesis (2013)
- [28] Y. F. Wang et al., *Phys. Rev. D* 64, 013012 (2001)
- [29] S. Ajimura et al, *PTEP* 2015 6, 063C01 (2015)
- [30] M. Harada, et al, arXiv:1502.02255 [physics.ins-det]
- [31] Y. Hino, *et al.*, *JINST* **14** (2019) no.09, T09001
- [32] X. Zhou et al., arXiv:1408.0877v2 [physics.ins-det],
- [33] http://www.reiko.co.jp/eng/product_film.html
- [34] https://www.hamamatsu.com/resources/pdf/etd/LARGE_AREA_PMT_TPMH1376E.pdf
- [35] https://www.hamamatsu.com/resources/pdf/etd/PMT_handbook_v3aE.pdf
- [36] J. S. Park, *et al.*, *JINST* **15** (2019) no.07, T07003
- [37] Y. Hino *et al.*, *JINST* **14** (2019) no.09, P09007
- [38] J. S. Park, *et al.*, arXiv:2005.01286 [physics.ins-det]
- [39] <https://grafana.com/>
- [40] N.A. Danilov, et al., *Radiochemistry* 49 (2007).
- [41] R. Ujiie, Tohoku University, Master Thesis (2021)
- [42] S. Meigo, private communication.
- [43] F. Tamura et al., *Nucl. Instrum. Meth. A* 647 (2011) 25.
- [44] Y. Abe, *et al.*, 2013 *JINST* **8** P08015
- [45] J. S. Park, et al, 2020 *JINST* **15** T09002
- [46] J. S. Jang, JSNS² internal note, jsns2-doc-372-v1.
- [47] E. J. Axton and A. G. Bardell, *Metrologia* 21, 59 - 74 (1985).
- [48] Double Chooz Collaboration, *JHEP* 1410 (2014) 086
- [49] Daya Bay Collaboration, *Chin.Phys.* C41 (2017) no.1, 013002.

- [50] S. Meigo et al., "Beam commissioning of spallation neutron and muon source in J-PARC", in Proceedings of PAC09, TU6PFP066, Vancouver, BC, Canada (2009), pg. 1439.
- [51] R. A. Reiter et al, Phys. Rev. Lett. 5, 22 (1960)
- [52] B. C. Nandi and M. S. Sinha, NIM B volume 40, 1972, 289-297
- [53] ZEUS Collaboration, Physics Letters B, Volume 718, Issue 3, 915-921 (2013).
- [54] J. Beringer et al. [Particle Data Group], Phys. Rev. D 86, 010001 (2012).
- [55] S. Meigo, JSNS² internal note, jsns2-doc-948-v1.
- [56] NEOS Collaboration, B. R. Kim et al., J.Radioanal.Nucl.Chem. 310 (2016) 1, 311-316
- [57] <https://www.phys.ksu.edu/personal/gahs/GLG4sim/>
- [58] J. Ashenfelter, *et al.*, JINST 14 (2019) no.03, P03026
- [59] F. P. An et al. [Daya Bay Collaboration], Phys. Rev. Lett. 108, 171803 (2012).
- [60] N. Agafonova et al., Phys. Rev. D100, 051301 (2019)
- [61] D. A. Brown, et al., Nuclear Data Sheets volume 148, February 2019, 1-142
- [62] L. Turko, arXiv:1811.05522 [nucl-ex]
- [63] N. Abgrall, et al., The European Physical Journal C volume 76, Article number: 617 (2016)
- [64] N. Charitonidis and C. Mussolini, "Possibilities for (very) low energy beams at CERN north area", NA61/SHINE at Low Energy workshop (2020).
- [65] S. Ajimura, et al., arXiv:2012.10807 [physics.ins-det]

Acknowledgement

I am thankful to Prof. Fumihiko Suekane, a supervisor of mine in my graduate course. He provided many opportunities and environments to perform studies for experimental particle physics.

I would like to acknowledge Prof. Takasumi Maruyama, a spokesperson of the JSNS² experiment. I learned a lot of things during work with him. He provided many chances to me in the JSNS² experiment. I am sure that His advice about not only physics and experiments but also life as a researcher really continuously helps me ever in the future.

I am grateful to Prof. Shoichi Hasegawa, a supervisor in JAEA scholarship. Thanks to his support, I am able to stay Tokai for three years and focus on my study. I appreciate acceptance from Hadron group in JAEA ASRC, which helps me a lot in my stay in Tokai.

Dr. Hisataka Furuta and Dr. Jungsic Park gave me a lot of knowledge about technical thing in performing studies on not only hardware but also software of the experiment. I would specially like to appreciate their great supports. Of course, I would like to acknowledge all collaborators of the JSNS² experiment, J-PARC staff and the members of research center for neutrino science. Again, I deeply thank to all people related to me for my Ph.D. degree achievement.